QUANTUM CHAOS IN THE RESONANT TUNNELING DIODE

A Thesis submitted for the Degree

of

Doctor of Philosophy of the University of London

by

Daniel Saraga

September 1999

Department of Physics & Astronomy

University College London

University of London

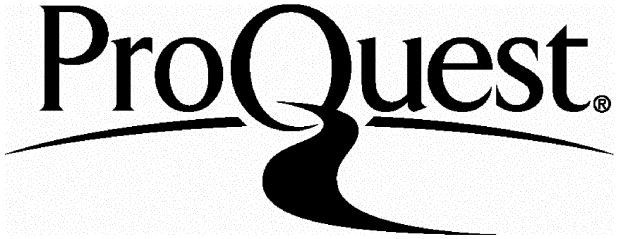

Abstract

The resonant tunneling diode in tilted fields was introduced recently as a new experimental probe of quantum chaos. However, its semiclassical interpretation in terms of classical structures (e.g., periodic orbits) remained controversial. The aim of this work is to achieve a better understanding of this system within the framework of quantum chaos. Our main finding is that the correct semiclassical description involves orbits of a new type (saddle orbits), which are complex and non-periodic.

The experimental data is analyzed in order to single out the oscillatory structure of the current. We use a simple theoretical model of the current across the diode, based on the Bardeen weak tunneling matrix element. Quantum calculations are performed, taking advantage of the scaling property of the Hamiltonian. We compare current amplitudes with experiments, and study scarring of wave functions as well as Wigner distributions. We propose a model describing the effects of tori quantization around a stable periodic orbit (PO). The classical dynamics are analyzed through Poincaré surfaces of section and a study of the relevant POs.

We develop a general semiclassical formalism for matrix elements given by a projection operator on a Gaussian. This allows us to carry out a detailed comparison of several semiclassical formulae, and to situate them within the context of general semiclassical theories of matrix elements. In particular, we discuss the different hypotheses one can make on the smoothness of the observable, as well as three levels of approximation.

PO theories are shown to be only partially successful in the description of the current across the diode. In addition to the saddle orbits, we propose another type of orbits, which are real and minimize the gradient of the phase. We show that they also give very accurate semiclassical contributions. Complex dynamics are investigated in order to calculate the contribution of complex POs and saddle orbits.

Contents

List of Tables

List of Figures

Acknowledgments

First of all, I would like to thank my supervisor, Dr Tania Monteiro, for her guidance during this PhD. She offered me a great subject, and pushed me forward through her intuition and sense of efficiency.

I would like to thank Professor Eugène Bogomolny for his warm welcome in Orsay, for enabling me to use his semiclassical formalism, and for offering me the saddle orbits *sur un plateau.*

I am also very grateful to Daniel Rouben, who gave me invaluable help with the numerical implementation of complex dynamics, the ghost hunt, and the developement of the cubic integration formula.

I wish to thank Evgueni Narimanov, for spicing up the semiclassical debate and for his patience in long emails. Greg Boebinger kindly provided us with a lot of unpublished data. Thanks to Dominique Delande for discussions and support.

Cheers to Paul Dando for office sharing, update on the cricket and useful discussions. Thanks to Paul Walker for office sharing and in-depth conversations. He helped me through many discussions on quantum chaos, complex dynamics and mesoscopics.

* * *

Sophie was the coolest office mate possible. Steve was warmer, but *ein fantastiche Mann.* Thanks to: the Italian *donne* Orsola, Serena and Silvia, oriental Aysun, *INTP-ish* Alexia, the *frogs* Luc, Franck and Stéphane, Diego, successful Bernhardt, the local men Keith and Chris, and the almost local one Mike.

Thanks to my family for love, support and giving me a real education, and to my brother for, well, being my brother.

I am grateful to the Swiss National Science Foundation and the Federal Office for Education and Science for a scholarship from the TMR program.

Chapter 1

INTRODUCTION

1.1 Motivations

The resonant tunneling diode in tilted fields (RTD) is a new experimental probe of quantum chaos, which was not fully understood when this work was started. Recent studies had shown very interesting effects, such as current oscillations related to unstable periodic orbits (Fromhold *et al.* 1994), manifestations of bifurcations (Muller *et al.* 1995), strong scarring (Wilkinson *et al.* 1996), and contributions from complex periodic orbits (Monteiro and Dando 1996). The interpretation of the experimental current was based on a "periodic orbit picture", involving heuristic arguments related to the Gutziller trace formula (Gutzwiller 1990) and the accessibility of the trajectories. However, the analysis of this system within the context of quantum chaos remained controversial.

The first goal of this work was to achieve a better understanding of the manifestations of quantum chaos in the RTD, and unambiguous interpretations of the experimental features. The starting point for a better *qualitative* picture was the study of the classical dynamics, systematic quantum calculations and the analysis of experimental data, to be used in conjunction with the heuristic approach based on the Gutzwiller trace formula.

This evolved into the more ambitious aim of reaching a *quantitative* description of the quantum and experimental behavior in terms of classical objects. For this, we shall need to **test, improve and propose semiclassical theories** for the current in the RTD.

1.2 Quantum chaos

The field of *quantum chaos* denotes the study of quantum systems whose classical counterpart exhibits chaos. Integrable systems form a very limited class, where there are as

many constants of motion in involution as there are degrees of freedom. In this case, the classical motion is confined on phase space tori. In chaotic[1] systems, there are not enough constants of motions and the dynamics are characterized by unstable trajectories, which are defined by an exponential (as the time t evolves) sensitivity to initial conditions. The trajectories can be ergodic, meaning that they fill all the available phase space. The only invariant structures are *periodic orbits* (POs), which end with the same position q and momentum p as they started. POs can be stable or unstable, and can only change their stability in bifurcations, where several POs coalesce.

In quantum mechanics, the Heisenberg uncertainty principle prohibits the notion of a trajectory (the exact knowledge of p and q at any given t). The unitary quantum evolution implies conservation of probability and the fact that the overlap between two wave functions is time-independent. Hence it is hard to consider a quantum equivalent to the classical notion of exponential sensitivity.

The correspondence principle states that somehow one should expect quantum mechanics to reflect classical mechanics when one approaches a macroscopic level. The *semiclassical* regime is at the interface between the two theories, and consists of the study of a dynamical system within the framework of quantum mechanics, specifically for states having very high energies. More precisely, it is defined when the typical classical actions are much larger than Planck's constant: $S \gg \hbar$, alternatively referred to as the $\hbar \to 0$ limit. This limit is singular (Berry 1989), meaning that quantum mechanics is not simply a wider theory encompassing classical dynamics; however, one still hopes to see some connections.

1.3 Semiclassical physics

Broadly speaking, there are two distinct approaches to semiclassical theories in the context of quantum chaos. The first one is *random matrix theory* (see e.g. Mehta 1991), based on the assumption that the chaotic nature of the dynamics can be modeled using a purely statistical approach. The results deal with statistical quantities such as correlations of the density of states or the level spacings distribution. Although initially developed by Wigner in 1961 for nuclear physics, it was found that this technique could be applied to

[1] In this work we shall study chaotic systems with *mixed dynamics*, i.e., whose phase space contains both chaotic and regular regions; this is what we mean by "chaotic systems". We shall never consider "hard chaos", where all the trajectories are unstable.

any generic chaotic system, reaching a certain level of universality.

On the other hand, the approach of *periodic orbit theory* uses specific characteristics of the chaotic system. One can expand a quantum solution as a power series of $\hbar$, and finally express the quantum object in terms of entirely classical quantities. This scheme was first derived for the one-dimensional (hence integrable) case. The WKB approximation (see e.g. Landau and Lifshitz 1977) states that the wave function ψ_n of an eigenstate of energy E_n can be approximated by

$$\psi_n(x) = \frac{C}{\sqrt{p(x)}} e^{iS(x_0,x;E_n)/\hbar} \quad , \tag{1.1}$$

where $S(x_0, x; E_n) = \int_{x_0}^{x} dx' p(x')$ is the classical action. It yields the Bohr-Sommerfeld quantization rule $S(E_n) = 2\pi\hbar(n + 1/2), n \in \mathbf{N}$. In its generalization to N-dimensional integrable systems called EBK (see e.g. Brack and Bhaduri 1997), the energy is quantized via the N action integrals defined on the N independent and irreducible closed loops $\mathcal{C}_j$ around the tori:

$$S_j(E) = \int_{\mathcal{C}_j} dq\, p = 2\pi\hbar\,(n_j + \mu_j/4) \quad , \quad n_j \in \mathbf{N} \quad , \quad j = 1, .., N \quad , \tag{1.2}$$

where μ_j are Maslov indices. The wave functions can also be built from the tori, using a N-dimensional WKB approximation. The density of states $d(E) = \sum_n \delta(E - E_n)$ arising from EBK can be written (Berry and Tabor 1977) as a sum over the contributions of each rational torus, which comprises of a continuous family of periodic orbits.

The quantization of non-integrable systems was pioneered by Gutzwiller (1990). It starts from the Feynman formulation of quantum mechanics, where the propagator $\langle q'|\exp(i\hat{H}t/\hbar)|q\rangle$ is expressed as a path integral ($\hat{H}$ is the quantum Hamiltonian). It is a sum, taken over all paths joining q to q', of an oscillating function $\exp(iW/\hbar)$, where W is the time integral of the classical Lagrangian along the path. In the semi-classical limit, one can use the *stationary phase approximation* (SPA): when $W/\hbar$ is large, one can expect most paths to interfere destructively; only the paths for which W is stationary contribute to the propagator. From Hamilton's principle, we know that these paths are the paths allowed by the classical dynamics. This semiclassical propagator can be Fourier transformed to give a semiclassical expression for the energy Green's function in terms of all the classical trajectories joining q to q'; in 2-D it reads $G(q', q) = \langle q'|(E - \hat{H})^{-1}|q\rangle \overset{\hbar\to 0}{\propto} \sum_{q\to q'} m_{12}^{-1/2} \exp[iS(q, q')/\hbar]$, where m_{12} is an off-diagonal element of the monodromy matrix M describing the stability of each trajectory. Gutzwiller evaluated its trace by SPA to express the density of states as a sum of two terms. The

Weyl term

$$\bar{d}(E) = (2\pi\hbar)^{-N} \int dq\, dp\, \delta[E - H(p,q)] \tag{1.3}$$

has a smooth dependence on the energy E and is given by the ratio of the phase space volume of the energy shell E to the volume occupied by each quantum state. The second term oscillates with E, and is given by the contribution of all the classical periodic orbits (in 2-D):

$$d_{\rm osc}(E) = (\pi\hbar)^{-1} \sum_{\rm PO} T|{\rm Tr}M - 2|^{-1/2} \cos(S/\hbar - \mu\pi/2) \quad , \tag{1.4}$$

which is called the *Gutzwiller trace formula* (GTF). Each periodic orbit (PO) contributes to an oscillatory term, whose frequency is given by the period $T = \partial_E S$ of the PO, while the amplitude is determined by the stability of the PO. A constant phase arises from the number of caustics μ along the PO.

Miller (1975) extended the GTF in the case of a stable PO, and found a quantization scheme similar to EBK, with wave functions localized on *quantized tori* around the PO. More surprising was the finding that wave functions could also exhibit a concentration of probability around unstable periodic orbits; this phenomenon was called scarring (Heller 1984).

1.4 The hydrogen atom in external fields

The main experimental probe of quantum chaos was for a long time the hydrogen atom in a magnetic field (with or without an electric field). It has been extensively studied and has exhibited number of phenomena that can guide our understanding of quantum chaos in the resonant tunneling diode (RTD).

Very accurate spectroscopy experiments can indirectly probe the density of states (DoS) of the hydrogen atom, by measuring the photoabsorption spectrum (the probability of having an electronic transition from the ground state to an excited state). The measured observable can be expressed as the DoS, weighted by the matrix element describing the transition. As the matrix element involves the ground state wave function which is very localized on the nucleus, the semiclassical theory (Du and Delos 1988, Bogomolny 1989) selects specific closed orbits (starting and ending at the nucleus), instead of the POs found in the GTF of the DoS.

The scaling property of the system means that it is possible to change the classical dynamics independently from the semiclassical regime (defined e.g. by the number of nodes

of a typical wave function). Alternatively, one can generate a spectrum corresponding to a single classical regime; its clean Fourier transform enables one to find precisely which closed orbit (CO) is responsible for a given oscillation.

Effects "beyond PO/CO theory" were studied. Bifurcations were found to have an influence on the experimental and quantum spectrum, in the form of enhancements of the related modulations (Main *et al.* 1994). Oscillations due to "ghost" orbits (complex POs found after a tangent bifurcation has removed a pair of real POs) were observed experimentally, although their effect is very weak as it is exponentially damped [$\propto \exp(-S_I/\hbar)$] by the imaginary part of the action S_I, both in the semiclassical limit and away from the bifurcation (Delande *et al.* 1994). Diffraction effects appeared in Rydberg atoms, where the inner electrons shell (described by quantum defect theory) is a quantum mechanical structure with a size smaller than the de Broglie wavelength of the semiclassical electron. It connects COs which would not be connected classically, yielding extra oscillations in the spectrum (Dando *et al.* 1998).

1.5 Mesoscopic experiments

The RTD belongs to the family of *mesoscopic* systems, which are solid-state systems small enough to retain quantum coherence. Recently, studies of electronic transport in mesoscopic systems exhibited a range of non-classical effects linked to the quantum interference of the electrons. The coherence length l_ϕ (the average length over which an electron can retain coherence) is limited by inelastic processes, such as electron-electron interaction and electron-phonon scattering. At low temperature, l_ϕ can be larger than the size L of the sample, which is typically around 1 μm.

Initially mesoscopic physics focused on disordered metals, where the motion of the electrons is diffusive: the elastic mean free path l_{mfp} (the average distance traveled by an electron before being scattered by impurities) is smaller that L. The quantum interference has two main effects on the transport properties. In *universal conductance fluctuations*, the conductance (as a function of energy) is found to have fluctuations around the classical conductance; its variance appears to be similar whatever the system. In *weak localization*, the average conductance has a minimum at zero magnetic field. The theoretical approach is based on statistical results; it models the disorder by random potentials, and also uses diagrammatic perturbation theory and supersymmetry methods (see Efetov 1997 for a review).

Technological advances in high-mobility semiconductor heterostructures brought the two-dimensional electron gas. This allowed for cleaner structures with less impurities, called *ballistic* when $l_{\rm mfp} > L$. The semiclassical regime is reached when the typical Fermi wavelength in the structure is much smaller than L. This leads naturally to the use of semiclassical expansions and to PO theories. A good review can be found in Richter (1997).

One can design lithographically billiard-like electrons cavities, attached to leads. The Landauer formula states that the conductance measured from one lead to the other can be expressed by the related transmission coefficients t_{nm}:

$$\mathcal{G}(E) = 2e^2/\hbar \sum_{n,m} |t_{nm}|^2 \quad , \quad t_{nm} \propto \int dy' \int dy \;\; \phi_n^*(y)\phi_m(y')G(x=0,y;x'=L,y') \, , \quad (1.5)$$

where $\phi_n(y)$ and $\phi_m(y')$ are the transverse functions in the incoming lead (at $x = 0$ in the $n^{\rm th}$ channel) and out-going lead (at $x' = L$). Using semiclassical approximations, the conductance may be expressed in terms of open "angle orbits" (see below). Universal conductance fluctuations were explained by considering the statistical distribution of the times spent by the trajectories in the cavity (see Baranger 1997). Quantum mechanical interference of time-reversed paths could explain weak localization effects (Baranger *et al.* 1993). On the other hand, it was noted that the effects on integrable systems depend strongly on the device. Antidot superlattices were also studied; they are arrays of periodically arranged "holes" acting as repulsive pillars. Peaks in the magneto-resistivity could be related to classical trajectories making cyclotron motion around a given number of pillars (Richter 1997).

1.6 Semiclassical matrix elements

Experiments cannot probe directly the density of states (DoS), but can measure an observable that gives indirect information. In a number of situations, one can express the measured observable $I(E)$ by the DoS weighted by the expectation value of an observable $\hat{A}$ (a diagonal matrix element):

$$I(E) = \sum_i \langle\psi_i|\hat{A}|\psi_i\rangle \delta(E - E_i) = -\frac{1}{\pi}\mathbf{Im} \int dq \int dq' A(q,q')G(q',q) \quad . \quad (1.6)$$

In the case of the RTD, $I(E)$ is the current flowing across the diode. To derive a semiclassical theory, one uses the semiclassical form for $G(q',q)$, as well as the stationary phase

approximation (SPA) to the integral above. Applying the latter can be non-trivial, because of the interplay between $A(q,q') = \langle q|\hat{A}|q'\rangle$ and $G(q',q)$. The result depends on the level of localization of $A(q,q')$ in position, momentum or phase space, compared to the oscillations of the semiclassical Green's function. Also of importance is the *level* of approximation used in conjunction with the SPA method. For example, one can neglect $A(q,q')$ in both the SPA *condition* and *integration*, or only in the latter, or in none. The general form of the semiclassical formulae is

$$I(E) \overset{\hbar\to 0}{\simeq} \sum_{\text{contr. orbits}} \mathcal{A}\exp(iS/\hbar) \quad , \tag{1.7}$$

where $\mathcal{A}$ is an amplitude determined by $\hat{A}$ and the stability of the contributing orbits. Several theories have been proposed before the study of the RTD began.

PO theory In the first theory, proposed in Wilkinson (1987) and Eckhardt *et al.* (1992), one assumes that the Wigner transform $A_W(p,q)$ of $\hat{A}$ is smooth in *phase space*, and can therefore be neglected in the SPA applied to (1.6). The contributing trajectories are then periodic orbits, and the observable is expressed, in the semiclassical limit, as the GTF weighted by the average of A_W taken over the PO. This result has been used for example in calculations of molecular transitions.

CO theory Du and Delos (1988) developed a semiclassical expression for the photoabsorption spectrum of a hydrogen atom in external field. As mentioned in page 17, the operator describing the transition of the electrons is very localized on the nucleus, and selects which trajectories can contribute to the spectrum: orbits that are closed at the nucleus [$q = q' = 0$], called closed orbits (COs). As one does not integrate over the Green's function, $\mathcal{A}$ contains $|m_{12}|^{-1/2}$ —instead of the prefactor $|\mathrm{Tr}M - 2|^{-1/2}$ found in the GTF or the PO theory.

Extension of PO theory In their work on molecular transitions, Zobay and Alber (1993) realized that the assumption that $\hat{A}$ is smooth in phase space is not compatible with its form as a projector on Gaussian wave functions. They included the variation of $A_W(p,q)$ in the integration, but still neglected it when deriving the SPA condition, which therefore gave POs.

Angle orbits Evaluating semiclassically the conductance in a microstructure, Baranger *et al.* (1993) applied the SPÀ to (1.5) taking into account *both* $G(y',y)$ and $A(y,y')$ (the

product of the lead functions ϕ_n). The condition selected "angle orbits" satisfying the condition $\sin\vartheta = \pm n\pi/kW$, where ϑ is the initial angle of the orbit, W the width of the lead, k the wave vector of the lead function and n its level. They also included the lead functions in the integrations.

1.7 Complex dynamics

Certain semiclassical formulae developed in this work will express the current in terms of complex orbits.[2] Complex dynamics have been used in semiclassical physics in order to describe tunneling phenomena in a range of different situations: tunneling through a barrier in the context of semiclassical scattering matrix theory (Miller 1974), tunneling between KAM tori (Takada *et al.* 1995), energy splitting in an ergodic double well (Creagh and Whelan 1999), chaos-assisted tunneling in an annular billiard (Frischat and Doron 1998) and in a kicked rotor (Shudo and Ikeda 1998). Complex trajectories also appear in the semiclassical expression for the time propagator in phase space (Xavier and de Aguiar 1997).

On the other hand, complex POs contributing to the GTF have been noticed and baptized "ghosts" in Kuś *et al.* (1993). In the simple model which was studied, they could be expressed analytically, as in Atkins and Ezra (1994). Ghosts have been calculated numerically for the hydrogen atom (Main and Wunner 1997). One could argue that ghost orbits are related to a tunneling phenomenon, the trajectory "borrowing" (invoking the uncertainty principle) a small amount of energy in order to be above the bifurcation, where a real PO exists. However, the GTF and tunneling describe two different situations, whose connection is not obvious to demonstrate.

1.8 The resonant tunneling diode

1.8.1 The Nottingham experiments

The study of quantum chaos in the resonant tunneling diode (RTD) started in Fromhold *et al.* (1994). In contrast to standard RTD experiments, the Nottingham group applied a strong magnetic field $\boldsymbol{B}$ to a RTD at a *tilt* angle $\theta \neq 0°, 90°$ relative to the normal of the barriers: this brought chaos to the classical dynamics. The resonant tunneling condition

[2] By "complex" we mean *in the complex plane*, not "complicated".

implies that one can experimentally probe the density of states by measuring current-voltage $I(V)$ traces, which exhibit quasi-periodic resonances sensitive to θ. The main physical considerations were stated. Firstly, the wave function describing the electrons prior to tunneling (the "initial state") is quantized in the lowest Landau level by the parallel component of $\boldsymbol{B}$. Secondly, phonon scattering induces decoherence and damps exponentially the current (with a coherence time $\tau \simeq 0.1$ ps). Thirdly, only classical trajectories which are *accessible* to the tunneling electrons can contribute. Fourthly, non-parabolicity implies an effective mass that is dependent on the voltage, and biases the comparison of experiments with theoretical calculations.

The key point was to *relate the resonances to unstable periodic orbits*, by analogy with the GTF. Each PO would give an oscillation in $I(V)$, with a voltage period ΔV given by the inverse of the period of the PO. In particular, they identified the PO t_0, related to the straight traversing PO at $\theta = 0°$ and giving periods $\Delta V \simeq 0.04$ V, and the PO s' with $\Delta V \simeq 0.02$ V. The results consisted of a comparison between the theoretical voltage periods (from classical dynamics) and the experimental ones, as well as a comparison of the $V - \theta$ domains of existence of the POs with the domains of their related experimental oscillations. As the experiments were made with a strong magnetic field, they probed the regime of strongly chaotic dynamics. The width of the RTD in these experiments was $L = 120$ nm.

This study was followed by experiments with a narrow well of width $L = 60$ nm (Fromhold *et al.* 1995a), which enabled the resolution of longer POs. The POs 1:3 and 1:4 were identified, and linked to oscillations with smaller voltage periods (a n:m PO makes n/m bounces with the emitter/collector barrier). Wide oscillations at high voltage were linked to stable trajectories; however, the comparison of theoretical and experimental periods did not show very good agreement in this case.

The next step taken by the Nottingham group was to perform numerical calculations to solve the related quantum mechanical problem (Fromhold *et al.* 1995b). They calculated energy levels of the closed quantum well, considering infinitely high barriers. They found that some eigenfunctions related to regularly spaced levels were *scarred* by (i.e., localized on) unstable POs, namely t_0 and s'. They related the number of nodes of the wave functions to the classical action of the PO by a quantization rule similar to Bohr-Sommerfeld. The probability distribution of the spacings of the energy levels was found to follow the Wigner form predicted by random matrix theory.

Crucially, they introduced a *model for the current* in the RTD; they used the transfer matrix element of Bardeen (1961), which weights each energy level by an overlap between the initial state and the eigenstate in the well. Using barriers of finite height, they found that levels which had a high matrix element were also scarred by POs.

1.8.2 The Bell Labs experiments and the beginning of controversy

Shepelyansky and Stone (1995) initiated the more theoretical approach to the RTD, by studying analytically and numerically the classical dynamics. They investigated two limits, when the energy E of the electrons is much higher, or smaller, than V; they related them to standard chaotic systems, such as the Fermi acceleration model and the standard map. They found that in those limits the classical dynamics does not depend on the independent values of V and B, but on their ratio $B/\sqrt{V}$. In particular, they identified $B - V$ lines of transition to chaos.

At the same time, Müller *et al.* (1995) from Bell Laboratories carried out similar RTD experiments, but recorded a much larger number of $I(V)$ traces. They varied the experimental parameters θ, L and in particular the magnetic field strength B in a systematic way, in contrast to the Nottingham group; this proved to be essential for comparisons with the transition lines identified in Shepelyansky and Stone (1995). They identified regions of period-two and three oscillations[3] (i.e., where ΔV is divided by two and three with respect to the broad and regular t_0 oscillations at $\theta = 0°$) in the $V - B$ parameter plane for different θ. They interpreted them as a manifestation of period-two (P2) and three (P3) *bifurcations* of the stable PO t_0, showing that the lines in the $V - B$ plane corresponding to the latter were close to the experimental regions —however, they got the period-two bifurcation line wrong. They pushed forward the idea of classical scaling, which they tested by comparing characteristics of wells of different widths; they also compared voltage periods. Their interpretation favored contributions of stable POs over unstable POs. Note that for the classical dynamics they worked in the low energy limit, which corresponds to the neglect of collisions with the emitter barrier.

The controversy of the interpretation of the current in the RTD in terms of classical POs started when the Nottingham group contested in Fromhold *et al.* (1997a) the findings of Müller *et al.* (1995). They emphasized the importance of the accessibility, that they

[3]They denoted these regions "peak-doubling" and "peak-tripling". We introduce here the denotation "*period*-doubling/tripling", as the underlying classical POs have double/triple-periods than t_0. The voltage periods ΔV are divided by two/three.

assessed using a classical distribution of the tunneling electrons. They also criticized the neglect of the emitter barrier: the PO 0:3 linked to the period-three bifurcation of t_0 at $\theta = 38°$ cannot contribute to the current as it does not have any contact with the emitter, a fact supported by calculations of the tunneling matrix element of the quantum states associated with this PO. They argued that another PO (1:3), which is not linked with the P3 bifurcation, is accessible to the tunneling electron and can therefore explain the experimental P3 oscillations. They agreed that the main P2 region at $\theta = 11°$ is a manifestation of the P2 bifurcation of t_0, but contested the role of its bifurcations in other cases because of its lack of accessibility.

The Bell Labs group replied in Boebinger *et al.* (1997), helped by the theoreticians Narimanov and Stone from Yale. They argued that the inclusion of the emitter barrier did not change the features of the bifurcations of t_0. They contested the accessibility criterium of the Nottingham group, arguing that the initial state also contains excited Landau levels, giving some accessibility to otherwise unaccessible POs. They noted that at $\theta = 38°$ the period-one oscillations (P1) extended to the P3 region, showing that the P1 PO t_0 (and therefore its bifurcations) has to be accessible. They stood by their interpretation of the P2 regions at $\theta = 11°$ and $\theta = 27°$ in terms of POs linked to bifurcations of t_0. Finally, they noted that a proper semiclassical theory of the current in the RTD was needed to assess unambiguously the role of the classical POs.

Another contribution on the theoretical side came in Monteiro and Dando (1996). The ratio $V/\sqrt{B}$ found in the large/small E limit by Shepelyansky and Stone (1995) was generalized to any situation, especially the more realistic model with both barriers: the dynamics could be *scaled* with respect to the magnetic field. Scaled quantum mechanical calculations were performed and Fourier transformed (FT) to obtain power spectra of the DoS. Because of the scaling, the latter were very clean, and the positions of most (~ 10 for each FT) of their peaks could be related precisely to the scaled action of POs. This was the beginning of a more systematic study of the classical POs in the RTD. The small contribution of a ghost (complex) PO was identified below the tangent (P1) bifurcation of t_0.

The Nottingham group extended their work in Wilkinson *et al.* (1996) and in the review Fromhold *et al.* (1997c). They included non-parabolicity in their calculations, and compared experimental and quantum mechanical $I(V)$ traces at fixed B. The effect of scattering on POs was studied by an adding ionized impurities. They calculated quantum

mechanical regions of P3 at $\theta = 38°$, and identified strong scarring by 1:3. Finally, they carried out experiments with a very narrow well ($L = 22$ nm) in order to increase the separation of the energy levels above the energy broadening due to phonon scattering. That way they identified contributing individual states that were scarred by POs, while in a wider well individual states could not be resolved experimentally. Hence they claimed that the RTD was "the only quantum system in which a periodic effect originating from individual scarred eigenstates is observed in experiments".

This claim was commented on by Monteiro *et al.* (1997b), who argued that the individual states of the very narrow well are not scarred in the proper sense. The fact that they are very low in the spectrum implied that the usual assumptions of semiclassical physics were not satisfied, in particular the random phase cancellations due to the action. It was argued that the scarring PO was not isolated because of its low action. The reply (Fromhold *et al.* 1997b) continued the debate about the proper definition of scarring, and argued that one could, following the literature, consider low energy states.

1.8.3 Theoretical contributions

This was the state of affairs when this PhD was started in September 1996. From then on some work had to be done by theoreticians: in order to clarify the relationships between experimental features and classical POs, one needed to develop a semiclassical theory for the current in the RTD.

Monteiro *et al.* (1997a) showed that the oscillatory part of the tunneling current is essentially independent on the details of the emitter barrier, such as its width or height. Scaled quantum calculations for the current were performed, using infinitely high barriers. They were then broadened and compared to experimental traces. It was found that different classical regimes (e.g., involving tori quantization, bifurcations or ghosts) give typical $I(V)$ traces. In this way, the period doubling bifurcation of t_0 at $\theta = 11°$ was located precisely in the experiment (as well as confirmed); the difference with the theoretical model was attributed to the voltage dependence of the mass. The other experimental P2 region at $\theta = 11°$ was not attributed to a bifurcation of t_0, but to the period-two PO s_1, as the Fourier transform of the scaled current spectrum peaks at the scaled action of s_1 (and not $2t_0$). Finally, the importance of the tangent bifurcation of t_0 was emphasized: it removes this P1 orbit, leaving no real PO contributing to the experimental and quantum P1 oscillations. It was proposed that a *ghost* (a complex PO) could be responsible for

oscillations which persist over a wide range of experimental parameters.

In Narimanov and Stone (1998b), the Yale group carried out an exhaustive analysis of the classical dynamics of the RTD, with or without the emitter barrier. They described how the shortest POs originated from resonances appearing at $\theta = 0°$, and pointed out the cusp bifurcation, a non-generic type of bifurcation due to the non-analyticity of the hard walls.

Narimanov and Stone (1998a) was a study of the strong scarring observed in the RTD. It was found that the cusp bifurcation yields a "metastability": certain orbits [e.g., s' or 1:3] cannot become extremely unstable as they are born and die in bifurcations where they cannot be very unstable.

In Saraga and Monteiro (1998b), we carried out systematic scaled quantum calculations at $\theta = 11°$ and $\theta = 27°$, which provided us with quantum amplitudes of the oscillations. We analyzed experimental data from Bell Labs and extracted experimental amplitudes that we showed could be described quantitatively by the quantum model. We applied the first semiclassical theory proposed in Bogomolny and Rouben (1998), which expressed the current in terms of normal orbits (perpendicular to the emitter wall). This theory did not include the variation of the Gaussian over the integrations. The comparison of semiclassical and quantum amplitudes across the whole transition from regularity to chaos showed that the semiclassical theory did not yield accurate results. We suggested the presence of effects "beyond" standard PO theory. We proposed a model taking into account tori quantization, which was in very good agreement with quantum calculations in regimes with a large stable island. It also explained "jumps" in the experimental period-one oscillations. We pointed out the contribution of two non-isolated POs ($2t_0$ and s') for the P2 region at $\theta = 27°$, as well as the persistent amplitudes of the quantum and experimental oscillations in the region where no real PO could be found, and where a ghost was suspected.

Narimanov *et al.* (1998b) was the most important contribution from the Yale group. They presented a semiclassical theory for the current in the RTD, starting from the Bardeen matrix element. Taking into account the localization of the initial state's Gaussian, they found that the contributing trajectories had to be *periodic orbits*. They included the Gaussian in the stationary phase-type integrations. Because they kept a generic expression for the initial state (they did not assume the lowest Landau level), they found a result in terms of an overlap integral. They showed that the summation over the repeti-

tions of a stable PO reproduces tori quantization effects. They performed the summation for an unstable PO in a similar fashion, and found that each PO contributes to a cluster of states, the instability of the PO acting as a sort of intrinsic level broadening. They compared individual $I(V)$ traces with experimental traces, and found good agreement. Finally, they used their semiclassical theory to assess qualitatively the regions of the parameter space where certain POs could contribute to the current. In this way, they explained the gap between two experimental P2 regions seen at $\theta = 31°$ by an "exchange bifurcation" taking place between four POs of the s'-type.

Bogomolny and Rouben (1998) from Orsay, Paris, provided us with the first semiclassical theory which we showed to be inaccurate. After discussing with them the importance of tori quantization effects, they included the variation of the Gaussian in the trace integrations and found another formula, which still expressed the current in terms of normal orbits (same paper). They showed the analytical equivalence between their formula and our tori quantization model for the current. Bogomolny and Rouben (1999) is an extended version of this work [see also the unpublished thesis of Rouben (1997)].

We tested this theory in Saraga *et al.* (1998). We showed that one could get a quantitative agreement with quantum results over a large range of classical dynamics. We exposed a shift (from the scaled action) in the frequency of the oscillations. The formula failed where $2t_0$ and s' are not isolated. Using complex dynamics, we found numerically the ghost PO at $\theta = 11°$ and showed that its contribution to the formula is too small to explain the quantum oscillations. Finally, we mentioned the equivalence of the normal orbit formula of Bogomolny and Rouben (1998) with the PO formula of Narimanov *et al.* (1998b), in the case of normal POs.

We pursued our work and showed (Saraga and Monteiro 1998a) that one needs a new type of orbit in order to achieve a satisfactory semiclassical description of the current. The *saddle orbits*, which are complex and non-periodic, were successful in both regions of failure of the normal orbit theory. They also showed a persistence in the classical limit, a surprising fact for complex trajectories.

In an extended version of their previous work, Narimanov and Stone (1999) proposed two other formulae to be used in the regions of failure of the PO theory. One expresses the current in terms of orbits closed at the center of the Gaussian. The second formula involves closed orbits having a minimal momentum transfer at the emitter barrier.

1.9 Plan of this work

We describe the experimental setup in chapter 2, and discuss a treatment of the data provided by Bell Labs (Muller *et al.* 1995). We present a large quantity of normalized $I(V)$ traces at $\theta = 11°, \theta = 27°$ and $\theta = 38°$, that we use to extract amplitudes and voltage periods.

We study the classical dynamics in chapter 3. We introduce the scaling, and discuss the behavior of the important POs (i.e., relevant to the experiment) as the dynamics vary from regularity to chaos. We interpret the accessibility and stability of the POs from a heuristic semiclassical perspective.

Quantum dynamics are discussed in chapter 4. We present wave functions and phase space distributions to illustrate generic situations of the RTD. We propose a semiclassical model for the current that takes into account tori quantization effects.

In chapter 5 we derive a general semiclassical formula for the current. We discuss the different possibilities for the contributing orbits: normal, periodic, closed, saddle or minimal orbits. We discuss the scaling and the voltage periods.

Chapter 6 consists of tests of the different semiclassical theories. We compare them with quantum results, for the amplitudes and the frequencies of the oscillations.

In chapter 7, we present the experimental results and compare them with quantum and semiclassical results. We also discuss problematic regions: at $\theta = 20°$ where the saddle orbit formula diverge, and at $\theta = 38°$ where the theoretical model fails to describe the experimental period-three signal.

We describe in chapter 8 the complex dynamics needed for ghost and saddle orbits. We discuss the ghost contribution, and present a cubic integration of the normal orbit formula near a tangent bifurcation. We also present a cubic approximation of saddle orbits around POs.

Chapter 2

THE RTD EXPERIMENTS

The Nottingham group was probably the first to apply a tilt angle to a resonant tunneling diode (Fromhold *et al.* 1994). Here we shall use exclusively the experiments made at Bell Labs by Müller *et al.* (1995), as they systematically varied the magnetic field, enabling comparisons with the scaled dynamics. In this chapter, we state the main physical considerations, describe our treatment of the data, and present *normalized* oscillatory traces at $\theta = 11°, \theta = 27°$ and $\theta = 38°$. We shall use them to extract amplitudes and periods, that we shall compare to quantum and semiclassical results in chapter 7. Note that we do not present traces at $\theta = 16°$ and $\theta = 20°$.

2.1 The experiments

2.1.1 Experimental setup

We start by describing how a double-barrier resonant tunneling diode is made, following Boebinger *et al.* (1993). Fig. 2.1 presents a schematic view. Different layers are grown on undoped semi-insulating GaAs substrates by molecular-beam epitaxy. First a wide emitter contact layer of n-type SiGaAs is deposited, followed by a GaAs setback layer. This is to ensure minimal diffusion of the Si impurities (which are the donors of the electrons) into the double-barrier structure; this enables very clean devices with little electron scattering by impurities (i.e., a large mean free path). A first tunnel barrier is created by an AlAs layer. The difference in the band-gap energies in the GaAs-AlAs heterostructure creates a triangular well and a barrier. This first well confines the electrons in a narrow channel in the X direction (perpendicular to the layers): the electrons accumulate in the triangular well in the form of a two-dimensional electron gas (2DEG) in a plane parallel to the layers

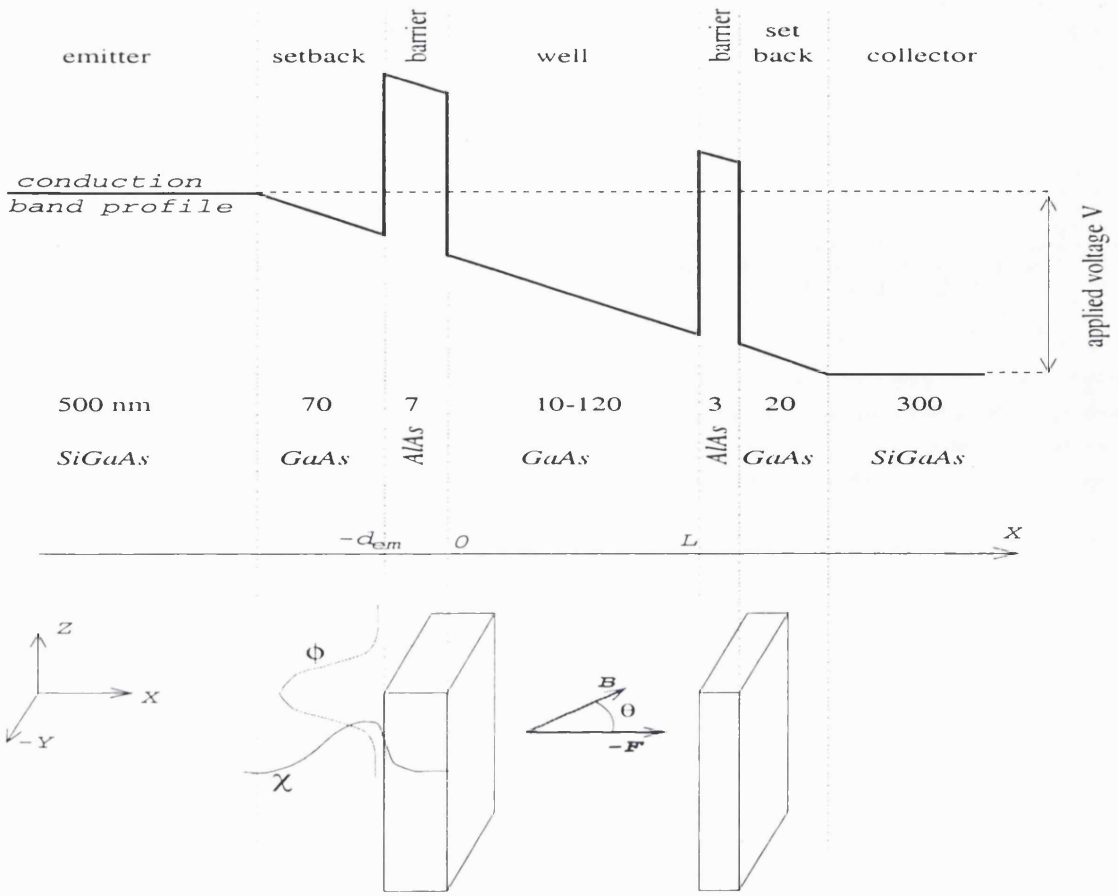

Figure 2.1: Schematic diagram of the RTD. We show the experimental setup (not to scale), with the conduction band profile and the different layers of semiconductors (with their thickness in nm). Below is the 3-D coordinates axis; the magnetic field $\boldsymbol{B}$ is at tilt angle θ with the electric field $-\boldsymbol{F}$ in the $X-Z$ plane. We also show a representation of the distribution of the electrons in the setback: a Gaussian distribution ϕ in Z due to the magnetic field $B\cos\theta$, and an Airy function χ in X due to the triangular well [see (5.14)]. The width of the well is $L = 120$ nm $= 2267$ a.u..

$(Y-Z)$. The (second) quantum well consists of a GaAs layer; it is followed by another AlAs barrier, a GaAs setback layer and a SiGaAs collector contact layer. A voltage V is applied between the emitter and the collector, creating an electric field $-\boldsymbol{F}$ across the diode, in the X direction.

The electrons provided by the emitter are attracted by the electric field and accumulate before the emitter barrier as a high-mobility 2DEG; then they pass through the barrier by the tunneling effect and enter the (nominally empty) quantum well. There they bounce back and forth against both barriers, before passing through the collector barrier and going to the collector, giving rise to a current I across the whole device.

In the experiments of interest to us, a large magnetic field $\boldsymbol{B}$ is also applied, at a tilt angle θ to the direction of the electric field. The $\boldsymbol{B}-\boldsymbol{F}$ plane defines the $X-Z$ coordinates. The classical motion of the electrons in the quantum well is chaotic for $\theta > 0°$. Note that from now on we shall call the setback layer "emitter".

2.1.2 Physical considerations

We present here some physical considerations, some of which (e.g., the scaling) will be discussed in more detail in the following chapters. The aim is to obtain a heuristic approach to interpret the experimental results. The width of the quantum well will always be $L = 120$ nm $= 2267$ a.u..

2.1.3 Energy-voltage ratio

The energy E of the 2DEG is given by the energy of the emitter contact as a result of their thermal equilibrium (as the tunneling is weak) (Fromhold *et al.* 1994). We measure the energy from the quantum well side of the emitter barrier ($X = 0$). As the voltage also acts across the setback, E changes with V; their ratio

$$R = \frac{E}{eV} = \text{constant} \tag{2.1}$$

is constant, and is given by the ratio of the setback + barrier thickness to the length of the whole device (Fromhold *et al.* 1994).

Alternatively, Müller *et al.* (1995) and Boebinger (1993) measured the $E-V$ dependence at $\theta = 0°$. Their result is different and yields $R = 0.15$. This is the value we shall consider in this work.

2.1.4 The initial state

The magnetic field also acts in the emitter region, and quantizes the Z degree of freedom of the 2DEG into Landau levels. At the energies considered, most of the electrons are in the lowest Landau state (Fromhold *et al.* 1997c), which has a Gaussian distribution in the plane of the barrier. In the X direction, the triangular well quantizes the electrons into its lowest level, which is a sum of Airy functions. We shall write explicitly the electron wave function before tunneling (the "initial state") in subsection 5.1.2.

2.1.5 Non-interacting electrons

The collector barrier is made substantially thinner than the emitter one in order to avoid the accumulation of electrons in the well, which are considered as non-interacting. Note that by "electron" we mean the quasi-particle in the semiconductor, which has the electron charge $-e$.

2.1.6 Effective mass

Considering a parabolic conduction band in GaAs, the effective mass of the electron is 0.067 times the free-electron mass m_e (Fromhold *et al.* 1997c). This will be our assumption throughout this work. However, non-parabolicity effects can arise; in that case one can use (Fromhold *et al.* 1997c): $m = 0.067 m_e(1 + K \times 2\,\mathrm{eV}^{-1})$. K is the kinetic energy of the electron in the middle of the well, and can be approximated by $K \simeq eV(R + 1/2)$. As the scaled (classical or quantum) dynamics depends only on the product $m \times V$, a voltage dependence of the mass results effectively in a shift of the voltage. For instance, the parabolas of constant dynamics $V = \epsilon L \times B^2$ (see subsection 3.1.2) are distorted into straight lines at high voltage.

2.1.7 Weak tunneling

The tunneling through the emitter barrier is weak, because the latter is substantially higher than the electron energy. In this situation, a good approximation is Bardeen's weak tunneling matrix element (Bardeen 1961); it was first used in Fromhold *et al.* (1997c) and will be described in chapters 4 and 5. In essence, it weights the current by an overlap $\mathcal{W}_i$ between the initial state (of the 2DEG) and the quantum wave function in the well.

The tunneling through the collector barrier can become more important because of the acceleration of the electrons across the quantum well. For $V \gtrsim 1$ V, the electrons can couple to the continuum of the collector contact, passing *above* the collector barrier. In any case, there should be no selection rule with the collector contact, as the energy of the electron is much higher than the occupied sites. The electrons can tunnel out to any state in the collector contact.

2.1.8 Resonant tunneling

A consequence of the weak tunneling approach is a type of Fermi golden rule, that states than the tunneling across the emitter barrier can only happen when the energy of the

initial state matches exactly one energy level of the quantum well (considered as bounded). Experimentally, this is seen as resonant tunneling, i.e., a peak in the current when the voltage yields the adequate energy.

2.1.9 Semiclassical interpretation

The Bardeen current reading

$$I(V) = \sum_i \mathcal{W}_i \delta[E(V) - E_i] \quad , \tag{2.2}$$

it is clear that changing V will, in effect, scan indirectly the density of states (DoS) of the quantum well. Following the Gutzwiller trace formula (GTF), the current-voltage traces should have a smooth part, and an oscillatory part related to periodic orbits (POs). The voltage period ΔV is proportional to the period ΔE of the oscillations of the energy spectrum. Hence, they should be given by the period T of periodic orbits, as $\Delta E = 2\pi\hbar/T$ from the GTF. The amplitude of the current oscillations, as for the density of states, should be related to the *stability* of the PO. For instance, we could expect very unstable POs to have a small contribution, or a sudden enhancement of a certain oscillation at *bifurcations* (where POs become degenerate, disappear or change their stability). Moreover, the amplitude should be related to some measure of the "accessibility" to the tunneling electrons. As the latter are focused around the "center" of the barrier ($z = 0$, neglecting a possible shift), off-center POs should give no significant contribution to the current. Note also that only POs connecting both barriers ("emitter POs") should contribute to the current, in contrast to the DoS where all POs contribute.

The scaling introduced in subsection 3.1.2 implies that the dynamics are constant along parabolas $\epsilon L = V/B^2$. Conversely, the semiclassical regime increases with B or V along such parabolas (i.e., the "effective" $\hbar$ decreases).

2.1.10 Damping

Electron-phonon scattering in the quantum well is an inelastic process, which therefore changes randomly the phase of the electron. This results in the decoherence of the electrons, which destroys their quantum interference effects, hence, the *oscillatory* part of the current. Introducing a *coherence time* τ, the decoherence can be modelled by an exponential damping $\exp(-T/\tau)$ for an electron spending a time T in the well. Fromhold *et al.* (1995b) estimated it as $\tau \simeq 0.1$ ps. In practice, only "period-one" to "three " oscillations

can be experimentally resolved. Alternatively, this implies an energy *broadening* of around $\Delta E \simeq 0.006$ eV. It is equivalent to a voltage broadening, and will overlap and therefore damp voltage oscillations of higher frequencies. It also means that experiments cannot resolve individual quantum levels.

2.2 Data processing

Previous work (Muller *et al.* 1995, Fromhold *et al.* 1994, Monteiro *et al.* 1997a) concentrated on explaining the position (i.e., the $V - B$ range) of experimental features. The amplitudes of the oscillations were not considered. In Fromhold *et al.* (1994), the oscillatory structure of the current was obtained by differentiating twice the current with respect to the voltage. Here we describe a method to extract *amplitudes* of the current oscillations that we can compare with quantum mechanical and semiclassical results.

First, we fit a 6^{th} degree polynomial to the raw data obtained from the Bell Laboratories (Muller *et al.* 1995). This describes the smooth background current, that varies slowly and monotonically with the voltage; it comes from the fact that increasing the voltage increases the energy of the electrons, enabling them to tunnel through the barrier more easily. It is not related to periodic orbits effects; in a way it corresponds to the Weyl term of the density of states (1.3). Hence we first subtract this smooth background from the raw data, as shown in Fig. 2.2 (a) and (b). This gives the pure oscillatory traces.

We analyze then the oscillatory traces at $\theta = 0°$. We show in Fig. 2.3 the magnitude of their envelopes, for all the magnetic field range $B = 0 - 12$ T. The rather strong dependence on the voltage shown by the envelopes does not fit within a "periodic orbit" framework. In this integrable case, we expect the semiclassical contribution of the POs to be constant with V. Similarly, the quantum mechanical model described in subsection 4.1.4 gives a constant amplitude, resulting from the perfect overlap between the wave function in the quantum well and the state of the electrons before tunneling. Therefore, we attribute these envelopes to details of the tunneling, such as the widths and heights of the barriers. As we are not interested in these effects, we try to remove them from the experimental data.

We see in Fig. 2.3 that the envelopes are similar in the voltage range $V = 0 - 0.6$ V. Hence we consider a trace at an average magnetic field as the representative of all other values. We took the $B = 4.9$ T envelope.

The last step is shown in Fig. 2.2 (c). We divide the oscillatory trace by the $\theta = 0°, B =$

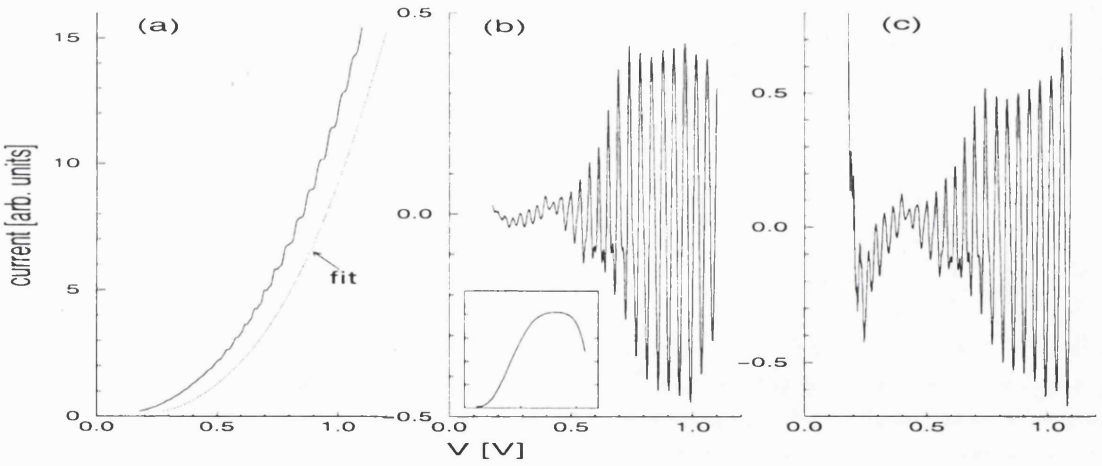

Figure 2.2: Processing of the experimental data. (a) Raw $I(V)$ trace at $\theta = 11°, B = 8$ T. The dotted line is a 6^{th} degree polynomial fit describing the smooth dependence of the background signal (it is shifted by 0.1 V to the right for clarity). (b) Oscillatory trace, obtained by subtracting the smooth background from the raw traces. The inset shows the $B = 4.9$ T envelope at $\theta = 0°$ [see Fig. 2.3]. (c) Normalized traces, obtained by dividing the oscillatory trace by the $\theta = 0°$ envelope.

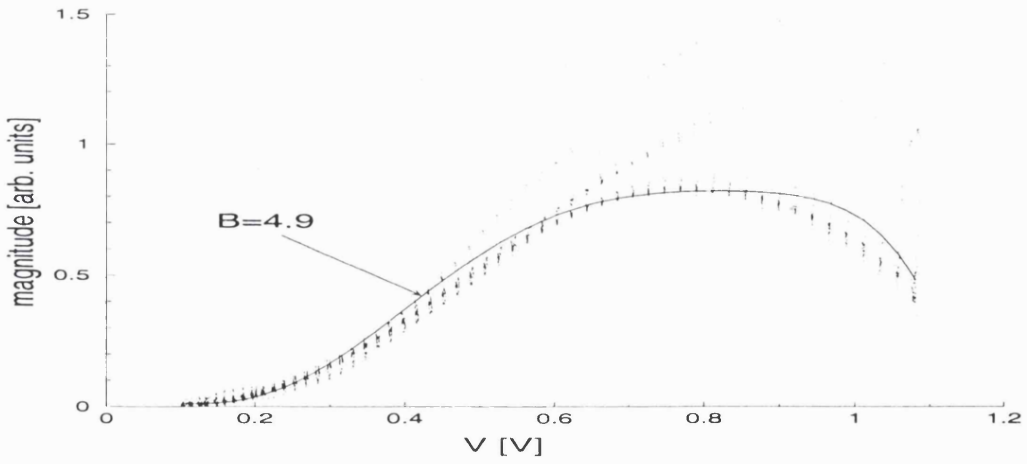

Figure 2.3: Envelopes of all oscillatory traces at $\theta = 0°$, from $B = 0$ to 12 T. The solid line is the envelope at $B = 4.9$ T, that we use for the processing of the experimental data.

4.9 T envelope to obtain the final processed trace. We call such a trace **normalized**.da The very large signal at low V is due to the very weak signal of both the $\theta = 0°$ and $\theta = 11°$ oscillatory traces.

2.3 Normalized $I(V)$ traces

2.3.1 Traces at $\theta = 11°$

We show the experimental results at $\theta = 11°$ in Fig. 2.5, where we plot the *normalized* $I(V)$ traces for fifty or so different magnetic field values ranging from $B = 0$ to 12 T. We also show in Fig. 2.4 a related plot of the positions of the maxima of the $I(V)$ traces, which is probably easier to read first.

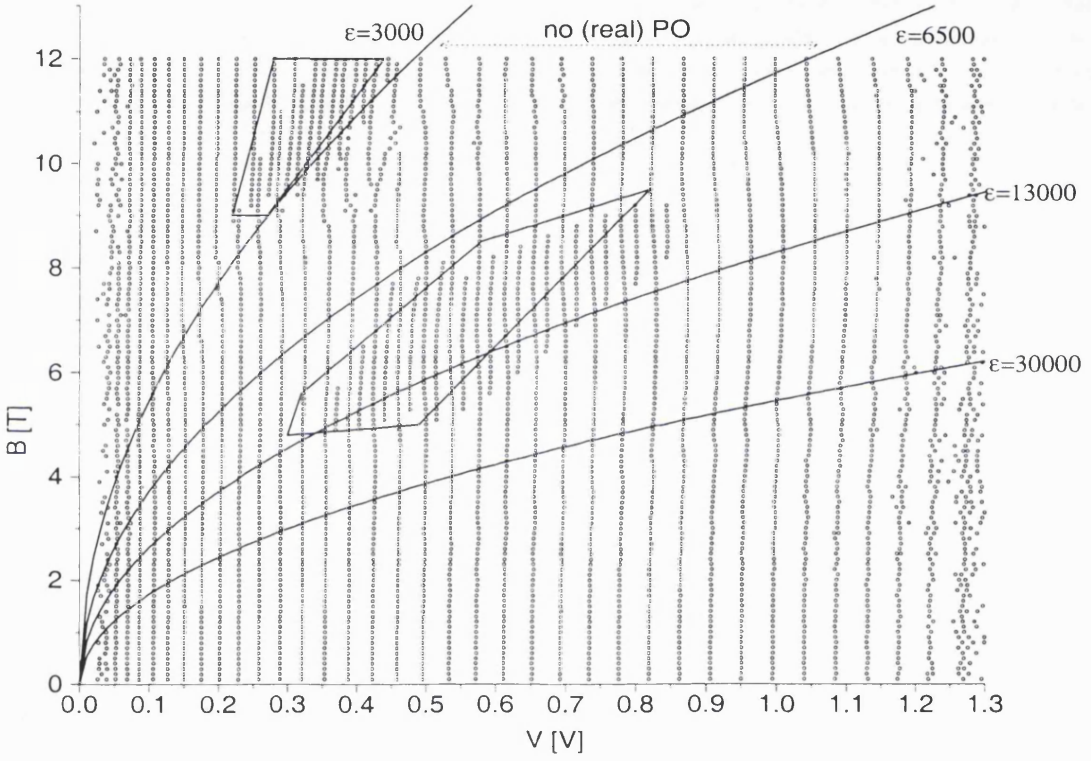

Figure 2.4: Maxima of the experimental $I(V)$ traces at $\theta = 11°$ for a range of magnetic field values $B = 0 - 12$ T. The parabolic lines correspond to fixed scaled classical dynamics, given by $\epsilon = F/B^2$. The period-doubling (P2) regions are roughly delimited by the polygons. No real periodic orbit giving a period-one contribution exists in the $\epsilon = 3000 - 6500$ range (dotted arrow).

The predominant experimental features are the following:

1. Regular period-one region

First we find a region of pure regular oscillations at high V and low B, below the parabola defined by $\epsilon = V/LB^2 = 19000$ a.u.. We call them **period-one** or **P1** oscillations. These oscillations are of the same period as the ones found at $\theta = 0°$.

At $\theta = 0°$ the dynamics are integrable and only the central straight traversing orbit

t_0 contributes to the current. The other POs (lying on concentric tori around t_0) do not contribute because the quantum state associated with them (via EBK quantization), being excited harmonic oscillator states, have no overlap with the initial state.

The voltage period of P1 oscillations at $\theta = 0°$ increases slightly with V (see also Fig. 2.4); this can be understood semiclassically as the time period of t_0 decreases with increasing energy.

2. Main period-doubling region

In the center of the Figure there is a first region where a secondary oscillation with a shorter voltage period is superimposed on the P1 oscillation. There is exactly one extra peak between the P1 peaks; we refer to this kind of oscillation as a **period-doubling** or **P2** oscillation.[1] The period-doubling region is easily seen in Fig. 2.4.[2]

Looking more closely in Fig. 2.6, we see that the traces evolve (as ϵ decreases) from a right-asymmetric to a left-asymmetric profile. The symmetric profile could be related to the period-doubling bifurcations of t_0 occurring near $\epsilon = 13000$.[3] The experimental locus of the symmetric profile has a more linear shape, and is displaced with respect to the classical parabola. This linear shape is very probably a consequence of the voltage dependence of the effective mass: we should replace the product mV by $m(V)V = m_0V(1 + \text{const} \times V)$; the (isolated) const $\times$ V term yields *lines* (instead of parabolas) of constant dynamics $\mathcal{E}_{\text{linear}} = V^2/B^2$. At $V = 0.5$ V —where we shall read experimental amplitudes—, the experiments yield $\epsilon = 9200$, that is, a 30% difference with the classical line. This will be our estimate of the effects of the voltage-dependent mass:

displace experimental features at $V = 0.5$ V by $\epsilon \to \epsilon \times 1.3$

We shall use this displacement when we consider experimental amplitudes and periods in chapter 7.

Note also in Fig. 2.6 how the P2 signal disappears with increasing voltage: the extra,

[1] The voltage period is actually *halved*. The terminology comes from the semiclassical picture, where periodic orbits related to the shorter voltage period oscillations have a *longer* period (actually twice the period of POs responsible of the P1 oscillations). Müller *et al.* (1995) used the term "peak-doubling" regions.

[2] Fig. 2.4 has been provided to us by G Boebinger and yields a slightly different period-two region.

[3] The quantum mechanical calculations reproduce very well the changeover from right to left-assymetric profiles (Monteiro *et al.* 1997a, Saraga and Monteiro 1998b).

smaller peaks become absorbed by the larger P1. This is a consequence of the increase of the broadening with voltage, due to the coupling to the continuum around $V = 1$ V, where the electron energy at the collector barrier is comparable to the barrier height.

Note finally that the P1 modulation of the P2 oscillations means that their amplitude as appearing in the trace is not the amplitude of the pure P2 signal. Hence we do not extract experimental P2 amplitudes here.

3. Ghost period-one region

An important region is between $\epsilon = 6500$ and 3000, where the amplitude of the P1 oscillations drops significantly. First it drops as ϵ decreases, reflecting a *dynamical* event. The PO responsible for the P1 oscillation (t_0) disappears in a tangent bifurcation[4] at $\epsilon = 6500$. Until $\epsilon \simeq 3000$ there is no real P1 PO which could be responsible for the experimental oscillations.

Secondly, the amplitude decreases along the parabolas in the classical limit (as V or B increases). Hence there is also a "$\hbar$-dependent" effect, that is a semiclassical contribution that depends on the semiclassical regime. Note that this phenomenon is not seen in the P1 oscillations in the regular region.

This situation is reminiscent of a "ghost periodic orbit", first noted by Kuś *et al.* (1993). It is one of the pair of complex POs which appears at a bifurcation; the contributing ghost has an action with a positive imaginary part $\mathbf{Im}\, S$. The amplitude of its contribution to the DoS is proportional to $\exp(-\mathbf{Im}\, S/\hbar)$, and therefore decreases exponentially (i) in the classical limit $\hbar \to 0$, (ii) as one changes a dynamical parameter to move away from the bifurcation (because $\mathbf{Im}\, S$ grows).

Note that the oscillations persist quite far away from the bifurcation; this is a surprising fact, as usually ghosts are damped very quickly and can only be seen in a very small range of the dynamical parameter (here, ϵ).

Hence we consider this region to be an *experimental manifestation of a ghost* —or at least complex trajectories— over an unusually large range of dynamical parameters. It will be referred to as a "no (real) PO" or "ghost" region.[5]

As the signal is pure, we extract experimental P1 amplitudes here. We read them at the medium voltage $V = 0.5$ V, which favors the best resolution.

[4] See subsection 3.2.3.

[5] A suitable name would be Edgar Wallace's "Valley of the Ghosts" (1928).

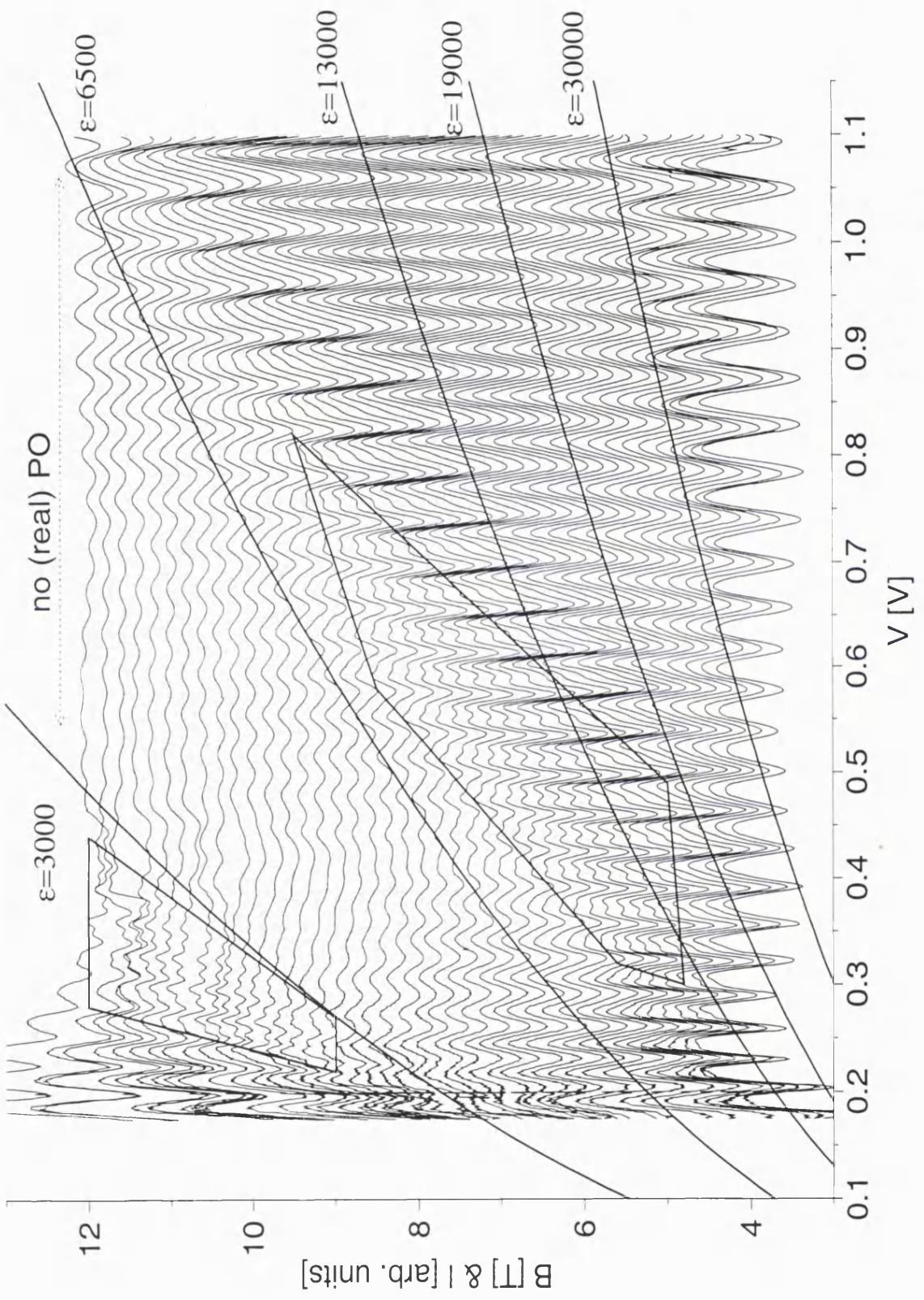

Figure 2.5: Normalized experimental $I(V)$ traces at $\theta = 11°$ for a range of magnetic field values $B = 0 - 12$ T. For each B, the current I is plotted vs. the voltage V, but shifted by a value corresponding to B. Same legend as Fig. 2.4.

4. Low ϵ period-doubling region

We have another P2 region on the left of the $\epsilon = 3000$ parabola, which we refer to as the "low ϵ" P2 region.

Again, it stands out more obviously in the plot of the maxima (Fig. 2.4). There is also a P1 signal superimposed; altogether this signal is not very clean, and we did not extract experimental amplitudes (moreover, it does not extend to the $V = 0.5$ V line where we read amplitudes).

This region occurs around $\epsilon = 2500$, where the second repetition of t_0 does not yield a strong current. As we shall see in section 3.2.3, there is on the other hand s_1, a P2 periodic orbit.

5. Noisy regions

Very low or high voltages yield noisy signals. At very low voltage the tunneling is very small and gives a very weak signal at any angle. The ratio of $\theta = 11°$ to $\theta = 0°$ therefore yields unreliable results. As mentioned above, high voltage yields substantial broadening and coupling to the continuum. As seen in section 2.2, the $\theta = 0°$ envelopes used to get the normalized traces depend on B for $V > 0.6$ V; using only the $B = 4.9$ T envelope therefore gives less reliable amplitudes.

2.3.2 Traces at $\theta = 27°$

We show the experimental traces at $\theta = 27°$ in Fig. 2.8, and the positions of the maxima in Fig. 2.7. The main features are:

1. Regular P1 region

Again, we have a region of P1 oscillations in the regular regime. The amplitudes decrease quickly with ϵ and disappear below $\epsilon = 18000$. This can be understood semiclassically, as t_0 (the PO contributing to the P1 current) is more off-center and should have a small accessibility to the tunneling electrons.

2. Jumps in P1 oscillations

If one follows, in Fig. 2.7, the maxima of the P1 current around $\epsilon = 60000$ and $\epsilon = 18000$, we see abrupt "jumps". In Fig. 2.8 the first jump can be noticed as the sudden disappearance of the P1 signal and a shift in the positions of the maxima.

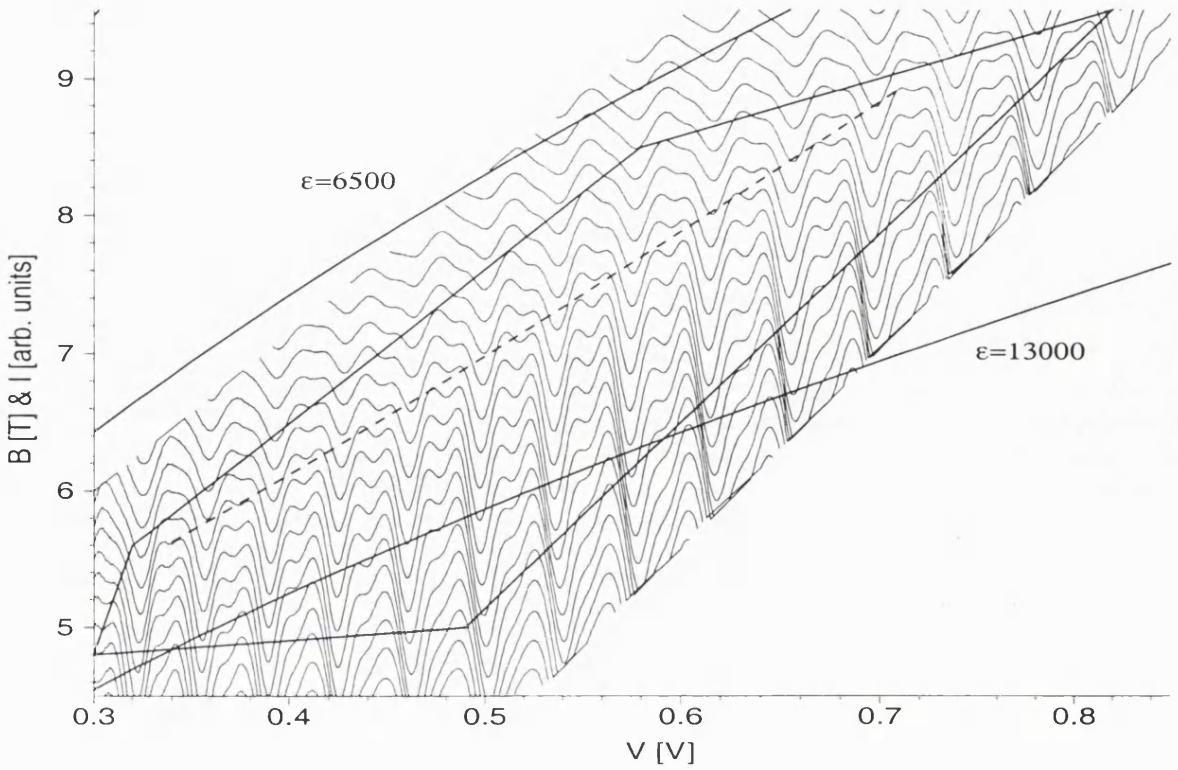

Figure 2.6: Details of the main P2 region at $\theta = 11°$. The dashed line is a quadratic interpolation of the positions of the experimental symmetric profile.

As will be explained in section 4.2, these jumps are an experimental manifestation of tori quantization effects in the island of stability surrounding the stable PO t_0. The jumps are the changeover between two tori that contribute to the current; experimentally they are most apparent around $V = 0.5$ V as it is the best voltage in term of resolution.

The first experimental jump happens between $B \simeq 1.6$ T at $V \simeq 0.3$ V and $B \simeq 2.3$ T at $V \simeq 0.5$ V; it corresponds to the changeover between the lowest torus ($k = 0$, the PO) and the first torus ($k = 1$), where k is a quasi-quantum number (see section 4.2). The second jump happens between $B \simeq 4$ T at $V \simeq 0.35$ V and $B \simeq 5$ T at $V \simeq 0.57$ V, and corresponds to the $k = 1 \rightarrow 2$ torus changeover.

Although one could expect similar jumps at $\theta = 11°$, they are hard to observe experimentally because they happen in the middle of the main P2 region.

3. Broad P2 region

The P2 region is very broad, and covers almost half of the parameter range from $\epsilon \simeq 15000$ to below $\epsilon = 3000$. The signal is quite pure, as there is no P1 oscillations superimposed; this will enable us to extract experimental amplitudes of P2 oscillations, read at $V = 0.5$ V.

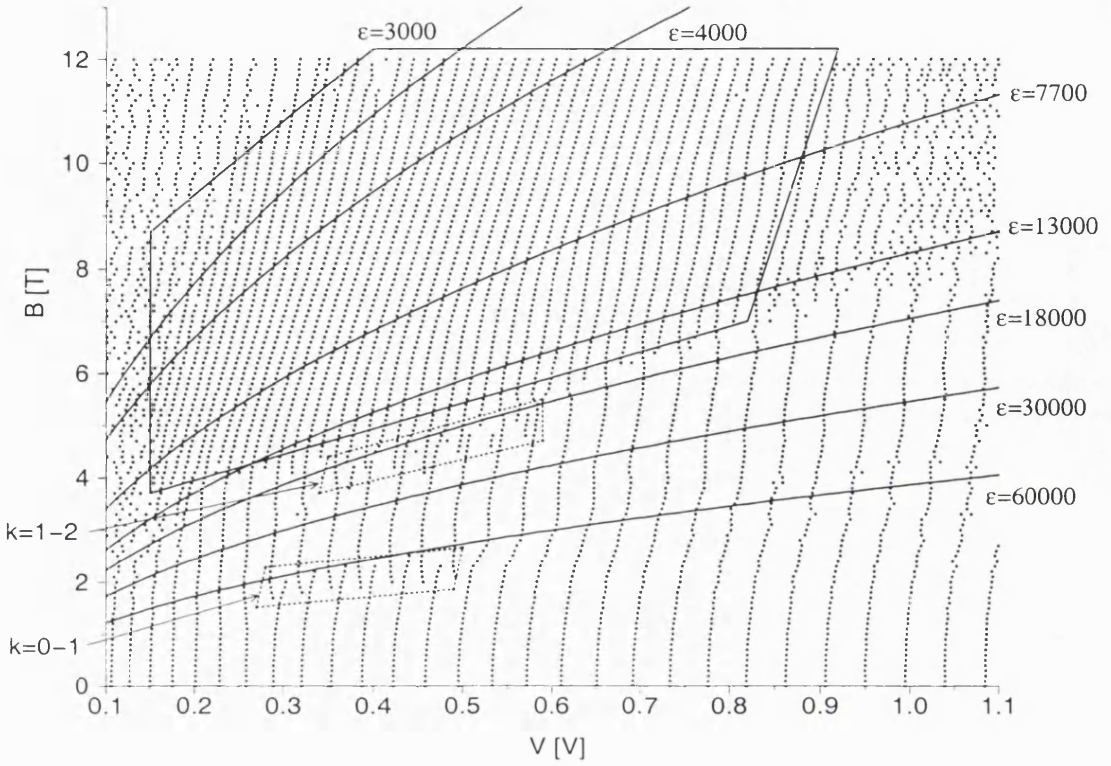

Figure 2.7: Maxima of the experimental $I(V)$ traces at $\theta = 27°$ for a range of magnetic field values $B = 1 - 12$ T. Same legend as Fig. 2.4. Jumps in the period-one current are in the regions indicated by $k = 0 - 1$ and $k = 1 - 2$.

The $\epsilon = 13000$ parabola corresponds to a period-doubling bifurcation of t_0, and is close to the rise of the P2 oscillations (see Fig. 2.7). It is a natural question to wonder whether the P2 signal is a manifestation of the bifurcation, as proposed in Müller *et al.* (1995). As we shall see in the following chapters, the answer is more complicated as there is another PO (s') which also gives a large P2 contribution.

The P2 amplitudes, although pure, are visibly smaller than the P1 amplitudes in the regular region. We attribute this to the damping of the signal, due to the decoherence coming from electron-phonon scattering in the well (see also subsection 2.3.4.)

4. Ghost P2 region

Another important line is $\epsilon = 7700$, where s' disappears in a tangent bifurcation. There are no P2 periodic orbits until $\epsilon \simeq 4000$, where a new PO (s'') starts contributing significantly. Hence we have another "ghost region" with apparently an absence of real POs that could contribute and explain the experimental oscillations.

Below and above this line the amplitudes decrease only slowly in the semiclassical

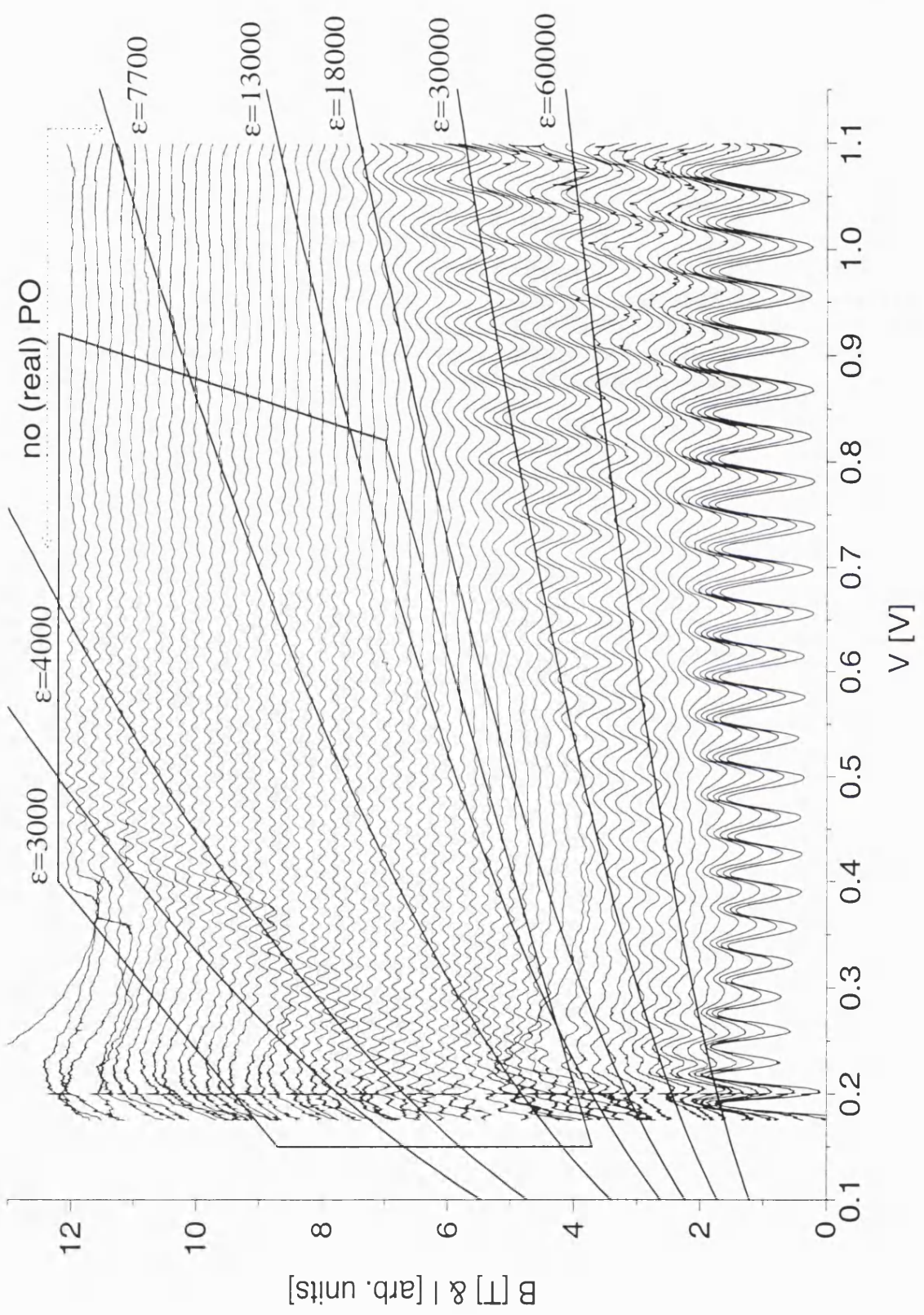

Figure 2.8: Normalized experimental $I(V)$ traces at $\theta = 27°$ for a range of magnetic field values $B = 1 - 12$ T. Same legend as Fig. 2.4 and 2.5.

limit (increasing B). This is remarkable, as the contribution of a ghost to the DoS is exponentially damped as $\hbar$ decreases. Note however that the current contribution of a real PO also has a strong $\hbar$ dependence because of the overlap with the Gaussian of the initial state, whose width is determined by $\sqrt{\hbar/eB\cos\theta}$.

Finally, the signal at very low voltage is even noisier than at $\theta = 11°$.

2.3.3 Traces at $\theta = 38°$

We present experimental traces at $\theta = 38°$ in Fig. 2.10, where the oscillations have been artificially multiplied by a factor two in order to see the small oscillations. The positions of the maxima are shown in Fig. 2.9.

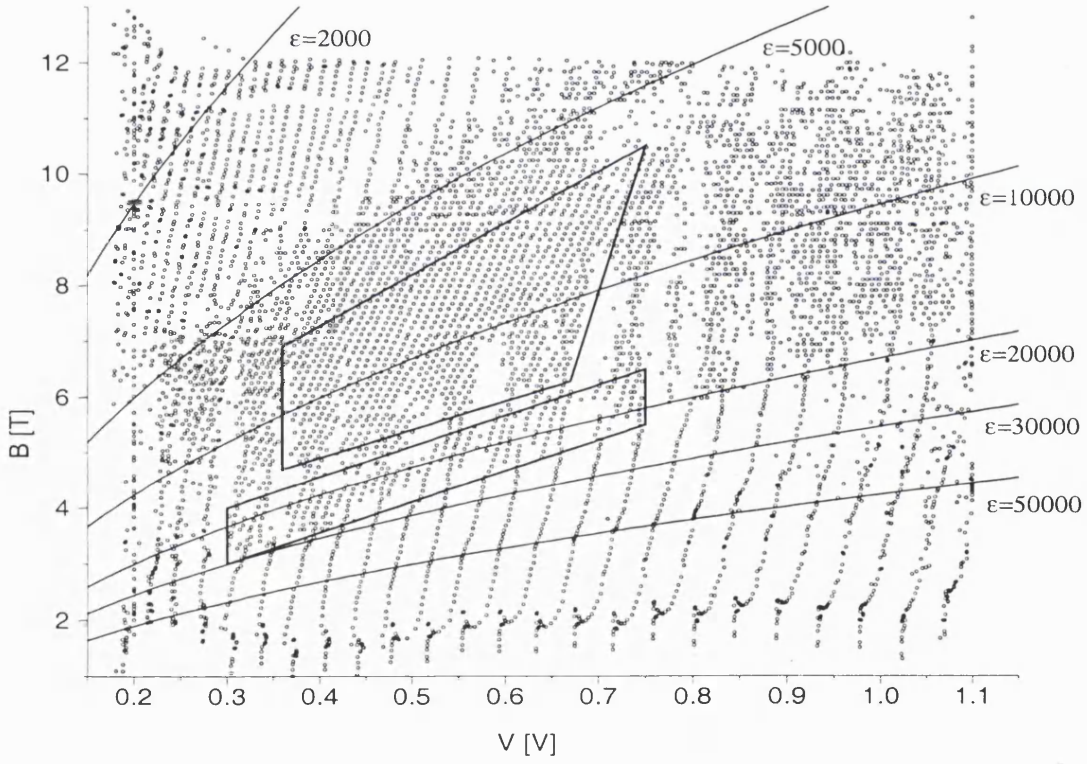

Figure 2.9: Maxima of the experimental $I(V)$ traces at $\theta = 38°$ for a range of magnetic field values $B = 1 - 12$ T. We consider two regions of period-three oscillations, in the polygonal regions.

Apart from the regular P1 oscillations, we have a fairly strong P2 oscillation in the chaotic corner (low V, high B). We did not investigate that region.

The most interesting feature at this angle is the presence of **period-three** (P3) oscillations. We divided them in two regions.

The first region around $\epsilon = 20000$ (high ϵ region) appears "gradually" from the P1 signal. It has been connected in Müller *et al.* (1995) to a period tripling bifurcation of t_0

at $\epsilon = 22000$. Fromhold *et al.* (1997a) contested that explanation on account of the low accessibility of t_0, and proposed another PO (1:3) as the origin of the oscillations. As we shall see in chapter 7, this is also a difficult controversy.

At lower ϵ the position of the maxima becomes messier; nevertheless we can see a small P3 signal extending in a quite broad range of B and V. This will be referred to as the low ϵ region.

The amplitudes of the P3 oscillations are quite small as a result of the phonon scattering damping, which grows exponentially with the period of the PO.

For both regions we extracted experimental P3 amplitudes, that we shall compare to theoretical results in section 7.3. As the quantum mechanical (QM) calculations do not include the damping, the comparison of the P3 amplitudes gives us information about the damping (or coherence) time τ in the well.

2.3.4 Estimation of the damping

We estimated the damping by looking at P2 ($\theta = 16°, 20°$ and $27°$) and P3 ($\theta = 38°$) amplitudes. We compared the maximal amplitudes (as ϵ varies) of the QM calculations and experimental readings. Their ratio should be equal to the inverse of the phonon emission damping:

$$\frac{\text{QM}}{\text{EXP}} = \exp[(T_M - T_0)/\tau] \quad , \tag{2.3}$$

where T_M is the total time of the contributing orbit at this maxima, and T_0 the period of the contributing PO t_0 at $\theta = 0°$. Here we considered "minimal orbits" (see subsection 5.2.6) for T_M, and calculated the times at $V = 0.5$ V. For each maximum, this relation yields one estimation of the damping time τ. Then we consider their average $\bar{\tau}$, and estimates the effect of the damping by $\exp[(T_M - T_0)/\bar{\tau}]$. Table 2.3.4 summarizes our findings. We found the average value $\bar{\tau} = 0.115$ ps, which corresponds to estimates given in Fromhold *et al.* (1994).

Hence we shall multiply by the experimental amplitudes by the number found in the last column in Table 2.3.4:

multiply experimental amplitudes by $\exp[(T_M - T_0)/\bar{\tau}]$, $\bar{\tau} = 0.115$ ps

Note that the 10% variations in τ above translate into a much larger uncertainty in the amplitudes, because of their exponential relationship.

θ	QM/EXP	T_M [ps]	τ [ps]	$\exp[(T_M - T_0)/\bar{\tau}]$
16°	6.64	.4312	.120	7.3
20°	6.76	.4478	.128	8.5
27°	13.24	.4577	.098	9.2
38°	86.31	.6958	.110	74

Table 2.1: Estimates of the damping time. Angle, ratio QM/EXP at the ϵ corresponding to the maximal amplitude, total time T_M of the contributing minimal orbit, damping time from (2.3), final damping given by the *average* $\bar{\tau} = 0.115$ ps.

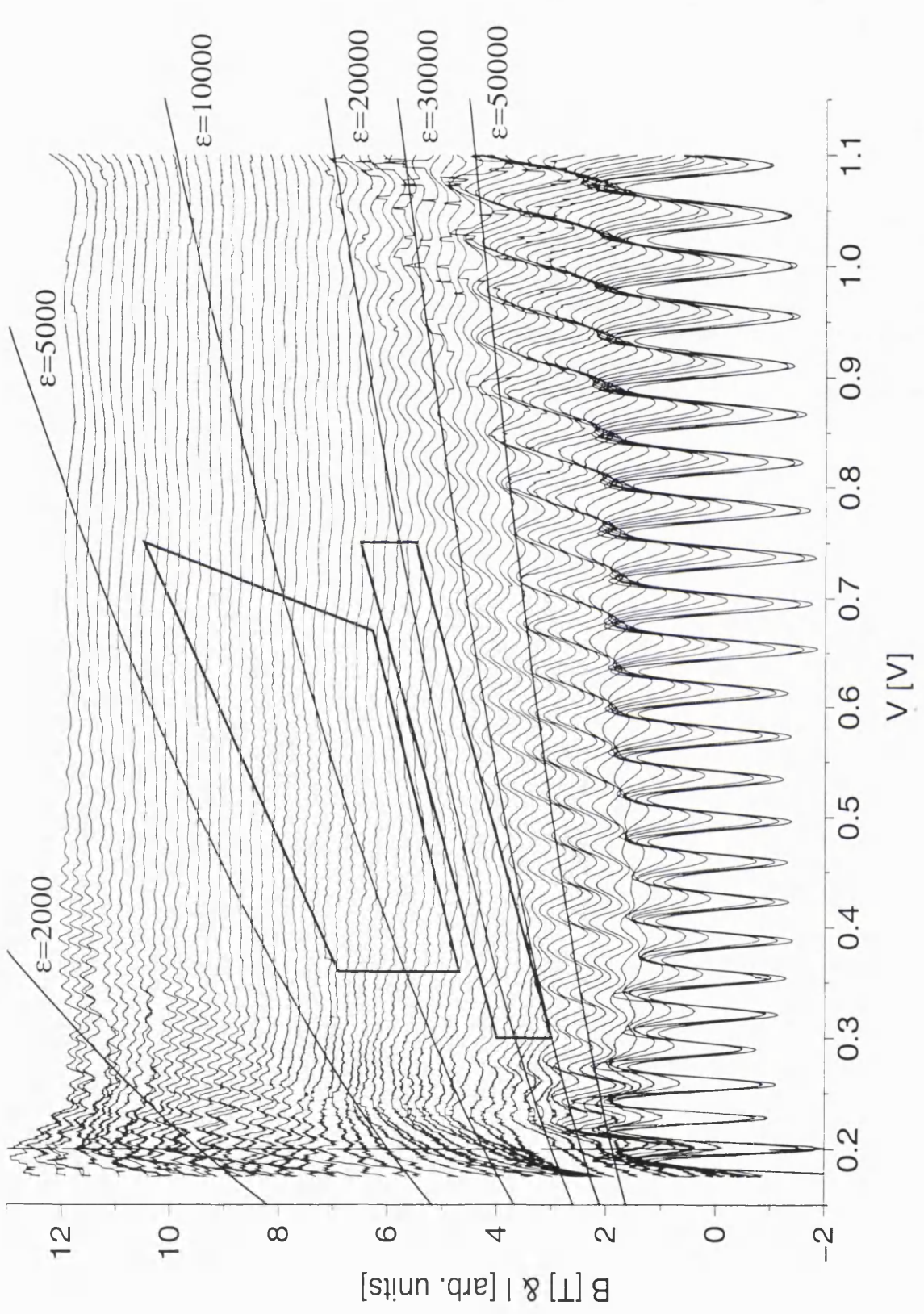

Figure 2.10: Normalized experimental $I(V)$ traces at $\theta = 38°$ for a range of magnetic field values $B = 1 - 12$ T. Same legend as Fig. 2.9.

Chapter 3

CLASSICAL DYNAMICS

The motivation to study the classical motion of the electrons within the quantum well comes from the general framework of quantum chaos and the quantum-classical correspondance principle. The semiclassical theories developed in chapter 5 will express a quantum object (the current) as a sum over trajectories belonging to certain classes, such as periodic orbits (POs), normal orbits (NOs) or saddle orbits (SOs).

We shall follow the heuristic semiclassical picture described in subsection 2.1.9, where the current is thought of as the density of states (DoS), weighted by a measure of the accessibility of the tunneling electrons. We shall keep in mind the Gutzwiller trace formula (GTF), which implies an oscillatory structure to the current given by periodic orbits [see (1.4) and Gutzwiller (1990)]. In this chapter, we shall exclusively analyze POs; the classical behavior of the other types of trajectories (NOs, CCOs, MOs, SOs) will be discussed in chapters 6 and 7, in connection with their semiclassical contribution. Chapter 8 will address more specifically the classical complex dynamics needed for ghosts (complex POs), as well as the link between SOs and POs.

We shall discuss the *scaling* property of the dynamics, which is a very important feature for a semiclassical analysis. Poincaré surfaces of section of phase space will give a *qualitative* picture of the classical dynamics. For instance, *bifurcations* will be discussed, as they are known to have profound effects on the DoS given by the GTF. A peculiarity of this system is a discontinuity brought by the hard walls, yielding a non-generic type of bifurcations, called *cusp bifurcations* in Narimanov and Stone (1998b).

What will be needed for a *quantitative* computation, in chapters 6 and 7, of the semiclassical oscillatory part of the current are the classical properties of the trajectories: (*i*) their *action*, that determines the frequency of the oscillations; (*ii*) their monodromy ma-

trix, that describes their *stability* and influences the amplitude of the oscillations; (*iii*) their starting position on the left wall z_0, that determines their *accessibility* to the tunneling electrons and modifies greatly the amplitudes of the oscillations, and (*iv*) their period, that influences the extent of the damping due to the decoherence induced by phonon scattering. Note that we shall only concentrate on the POs that are believed to contribute to the current. We shall not carry out an exhaustive analysis, which can be found in the very complete work of Narimanov and Stone (1998b).

3.1 Classical dynamics: theory

We consider an electron with charge $-e$ and energy E, which is confined in a well of length L by two high tunneling barriers, situated at $X = 0$ (emitter) and $X = L$ (collector). Fig. 2.1 presents a schematic view of the system. The band edge mass of the electron in GaAs is $m = 0.067 m_e$ (see subsection 2.1.6). A voltage V is applied across the diode, creating a negative constant electric field $\boldsymbol{F}$ perpendicular to the barriers, along the X axis. A constant magnetic field $\boldsymbol{B}$ is applied, in the (X, Z) plane, at an angle θ with $-\boldsymbol{F}$. In the asymmetric gauge $\boldsymbol{A} = B(0, X\sin\theta - Z\cos\theta, 0)$, the Hamiltonian governing the motion of the electron reads:

$$H(\boldsymbol{P},\boldsymbol{Q}) = \frac{1}{2m}(\boldsymbol{P} + e\boldsymbol{A})^2 + e\boldsymbol{F}\boldsymbol{Q} \tag{3.1}$$

$$= \frac{1}{2m}\boldsymbol{P}^2 - eFX + \frac{e^2B^2}{2m}(X\sin\theta - Z\cos\theta)^2 + \frac{eB}{m}(X\sin\theta - Z\cos\theta)P_Y . \tag{3.2}$$

An electron with an energy lower than the heights of the potential barriers[1] undergoes specular reflections at the barriers, considered to be "hard walls". They are described by the flip $P_X \to -P_X$ of the X momentum, at $X = 0$ and $X = L$.

3.1.1 Reduction to two dimensions

As H is independent of Y, it follows directly from Hamilton's equations that $P_Y = m\dot{Y} - eB(X\sin\theta - Z\cos\theta)$ is constant. One can remove P_Y by the canonical change of variables

$$Z \to z = Z - \frac{P_Y}{eB\cos\theta} = X\tan\theta - \frac{m\dot{Y}}{eB\cos\theta} \tag{3.3}$$

generated by the transformation function $\mathcal{F}_3(\boldsymbol{q},\boldsymbol{P}) = -\boldsymbol{q}\boldsymbol{P} - P_Y P_Z/(eB\cos\theta)$. We shall use atomic units, with the reference length $x_{\rm au} = 5.29177\ 10^{-11}$ m, magnetic field $B_{\rm au} =$

[1] In experiments with high voltages ($V \simeq 1.0$V), the energy of the electron at the collector barrier can exceed its height; see subsection 2.1.7.

2.35051 10^5 T, electric field $F_{\rm au} = 5.14220\ 10^{11}$ V/m and time $t_{\rm au} = 2.41888\ 10^{-17}$ s. Then $e = m_{\rm e} = \hbar = 1$, and the two-dimensional Hamiltonian reads:

$$H(\boldsymbol{p},\boldsymbol{q}) = \frac{1}{2m}(p_x^2 + p_z^2) - Fx + \frac{B^2}{2m}(x\sin\theta - z\cos\theta)^2 \quad . \tag{3.4}$$

The length of the well in the experiments we analyze in this work is $L = 120$ nm $= 2267$a.u..

3.1.2 Scaling

As proposed in Monteiro and Dando (1996), we scale the time by B, which changes the momentum:

$$t \to \tilde{t} = Bt \Rightarrow \begin{cases} \boldsymbol{q} \to \tilde{\boldsymbol{q}} &= \boldsymbol{q} \\ \\ \boldsymbol{p} \to \tilde{\boldsymbol{p}} &= \boldsymbol{p}/B \quad . \end{cases} \tag{3.5}$$

We define related scaled parameters, and consider that the ratio of the electron energy to the applied voltage is constant:[2]

$$\text{scaled energy} \quad : \quad \tilde{E} = \frac{E}{B^2} \tag{3.6}$$

$$\text{scaled electric field} \quad : \quad \epsilon = \frac{F}{B^2} \tag{3.7}$$

$$\text{ratio} \quad : \quad R = \frac{E}{V} = \frac{\tilde{E}}{\epsilon L} \quad . \tag{3.8}$$

The scaled Hamiltonian now reads:

$$\tilde{H}(\tilde{\boldsymbol{p}},\boldsymbol{q}) = RL\epsilon = \frac{1}{2m}(\tilde{p_x}^2 + \tilde{p_z}^2) - \epsilon x + \frac{1}{2m}(x\sin\theta - z\cos\theta)^2 \quad , \tag{3.9}$$

and the dynamics depends only on $\{\epsilon, R, \theta\}$. The scaling can be understood the following way: increasing B tightens the cyclotron motion of the electron around the magnetic field; however, the electron can reach the barrier quicker through an increase of the electric field; the balance is reached when ϵ is constant and the extra acceleration of the voltage compensates exactly the effects of increasing the magnetic field.

Note that the mass always appears as a product with ϵ; this means that effects of a voltage-dependence of the mass can be incorporated in a shift of ϵ (see subsection 2.1.6).

The classical action scales as well with B:

$$S(E,F,B,\theta) = \int d\boldsymbol{q}\,\boldsymbol{p} = B\tilde{S}(\epsilon,R,\theta) \quad \text{with} \quad \tilde{S} := \int d\boldsymbol{q}\,\tilde{\boldsymbol{p}} \quad . \tag{3.10}$$

[2] As discussed in subsection 2.1.3, the experimental value is approximately $R = 0.15$.

From a semiclassical perspective (see chapter 5), this fact implies that B plays the role of the inverse of an effective Planck's constant $\hbar$; it measures the *semiclassical regime*, i.e., how close the system is to the quantum limit or, on the other hand, to the classical limit.

At the same time, one is able to *change the classical dynamics* (controlled by ϵ) *without changing the effective* $\hbar$. This enables us, when studying the quantum properties, to distinguish between effects due to the change of dynamics and effects due to the change of the semiclassical regime. This is not the case for non-scaling systems, where each step in the ladder of the energy eigenvalues (which ranges from the quantum limit to the classical one) corresponds to a different classical dynamics situation.

We also consider the ratio of the scaled action to the scaled action in the $B = 0$ case:

$$\hat{S} := \frac{\tilde{S}}{2L\sqrt{2mL\epsilon(R+1/2)}} \quad . \tag{3.11}$$

We shall see in subsection 5.3.3 that $\hat{S}$ is the proper measure of the semiclassical regime. From now on, "scaled action" will usually mean $\hat{S}$.

3.1.3 Evolution

It is worth introducing the rotated coordinates $\{u, v\}$ which are respectively parallel and perpendicular to $\boldsymbol{B}$:

$$\begin{cases} x &= u\cos\theta - v\sin\theta \\ z &= u\sin\theta + v\cos\theta \quad . \end{cases} \tag{3.12}$$

They are decoupled (the energy of each mode is conserved), which means that the motion is integrable between the bounces. Solving Hamilton's equations, one finds

$$\begin{cases} u(\tilde{t}) &= \frac{1}{2m}\epsilon\cos\theta\tilde{t}^2 + \frac{1}{m}\tilde{p}_u^0\tilde{t} + u_0 \\ v(\tilde{t}) &= \tilde{p}_v^0\sin(\tilde{t}/m) + (v_0 + \epsilon m\sin\theta)\cos(\tilde{t}/m) - m\epsilon\sin\theta \quad , \end{cases} \tag{3.13}$$

where the 0 sub/superscripts indicate the starting conditions at $\tilde{t} = 0$. The effect of a bounce is to mix the energy of the modes, destroying the integrability. The transcendental equations $x(\tilde{t}_b) = \{0, L\}$, which give the times $\tilde{t}_b$ of the bounces, have to be solved numerically.

Note that the global properties of a trajectory (such as its action) can be decomposed in a sum of each intermediate analytical path between two bounces and the effect of the bounces.

3.1.4 Poincaré surface of section

Looking at trajectories in the configuration space (x, z) only gives partial information, as the complete description of a state in classical dynamics involves the knowledge of each phase space point $(x, z; \tilde{p}_x, \tilde{p}_z)$ at a given time $\tilde{t}$. In order to avoid the difficulty of visualizing a 4-D space, one defines a 2-D slice of the phase space, called a *Poincaré surface of section* (SoS) (Ozorio de Almeida 1988). For example, one can consider x constant: $\{x = x_{\mathrm{SoS}}, z; \tilde{p}_x > 0, \tilde{p}_z\}$; then $\tilde{p}_x$ is fixed (up to the sign) by energy conservation, which is the fact that a trajectory is confined to the 3-D energy surface defined by $H(\tilde{\boldsymbol{p}}, \boldsymbol{q}) = \tilde{E}$. One records the succession of a large number of crossings $(z, \tilde{p}_z)$ of the repetitions of many different trajectories. We shall present several SoS in the next section.

The limit of the SoS is given by $p_x(x_{\mathrm{SoS}}, z, p_z; \tilde{E}) = 0$, e.g.,

$$\tilde{p}_z(z) = \pm\sqrt{2m(\tilde{E} + \epsilon x_{\mathrm{SoS}}) - (x_{\mathrm{SoS}} \sin\theta - z\cos\theta)^2} \quad . \tag{3.14}$$

Note that changing the unshifted initial coordinates Z_0 does not change the shape of a trajectory, but merely translates it. On the contrary, changing the shifted coordinate z_0 changes the velocity $\dot{Y}_0$. At a given energy E, this changes the starting $\dot{X}_0$, modifying the trajectory.

One can also identify the surface of the turning points, where a particle runs out of kinetic energy ($\dot{x} = \dot{z} = 0$):

$$z(x) = \left[x\sin\theta \pm \sqrt{2m(\tilde{E} + \epsilon x)}\right] / \cos\theta \quad . \tag{3.15}$$

This surface will play an important role in the cusp bifurcation discussed in subsection 3.2.4, and will be referred to as the "soft energy surface" (in contrast to the "hard" barriers).

3.1.5 Periodic orbits

A very important class of trajectories are *periodic orbits* (POs). They are defined by the fact that their final position and momentum $(\boldsymbol{q}', \boldsymbol{p}')$ coincide with their initial position and momentum $(\boldsymbol{q}, \boldsymbol{p})$:

$$\mathbf{PO}: \quad (\boldsymbol{q}, \boldsymbol{p}) \to (\boldsymbol{q}', \boldsymbol{p}') = (\boldsymbol{q}, \boldsymbol{p}) \quad . \tag{3.16}$$

They close themselves smoothly after a time T (the period), and keep on the same path indefinitely.

3.1.6 Stability

The stability of an orbit describes the way neighboring orbits behave. Writing $\mu = (z, p_z)$ the coordinates on a SoS, one considers an iteration of the Poincaré map $\mu_0 \to \mu$, as well as neighboring trajectories starting with $\mu_0 + \delta\mu_0$. The linearization of the map defines the 2×2 reduced *monodromy (stability) matrix* M:

$$\begin{pmatrix} \delta z' \\ \delta p_z' \end{pmatrix} = M \begin{pmatrix} \delta z \\ \delta p_z \end{pmatrix} = \begin{pmatrix} m_{11} & m_{12} \\ m_{21} & m_{22} \end{pmatrix} \begin{pmatrix} \delta z \\ \delta p_z \end{pmatrix} \quad . \tag{3.17}$$

One can obtain analytical expressions for M by evaluating partial derivatives in (3.13), in contrast to the usual situations in mixed systems like the H atom in external fields —where one needs numerical evolution. There are corrective terms due to the energy conservation and the cut at constant x; their analytic expressions are given in the Appendix A.1. M is symplectic and has unit determinant, because of the area conservation property of Hamiltonian systems (Ott 1993, Lichtenberg and Lieberman 1983). This yields two possibilities for its eigenvalues $\lambda_\pm$, that can be related to the (real) value of its trace.

Unstable orbit: $|\mathrm{Tr}M| > 2 \Leftrightarrow \lambda_+ = \lambda_-^{-1} \in \mathbb{R}$. The eigenvector of $|\lambda_+| > 1$ determines locally the unstable manifold (where the points of the map on the SoS move away from the orbit at each iteration), while $\lambda_- < 1$ is linked to the stable manifold (where points are attracted to the orbit and reach it after an infinite time). The orbit can be direct ($\mathrm{Tr}M > 0$) or indirect ($\mathrm{Tr}M < 0$). In a SoS, an unstable periodic orbit can be found (with difficulty) by the hyperbolic structure around it.

Stable orbit: $|\mathrm{Tr}M| < 2 \Leftrightarrow \lambda_+ = \lambda_-^* = \exp(i\gamma)$, which defines the *winding angle* $\gamma \in \mathbb{R}$. Neighboring trajectories wind around the stable orbit, staying at a finite distance. A stable periodic orbit is more easily located in a SoS by the elliptic shape surrounding it (an "island of stability" or "stable island").

A periodic orbit (PO) can only appear or change its stability class (i.e., stable/unstable) in **n-bifurcations**, where the monodromy matrix of the n^{th} repetition of the PO has a trace equal to two: $\mathrm{Tr}(M^n) = 2$. The most important types of bifurcations[3] for us are:
(a) *Tangent bifurcation (TB)* $[n = 1]$, where $\mathrm{Tr}M = 2$. Two POs coalesce and "annihilate" each other, leaving no real PO (but a pair of complex conjugate POs).
(b) *Pitchfork bifurcation (PB)* $[n = 2]$, where $\mathrm{Tr}M = -2$. The central PO changes its

[3]The classification of the five generic types can be found in Ozorio de Almeida (1988).

stability, while a pair of identical satellite POs appears from the central PO, with twice the period. We observed that $m_{21} = 0$ if the satellite orbits have $p_z = 0$, and $m_{12} = 0$ if they have $p_z \neq 0$.

(c) *Period-tripling bifurcation* $[n = 3]$, where $\mathrm{Tr}M = -1$. The central PO does not change its stability, but touches briefly a satellite PO.

The *scaled* monodromy matrix is defined with respect to $(z, \tilde{p}_z)$:

$$\tilde{M} = \begin{pmatrix} \tilde{m}_{11} & \tilde{m}_{12} \\ \tilde{m}_{21} & \tilde{m}_{22} \end{pmatrix} = \begin{pmatrix} m_{11} & Bm_{12} \\ \dfrac{1}{B}m_{21} & m_{22} \end{pmatrix} \quad . \tag{3.18}$$

Note that the trace is invariant: $\mathrm{Tr}\tilde{M} = \mathrm{Tr}M$.

3.1.7 Time-reversal symmetry

The 3-D problem (3.2) is not invariant through time-reversal[4] ($t \to -t$), because of the presence of the magnetic field. However, the 2-D problem (3.4), being of the form kinetic energy + potential, has *time-reversal symmetry.*[5] A first consequence is the symmetry in p_z of the SoS defined on the walls $x_{\mathrm{sos}} = \{0, L\}$.[6] Time-reversal symmetry implies that the time-reversed trajectory of a periodic orbit (PO) is *also* a PO.

Generic POs (e.g., s_*) are "topologically" equivalent to a circle in phase space and would correspond to the rotation motion in a pendulum; they are distinct in phase space from their time-reversed partner, although they follow the same path in position space.

In fact, most of the important POs in the RTD are *self-retracing* **(SR)**. They have the topology of a line and correspond to the librations of a pendulum. They are defined by the fact that they coincide in phase space with their time-reversed companion. They must have two points where there momentum is reversed; this can happen either if $p_z = 0$ at a bounce, or if they reach the soft energy surface defined by (3.15) where their momentum becomes zero.

Because we are interested in the current which is built on the left wall, we have to propagate trajectories from the left wall back to the left wall; this defines in some sense

[4]We define the "time-reversed" of an orbit as the trajectory obtained by flipping the momentum $\boldsymbol{p} \to -\boldsymbol{p}$ at the end of the orbit and evolving it from then.

[5]The proper time-reversal in 2-D taking into account the third dimension would involve changing $\dot{Y}$, which would change z and destroy the time-reversal symmetry.

[6]This is due to the $p_x \to -p_x$ reflection of the bounce, which means that the time-reversed of a point of the SoS is itself another point of the SoS. This would not be the case for a SoS taken in the middle of the well, as the time-reversed point would not satisfy the condition $p_x > 0$.

particular points on a PO where the PO "starts" and "ends". This is important for the monodromy matrix, which changes with the starting point (although its trace is independent of such a choice and is a truly global property of the PO). Some SR POs have a further property: taking their time-reversal at their end point (defined to be on the left wall), one finds oneself on the portion of the trajectory on which we started the PO. This happens when the end point is one of the points where the momentum is reversed (i.e., one must have $p_z = 0$ on the left wall). They will be called *time-symmetric* **(TS)** trajectories. For instance, t_u is TS while t_v is not: taking the time-reversal of the latter at the end point where $p_z \neq 0$, we find ourselves on the second portion of the trajectory (see Fig. 3.2 below).

TS POs have the important property:

$$m_{11} = m_{22} \quad . \tag{3.19}$$

In effect, consider a monodromy matrix M. Its time-reversed M^{TS} is given by its inverse M^{-1}, with the change $\delta p_z \to -\delta p_z, \delta p'_z \to -\delta p'_z$. Then

$$M^{-1} : \begin{cases} \delta z = m_{22}\delta z' - m_{12}\delta p'_z \\ \delta p_z = -m_{21}\delta z' + m_{11}\delta p'_z \end{cases} \Rightarrow M^{\mathrm{TS}} : \begin{cases} \delta z = m_{22}^{\mathrm{TS}}\delta z' + m_{12}^{\mathrm{TS}}\delta p'_z \\ \delta p_z = m_{21}^{\mathrm{TS}}\delta z' + m_{11}^{\mathrm{TS}}\delta p'_z \end{cases} . \tag{3.20}$$

As $M = M^{\mathrm{TS}}$ for a TS PO, $m_{11} = m_{22}$.

For SR POs that are not TS, the time-reversed pairs are not distinct in phase space; however, their monodromy matrix are distinct. Their link is given by $m_{11} = m_{22}^{\mathrm{TS}}$, $m_{22} = m_{11}^{\mathrm{TS}}$, $m_{12} = m_{12}^{\mathrm{TS}}$, $m_{21} = m_{21}^{\mathrm{TS}}$. This relation also holds for non SR-POs.

All perpendicular POs (starting with $p_z = 0$ on the left wall) are TS POs: for example $t_0, t_1, t_u, s', s_1, 1{:}3, 3{:}3$. Non-perpendicular POs are not TS; they can be SR (e.g., t_v and 2:3) if they have a perpendicular bounce on the right wall or have a turning point on the energy surface, or they can be non-SR (e.g., s_*).

3.2 Periodic orbits in the RTD

In the following, we present the important POs in the resonant tunneling diode (RTD) at different tilt angles θ. We analyze their behavior according to the heuristic semiclassical interpretation: a PO can contribute to the current if it satisfies the following conditions. (*i*) It hits both walls, to connect the emitter to the collector. (*ii*) It is not too unstable, so that its contribution to the density of states (DoS) given by the Gutzwiller trace formula

(1.4) is significant. Also, one can expect the current to show an enhancement of the P1/P2/P3 oscillations around P1/P2/P3 bifurcations.[7] (*iii*) The starting position $|z_0|$ of the PO is not too large, so that the initial state, given by a Gaussian distribution, can "feed" the PO. Note that the localization of the initial state increases with the magnetic field value. Roughly speaking only a PO with $z_0 <\sim 400$ a.u. can be expected to give a significant contribution at average B. (*iv*) The action and period of the PO are small in order to give period-one, two or three oscillations that can be seen experimentally (this is because of the damping due to phonon emission). This approach corresponds actually to one of the semiclassical formulae presented in chapter 5: the "hard limit" PO formula (5.64). It will be tested quantitatively in section 6.1; here we only present a qualitative interpretation.

3.2.1 $\theta = 0°$; integrable case

At $\theta = 0°$ the dynamics are integrable, as the bounces do not mix the decoupled motions. Trajectories simply wind around the magnetic field (cyclotron motion), while being accelerated by the electric force. One has as many constants of motion as degrees of freedom, and using action-angle variables, one can reduce the dynamics to a motion on tori —"doughnut" shaped surfaces— (see e.g. Gutzwiller 1990).

We show in Fig. 3.1 (a) a Poincaré surface of section at $\theta = 0°$. The trajectories are confined on torus-like structures around t_0; the central traversing PO running through the center ($z = 0\ \forall x$) is shown in the inset. A torus is said to be resonant when the periods of the motions along the decoupled degrees of freedom are commensurate; it supports then a continuous family of periodic orbits. As t_0 is centered on $z = 0$, we can expect a perfect overlap with the Gaussian initial state, yielding a strong period-one (see next subsection) current. In (b) we see that the stability of t_0 changes with ϵ, having resonances where $\mathrm{Tr}M^n = 2$. Note that in this integrable case the GTF is not valid as POs are not isolated; one should use instead EBK quantization or an equivalent version expressed in terms of tori (Berry and Tabor 1977). Indeed, applying the GTF would yield significant oscillations with ϵ (for example, enhancements where $\mathrm{Tr}M = 2$) which are not seen in the experimental current. We also show $\tilde{m}_{21}$, which will be used in a quantitative semiclassical theory (HLNO) tested in section 6.1.

As θ increase above zero, the bounces against the barriers mix the decoupled motions;

[7] At n-bifurcations the GTF diverges as $\mathrm{Tr}(M^n) = 2$, and the QM DoS shows a finite enhancement of the related oscillations.

this increases gradually the part of phase space that is filled with unstable trajectories. The general framework to understand such transition from integrability to chaos is the KAM theorem (see e.g. Gutzwiller 1990); in particular it states that the resonant tori are destroyed and replaced by a pair of stable-unstable POs.

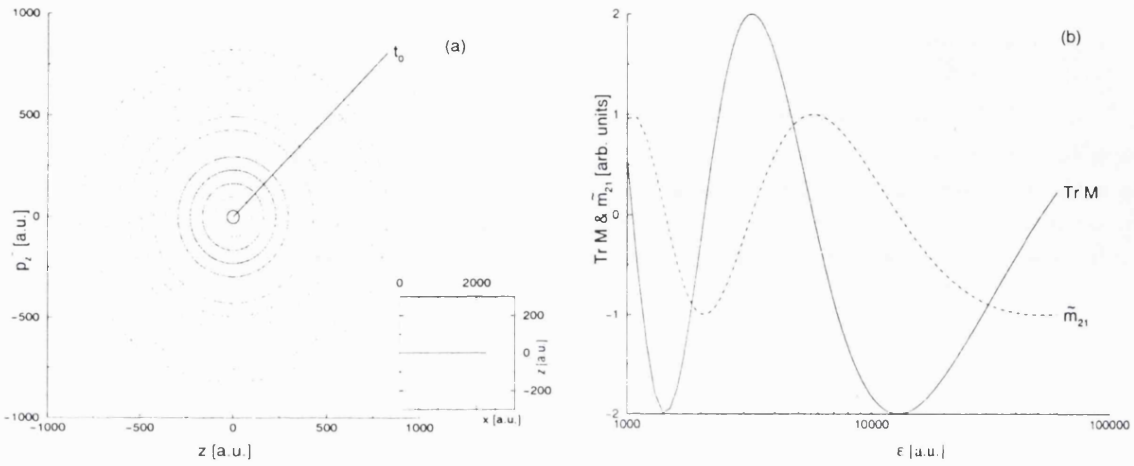

Figure 3.1: (a) Poincaré surface of section at $\theta = 0°$, $\epsilon = 20000$. The inset shows the shape (x, z) of t_0, the straight 1:1 PO running at the center. (b) Evolution of TrM and $\tilde{m}_{21}$ for t_0, as the dynamical parameter ϵ changes.

3.2.2 The relevant POs

The most important periodic orbits in the RTD are *emitter* POs, which hit both left and right walls. We shall not discuss *collector* POs (which hit only the right wall), as these only contribute to the DoS, and not to the current. One denotes POs either by a name (e.g. t_0, s'), or by $n:m$, where n/m is the number of bounces on the left/right wall (e.g. 1:3). The n^{th} repetition of a PO is denoted by adding n (e.g. $2t_0$). The partner PO in a tangent bifurcation (that does not contribute to the current) is denoted by adding a "$-$" (e.g. t_0^-, s'_-); note that the "$-$" does not necessarily means that the PO is unstable at the bifurcation. t or s refer to a family of similar-looking POs $(t_0, t_1, ..)$.

A very important fact in this system is that the actions S of all the shortest emitter POs (and their repetitions) are very close to each other. This is due to the fact that most of the energy lies in the x motion, while the z motion, which distinguish the different POs, does not change the value of S by much. Also, we shall establish in subsection 5.3.4 a connection between the scaled action of a PO and the voltage period of the oscillations they generate. Table 3.2.2 presents the situation for the main POs in the RTD.

Period	POs	Scaled action	Voltage period
P1	t	$\hat{S} \approx 1$	$\Delta V \approx 0.04V$
P2	$2t, s$	$\hat{S} \approx 2$	$\Delta V \approx 0.02V$
P3	$3t$, 1:3, 2:3, 3:3	$\hat{S} \approx 3$	$\Delta V \approx 0.01V$

Table 3.1: The main POs, with their scaled action and the related voltage period of the current oscillations (see subsection 5.3.2 and Table 7.1.2). P1/2/3 refer to the three types of oscillations observed in the experiments, as mentioned in section 2.3.

We show in Fig. 3.2 the shape of the main POs. In (a) we have the most important PO in the RTD (t_0), which is a deformation from the straight PO at 0°. It has been quickly recognized as being responsible for the P1 oscillations in the current (Fromhold *et al.* 1994). One shows also two orbits, t_u and t_v, which are born in two pitchfork bifurcations of t_0; they have twice the period of t_0 and should contribute to the P2 oscillations of the current. The main POs responsible for the P3 current at $\theta = 38°$ are shown in (b): 1:3, 2:3 and 3:3. (c) and (d) presents some P2 POs. s' and s_1 belong to the same family 1:2; s_1 has one extra cyclotron rotation. The (x, y) shape of s_1 is shown in (d), which illustrates the fact that the 3-D system does not have time-reversal symmetry and does not allow self-retracing POs (see subsection 3.1.7). We show s_* in (c), which is born in a (synchronous) pitchfork bifurcation with s' at 27°, and is the only PO shown here which is not self-retracing. Two collector POs are shown in (d).

3.2.3 $\theta = 11°$; cascade of tangent bifurcations

SoS

We show in Fig. 3.3 a Poincaré SoS at $\theta = 11°$. One sees clearly the transition from regularity to chaos as ϵ decreases. In the $\epsilon \to \infty$ limit (e.g., $B \to 0$) the dynamics becomes integrable. Increasing B at fixed F gives more cyclotron rotations; this means that the bounces will rapidly separate two neighboring trajectories, as their angles just before the bounce are highly sensitive to their initial conditions.

(a) At $\epsilon = 20000$, the dynamics is dominated by the island of stability of t_0, which is surrounded by a sea of unstable trajectories. This large stable island is the remnant of the torus structure existing for the integrable dynamics at $\theta = 0°$. It has slightly moved to the right. It is responsible for the regular P1 oscillation seen at high ϵ in Fig. 2.5.

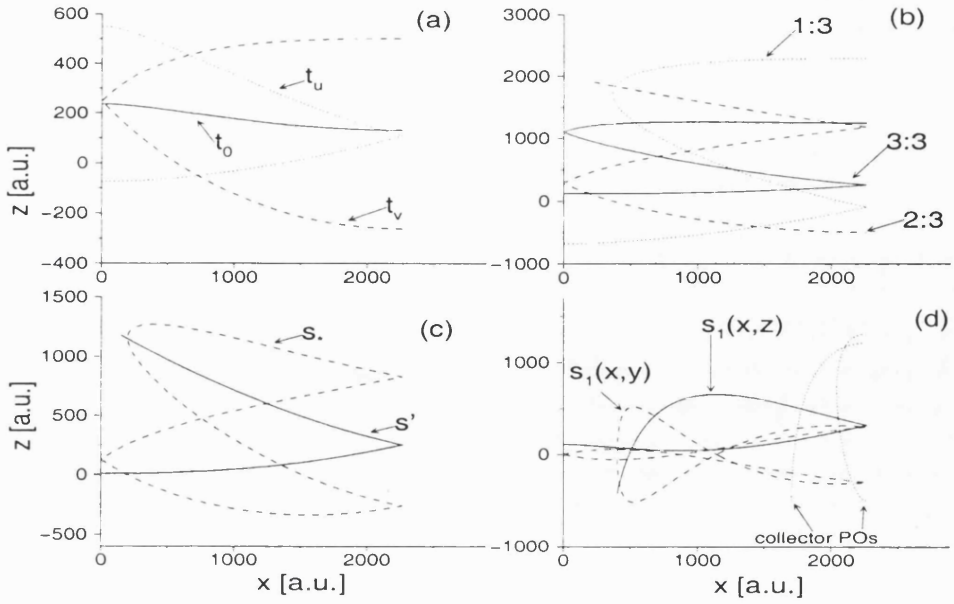

Figure 3.2: Shape (x, z) of the important POs. The hard walls (barriers) are at $x = 0$ and $x = L = 2267$ a.u.. (a) $\theta = 11°, \epsilon = 14000$. (b) $\theta = 38°, \epsilon = 25000$. (c) $\theta = 27°, \epsilon = 15000$. (d) $\theta = 11°, \epsilon = 2500$, with also the (x, y) projection of the 3-D motion of s_1, as well as two collector POs.

The stable structure on the left is not important for the current (it has a large action and the related oscillations cannot be resolved experimentally). The unstable PO t_u cannot be easily seen as it is unstable, while the stable t_v has just appeared from the top of the SoS.

(b) t_u has moved *inside* the island of stability, and can be recognized by two hyperbolic structures on the $p_z = 0$ axis. It is about to undergo a P2 pitchfork bifurcation with t_0. The two elliptic structures off-axis ($p_z \neq 0$) belong to t_v, which has also moved inside the island.

(c) t_0 has become unstable (hyperbolic structure) in a pitchfork bifurcation with t_u. It will restabilize in a second P2 pitchfork bifurcation with t_v.

(d) The island shrinks as ϵ decreases, until t_0 disappears in a tangent bifurcation around $\epsilon = 7000$.

(e) There is no t POs for a substantial range, but only the unstable s_1 lost in a sea of chaotic trajectories. It will move towards the center of the SoS.

(f) A new t PO called t_1 has appeared unstable from the edge of the SoS. Here it has become stable; it will disappear at lower ϵ in a tangent bifurcation with the unstable PO t_1^-.

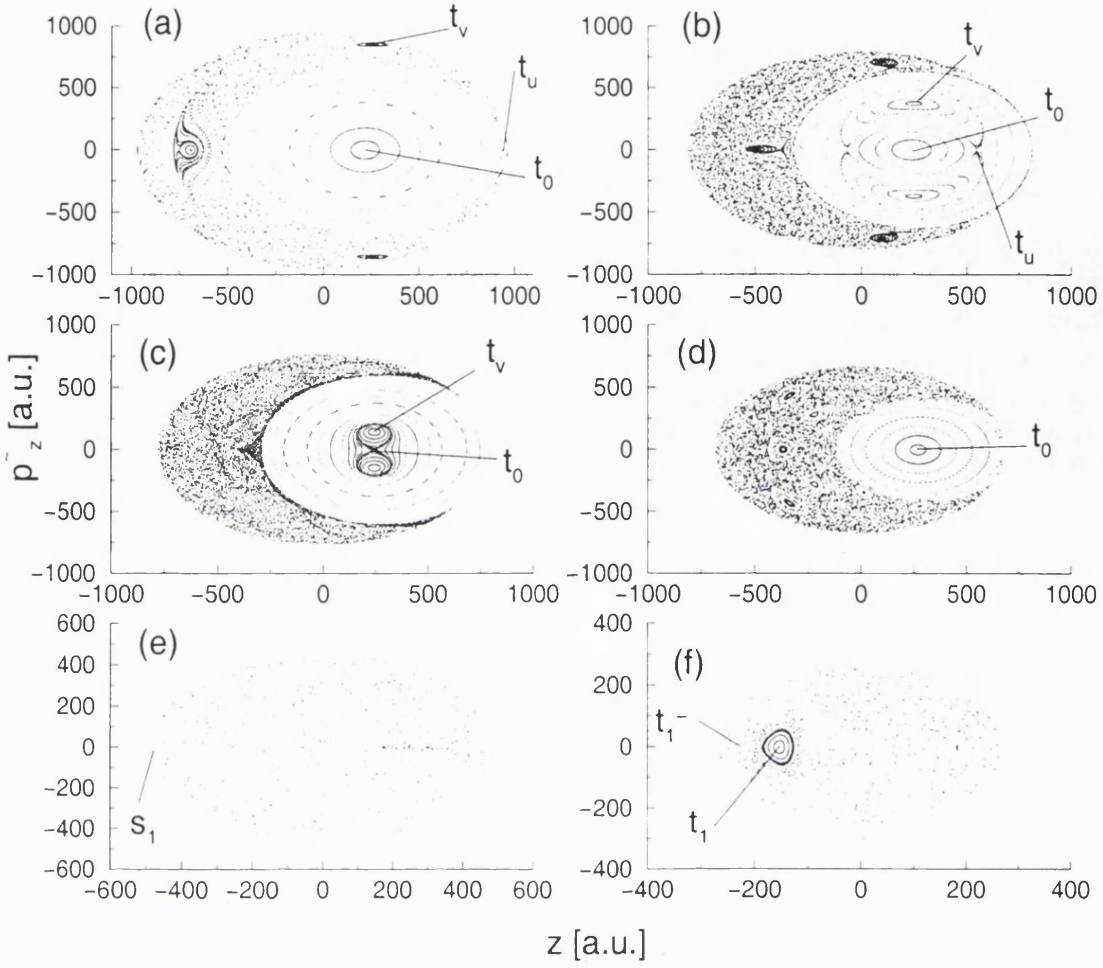

Figure 3.3: Poincaré surfaces of section at $\theta = 11°$. (a) $\epsilon = 20000$. (b) $\epsilon = 14000$. (c) $\epsilon = 13000$. (d) $\epsilon = 10000$. (e) $\epsilon = 5000$. (f) $\epsilon = 1500$.

Accessibility and stability

Fig. 3.4 (a) shows the starting position z_0 of the POs as ϵ is increased. A striking feature is the "cascade" of tangent bifurcations (TBs) of t POs, where a pair of stable and unstable POs (e.g., t_1 and t_1^-) appears. They separate and move towards the edge of the SoS. The unstable partner is the first to disappear in a "cusp bifurcation" when its starting position encounters the edge of the SoS (the soft energy surface of zero momentum); see subsection 3.2.4. The stable partner PO survives longer, but also disappears at the edge of the SoS. t_1 is present in the region where weak experimental P1 oscillations can be seen in Fig. 2.5.

t_0 does not encounter the edge of the SoS and tends, in the $\epsilon \to \infty$ limit, towards the straight traversing PO that exists at $\theta = 0°$. The stable s_1 PO goes through the center ($z = 0$) at $\epsilon = 2800$; this should highly favor its contribution to the current.

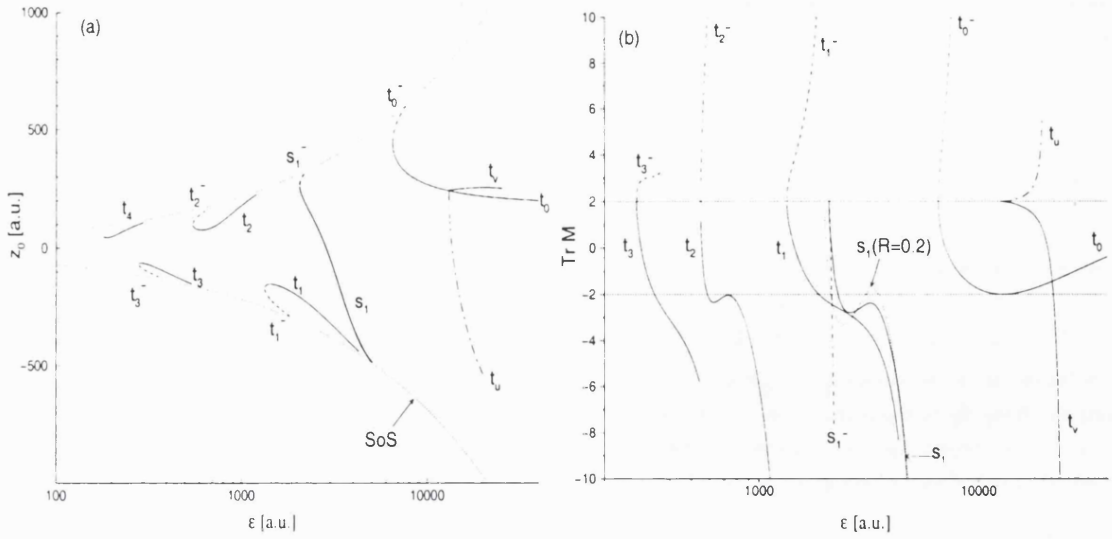

Figure 3.4: Evolution of (a) z_0 and (b) TrM with ϵ at $\theta = 11°$, for the main POs (t and s_1). (a) The continuous dotted lines indicate the limit of the SoS (for $p_z^0 = 0$). (b) The horizontal dotted line indicates Tr$M = \pm 2$; we also show s_1 for $R = 0.20$.

Note the interval between the disappearance of t_1 at $\epsilon = 4279$ and the tangent bifurcation of t_0 at $\epsilon = 6539$. The absence of t POs, producing P1 oscillations in a semiclassical theory based on POs, is in flagrant contradiction with experimental results and quantum calculations; this is the "no (real) PO" region mentioned in Fig. 2.5.

Fig. 3.4 (b) is a bifurcation diagram showing the evolution of TrM as ϵ is increased. $t_{0,1,..}$ undergoes a series of tangent bifurcations where it is born with its unstable partner $t^-_{0,1,..}$. Both have Tr$M = 2$ at the bifurcation; slightly after the stable partner will have Tr$M < 2$, while the unstable partner will have Tr$M > 2$. The TB at $\epsilon = 6539$ is especially important: for $\epsilon < 6539$ there is no (real) PO t_0 for a substantial ϵ range. Note that the TB does not yield any special enhancement of the experimental current, as would be expected for the DoS. As all TBs of time-symmetric POs observed in the RTD, it has $m_{11} \to 1, m_{12}$ finite and $m_{21} \to 0$. The stable partners (except t_0) destabilize rapidly, and become massively unstable before disappearing at the edge of the SoS.

t_0 undergoes a double pitchfork bifurcation (PB) around $\epsilon = 13000$, where Tr$M \to -2$. In the first one at $\epsilon = 12822$, t_0 becomes (as ϵ increases) unstable and a pair[8] of non-perpendicular satellite POs (t_v) is born; t_v has $p_z^0 \neq 0$ and is therefore not time-symmetric (see subsection 3.1.7); in that case $m_{12} \to 0$ at the bifurcation. Then t_0 restabilizes at the second bifurcation at $\epsilon = 13112$, and a pair of perpendicular ($p_z^0 = 0$) time-symmetric

[8]They are indistinguishable as they go along the same path.

(TS) POs (t_u) is born; in this case $m_{21} \to 0$. The periods and actions of t_u and t_v are close to double those of t_0, which is why we call such bifurcations *period doubling* (P2). Note that the second repetition $2t_0$ has $\mathrm{Tr}M \to 2$ at the PBs, and that its off-diagonal elements follow those of t_0: $m_{12} \to 0$ at $\epsilon = 12822$, $m_{21} \to 0$ at $\epsilon = 13112$. Note also $\epsilon = 7051$, where $\mathrm{Tr}M = 0$. This corresponds to a P4 bifurcation, but has the peculiar property that the second repetition $2t_0$ has both $m_{12} \to 0, m_{21} \to 0$ (while those of t_0 are finite).

The period-doubling bifurcations occur in the main P2 experimental region seen in Fig 2.5; we can expect such bifurcation to produce an enhancement of the P2 signal as the GTF has a divergence for the second repetition of t_0. Hence, we could interpret the P2 region has a result of a bifurcation.

s_1 at 11° is presented for two values of $R = E/V$. Here s_1 has *metastability*: it is weakly unstable in a significant range of ϵ ($|\mathrm{Tr}M|$ is larger, but close to 2). This interesting feature is due to a "failed" PB: increasing the energy/voltage ratio to $R = 0.2$ will make s_1 undergo a double PB with $\mathrm{Tr}M = -2$. Usually, the instability of a PO in the RTD increases very quickly as it moves (in ϵ) away from the bifurcation where it was born, yielding a very weak contribution to the DoS. The accessibility is also favored, as z_0 passes through 0 around $\epsilon = 2800$. This is the "low ϵ" P2 region discussed in Fig. 2.5, which is therefore due to the combined effect of (*i*) the failed bifurcation that prevents the instability from growing and weaken the contribution to the DoS, and (*ii*) the maximum of accessibility when $z_0 = 0$. Note that the failed PB bifurcation would yield an enhancement of the P4 signal in the DoS (as s_1 is already P2); the P2 region is not an usual "bifurcation" effect.

3.2.4 $\theta = 27°$; cusp bifurcations

The hard bounces on the barriers bring a discontinuity in the dynamics. The definition of the bounce is to flip the x momentum. This is quite different from the turning point existing for SR trajectories when they reach the zero momentum ("soft energy") surface; this phenomenon is "natural" (i.e., created by a force) and "soft" as there is no discontinuity in the momentum.

The intersection of the energy surface and the left wall plays a particular role in the dynamics; it is called the "edge of the SoS" and depends on the initial p_z^0 of the trajectory under investigation. A trajectory hitting the wall will have some essential difference with a trajectory having a turning point on the energy surface. This is the origin of the *cusp*

bifurcation[9], which will be explained in more detail below.

SoS

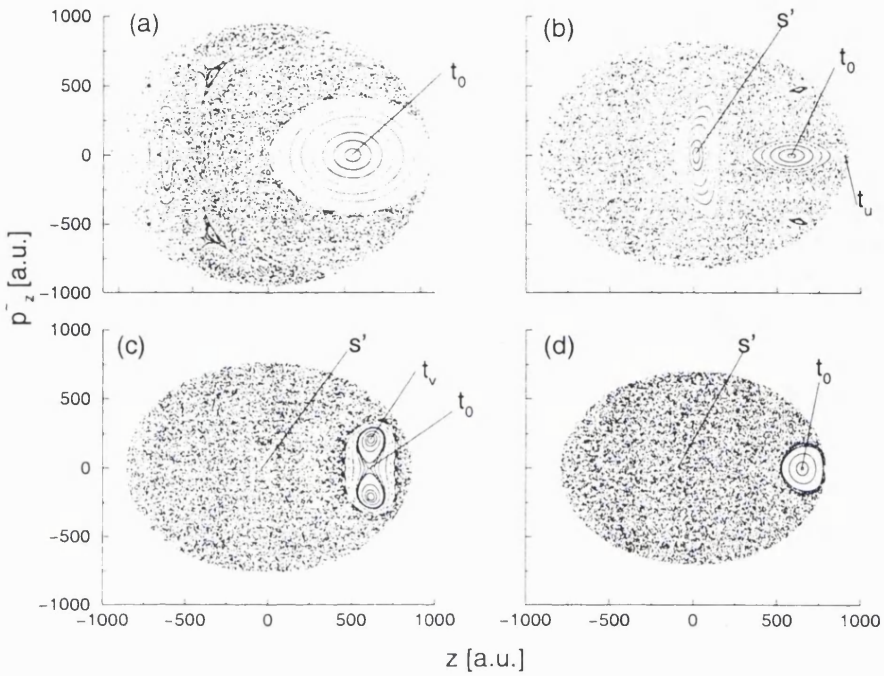

Figure 3.5: Poincaré surfaces of section at $\theta = 27°$. (a) $\epsilon = 20000$. (b) $\epsilon = 15000$. (c) $\epsilon = 13000$. (d) $\epsilon = 11000$.

First we start by showing a few SoS in Fig. 3.5. The situation is similar to the one at $\theta = 11°$.

In the regular regime (a), the main structure is the large island of stability surrounding t_0. One can note that this PO has moved quite a way from the center; we could hence expect a weak P1 experimental signal as the accessibility of t_0 is low. This is partially seen in Fig. 2.8 where the P1 signal disappears for $\epsilon <\sim 20000$; however the significant experimental P1 signal at higher ϵ is surprising.

In (b) a stable structure has appeared with s'; here this stable island is of the same size as the one around t_0, but it will shrink rapidly and disappear when s' becomes unstable.

(c) t_0 has undergone a pitchfork bifurcation with the unstable P2 PO t_u, that has consequently disappeared; t_0 will have another pitchfork bifurcation with the non-TS PO ($p_z^0 \neq 0$) t_v at a lower ϵ. The stable island around t_0 shrinks even more (d) and will disappear in a tangent bifurcation at lower ϵ.

[9]This name was given in Narimanov and Stone (1998b), which also presented a detailed study of this phenomenon.

The study of the SoS can help us to define three distinct dynamical regimes:

1. High $\epsilon >\sim 20000$: fairly regular dynamics, dominated by the island of stability of t_0.

2. Intermediate regime: several coexisting POs contributing to the current (here: t_0 and s'), or absence of real contributing POs (at $\theta = 11°$).

3. Low $\epsilon <\sim 3000$: chaotic regime: only unstable POs, lost in a sea of chaotic trajectories.

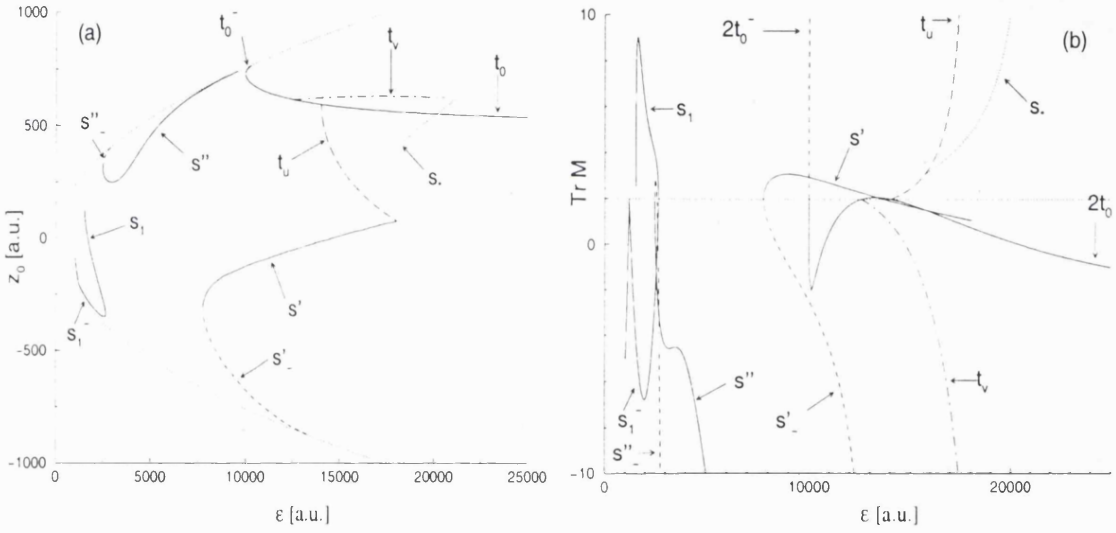

Figure 3.6: (a) Evolution of the starting position z_0 with ϵ at $\theta = 27°$. For t_v, we show the central leg. The dotted lines with parabolic shapes indicate the edge of the SoS for normal trajectories ($p_z^0 = 0$). (b) Trace of the stability matrix. The horizontal line is the locus of tangent bifurcations (Tr$M = 2$).

t orbits

Fig. 3.6 shows the situation at $\theta = 27°$. t_0 is born with its unstable partner t_0^- in a tangent bifurcation at $\epsilon = 9971$. At $\epsilon = 12570$, it destabilizes in a P2 pitchfork bifurcation where the non-TS PO t_v is born stable. The P2 pitchfork bifurcation at $\epsilon = 14014$ restabilizes t_0 and gives birth to the stable TSPO t_u. t_0 remains stable and tends towards the straight traversing orbit existing at $\theta = 0°$ in the $\epsilon \to \infty$ limit.

Müller *et al.* (1995) proposed that the experimental P2 region seen in Fig. 2.8 is a manifestation of the pitchfork bifurcations, as the latter occur around one edge of the P2 region. However, it is clear from Fig. 3.6 (a) that t_0, having a starting position z_0 around

500 a.u., is apparently not accessible to the tunneling electrons, and would yield a very low P1 or P2 current. This fact was pointed out in the comment by Fromhold *et al.* (1997a).

t_u becomes rapidly more unstable and its "central leg" (see Fig. 3.7) moves towards the center. Its outer leg, though, moves towards the edge of the SoS and finally hits the energy surface. We could only follow it until $\epsilon = 18010.3$, where the outer leg hits the wall less than 0.01 a.u. from the edge of the SoS. We believe that later t_u meets s' in a "cusp bifurcation", and that we could not follow it further because of its very high instability ($\mathrm{Tr}M \simeq 200$): the linear extrapolation of the z_0 vs. ϵ curve of t_u indeed meets s' at $\epsilon = 18039$. Details of the cusp bifurcation are discussed in Fig. 3.7.

t_v rapidly loses its stability and becomes more unstable as ϵ increases. Although its central leg hits the left wall approximately at the same place, its starting z momentum increases which makes the corresponding edge of the SoS (the maximum z allowed by the available energy) move towards the center [see (3.14)]. We could follow t_v until $\epsilon = 20529.7$, where the outer leg and is less than 1 a.u. away from the edge of the SoS. Because of its high instability ($\mathrm{Tr}M \simeq -500$), one can think that it survives slightly longer; extrapolating t_v and s_* further, one can infer a cusp bifurcation at $\epsilon = 21242$ where the position of both POs merge.

t_0^- moves towards the edge of the SoS and disappears in a cusp bifurcation at $\epsilon = 10263$, where its starting position meets the soft energy surface. We did not investigate t POs at low ϵ.

s orbits

s' presents three types of bifurcations. It is born in a tangent bifurcation at $\epsilon = 7757$ with a stable partner s'_-, where as usual $m_{21} = 0$. Its central leg moves towards the center of the SoS, and it undergoes a synchronous pitchfork bifurcation at $\epsilon = 13652$ where $m_{12} = 0$. There it becomes stable, and a new satellite PO (s_*) appears; it is non-SR, has $p_z^0 \neq 0$ and has the *same* period as s'. We believe that this non-generic type of bifurcation can only happen in systems with time-reversal symmetry.[10] Finally, it disappears with t_u in a non-generic type of bifurcation, called cusp bifurcation (CB) at $\epsilon = 18039$, and described in Fig. 3.7.

As mentioned in Narimanov and Stone (1998a), the presence of the CB yields a metastability for the PO s': $\mathrm{Tr}M$ is not expected to become much larger than 2 as it

[10] The Poincaré index theorem (Greene *et al.* 1981) is satisfied, as the satellite PO can generate two fixed points in the SoS, although it has the same period as the central PO which generates one fixed point.

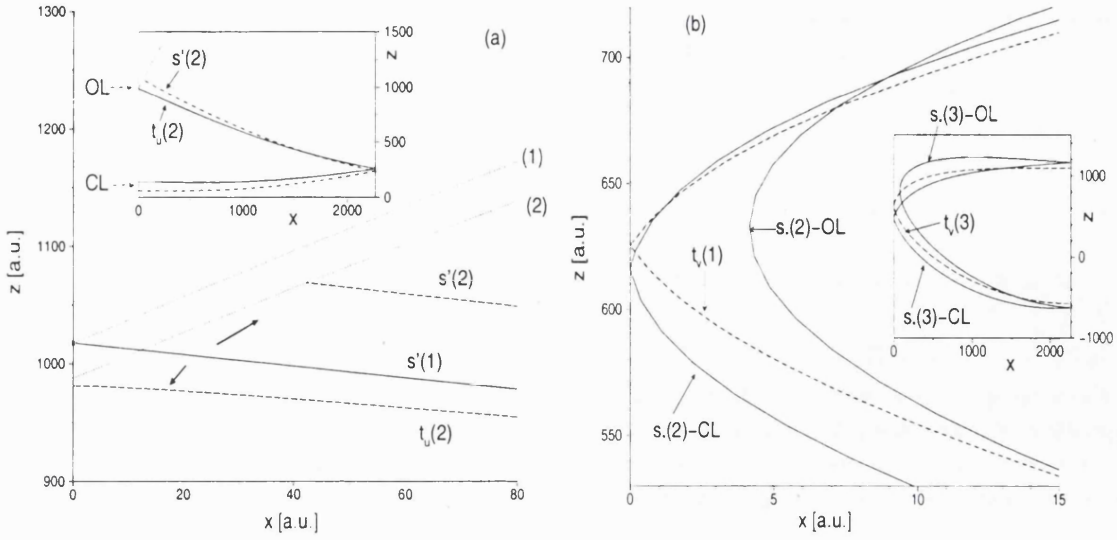

Figure 3.7: Details of cusp bifurcations at $\theta = 27°$ with (x, z) shapes; the insets show the global shapes. (a) s' appears at $\epsilon = 18039$ (1) with its outer leg (OL) having a turning point *exactly* at the intersection of the soft energy surface of zero momentum [dotted line (1)] and the left wall. Decreasing ϵ to 17000 (2), the OL extremity can either move along the soft energy surface to give s', or along the left wall for t_u. The central legs are indicated by (CL) in the inset. (b) s_* appears around $\epsilon = 21242$ (not shown as it is an extrapolation, see text), with its central (CL) and outer (OL) legs superimposed. The outer leg can either move inside the well, giving a (non self-retracing) s_* orbit at $\epsilon = 21134$ [s_*(2)-OL], or along the left wall giving a t_v orbit at $\epsilon = 20259$ (1); in the latter case the central and outer leg are superimposed as the PO is self-retracing. Here the central legs of both POs hit the left wall. The inset is at $\epsilon = 19000$ (3).

must vary from 2 at the TB to the small value it has at the CB (here, $\mathrm{Tr}M = 1.0179$). It is the reason for the strong scarring of the quantum wavefunction, persisting over a large range of ϵ values.[11] This metastability prevents the usual vanishing of the contribution to the DoS of an increasingly unstable PO. Moreover, the trace is close to two which means that the contribution is especially large, and s' has a favorable accessibility, with a maximum around $\epsilon = 14500$, where $z_0 = 0$. Hence, one could suppose that the experimental P2 region could be due to s' as proposed in Fromhold *et al.* (1994), instead of $2t_0$. We shall see in chapter 6 that the situation is indeed intricate, and that even quantitative PO formulae cannot identify clearly which PO is responsible for the current (on the contrary to the saddle orbit theory, which gives an unambiguous answer).

The central leg of s_* moves across the center of the SoS. Similarly to t_v, the increase of its initial z momentum means that the corresponding edge of the SoS moves towards

[11] Some scarred wave functions are shown in section 4.3.

the center. We could follow s_* until $\epsilon = 21134$, where its outer leg is very close to the central leg; they both tend towards the intersection of the left wall and the energy surface (see Fig. 3.7). This scenario is consistent with the cusp bifurcation of t_v described above.

s'' is born stable in a TB at $\epsilon = 2461$ with the unstable s''_-. Both POs move towards the edge of the SoS. s''_- disappears at $\epsilon = 2876$, while s'' disappears at $\epsilon = 9554$. In both cases it is because their central leg encounters the edge of the SoS.[12]

The tangent bifurcation of s' at $\epsilon = 7700$ does not yield any visible enhancement of the P2 experimental current (see Fig. 2.8). On the contrary, it marks the upper bound of the "no (real) PO" region, that extends until s'' becomes weakly unstable ($\epsilon \simeq 4000$) and can be expected to contribute to the P2 current. As its name suggests, that region is remarkable because no PO can be found to explain the experimental oscillations, similarly to the situation at $\theta = 11°$.

The star-shaped POs s_1 and s_1^- coalesce in a TB that occurs in the reverse order than usual (e.g., $\theta = 11°$). s_1^- was actually born in a TB at lower ϵ.

According to Narimanov and Stone (1998b) the s orbits have, at a cusp bifurcation, a finite TrM taking a non-specific value (e.g., Tr$M = 1.0179$), while the t orbits have Tr$M \to \infty$. This peculiar idea of "infinite" instability might be due simply to the fact that they defined, like us, a monodromy matrix with respect to the z coordinates; this is however a poor choice when the trajectory goes parallel to z like at the cusp bifurcation.

Soft wall model

We studied a model of the RTD where we replaced the hard walls by "soft" walls described by exponential barriers. In that case the cusp bifurcations disappear, and are replaced by standard bifurcations where Tr$M = 2$.

3.2.5 $\theta = 38°$; period-tripling

SoS

We present some SoS in Fig. 3.8. We see at $\epsilon = 40000$ (a) the effect of a high tilt angle θ: here we have much more structure, e.g. in the basin surrounding the stable island of

[12] This scenario is not consistent with the one described in Narimanov and Stone (1998b), where s'' and t_0^- undergo a cusp bifurcation. This would imply that s'' disappears later with t_0^- at $\epsilon = 10263$, and that the outer leg moves towards the left wall until it becomes superimposed with the central leg exactly at the bifurcation.

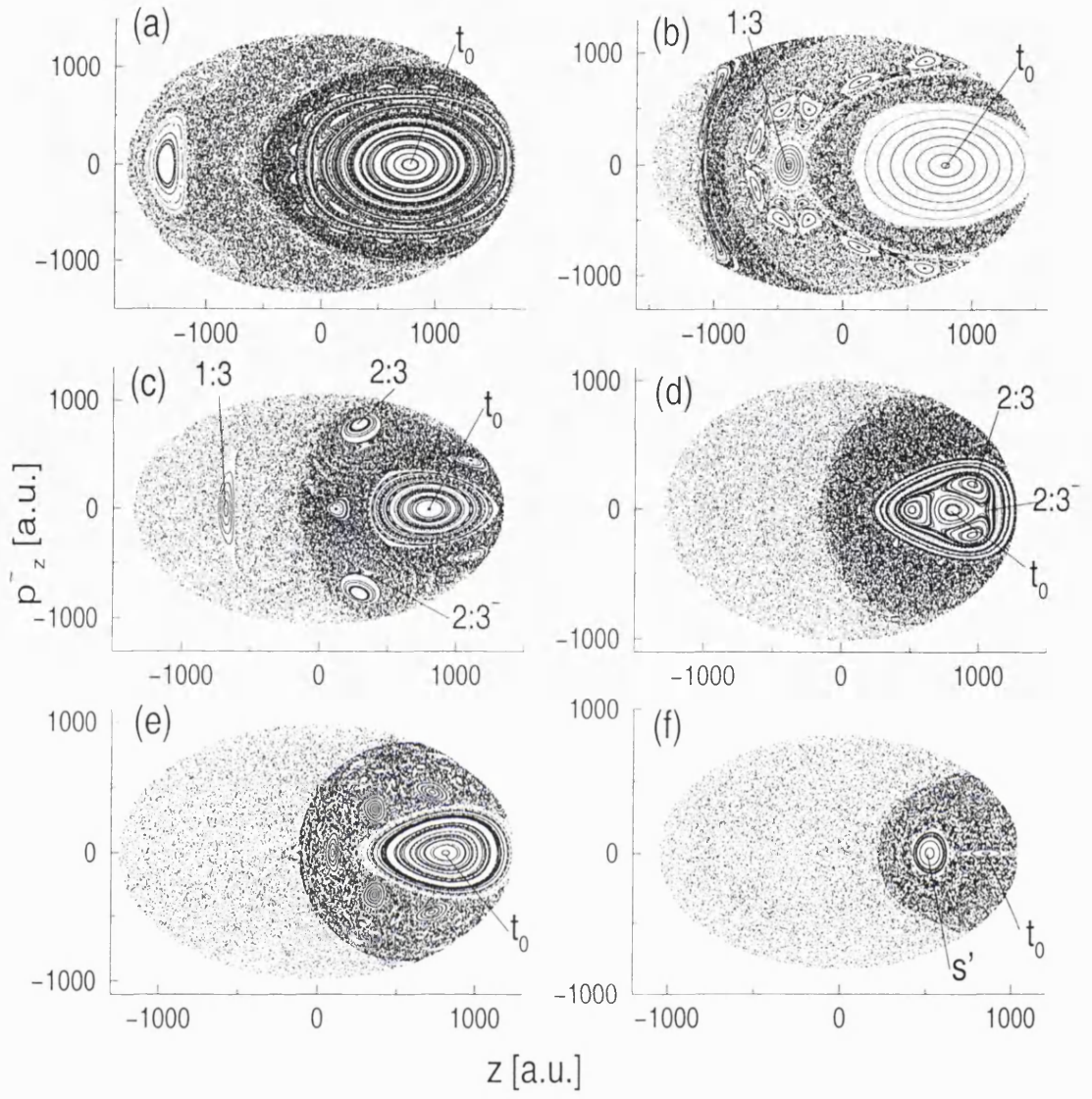

Figure 3.8: Poincaré surfaces of section at $\theta = 38°$. (a) $\epsilon = 40000$. (b) $\epsilon = 30000$. (c) $\epsilon = 25000$. (d) $\epsilon = 22500$. (e) $\epsilon = 21500$. (f) $\epsilon = 15000$.

t_0. This PO has moved far from the center; this should yield a very weak contribution to the current, a fact which conflicts with the experimentally observed P1 oscillations (see Fig. 2.10). There are islands chains (stable periodic orbits with high periodicity) around the stable island. Note that the island on the left is related to a PO with high period, that does not contribute to the experimental current. A remarkable fact is the presence of "dynamical barriers", which confine trajectories to one area of the SoS for a very long (but finite) time. They can be seen as the darker regions, which contain many more crossings of the SoS than the lighter areas.[13]

[13]In (b) we have used a different number of trajectories for different regions of the SoS.

At $\epsilon = 30000$ (b) one has the P3 orbit 1:3, which is stable here and quite accessible to the tunneling electrons as it is close to the center. Two islands chains stretch around its island of stability and the one around t_0. The pair of elongated islands on the left is again related to some high period PO.

1:3 has moved away from the center at $\epsilon = 25000$ (c), and three more P3 orbits have appeared. The stable 2:3 is recognized by the pair of stable islands with opposite $p_z \neq 0$; next to it we see the unstable $2{:}3^-$ with a hyperbolic structure. 3:3 is stable, and one of its legs hits the SoS near the center. Hence, it is also a candidate for P3 oscillations.

At $\epsilon = 22500$ (d) both the unstable $3{:}3^-$ —which has appeared in the meantime— and the stable 3:3 have moved inside the island of stability of t_0. We approach the period-tripling bifurcation of t_0, which strictly speaking occurs only with the unstable $3:3^-$. However, it is very hard to separate it from the tangent bifurcation that annihilates 3:3 and $3{:}3^-$, as both events occur in very small ϵ range. The pair of 2:3 and $2{:}3^-$ POs has already vanished in a tangent bifurcation, and 1:3 has become unstable.

After the bifurcation (e), the orientation of the island of stability of t_0 has changed (it now points towards the left), as usual in "touch-and-go" period-tripling bifurcations (Mao and Delos 1992). Note that t_0 has not changed its stability, unlike in P2 bifurcations.

Finally at $\epsilon = 15000$ all important P3 POs have vanished, and one sees the stable P2 s' and P1 t_0, surrounded by a chaotic sea.

Accessibility and stability

Fig. 3.9 (a) shows the evolution of the starting position of the important POs at $\theta = 38°$ as the dynamical parameter ϵ changes; (b) presents the evolution of their stability.

t_0 is born in a tangent bifurcation at $\epsilon = 11796$; its unstable partner t_0^- disappears shortly afterwards in a cusp bifurcation. One finds several 1:2 POs: s_1, s''' and s'' at low ϵ, and s' at a higher ϵ. Apart from s''', they all start in the central region accessible to the tunneling electrons.

The P3 orbits have a complicated structure. 1:3 follows to some extent the behavior of s' described for $\theta = 27°$. It is born unstable in a tangent bifurcation at $\epsilon = 17196$. Its partner $1{:}3^-$ destabilizes rapidly, and disappears at the edge of the SoS at $\epsilon = 20980$.[14] 1:3 restabilizes at $\epsilon = 24189$ in a synchronous pitchfork bifurcation. It moves towards the

[14] According to Narimanov and Stone (1998b), it disappears in a cusp bifurcation with the PO 0:3. We did not investigate bifurcations involving collector POs.

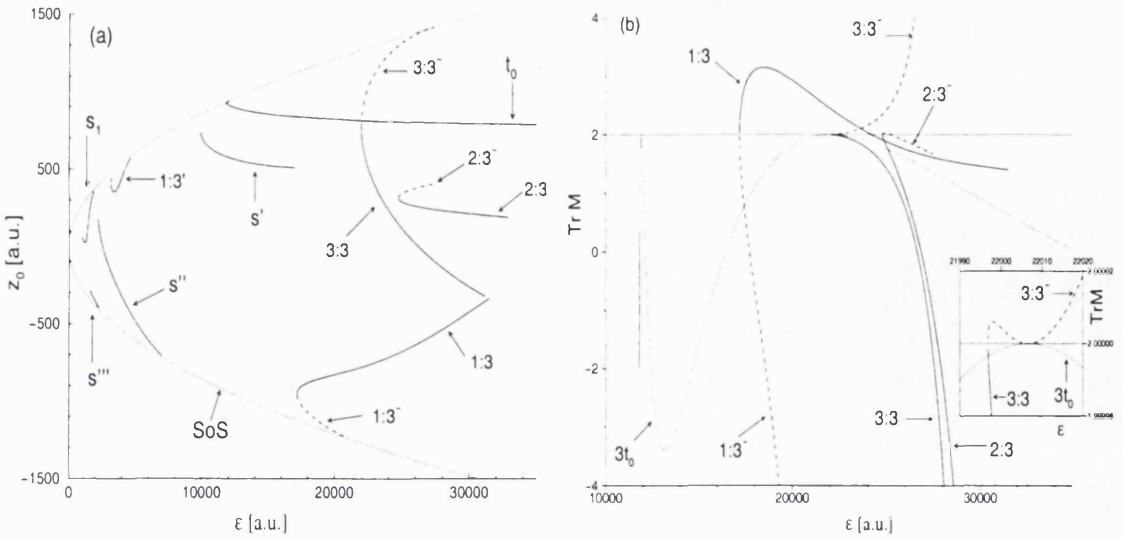

Figure 3.9: (a) Evolution of z_0 with ϵ at $\theta = 38°$. (b) Evolution of TrM. The inset shows details of the period-tripling bifurcation between $\epsilon = 21990$ and 22010.

center of the SoS, and finally disappears in a cusp bifurcation with 3:3 around $\epsilon = 31220$, as described in Fig. 3.10 (a). There is another pair of 1:3-type POs at lower ϵ.

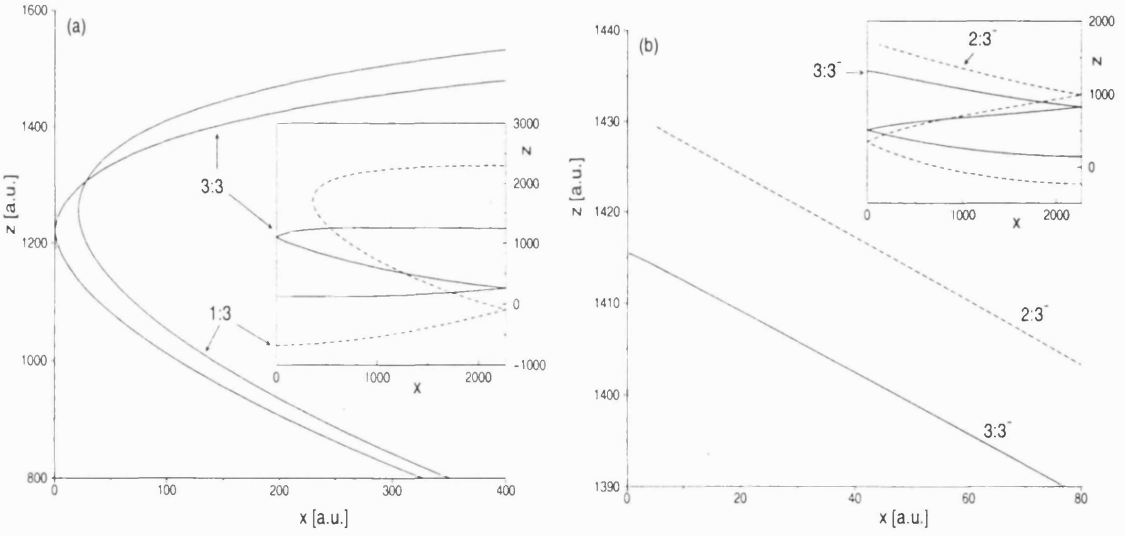

Figure 3.10: Details of cusp bifurcations at $\theta = 38°$. (a) The outer leg of 3:3 which makes a hard bounce on the left wall approaches the edge of the SoS at $\epsilon = 31000$, while the point where 1:3 turns back get closer to the left wall. Both POs should merge at a later ϵ. The inset shows the POs at $\epsilon = 25000$. (b) Similar scheme with 3:3$^-$ and 2:3$^-$ at $\epsilon = 27300$. The inset is at $\epsilon = 25000$.

3:3 and 3:3$^-$ are born in a tangent bifurcation at $\epsilon = 21996.84$; this is just before the period-tripling bifurcation that the unstable PO 3:3$^-$ undergoes with $3t_0$ at $\epsilon = 22006.6$ [see inset in (b)]. This is a "touch-and-go" bifurcation, where the POs coincide at the

bifurcation without disappearing or changing their stability. Then the outer leg of $3{:}3^-$ moves towards the edge of the SoS, and it becomes highly unstable. It finally disappears in a cusp bifurcation with $2{:}3^-$ around $\epsilon = 27380$, as described in Fig. 3.10 (b). This is not seen on the z_0 graph, as we follow the outer leg of $3{:}3^-$ (which makes a normal bounce against the left wall) and the central leg of $2{:}3^-$. 3:3 stays stable until $\epsilon = 27540$. Then it becomes very unstable and disappears in a cusp bifurcation with 1:3 around $\epsilon = 31220$.

$2{:}3$ and its unstable partner $2{:}3^-$ are born in a tangent bifurcation at $\epsilon = 24749$. The latter will disappear in a cusp bifurcation with $3{:}3^-$ around $\epsilon = 27380$, while the former disappears at $\epsilon = 32920$, when its starting position encounters the edge of the SoS corresponding to its starting momenta $p_z^0 \neq 0$.

Origin of the P3 oscillations

As shown in Fig. 2.10, period-three oscillations are observed in the experiments. Because the decoherence damps them by roughly a factor of one hundred with respect to P1 oscillations, they must have a high amplitude to be visible.

Fromhold *et al.* (1995a) proposed that 1:3 was responsible for the P3 oscillations. Our study shows that indeed it is fairly centered when it appears ($\epsilon = 31000$). Then it moves away from the center, but at this angle the Gaussian initial state of the electrons should be displaced[15] towards negative z, yielding a possible contribution to the current. This PO is also favored by its cusp bifurcation and the consequent metastability.

On the other hand, Müller *et al.* (1995) interpreted the P3 region as a manifestation of the period-tripling bifurcation of t_0 at $\epsilon = 22000$. This stemmed from the fact that in the plot of maxima (Fig. 2.9), the P3 region starts indeed around that ϵ. The stability of $3t_0$ is favorable all way through. However, Fromhold *et al.* (1997a) contested that interpretation, arguing that t_0 was far too off-center ($z_0 \simeq 800$a.u.) to be able to contribute to the current, especially with the shift of the initial state.

This was replied to in Boebinger *et al.* (1997), where it was noted that P1 oscillations were observed experimentally despite the low accessibility of t_0. It was proposed that higher Landau levels in the initial state could explain this fact. They also proposed that the current came from 3:3, which is linked with the period-tripling bifurcation of t_0. It is indeed very accessible around $\epsilon = 26200$, and is also stable over a large ϵ range.

Note that $2{:}3$ POs are quite accessible; their instability however makes them less

[15] See subsection 5.1.2.

serious candidates. Finally, there is apparently no good candidate for the "low ϵ" P3 region around $\epsilon = 10000$.

In an attempt to close this controversy, we shall study this region in section 7.3; we shall compare a series of semiclassical theories with quantum mechanical calculations and experimental amplitudes.

3.2.6 Conclusions

The approach that we presented here is qualitative. We studied the classical dynamics to use a heuristic approach to the current: a GTF density of states where only emitter POs with small starting position $|z_0|$ can contribute. We asserted the following facts:

1. The regular P1 region at $\theta = 11°$ is associated to t_0; the low ϵ region to t_1.
2. A substantial P1 region at $\theta = 11°$ cannot be linked to any real PO.
3. The main P2 region at $\theta = 11°$ is a manifestation of the double pitchfork bifurcation of t_0.
4. The low ϵ P2 region comes from the high accessibility of s_1, helped by the metastability arising from its "failed" bifurcation.
5. The P1 regions at $\theta = 27°$ and $\theta = 38°$ are linked to t_0, which has a large island of stability. However, its accessibility is apparently very low; this apparent paradox will be explained by tori quantization effects in section 4.2.
6. Two distinct POs can contribute to the P2 region at $\theta = 27°$: $2t_0$ which is stable but apparently not accessible, and s' which is accessible and has metastability following its cusp bifurcation.
7. This region also contains an ϵ range with no real PO which could be responsible for the observed oscillations.
8. The origin of the high ϵ P3 region at $\theta = 38°$ is controversial as several POs could contribute: $3t_0$, 1:3 or 3:3.
9. No real PO has been found that could explain the low ϵ P3 region at $\theta = 38°$.

As noted in Boebinger *et al.* (1997), the only way to answer these questions is via a semiclassical theory of the current. We shall derive such formulae in chapter 5 and use them in chapters 6 and 7.

Chapter 4

QM CALCULATIONS

Quantum mechanical (QM) calculations of the energy levels in the resonant tunneling diode are a natural step towards a better theoretical understanding of the system. From the Gutzwiller trace formula (GTF) perspective, the energy density of states (DoS) high above the ground state has modulations that are linked to periodic orbits (POs). Using the classical scaling property (Monteiro and Dando 1996), one can carry out scaled quantum calculations giving energy levels that correspond to the same classical regime. This yields very clean power spectra, that can give precise information about the POs contributing to the DoS, such as their scaled action.

e describe here a model for the tunneling current inspired from Fromhold *et al.* (1995b). The DoS is weighted by the Bardeen (1961) matrix element describing the transfer from the emitter state to the state in the quantum well. This can be used to identify which POs contribute to the current. Monteiro *et al.* (1997a) compared qualitatively quantum and experimental current-voltage traces. In this work, we carry out systematic calculations for different angles, and we extract quantum amplitudes and frequencies that correspond to the experimentally observed oscillations. They will be used for *quantitative* comparisons with semiclassical theories and experimental results in chapters 6 and 7.

Scarring was first mentioned in Fromhold *et al.* (1995b), and sparked some debate (Wilkinson *et al.* 1996, Monteiro *et al.* 1997b, Fromhold *et al.* 1997b). It was followed by a study (Narimanov and Stone 1998a) which pointed out the cusp bifurcation (see chapter 3) as responsible for the unusually strong scarring. Here we shall extend this study to phase space, where we shall compare Wigner distributions with surfaces of section.

This will also illustrate the presence of tori quantization around stable POs. Although not an unexpected phenomenon, its influence on the accessibility of stable POs is crucial.

For instance, it explains the period-one oscillations where the contributing PO t_0 is not accessible [see Fromhold *et al.* (1997a) and Boebinger *et al.* (1997)], as well as "jumps" observed in the experimental data. We propose here a model for the current, in the case of a large stable island, that takes into account tori quantization effects.

4.1 QM calculations: theory

4.1.1 General considerations

Consider a conservative quantum mechanical system defined by an Hamiltonian $\hat{H}$. If the system is bounded, the time-independent Schroedinger's equation

$$\hat{H}|\psi_i\rangle = E_i|\psi_i\rangle \tag{4.1}$$

has a discrete and infinite ($i = 1, 2, ...$) set of eigenvectors (the wave functions $|\psi_i\rangle$) and eigenvalues (the allowed energies E_i). One represents the distribution of all the quantized energies by the density of states

$$d(E) = \sum_{i>0} \delta(E - E_i) \quad , \tag{4.2}$$

also called *spectrum*. This is one of the most important quantities studied in the field of quantum chaos. In the integrable case, one is usually able to solve the Schroedinger's equation analytically and classify the energy levels with as many quantum numbers as there are degrees of freedom. In the non-integrable case, one needs a numerical solution through the diagonalization of matrices. One considers a finite basis ($m = 1, 2, ..M$) of orthonormal trial functions f_m. One writes a truncated expansion of each wave function: $|\psi_i\rangle \simeq \sum_{m=1}^{M} c_m^{(i)} |f_m\rangle$, as well as matrix elements of the Hamiltonian: $H_{mm'} = \langle f_m|\hat{H}|f_{m'}\rangle$. (4.1) yields the matrix eigenvalue problem

$$\langle f_m|\hat{H}|\psi_i\rangle \simeq \sum_{m'=1}^{M} H_{mm'} c_{m'}^{(i)} = E_i c_m^{(i)} \tag{4.3}$$

for the vector made of the complex expansion coefficients $\{c_m^{(i)}\}_{m=1,..M}$. Choosing carefully an adequate basis of trial functions can help considerably the task of the numerical diagonalization of $H_{mm'}$, as it can reduce the dimension M that is needed for accurate results.

4.1.2 The RTD and the trial functions basis

The resonant tunneling diode (RTD) model is described in detail in chapters 2 and 3, the latter introducing the reduction to two dimensions and the scaled dynamics. We consider[1] the two-dimensional unscaled problem (3.4)

$$\hat{H} = \frac{1}{2m}(\hat{p}_x^2 + \hat{p}_z^2) - F\hat{x} + \frac{B^2}{2m}(\hat{x}\sin\theta - \hat{z}\cos\theta)^2 \quad . \tag{4.4}$$

Assuming barriers of infinite height, the boundary conditions read

$$\psi_i(x = 0, z) = \psi_i(x = L, z) = 0 \quad . \tag{4.5}$$

It is useful to consider first the integrable case at $\theta = 0°$, which is separable into two independent one-dimensional problems. The x degree of freedom is subject to a triangular well with an infinite barrier, yielding wave functions expressed as a sum of Ai and Bi Airy functions. The z wave functions are harmonic oscillator (HO) states (Landau and Lifshitz 1977) as the magnetic field creates a quadratic potential.

The problem is not separable at non-zero tilt angle θ, but one can still expect the wave functions to be close to the $\theta = 0°$ ones, which could therefore be an adequate choice of trial functions basis. However, the Airy functions are not very convenient to work with, because of the condition of having a vanishing wave function at the barriers. It is preferable to neglect the electric field and consider sinusoidal wave functions.[2] As θ bends all dynamics around the magnetic field (in the $z = x\tan\theta$ direction), it was found advantageous to use harmonic oscillator functions that are shifted and follow the magnetic field. We used the expansion

$$\psi_i(x,z) = \sum_{n=1}^{N_{\max}} \sum_{l=0}^{L_{\max}} c_{nl}^{(i)} f_{nl}(x,z) \quad , \quad f_{nl}(x,z) = \chi_n(x)\varphi_l(z,x) \tag{4.6}$$

$$\text{with} \quad \begin{cases} \chi_n(x) = \sqrt{\frac{2}{L}}\sin\left(n\pi\frac{x}{L}\right) \\ \varphi_l(z,x) = \left(\frac{\beta}{\pi\hbar}\right)^{\frac{1}{4}} \sqrt{\frac{1}{2^l l!}} e^{-\frac{\beta}{2\hbar}(z - x\tan\theta)} \mathrm{H}_l\left[(z - x\tan\theta)\sqrt{\frac{\beta}{\hbar}}\right] \end{cases} \tag{4.7}$$

where H_l are Hermite polynomials and $\beta = B\cos\theta$ is the effective magnetic field acting on z. Note that the basis functions are not separable.

This basis gives a band structure to the matrix elements of Hamiltonian: they are significant only in a certain width around the diagonal ($n' = n \pm \delta n, l' = l \pm \delta l$). In this

[1] In the following we shall use atomic units where $e = m_e = \hbar = 1$. We shall write $\hbar$ nevertheless, to keep track of this measure of the semiclassical regime.

[2] Another possible choice of functions vanishing at the barrier is Gegenbauer polynomials (Abramowitz and Stegun 1964).

case, one can use a Lanczos algorithm for the diagonalization of band matrices, which considerably reduces the processing time.

4.1.3 Scaled Schroedinger's equation and Fourier transforms

Consider the $\theta = 0°$ case in the absence of the magnetic field ($B = 0$). We can use perturbation theory in the case of a weak electric field ($V = FL \ll E$)[3]. The unperturbed problem has the sinusoidal wave functions $\chi_{\mathcal{N}}$ (4.7) indexed by $\mathcal{N}$ and has energies given by

$$E^0(\mathcal{N}) = \frac{1}{2m}\left(\frac{\mathcal{N}\pi\hbar}{L}\right)^2 \quad . \tag{4.8}$$

The perturbed energy E is given by the average of the perturbation over the unperturbed wave function, yielding $E = E^0 - V/2$. This enables us to write an "effective quantum number" for the perturbed problem:[4]

$$\mathcal{N} = \frac{L}{\pi\hbar}\sqrt{2m(E + V/2)} = \frac{BL}{\pi\hbar}\sqrt{2mL\epsilon(R + 1/2)} \quad . \tag{4.9}$$

We extend this approach to $B, \theta \neq 0$ situations. The second relation should be used for constant scaled dynamics (fixed by $\epsilon = F/B^2$) and constant ratio $R = E/V$, establishing the link between $\mathcal{N}$ and B. The scaled energy is then $E/B^2 = RL\epsilon$ and will be constant; the quantum levels indexed by $\mathcal{N}$ will be directly related to B. We rearrange the Schroedinger's equation into a generalized eigenvalue problem:

$$(\hat{x}\sin\theta - \hat{z}\cos\theta)^2 - 2m\epsilon(\hat{x} + RL)|\psi_i\rangle = \frac{\nabla^2}{\hbar^2 B_i^2}|\psi_i\rangle \quad , \tag{4.10}$$

where the eigenvalues are the magnetic field values (or equivalently the $\mathcal{N}_i$), instead of the usual energies. Solving the corresponding diagonalization problem yields a ladder of quantum states which all correspond to the same classical dynamics (governed by ϵ and R). Going higher up on the ladder (increasing i) means increasing $\mathcal{N}$, that is, the semiclassical regime. Therefore we consider a *scaled* density of states:

$$\tilde{d}(\mathcal{N}) = \sum_i \delta(\mathcal{N} - \mathcal{N}_i) \quad . \tag{4.11}$$

$\mathcal{N}$ measures how "semiclassical" the system is. For instance, the number of nodes of a wave function is given roughly by $\mathcal{N}$, and enables us to define an "effective" $\hbar$ by $\hbar_{\text{eff}} = 1/\mathcal{N}$. This is due to the fact that most of the energy (and therefore the oscillations)

[3]Note that this condition ($R = E/V \gg 1$) is not satisfied in the experimental setup, as $R \simeq 0.15$.

[4]The same definition is derived in a classical approach in subsection 5.3.3.

lies in the x motion.[5] Besides, the coefficients $c_{nl}^{(1)}$ of the expansion of the wave function peak around $n \simeq \mathcal{N}$ and the maximum n needed for convergence is given, as a rule of thumb, by $2\mathcal{N}$.

Now we consider the power spectrum, which is a Fourier transform (FT) of the density of states made with respect to a variable conjugate to the action. Because of the underlying oscillatory structure predicted by the semiclassical theory of Gutzwiller, it should present peaks at the corresponding classical actions. A problem in a generic system is that the classical actions (hence the frequencies of the spectral oscillations) vary over the energy window used for the FT, yielding a noisy power spectrum. In the scaled model, one has a natural variable for the FT: the inverse of the effective $\hbar$, which is $2\pi\mathcal{N}$. The conjugate variable is the scaled action $\hat{S}$ defined by (3.11). This technique is called "inverse $\hbar$ spectroscopy". As this action is constant all along the $\mathcal{N}$ window (as the scaled dynamics are fixed by ϵ), the FT is much cleaner. We always consider the window $\mathcal{N} \in [12, 43]$ corresponding to the voltage range of the experiments. We used a Welch window $w(\mathcal{N})$ (Press *et al.* 1989); see (5.87) for a similar definition of Fourier transforms in the semiclassical case.

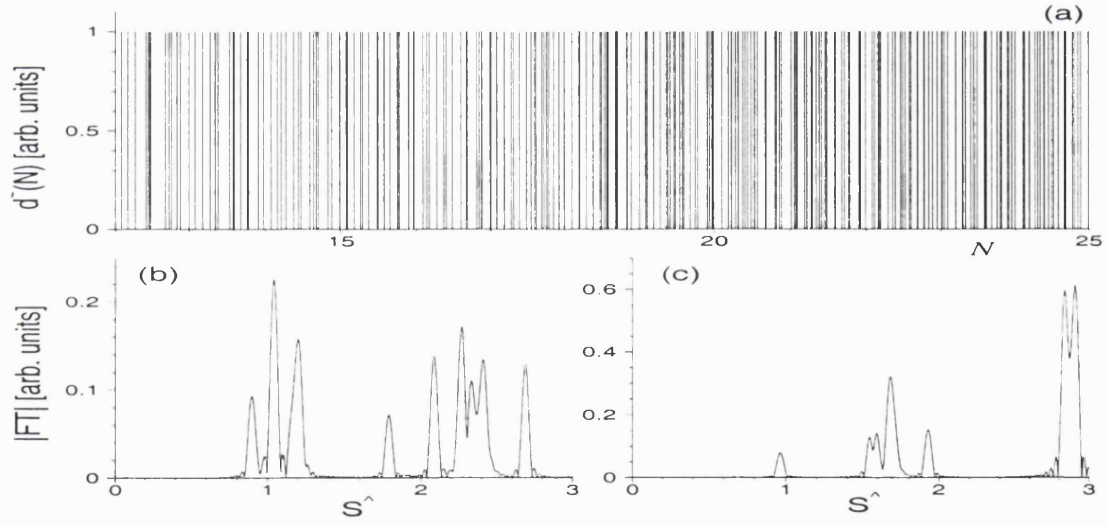

Figure 4.1: (a) QM density of states at $\theta = 11°, \epsilon = 5000$. We assigned the value $\delta(0) := 1$. (b) Power spectrum at $\epsilon = 5000$. (c) Power spectrum at $\epsilon = 10000$.

We show an example of a quantum mechanical (QM) spectrum in Fig. 4.1 (a), truncated at $\mathcal{N} = 25$ for visibility. There is apparently no structure to the large number (847) of states, which is probably linked to the non-integrability of the problem: the absence

[5] See the discussion on wave functions in the tori quantization regime in page 90.

of conserved quantities (classically) and good quantum numbers (quantum mechanically). One could say that it illustrates the underlying randomness of the classical chaos. However, the corresponding FT (the power spectrum) shown in (b) is much cleaner. According to the GTF, it is made of peaks corresponding to periodic orbits (POs): the positions of the peaks are their scaled classical actions $\hat{S}$, while the amplitudes are related to the stabilities . (c) shows another power spectrum at $\epsilon = 10000$. Their differences can be interpreted as coming from a change in the classical properties of the POs.

4.1.4 Bardeen model for the current

In order to understand the experimental results, we need an expression for the tunneling current from the emitter well to the wide quantum well through the left barrier. Assuming that the tunneling is small as a result of a high barrier, one can use the Bardeen weak tunneling matrix element (Bardeen 1961). A clear derivation of the Bardeen expression can be found in Bogomolny and Rouben (1999). It is based on the following points (see Fig. 4.2) :

- One uses a first order perturbation theory to express the global wave function and the energy. The unperturbed system is the left well without the right well.
- One uses the fact that the perturbation vanishes for $x < -d$, the corresponding fact for the right barrier, and the approximation that $E_i \simeq E$ (resonant tunneling condition).
- The volume integration for the expectation value of the perturbation is transformed in a surface integral on the left barrier, using Gauss' theorem and the fact that the wave functions vanishes for $x \gg 1$.
- The current is finally obtained by taking the imaginary part of the first order energy.

The Bardeen expression reads

$$I(E) = \sum_i \mathcal{W}_i \delta(E - E_i) \tag{4.12}$$

$$\mathcal{W}_i = \frac{\pi\hbar^3}{2m^2} \left| \int dz \left\{ \Phi^*(x=0,z)\partial_x\psi_i(0,z) - \partial_x\Phi^*(0,z)\psi_i(0,z) \right\} \right|^2 , \tag{4.13}$$

where Φ is the initial state in the emitter well (5.14).

As $\psi_i(0,z) = 0$ in the infinite barriers model, the second term in (4.13) vanishes. $\partial\psi_i/\partial x$ gives a $n\pi/L$ factor for each $c_{nl}^{(i)}$ coefficient of the sinusoidal x trial function. The

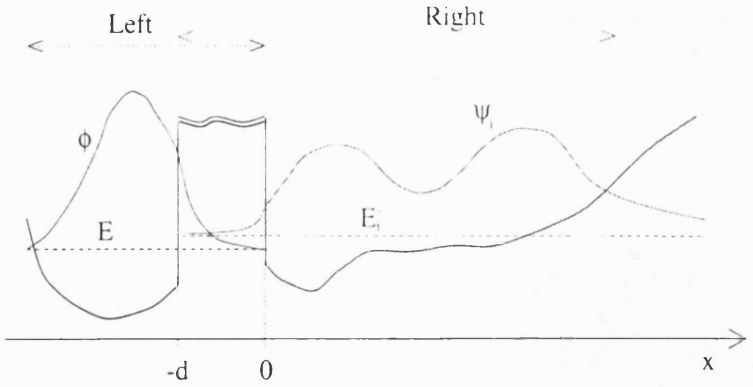

Figure 4.2: Bardeen approximation for the tunneling current through a barrier $-d < x < 0$ separating two quantum wells. We consider the left well in the absence of the second one, with the wave function Φ and the energy E, as well as the right well in the absence of the left well, with the wave function ψ_i and the energies E_i.

overall effect is to bring a quadratic dependence of the current on $\mathcal{N}$, as the coefficients of the expansion are peaked around $n \simeq \mathcal{N}$. This disappears when normalizing the current to the $\theta = 0° = 0$ amplitude.[6] Hence the normalized quantum current that we use reads

$$I_{\mathrm{QM}}(E) = \sum_i |\langle \Phi | \psi_i \rangle_{x=0}|^2 \, \delta(E - E_i) \quad . \tag{4.14}$$

Because we consider the lowest Landau state for the z dependence of the initial state Φ (5.14), the overlap in z gives a selection rule: only the $l = 0$ coefficients of the wave function contribute. At $\theta = 0°$, the wave function is made of centered HO states; the selection rule yields a current of constant amplitude. In the case of a displaced initial state, more channels contribute.

Note that the philosophy of the Bardeen treatment is to separate the tunneling in two isolated and bounded systems, and to connect them through an overlap of the corresponding wave functions. There lies the justification for considering the problem of the wide quantum well with high barriers as a closed system —and for studying the corresponding bounded classical problem. As the overlap is made on the emitter barrier, only quantum states of the well that reach the left wall can contribute to the current, which is fairly intuitive.

The question of using infinite or finite barriers has been addressed in Monteiro *et al.* (1997a), where it was shown that the only difference between the two models is a smooth envelope that disappears when normalizing to $\theta = 0°$.

[6] We normalize all amplitudes (experimental, quantum and semiclassical) to the $\theta = 0°$ amplitudes.

Finally, it is worth noting that the model presented here completely neglects effects arising from the tunneling through the right barrier at the collector. This is justified as the energy of the outgoing electrons is much higher than the Fermi level of the collector (as a result of the voltage drop). Therefore, there is no selection rule imposed on them: they can tunnel out into any of the collector states, which are all available at that energy. We also consider perfect reflections at the barriers. Reflection coefficients have been considered in the semiclassical theory presented by Bogomolny and Rouben (1999).

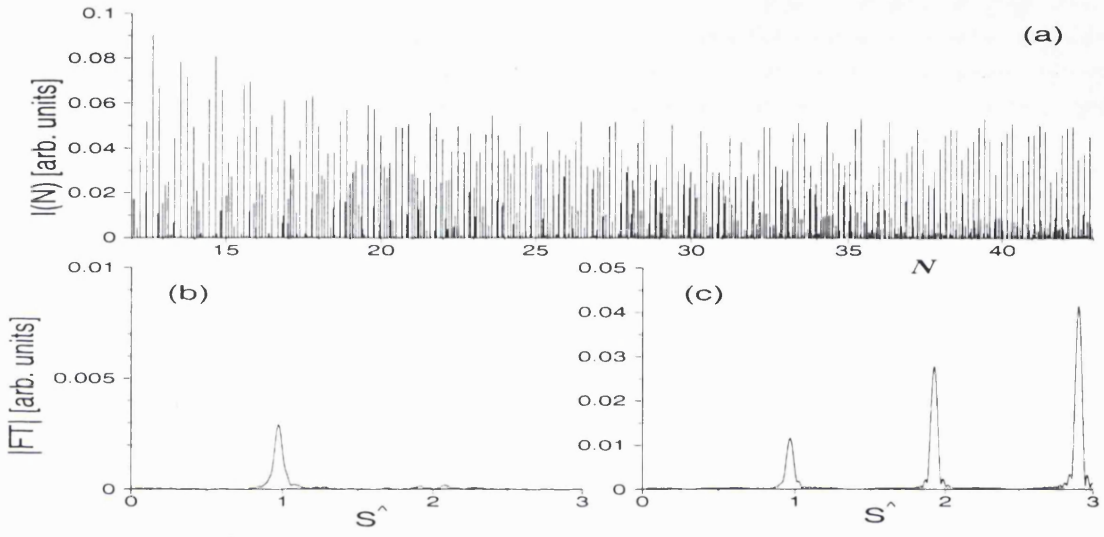

Figure 4.3: (a) QM current spectrum at $\theta = 11°, \epsilon = 5000$. Fourier transform of the current at (b) $\epsilon = 5000$ and (c) $\epsilon = 10000$.

We show in Fig. 4.3 a quantum current spectrum and two Fourier transforms for the same parameters as in Fig. 4.1. First we can see that the current spectrum (a) has fewer significant peaks than the density of states. This is due to the fact that most of the eigenstates do not contribute to the current, either because they do not reach the left wall, because they are not accessible to the initial state, or because they are too "ergodic". We can discern a slight period-one modulation in the spectrum. Its Fourier transform (b) indeed has a weak peak at a scaled action close to one, corresponding to period-one oscillations (see Table 3.2.2). It has less structure than the power spectrum of the DoS. At $\epsilon = 10000$ the current oscillations are stronger, and one sees peaks at higher actions, corresponding to period-two and three oscillations.

4.1.5 Damping time and energy broadening

Inelastic processes (such as phonon emission) change suddenly the phase of the electrons and effectively destroy their coherence. One can define a coherence length l_ϕ or time τ after which the electrons, on average, loose their coherence. In the time domain, we can model this decoherence by adding an exponential damping $\exp[-T/\tau]$ to the current, where T is a measure of the time that the electrons spend in the well. In the energy domain, one considers the Fourier transform of the damping function:

$$\int dt e^{\frac{i}{\hbar}Et} e^{-\frac{t}{\tau}} = \frac{\hbar}{\pi} \frac{\Delta E}{\Delta E^2 + E^2} = \mathcal{L}(E; \Delta E) \quad , \quad \Delta E = \frac{\hbar}{\tau} \quad , \tag{4.15}$$

which is a Lorentzian with a width ΔE given by an energy-time "uncertainty relation". A damping in time introduces a broadening of the current spectrum, which can be written as a convolution of the spectrum with the Lorentzian:

$$I_{\Delta E}(E) = \sum_i \mathcal{W}_i \mathcal{L}(E - E_i; \Delta E) \quad . \tag{4.16}$$

It is a smooth function of the energy in contrast to the "stick spectrum" (4.12). Note that ΔE governs the resolution of the spectrum; as it increases, the periodicity of higher orders will overlap and be damped. Our estimated value of $\tau \simeq 0.115\,\mathrm{ps}$ (see section 2.3.4) yields a broadening of $\Delta E \simeq 0.006$ eV.

This limitation of the resolution is seen in the experiments, where only P1, P2 and P3 oscillations are visible. This can be translated into the scaled action: only scaled actions smaller than 4 are relevant to the experiment. This is the reason why we limit ourselves to Fourier transforms and classical POs up to actions three or four.

4.1.6 Wigner distributions

Because of Heisenberg's uncertainty principle, quantum mechanics do not allow the classical concept of a trajectory —that is, the pair of well-defined position and momentum at each time—, nor a proper probability distribution in phase space. One can however define *quasi-probability* distributions which can give some phase space information. The Wigner distribution of a wave function $|\psi\rangle$ is defined by a Fourier transform of correlations of the wave function (Hillery *et al.* 1984, Brack and Bhaduri 1997):

$$W_i(\boldsymbol{q}, \boldsymbol{p}) := \frac{1}{2\pi\hbar} \int d\Delta\boldsymbol{q} e^{i\boldsymbol{p}\Delta\boldsymbol{q}/\hbar} \psi_i(\boldsymbol{q} - \frac{1}{2}\Delta\boldsymbol{q}) \psi_i^*(\boldsymbol{q} + \frac{1}{2}\Delta\boldsymbol{q}) \tag{4.17}$$

$$= \sum_{n,l} \sum_{n',l'} c_{nl}^{(i)} c_{n'l'}^{(i)*} W_{n,n'}^x(x; p_x + p_z \tan\theta) W_{l,l'}^z(z - x\tan\theta; p_z) \quad , \tag{4.18}$$

where $c_{nl}^{(i)}$ are the coefficients of the expansion (4.6) of the wave function on the shifted HO and sine basis. As we shall always consider distributions very close to the barriers, we can approximate the Wigner transform of the sine function by

$$W_{n,n'}^{x}(x;p_x) \overset{x\ll 1}{\simeq} \frac{8\pi^2}{3\hbar} nn' \left(\frac{x}{L}\right)^3 \quad . \tag{4.19}$$

The Wigner function for the HO states is given by (Bartlett and Moyal 1948)

$$W_{l,l'}^{z}(z;p_z) = \frac{(-1)^{l'} i}{4\pi} \sqrt{\frac{l'!}{l!}} e^{-i(l-l')\vartheta} \zeta^{\frac{l-l'}{2}} e^{-\zeta/2} \mathrm{L}_{l'}^{l-l'}(\zeta) \quad , \tag{4.20}$$

with $\zeta = \frac{4m}{\beta\hbar}\left(p_z^2/2m + \beta^2 z^2/2m\right)$ and $\tan\vartheta = p_z/z\beta$; $\mathrm{L}_{l'}^{l}$ is a generalized Laguerre polynomial (Abramowitz and Stegun 1964). The Wigner distribution $|W_{l,l'=l}^{z}|^2$ of a l-excited HO state is therefore localized on concentric rings with radii related to ζ. A drawback of the Wigner function is that it can take negative values, making its interpretation as a probability distribution difficult. A way around that problem is to convolve the Wigner distribution with a smoothing function. In the case of a Gaussian, one obtains the Husimi distribution (Leboeuf and Saraceno 1990) which is always positive and can be written as

$$\mathcal{H}_i(\boldsymbol{q},\boldsymbol{p}) := |\langle(\boldsymbol{q},\boldsymbol{p})_{\beta_{\mathrm{cs}}}|\psi_i\rangle|^2 \quad , \tag{4.21}$$

where $|(\boldsymbol{q},\boldsymbol{p})_{\beta_{\mathrm{cs}}}\rangle$ is a coherent state (Cohen-Tannoudji *et al.* 1973), that is, a ground state harmonic oscillator centered on the phase space point $(\boldsymbol{q},\boldsymbol{p})$. The strength β_{cs} of the HO determines the balance between the resolution in $\boldsymbol{q}$ and $\boldsymbol{p}$. We used an unshifted basis for the computation of Husimi distributions.

We have computed Wigner and Husimi distributions for 2-D cuts in phase space, similarly to the classical Poincaré surfaces of section. We have usually considered the left wall ($x = 0$), as states contributing to the current must reach the emitter.

* * *

We shall use scaled quantum calculations to obtain a density of states and a current spectrum at fixed classical dynamics, the current weighting being constructed from an overlap between the numerical wave function and the initial state. We get the power spectrum by performing a Fourier transform, always over the same $\mathcal{N}$ range. For the current, the positions of the peaks are clearly related to the three periods of the experimental oscillations; their amplitudes are the main quantum quantity we shall consider. In chapters 6 and 7, we shall compare them with semiclassical amplitudes (and experimental ones where

available) over a large range of different scaled dynamics ϵ and for a few tilt angles θ. In this work, we shall not present (*i*) studies of the density of states, as we are primarily interested in the current, (*ii*) Husimi distributions, as they did not give more information than the Wigner functions, and (*iii*) current-voltage traces, which can be found in Saraga and Monteiro (1998b).

4.2 Semiclassical tori quantization model

4.2.1 Tori quantization of the density of states

It is well known (Miller 1975) that the semiclassical contribution of the repetitions of a stable periodic orbits to the Gutzwiller trace formula can be rewritten as

$$d(E) = \frac{T}{\hbar} \sum_{N,k} \delta[S(E) - S_{N,k}] \quad , \quad S_{N,k} = 2\pi\hbar[N + \gamma(k + 1/2)/2\pi + \mu/4] \quad , \tag{4.22}$$

where S, T, γ and μ are respectively the action, period, winding angle and Maslov index of the PO. Note that they all depend on the energy E. This scheme is called tori quantization.[7] Using $\partial S(E)/\partial E = T$, we can "reverse" a Taylor expansion into

$$d(E) = \frac{1}{\hbar} \sum_{N,k} \delta(E - E_{N,k}) \quad , \quad S\left(E_{N,k} - E_k^{\perp}\right) = 2\pi\hbar(N + \mu/4) \quad . \tag{4.23}$$

There the energy $E_{N,k}$ is implicitly defined by the second relation. This situation corresponds to a particle having an integrable motion separable in two directions: one is along the stable PO, where its action is quantized via WKB (Landau and Lifshitz 1977) by a principal quantum number N and its energy is $E_{N,k} - E_k^{\perp}$; the other is a harmonic oscillator in the plane perpendicular to the trajectory, with an energy $E_k^{\perp} = \hbar\Omega(k + 1/2)$ quantized by the quantum number k.

In some sense this relation states that the dynamics in the vicinity of a stable periodic can be approximated by a quadratic potential. In the case of a time-symmetric normal PO (see subsection 3.1.7), the effective quadratic Hamiltonian in the perpendicular plane $(q_\perp, p_\perp)$ takes the form (Bogomolny and Rouben 1999)

$$H_\perp(p_\perp, q_\perp) = \frac{1}{2}\Omega\hbar\left(\frac{1}{\alpha\hbar^2}p_\perp^2 + \alpha q_\perp^2\right) \quad , \quad \alpha = \frac{\sin\gamma}{m_{12}\hbar} \quad , \quad \Omega = \frac{\gamma}{T} \tag{4.24}$$

[7] The denomination comes from the similarity with the EBK quantization of the energy via action-angle torus structures in integrable systems. Also, excited quantum HO states have a Wigner distribution localized on tori; we refer to these states as *quantized tori* states.

where m_{12} is an element of the monodromy matrix. Ω is the frequency of the harmonic motion. Note that the HO has an effective mass depending only on the dynamical properties of the PO.

Hence, one can write a separable form for an approximation of the RTD wave function when tori quantization is relevant:

$$\psi_i^{\mathrm{TQ}}(x,z) = \psi_N^{\parallel}(x)\,\psi_k^{\perp}(z - z_{\mathrm{PO}}(x)) \tag{4.25}$$

$$\psi_k^{\perp}(z) = \left(\frac{\alpha}{\pi\hbar}\right)^{1/4} \sqrt{\frac{1}{2^k k!}}\, e^{-\alpha z^2/2\hbar}\, H_k(z\sqrt{\alpha/\hbar}) \quad , \tag{4.26}$$

where $(x, z_{\mathrm{PO}}(x))$ are the coordinates of the PO and $\psi_k^{\perp}$ is the k^{th} excited harmonic oscillator eigenfunction. The longitudinal wave function $\psi_N^{\parallel}$ should take the WKB form (1.1).

4.2.2 Current

With the hypothesis (4.25) and neglecting the shift of the initial state z_S (see subsection 5.1.2), the current for the semiclassical tori quantization model, normalized to $\theta = 0°$, reads

$$I_{\mathrm{TQ}}(E) = \sum_i \left|\langle\Phi|\psi_i^{\mathrm{TQ}}\rangle_{x=0}\right|^2 \delta(E - E_i) = \sum_{N,k} \mathcal{W}_k \delta(E - E_{N,k}) \quad . \tag{4.27}$$

The overlap is given by (Gradshteyn and Ryzhnik 1994)

$$\mathcal{W}_k = \left|\int dz \phi(z) \psi_k^{\perp}(z - z_0)\right|^2 = \frac{1}{2^{k-1}k!} \frac{\sqrt{\alpha\beta}}{\alpha+\beta} \left(\frac{\beta-\alpha}{\beta+\alpha}\right)^k e^{-\frac{\alpha\beta}{\alpha+\beta} z_0^2/\hbar} H_k^2\left(-\beta z_0 \sqrt{\frac{\alpha}{|\beta^2 - \alpha^2|\hbar}}\right), \tag{4.28}$$

where z_0 is the starting position of the PO on the left wall and ϕ is the ground state HO of the initial state (5.14). In our scaled model, we consider the current as a function of $\mathcal{N}$:

$$I(\mathcal{N}) = \frac{\hat{S}_0}{\hat{S}} \sum_{N,k} \mathcal{W}_k \delta(\mathcal{N} - \mathcal{N}_{N,k}), \quad , \quad \mathcal{N}_{N,k} = [N + \gamma(k + 1/2)/2\pi + \mu/4]/\hat{S} \quad , \tag{4.29}$$

where $\hat{S}_0$ is the scaled action of the PO t_0 at $\theta = 0°$. The weighting (4.28) "scales" as well with B as $\beta = B\cos\theta$ and $\alpha = B\sin\gamma/\tilde{m}_{12}$. Note that $\mathcal{W}_k$ also depends (indirectly) on N, as it depends on B which is related to $\mathcal{N}_{N,k}$.

4.2.3 Comments

The number of HO states (the maximum k in the sum) should be finite and can be estimated by the number of allowed states in the area $\mathcal{A}$ of the stability island: $k_{\max} \sim \mathcal{A}/(2\pi\hbar)$. As the area of the stability island scales with B (because of the scaled momentum), the

number of allowed tori is proportional to B. Alternatively, we see from (4.26) that the spatial spacing between the quantized tori (given by $\sqrt{\hbar/\alpha}$) decreases with B meaning that more tori are allowed in a stability island. However, we noticed that usually that number is exceeded by the number of quantized tori seen in the numerical quantum eigenfunction or by the number of tori needed in the tori model to reproduce the QM current.

For each k, the tori series in N represents effectively a period-one series with a separation in $\mathcal{N}$ given by $1/\hat{S}$. The following $k+1$ series in N is dephased from the k series by $\gamma/(2\pi\hat{S})$. At a period-doubling bifurcation, the winding angle γ becomes equal to π; this yields a strong P2 signal as the k and $k+1$ P1-series become exactly π out-of-phase and present a P2 periodicity.

In the integrable limit ($\epsilon \to \infty$ or $\theta \to 0$), we have $\alpha \to \beta$ as the motion becomes separable. In that case, the weighting becomes

$$\mathcal{W}_k^\beta = \frac{1}{k!}\left(\frac{\beta z_0^2}{2\hbar}\right)^k e^{-\beta z_0^2/2\hbar} \quad . \tag{4.30}$$

Finally, we considered in practice only the stable PO t_0 contribution to the quantized tori model as it has the largest and most persistent island of stability.

4.2.4 Current spectra

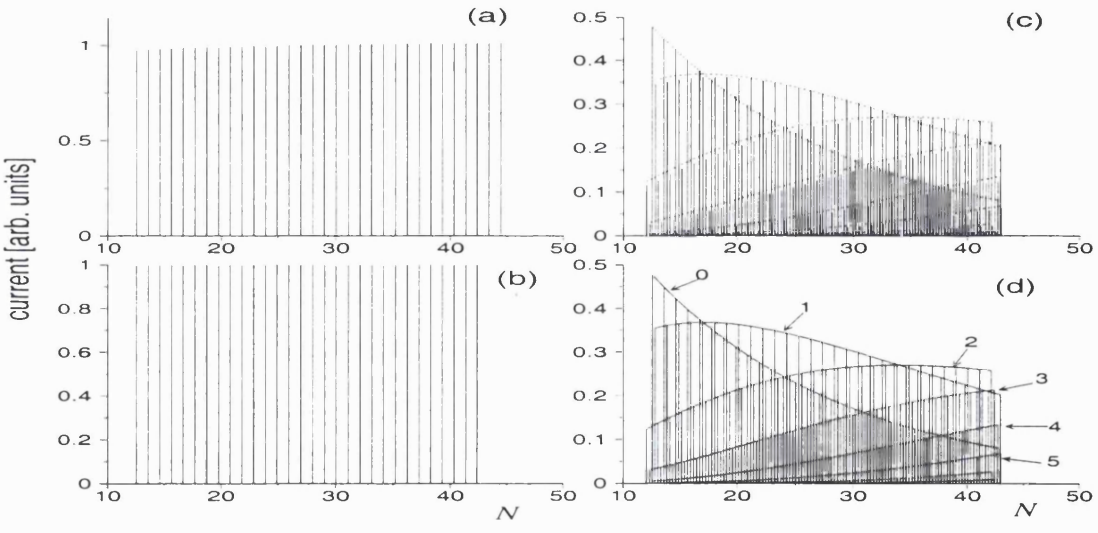

Figure 4.4: Tori quantization model (4.29) for the current spectrum. (a) QM current spectrum and (b) tori model at $\theta = 0°, \epsilon = 20000$. (c) QM and (d) tori model at $\theta = 27°, \epsilon = 40000$. The numbers denote the k quantum number of the excited HO states in the tori model. The tori model is built with t_0 only. The dotted lines in (c) are the envelopes of the tori model in (d). The horizontal axis is $\mathcal{N}$.

We show in Fig. 4.4 a comparison between the tori quantization model for the current spectrum (4.29) and the results of QM calculations. At $\theta = 0°$ only the $k = 0$ tori series contributes to the current, because of a selection rule imposed by the initial state: in that case $z_0 = 0, \alpha = \beta \Rightarrow \mathcal{W}_{k>0} = 0$. The separation between each quantized $\mathcal{N}$ is given by $1/\hat{S}$, and yields a Fourier transform peaked at $\hat{S}$, i.e., a strong period-one signal. The amplitude of the current is constant. The tori model is far more efficient than the "hard limit" formulae (see section 6.1).

The tori model is also very good at $\theta = 27°$ in the regular regime (high ϵ), where the stable island of t_0 occupies a good third of the surface of section. The QM spectrum shows regular spacings which are typical of tori quantization (see Table 4.1 in the next section). They are very precisely described by our tori model [the dotted lines in (c)], and can be understood the following way. t_0 is fairly off-center ($z_0 \sim 500$ a.u.) and inaccessible; hence the usual "Gutzwiller" contribution of the PO (the $k = 0$ tori series) decreases with increasing magnetic field (or $\mathcal{N}$). As B increases, the initial state focuses more on $z = 0$ and the contribution of the k series also decreases exponentially.[8] The initial state selects sequentially outer tori (i.e., higher k) that have a substantial probability in the $z = 0$ region. At the same time, the torus rings move in z towards z_0. These are the reason for the succession of envelopes seen in Fig. 4.4 (d).

The changeover between two successive tori series happens when they are equally favored by the initial state. Assuming $\alpha = \beta$, this occurs at

$$B_{k \to k+1} = 2(k+1)\hbar/(z_0^2 \cos\theta) \quad . \tag{4.31}$$

As $z_0 \simeq 500$ a.u. for any ϵ at $\theta = 27°$, the $k = 0/1$ and $k = 1/2$ changeover always occur at $B \simeq 2$ T and $B \simeq 4$ T respectively. These values correspond to the "jumps" seen in the experiments, read for $V = 0.5$ V (where the experimental resolution is the best, see Fig. 2.7). At $\theta = 11°$, t_0 is more central and only the first changeover is in the experimental range. This fact is however less obvious to see experimentally, as it occurs in a period-doubling region where the tori series are exactly out-of-phase.

The extent of the success of the tori model at $\theta = 27°$ is somewhat surprising. *All* the quantum states contributing to the current can be described by that scheme. This means that, apart from the t_0 stable island, no classical structure (e.g., unstable trajectories in the $z = 0$ region) contribute to the current in the regular regime (low B).

[8] This is seen in the scaled model where $\alpha = B\tilde{\alpha}$ and the argument of the exponential factor in $\mathcal{W}_k$ reads $-Bz_0^2\tilde{\alpha}/(\tilde{\alpha} + \cos\theta)$, z_0 being constant. The maxima arise from the Hermite polynomials.

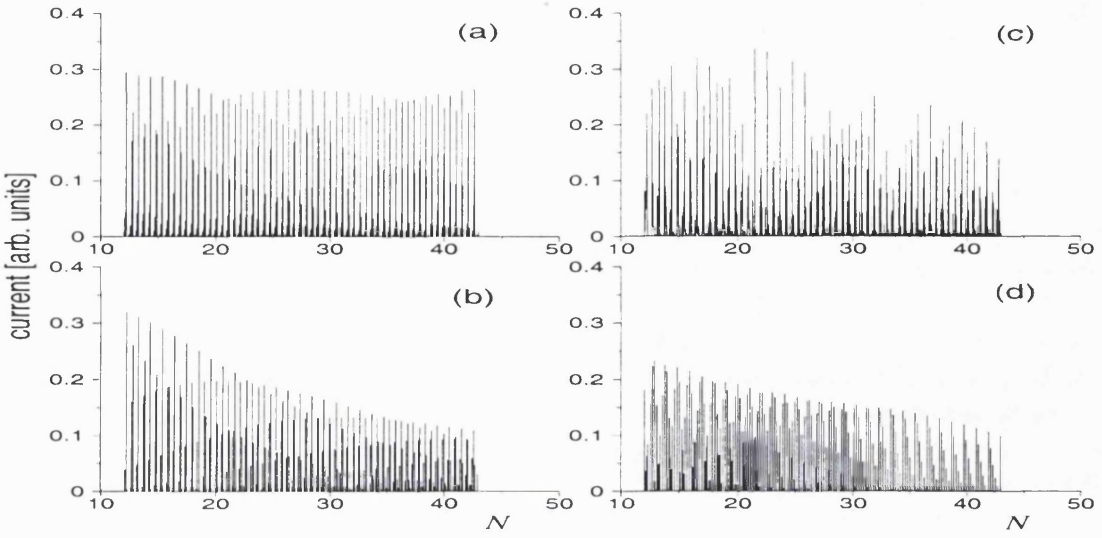

Figure 4.5: Tori quantization model for the current spectrum at $\theta = 27°$. (a) QM current spectrum and (b) tori model at $\epsilon = 16000$. (c) QM and (d) tori model at $\epsilon = 10000$.

We show the situation at $\theta = 27°$ for lower ϵ in Fig. 4.5. At $\epsilon = 16000$ we approach the period-doubling bifurcation of t_0; $\gamma = 0.88\pi$ and we have a strong P2 signal. The k and $k+2$ series almost overlap, with the $k+1$ series in between. The tori model is still efficient, but we see that the QM spectrum is slightly irregular, where the envelopes have "hiccups". This probably comes from the PO s', which has a very important contribution to the P2 current at this ϵ.

At $\epsilon = 10000$ t_0 is about to disappear in a tangent bifurcation and has a very small island of stability. There the tori model is not justified and cannot reproduce the disordered QM spectrum.

4.2.5 Amplitudes

We performed Fourier transforms of the tori model current to get P1 and P2 amplitudes, that we compare with QM results in Fig. 4.6. The agreement is rather good. Surprisingly, the approximation $\alpha \equiv \beta$ (4.30) works better than the use of the proper harmonic constant α, as the latter diverges at period-doubling bifurcations having $m_{12} \to 0$.

The tori model describes accurately the P1 quantum oscillations for $\epsilon > 7000$. Despite the low accessibility of t_0 at $\theta = 27°$, we see that this PO nevertheless contributes to the current (c), via its outer tori. This fact is significant with respect to the issue of accessibility. In Fromhold *et al.* (1997a) it was argued that off-center POs could not contribute because of the initial state; in the reply (Boebinger *et al.* 1997), the possibility of

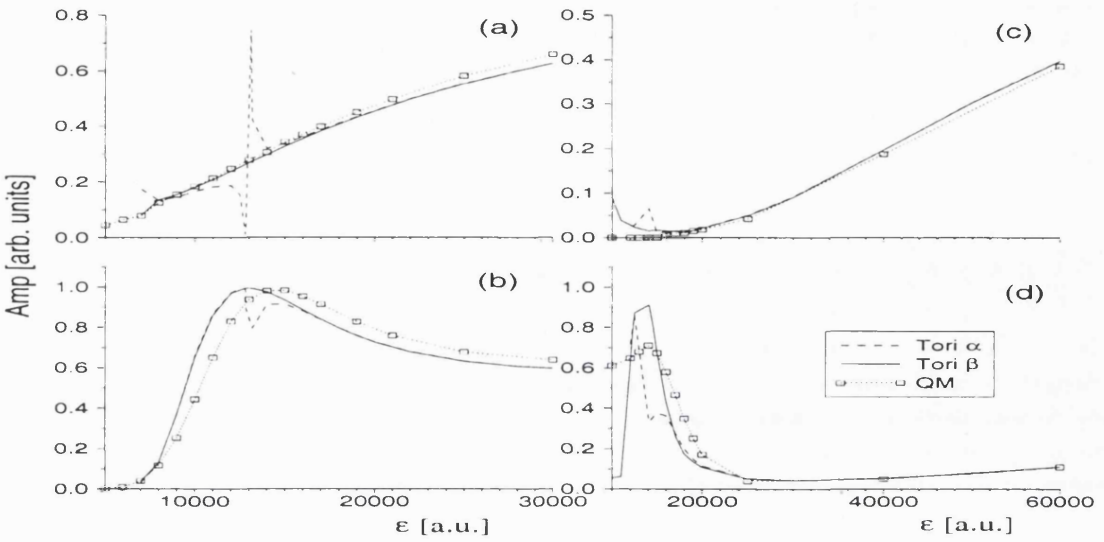

Figure 4.6: Amplitudes of the tori quantization model compared with QM results. We also consider the tori model with the approximation $\alpha \equiv \beta$ (4.30), indicated by "Tori β". (a) P1 and (b) P2 at $\theta = 11°$. (c) P1 and (d) P2 at $\theta = 27°$.

higher excited Landau levels in the initial state was raised to explain period-one oscillations at high θ. Here we show that tori quantization enables an off-center PO to contribute with an initial state containing the lowest Landau level only.

The P2 region at $\theta = 11°$ (b) is due to tori dephasing (as $\gamma = \pi$ at the period-doubling bifurcation). This is a confirmation of the interpretation made by the Bell Labs group (Muller *et al.* 1995), that the main P2 region at $\theta = 11°$ is a manifestation of a bifurcation of t_0. Tori dephasing is also responsible for the maximum of the P2 amplitude at $\theta = 27°$ (d). In the latter case, the agreement with QM results is not as good, as a result of the competing contribution of s' (see subsection 6.2.2).

The first semiclassical formulae that we considered were the "hard limit" formulae (5.64) and (5.49). They failed to describe tori quantization, and consequently gave a far too small contribution to off-center POs (see section 6.1). After we mentioned the success of our tori model, Bogomolny and Rouben (1998) developed their more elaborate NO formula (5.47); they showed that the latter was *analytically equivalent* to our model in the case of a time-symmetric trajectory such as t_0. Narimanov and Stone (1998b) also showed that their PO formula was analytically equivalent to an overlap of HO states in phase space. Interestingly, they derived a similar relation for *unstable* POs, where they found that the instability created an intrinsic level broadening, and that each PO described a contribution to a cluster of levels.

The accuracy of the amplitudes of the tori model is especially surprising for low ϵ at $\theta = 11°$, where the stable island around t_0 has a small area, and where we used more tori than the maximum number given by the area. This can be explained by the fact that the tori model is formally equivalent to the PO/NO formula for time-symmetric stable POs, which should work whatever the size of the stable island, and even for unstable orbits.

4.3 Quantum states

In this section, we present a few quantum states illustrating typical situations in the RTD.

Ergodic states

When the dynamics are predominantly unstable, both the density of states and the current are irregular (see Fig. 4.1 and 4.3). We can expect quantum wave functions to show an irregular behavior and to be spread apparently randomly across all configuration space. The notion of ergodicity is defined in classical dynamics to describe the property of a chaotic trajectory that fills all the energy surface in phase space. Although our Wigner distributions are only a part of the whole phase space picture (as they are 2-D cuts similar to Poincaré sections), they can help us to assess whether a quantum state is "ergodic" or not. In practice, we shall call a quantum state ergodic if its configuration or phase space distribution has a random character, and shows no link to any single identifiable classical structure.

At $\theta = 27°, \epsilon = 9000$ the classical dynamics are fairly chaotic and a surface of section looks like a sea of unstable trajectories with no visible stable islands (see Fig. 3.5 for a surface of section at $\epsilon = 10000$, bearing in mind the disappearance of t_0 in a tangent bifurcation at $\epsilon = 9970$). The current spectrum is irregular (see Fig. 4.5 at $\epsilon = 10000$).

We show in Fig. 4.7 typical examples of ergodic states in the RTD, calculated in this situation. Here we have taken two successive eigenstates appearing in the density of states, that give actually no contribution to the current. They clearly show irregular behavior and do not seem to be linked to any classical structure. Note that the range $z \in [-2000, 2000]$ a.u. is smaller than the allowed range at the right wall ($x = L$), on the top of the graph.

The Wigner distributions on the collector barrier also show ergodic behavior. They oscillate wildly and have significant values across the whole surface of section.

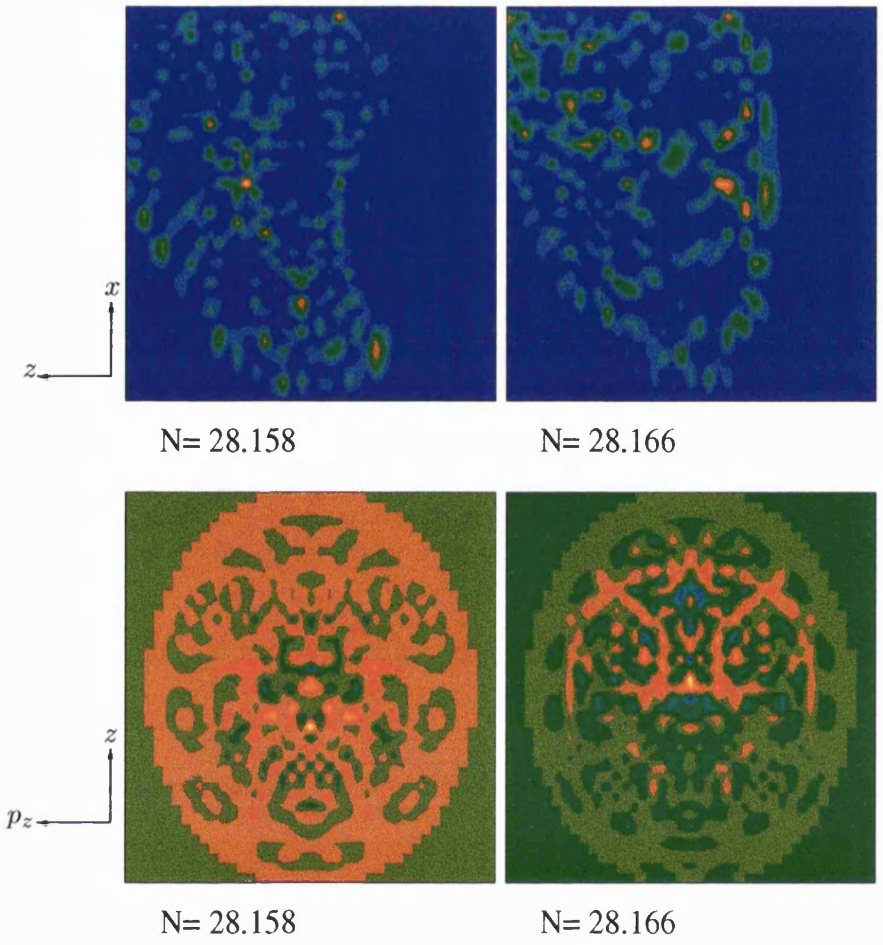

Figure 4.7: Ergodic wave functions (top) and Wigner distributions (bottom) at $\theta = 27°, \epsilon = 9000$, labelled by their eigenvalue $\mathcal{N}_i$. For the wave functions, the vertical axis is $x \in [0, L = 2267]$ a.u., the horizontal axis is $-z \in [-2000, 2000]$a.u.. Blue is zero probability, red is high. For the Wigner distributions, the vertical axis is z, the horizontal axis is $-p_z$; the range is always adapted to the size of the (classically allowed) surface of section. Here, the Wigner distributions have been calculated on the right (collector) barrier. The scale goes from blue (negative) to yellow (positive) through zero (dark green). Note that the scales vary slightly for different plots.

Tori quantization

We present in Fig. 4.8 a few Wigner and wave functions for $\theta = 11°, \epsilon = 15000$, where the large island of stability around t_0 is a dominating feature of the classical dynamics (see Fig. 3.3). Here we only considered eigenstates with a significant contribution to the current. The distributions are not ergodic; on the contrary they are clearly localized.

The wave functions are a good illustration of the approximate separability described in section 4.2. They are clearly localized on the classical periodic orbit t_0 (shown for

$\mathcal{N} = 20.894$). Along the trajectory they have a simple oscillatory structure with N maxima; the separation between the maxima decreases with x because of the electric field. Perpendicularly to the PO, each wave function has $k+1$ maxima, like a harmonic oscillator state of the k^{th} level.

The Wigner functions have been calculated on the emitter barrier; they clearly show localization on ring structures, as would be expected from HO-like states. The $k = 0$ state has a single peak centered on the PO position in the surface of section. The $k = 1$ Wigner distribution has negative value on the PO, and is localized on a ring around it. The $k = 2$ state has a positive outer ring, a negative intermediate ring and a positive peak in the center. They are slightly asymmetric as they have higher values towards the center of the surface of section.

We arranged in Table 4.1 the eigenstates according to the separable approximation of the tori quantization scheme (4.25). We can classify the eigenvalues $\mathcal{N}_i$ according to the two "pseudo quantum numbers" which give the number of oscillations parallel (N) and perpendicular (k) to the periodic orbit. Note that because k is small the number of oscillations of the wave function is roughly given by $\mathcal{N}$, which is therefore a good measure of the effective $\hbar$.

			$\to 20.365_{3,18}$	$\dot{\to}$
			1.030	
	$\dot{\to} 20.352_{1,19}$	$\overset{.511}{\to} 20.863_{2,19}$	$\overset{.532}{\to} 21.395_{3,19}$	$\overset{.549}{\to} 21.944_{4,19}$
	1.032	1.031	1.030	
$20.894_{0,20}$	$\overset{.490}{\to} 21.384_{1,20}$	$\overset{.510}{\to} 21.894_{2,20}$	$\overset{.531}{\to} 22.425_{3,20}$	$\dot{\to}$
1.033	1.032	1.032		
$21.927_{0,21}$	$\overset{.489}{\to} 22.416_{1,21}$	$\overset{.510}{\to} 22.926_{2,21}$	$\dot{\to}$	

Table 4.1: Arrangement of the quantized numbers (eigenvalues) $\mathcal{N}_i = \mathcal{N}_{k,N}$ of the eigenstates of Fig. 4.8, according to the torus number k and the longitudinal number N. The numbers above the arrows indicate the $k \to k+1$ transition differences in $\mathcal{N}$, the numbers between the lines indicate the $N \to N+1$ transitions.

According the tori quantization scheme, the separation in $\mathcal{N}$ between two consecutive N should be $1/\hat{S} = 1.033$ as the scaled action of t_0 is $\hat{S} = 0.967$. The separation between

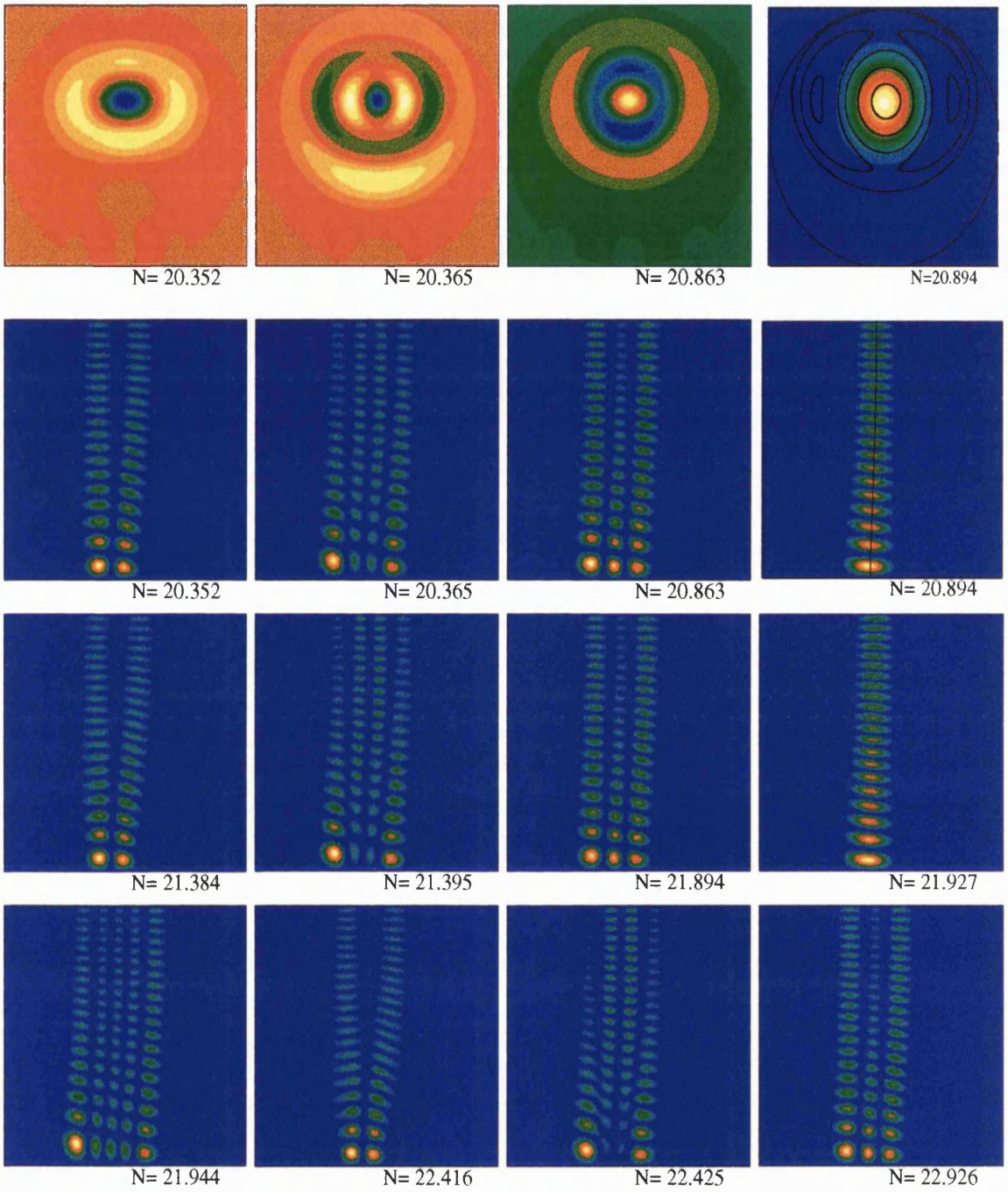

Figure 4.8: Wigner distributions on the emitter barrier (top row) and wave functions (bottom rows) in the tori quantization regime at $\theta = 11°, \epsilon = 15000$; they are labelled by their eigenvalue $\mathcal{N}_i$ and their orientation is the same as in Fig. 4.7. The four Wigner distributions correspond to the first four wave functions. For $\mathcal{N}_i = 20.894$ we also show in solid lines the classical structures: t_0 for the wave function and the main features of the Poincaré surface of section [see also Fig. 3.3 (b)] for the Wigner distribution. In the first two rows, the torus numbers are (left to right): $k = 1, 3, 2$ and 0.

two consecutive tori should be $\gamma/(2\pi\hat{S}) = 0.477$ as the winding angle is $\gamma = 0.925\pi$. We have computed the differences of the quantum results and show them in the table. The differences with N are in agreement, while there is a small discrepancy between QM and tori quantization for the k differences, which in the QM case show a dependence on N.

Distorted tori

More semiclassical states (i.e., at higher $\mathcal{N}$) can show more structure than straightforward tori quantization, as illustrated in Fig. 4.9. Both Wigner distributions at $\mathcal{N}_i = 35.305$ and $\mathcal{N}_i = 35.316$ have the *same* pseudo quantum number $k = 2$, although they are consecutive states in the current ladder. The tori are somewhat distorted in different ways. It seems that the outer torus of $\mathcal{N}_i = 35.305$ is "pushed" towards higher p_z to be localized on t_v, while being pushed inwards in z to "avoid" t_u; the situation is the opposite for $\mathcal{N}_i = 35.316$ which localizes on t_u. Their wave functions show the breakdown of separability, and do not allow for the attribution of the pseudo quantum number N by counting the longitudinal oscillations. The $\mathcal{N}_i = 36.880$ state is a $k = 1$ torus, distorted from a circular ring into a more angular shape, which seems to localize on t_u.

Scarring

A highly excited quantum state is said to be "scarred" (Heller 1984) when it is localized on an unstable classical periodic orbit. Scarring is a fairly surprising phenomenon, as one would expect the instability of the trajectory to "spread out" (in a time-dependent picture) a quantum wave packet. It turns out that actually quantum states can have a large concentration of probability around a PO that is not too unstable.

The RTD proved to be a very interesting experimental device with respect to scarring. In particular, it was found that unstable POs such as s' were scarring quantum states over a large range of experimental parameters. As the scarred states also give a strong contribution to the current, this was referred to as "strong scarring". As explained in Narimanov and Stone (1998a), the strong scarring of s' is related to the fact that it has metastability (i.e., the PO is not very unstable) over a large ϵ range. This in turn comes from peculiar properties of the classical dynamics, namely the cusp bifurcation (see subsection 3.2.4).

We show in Fig. 4.10 typical scarring from s'-type classical POs. At $\epsilon = 12750$ the scarring comes clearly from s'_-, which here is very unstable ($\mathrm{Tr}M = -16$, compared to

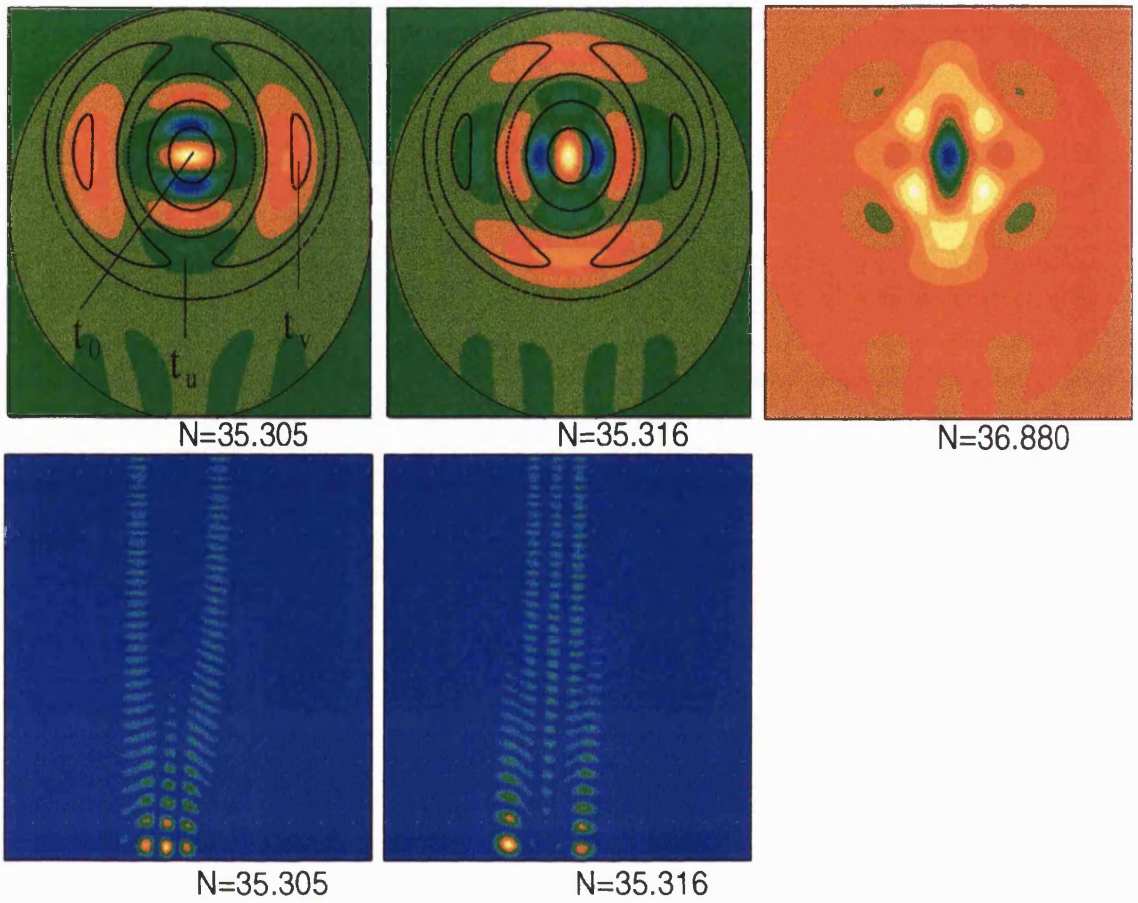

Figure 4.9: Wigner distributions on the emitter barrier (top row) and wave functions (bottom row) at $\theta = 11°, \epsilon = 15000$ for $\mathcal{N} \simeq 35$. We also show the main features of the classical surface of section in solid lines, as well as the location of some POs (t_0, t_u and t_v).

$\mathrm{Tr}M = 2.2$ for s'). The situation is less clear at $\epsilon = 9000$, as both POs s'_- and s' are very close (they bifurcate at $\epsilon = 7700$).

Fig. 4.11 shows an interesting example, where the quantum state is scarred by a *ghost* PO, instead of another real PO nearby. We also show the corresponding complex saddle orbit (defined in subsection 5.2.1), which is close to the scarring trajectory.

Non-isolated POs

In Fig. 4.12 (left) we present a Wigner function of a state giving a large contribution to the period-two quantum current at $\theta = 27°$. It has the familiar ring structure of a quantized torus centered on the stable PO t_0. However, the ring is distorted and is also localized the other PO, s'. As we shall see in subsection 6.2.2, both POs give a substantial contribution to the semiclassical current. Their current frequencies are very close to each

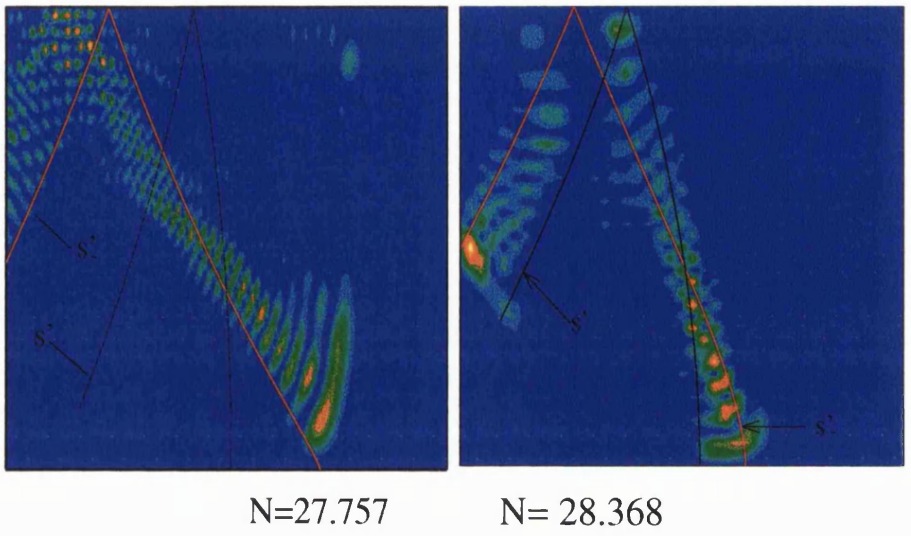

Figure 4.10: Scarred wave functions at $\theta = 27°$ for $\epsilon = 12750$ (left) and $\epsilon = 9000$ (right) with the classical POs s' and s'_-.

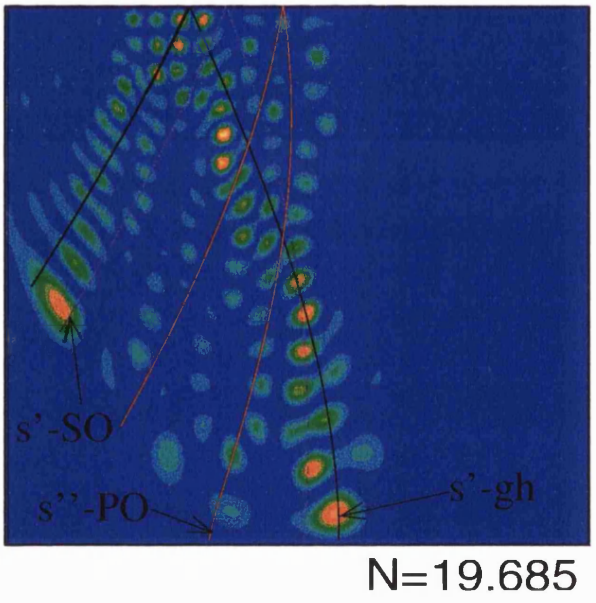

Figure 4.11: Wave function at $\theta = 27°, \epsilon = 7000$ and classical s' orbits [PO, complex ghost PO ($s'_{\rm gh}$) and saddle orbit ($s'-SO$)]. For complex orbits, we show the real part of the trajectory ($\mathrm{Re}\, x, \mathrm{Re}\, z$).

other (1.9158 for $2t_0$ and 1.9054 for s'), and are not distinguishable in the quantum power spectrum of the current. Hence it appears that these POs are not isolated, as the quantum state cannot distinguish them and is localized on both of them. Similarly, both POs are in the localization region of the wave function (right).

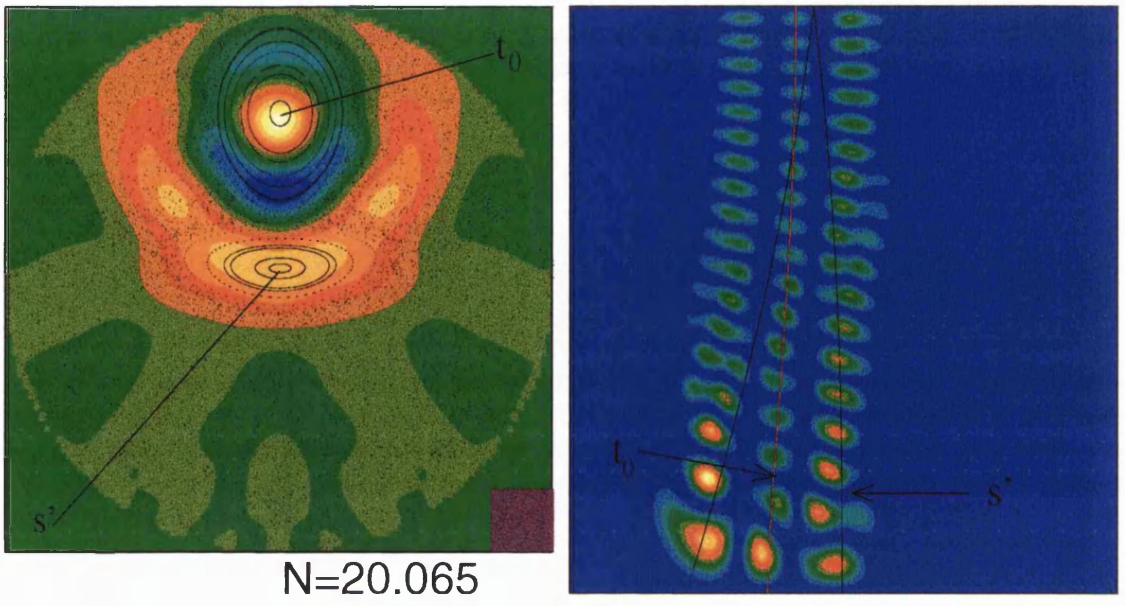

Figure 4.12: Left: Wigner distribution (color plot) at $\theta = 27°, \epsilon = 16000$ and classical Poincaré surface of section (dots), on the emitter wall. The square on lower-right corner represents $\hbar$. Right: corresponding wave function, with the POs t_0 and s'.

Wave and Wigner functions

We show without comment a series of wave functions in Fig. 4.13. The related Wigner distributions (on the collector barrier) are shown in Fig. 4.14.

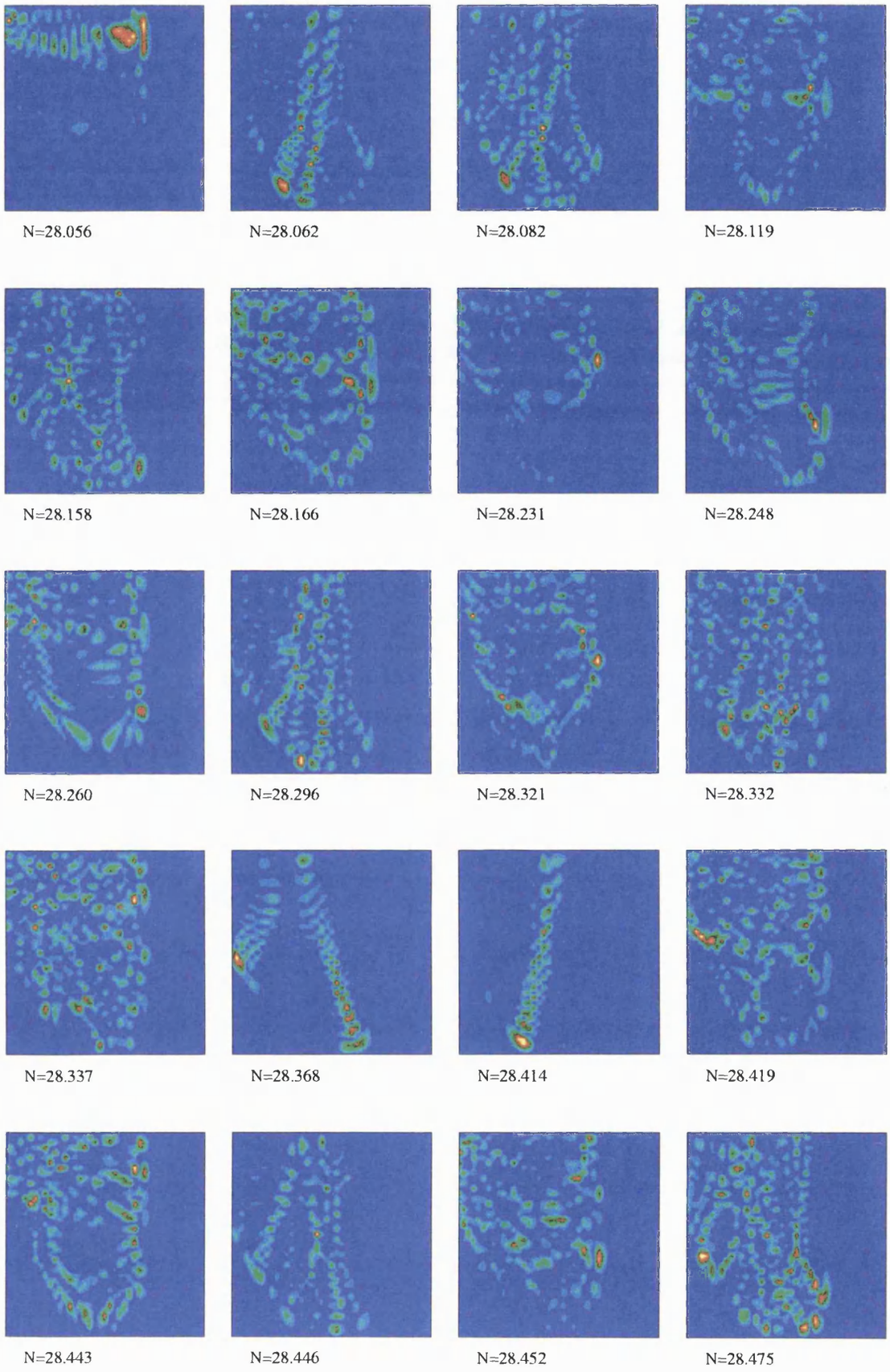

Figure 4.13: Series of wave functions at $\theta = 27°, \epsilon = 9000$.

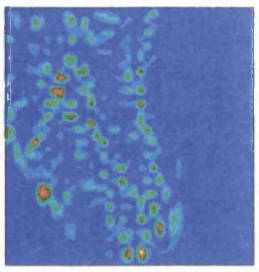

N=28.546

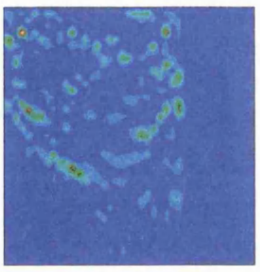

N=28.555

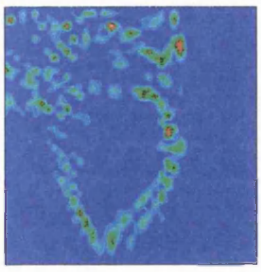

N=28.586

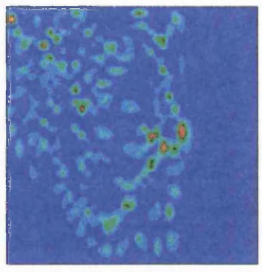

N=28.599

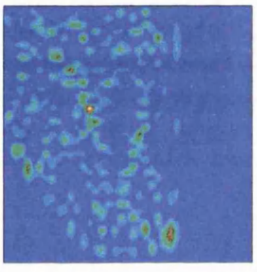

N=28.621

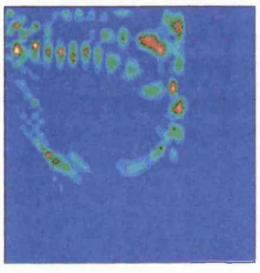

N=28.643

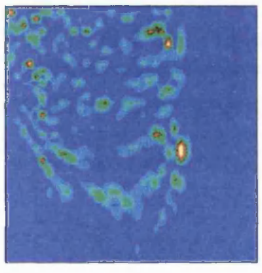

N=28.652

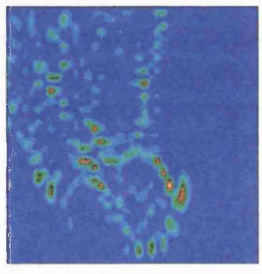

N=28.698

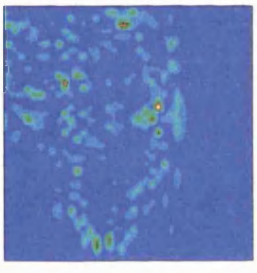

N=28.735

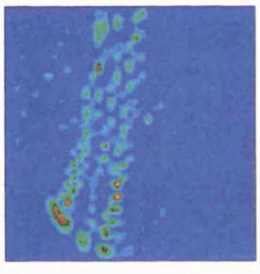

N=28.748

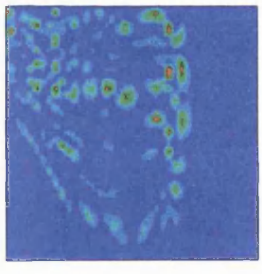

N=28.777

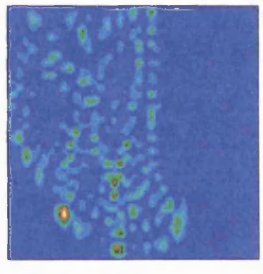

N=28.788

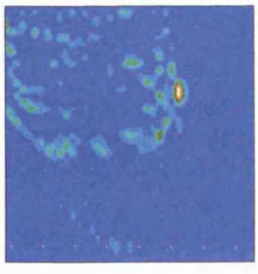

N=28.844

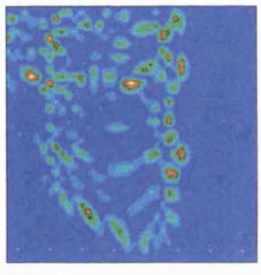

N=28.865

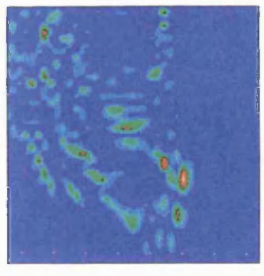

N=28.886

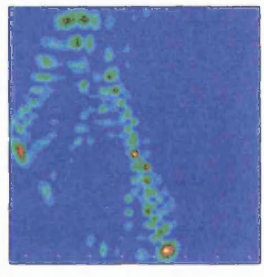

N=28.907

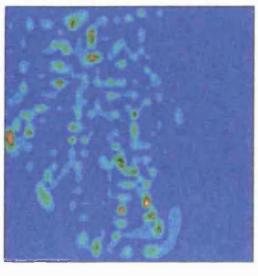

N=28.938

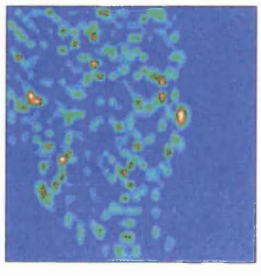

N=28.942

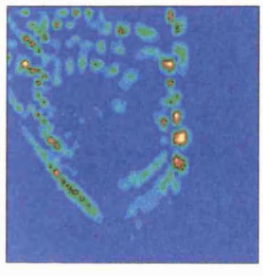

N=28.950

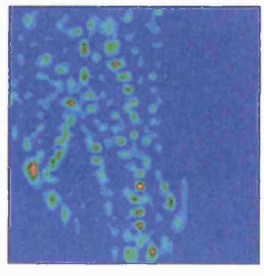

N=28.953

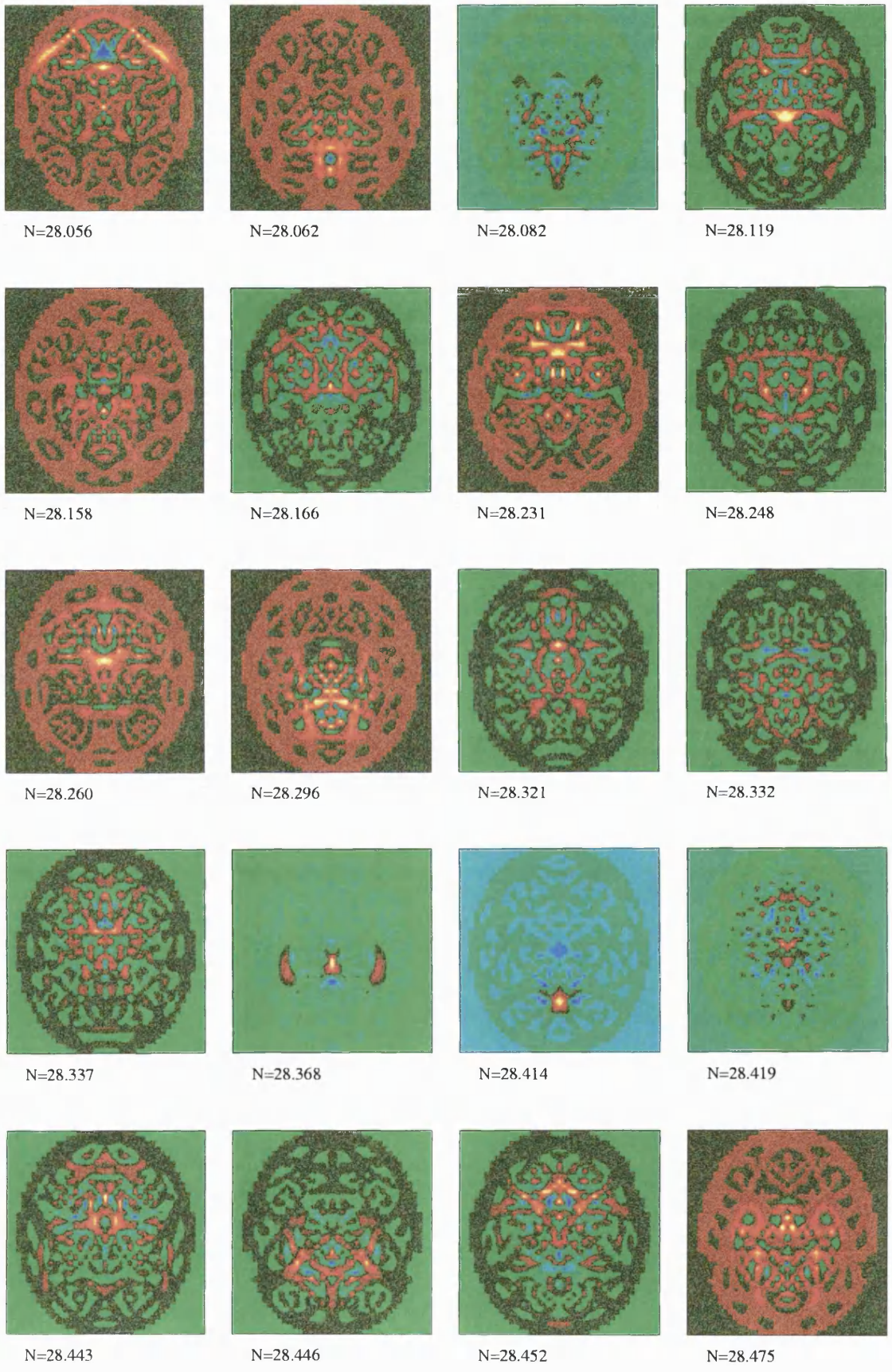

Figure 4.14: Series of Wigner distributions at $\theta = 27°, \epsilon = 9000$ (collector barrier).

N=28.546

N=28.555

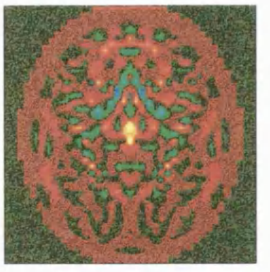

N=28.586

N=28.599

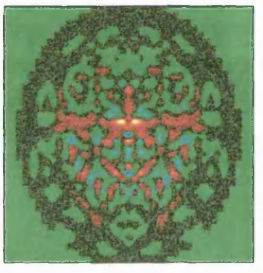

N=28.621

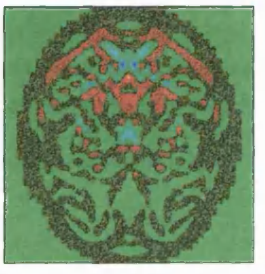

N=28.643

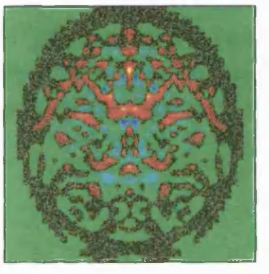

N=28.652

N=28.698

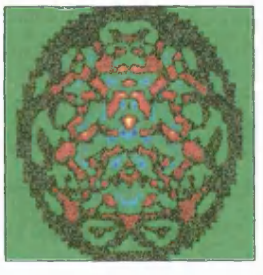

N=28.735

N=28.748

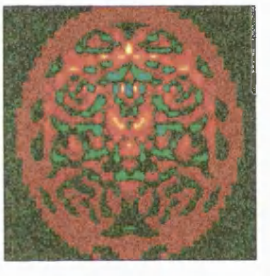

N=28.777

N=28.788

N=28.844

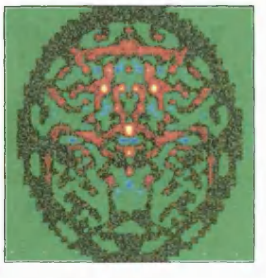

N=28.865

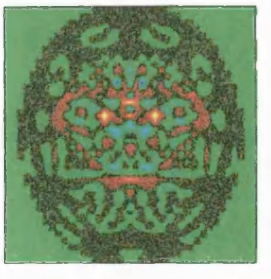

N=28.886

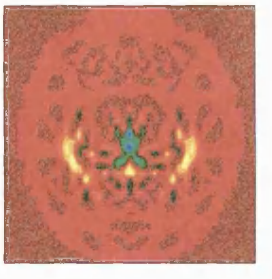

N=28.907

N=28.938

N=28.942

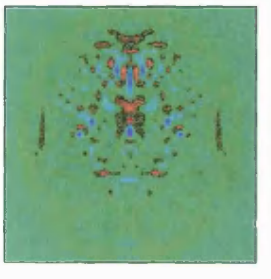

N=28.950

N=28.953

Chapter 5

SEMICLASSICAL THEORIES

The heuristic approach used in the experimental (chapter 2), classical (3) and quantum (4) analysis can only give a qualitative understanding of the observed current. A quantitative description requires a proper and more rigorous semiclassical formula for the current. It should start from the quantum observable and end up as an expression in terms of classical trajectories.

When we started this study of the resonant tunneling diode in 1996, no published semiclassical formula existed. The Bardeen formalism presented in subsection 4.1.4 had only been used in quantum calculations (Fromhold *et al.* 1995b, Monteiro *et al.* 1997a). Two independent groups started working on a formula: E Narimanov and D Stone in Yale, and E Bogomolny and D Rouben in Orsay (Paris). Altogether, they proposed five different formulae. We hope that the formalism we present here clarifies the links between them, the underlying assumptions and their theoretical limitations. Also, it situates them in the general context of semiclassical formulae of matrix elements.

In particular, we discuss the interplay between the oscillations of the semiclassical Green's function (which involve the classical action) and the localization of the observable. The associated relative length scales have a profound influence on the semiclassical picture as they determine (*i*) the type of contributing trajectories and (*ii*) the explicit role of the classical properties. We find five different types of orbits: saddle (SO), periodic (PO), normal (NO), central closed (CCO) and minimal (MO).

Our main finding here is the *saddle orbit formula* [eq. (5.44) and (5.35)]; it was foreseen in the work of Bogomolny and Rouben (1999) who pointed out the fact that the current should be expressed in terms of saddle orbits. Another finding is the discovery of the minimal orbits (5.69), which shows that it is possible to relax somehow the requirement of

stationary phase and still get an accurate result. We present three levels of approximation: (*i*) the SO level, with no approximation; (*ii*) the intermediate formulae (NO, PO, CCO, MO), where we neglect one term in the stationary phase condition but still consider its variations in the integrations; (*iii*) the "hard limit" level, where we neglect one term in both the condition and the integrations (the usual stationary phase approximation).

The scaling and the link between voltage periods and classical characteristics are also discussed. Actual tests and applications of the semiclassical formulae will be made in chapters 6 and 7. More details about complex contributions and saddle orbits can be found in chapter 8.

5.1 Derivation of the semiclassical formula

5.1.1 Bardeen weak tunneling matrix element

The Bardeen (1961) approach to tunneling across a barrier can be used when the tunneling is assumed to be weak, corresponding to a high barrier. In effect, it separates the systems in two parts: on the one hand the emitter and its wave function Φ (the "initial state"), on the other hand the quantum well and its wave function ψ_i. It is also described in subsection 4.1.4 and Fig. 4.2. The current $\mathcal{J}_{\rm em}$ flowing from the emitter to the quantum well is expressed as the density of states of the well, weighted by a matrix element $|\mathcal{M}_i|^2$ which couples Φ to ψ_i on a cut taken at constant x:

$$\mathcal{J}_{\rm em}(E) = neJ \quad , \quad J = \frac{2\pi}{\hbar} \sum_i |\mathcal{M}_i|^2 \delta(E - E_i) \tag{5.1}$$

$$\mathcal{M}_i = \frac{\hbar^2}{2m} \int d\boldsymbol{q} \left\{ \Phi^*(\boldsymbol{q}) \frac{\partial \psi_i}{\partial x}(\boldsymbol{q}) - \frac{\partial \Phi^*}{\partial x}(\boldsymbol{q}) \psi_i(\boldsymbol{q}) \right\} \delta(x) \quad , \quad \boldsymbol{q} = (x, z) \quad . \tag{5.2}$$

Here n is the surface concentration of the emitter, e the electron charge, m its mass and E_i are the energy levels in the quantum well. The cut is taken at the boundary of the barrier which is on the side of the well: $x = 0$. We consider here the two-dimensional problem discussed in subsection 3.1.1, and use *unscaled* variables in SI units. We shall discuss the effect of scaling on the final formulae in subsection 5.3.3.

Experimentally, the collector barrier (the right wall) is made substantially thinner than the emitter barrier in order to avoid the accumulation of electrons in the well and the interaction between them. We assume that there is only one electron in the well, and that the global current $\mathcal{J}_{\rm RTD}$ across the whole RTD is determined solely by the tunneling through the emitter barrier: $\mathcal{J}_{\rm RTD} = \mathcal{J}_{\rm em}$. See also section 2.1 for more considerations on

the approximations made.

We introduce the energy Green's function

$$G(\boldsymbol{q}',\boldsymbol{q}) = \langle \boldsymbol{q}'|\hat{G}_E|\boldsymbol{q}\rangle = \lim_{\eta\to 0_+}\langle \boldsymbol{q}'|(E+i\eta-\hat{H})^{-1}|\boldsymbol{q}\rangle \quad . \tag{5.3}$$

For a separable observable $\hat{A} = |\Theta\rangle\langle\Theta|$, it satisfies the relations

$$\begin{aligned} -\frac{1}{\pi}\mathbf{Im}\,\mathrm{Tr}\hat{A}\hat{G}_E &= -\frac{1}{\pi}\mathbf{Im}\int d\boldsymbol{q}\int d\boldsymbol{q}'\Theta(\boldsymbol{q})\Theta^*(\boldsymbol{q}')G(\boldsymbol{q}',\boldsymbol{q}) \qquad (5.4)\\ &= \sum_i\langle\psi_i|\hat{A}|\psi_i\rangle\lim_{\eta\to 0_+}\frac{1}{\pi}\frac{\eta}{(E-E_i)^2+\eta^2} = \sum_i\langle\psi_i|\hat{A}|\psi_i\rangle\delta(E-E_i)\\ &= \sum_i\int d\boldsymbol{q}\int d\boldsymbol{q}'\psi_i^*(\boldsymbol{q})\Theta(\boldsymbol{q})\Theta^*(\boldsymbol{q}')\psi_i(\boldsymbol{q}')\delta(E-E_i) \quad . \qquad (5.5)\end{aligned}$$

The third line is very similar to (5.1) and (5.2); the derivatives of ψ_i are transferred into derivatives of the Green's function in (5.4) and the current can be written[1]

$$\begin{aligned} J &= -\frac{\hbar^3}{2m^2}\mathbf{Im}\int dz\int dz'\left\{\Phi(\bar{\boldsymbol{q}})\Phi^*(\bar{\boldsymbol{q}}')\partial^2_{xx'}G(\bar{\boldsymbol{q}}',\bar{\boldsymbol{q}}) - \partial_x\Phi(\bar{\boldsymbol{q}})\Phi^*(\bar{\boldsymbol{q}}')\partial_{x'}G(\bar{\boldsymbol{q}}',\bar{\boldsymbol{q}})\right.\\ &\left.-\Phi(\bar{\boldsymbol{q}})\partial_{x'}\Phi^*(\bar{\boldsymbol{q}}')\partial_x G(\bar{\boldsymbol{q}}',\bar{\boldsymbol{q}}) + \partial_x\Phi(\bar{\boldsymbol{q}})\partial_{x'}\Phi^*(\bar{\boldsymbol{q}}')G(\bar{\boldsymbol{q}}',\bar{\boldsymbol{q}})\right\} \qquad (5.6)\end{aligned}$$

where $\bar{\boldsymbol{q}} = (x=0,z)$. The first step in a semiclassical treatment is to use the semiclassical approximation of the Green's function (Gutzwiller 1990, Brack and Bhaduri 1997):

$$G(\boldsymbol{q}',\boldsymbol{q}) \overset{\hbar\to 0}{\simeq} \frac{2\pi}{(2\pi i\hbar)^{3/2}}\sum_{\boldsymbol{q}\to\boldsymbol{q}'}\sqrt{D_{\mathrm{SC}}}e^{iS(\boldsymbol{q},\boldsymbol{q}')/\hbar} \quad , \tag{5.7}$$

given here for two degrees of freedom. The quantum Green's function is expressed as a sum over all the classically allowed trajectories going from $\boldsymbol{q}$ to $\boldsymbol{q}'$ with energy E. Their classical action is S. We did not include the phase $-i\mu\pi/2$ arising from the number μ of conjugate (or focal) points along the trajectory; these are points where a bunch of trajectories converge on a single point. μ would become, after the integration (5.19) below, an "effective Maslov index" μ_{eff} (Bogomolny and Rouben 1999). As we shall primarily deal with the contributions from well separated trajectories, the constant phase carried by μ will not change the semiclassical amplitudes. We shall not take the phase into account, apart from the cases where it is relevant (e.g. in Fig. 6.5). Similarly, we have written D_{SC} instead of $|D_{\mathrm{SC}}|$.

The determinant D_{SC} can be viewed as a density of classical paths, and can be shown to be (Brack and Bhaduri 1997)

$$D_{\mathrm{SC}} = \det\begin{pmatrix}\dfrac{\partial^2 S}{\partial\boldsymbol{q}\partial\boldsymbol{q}'} & \dfrac{\partial^2 S}{\partial\boldsymbol{q}\partial E}\\ \dfrac{\partial^2 S}{\partial E\partial\boldsymbol{q}'} & \dfrac{\partial^2 S}{\partial E^2}\end{pmatrix} = \frac{m^2}{pp'}\frac{\partial^2 S}{\partial q_\perp\partial q'_\perp} = \frac{m^2}{pp'}\frac{-1}{m_{12}^\perp} = \frac{m^2}{p_x p'_x}\frac{-1}{m_{12}} \quad . \tag{5.8}$$

[1] Formally, $\mathcal{M}_i = i\langle\Theta|\psi_i\rangle$ with $|\Theta\rangle = \hbar/(2m)|\left(\hat{p}_x\hat{\delta}_x + \hat{\delta}_x\hat{p}_x\right)\otimes\mathbb{1}_z|\Phi\rangle$, $\hat{\delta}_x = |x=0\rangle\langle x=0|$.

Here p, p' are the moduli of the initial and final classical momenta and $q_\perp, q'_\perp$ are coordinates which are perpendicular to the trajectory at the initial and final points. $M^\perp$ and M are the monodromy matrices defined with respect to $(q_\perp, p_{q_\perp})$ and (z, p_z) coordinates respectively.

One can show (Narimanov and Stone 1999, Bogomolny and Rouben 1999) that in the RTD:

$$G(0,z;0,z') = 0 = \partial_x G(0,z;0,z') = \partial_{x'} G(0,z;0,z') \tag{5.9}$$

$$\partial^2_{xx'} G(0,z;0,z') = 4 \times \frac{p_x p'_x}{\hbar^2} G(0,z;0,z') \quad . \tag{5.10}$$

These relations arise from the fact that we consider infinitely high barriers at $x = 0$. This implies that a family of distinct trajectories connecting $(x,z) \to (x',z')$ coalesce as one takes the limit $x, x' \to 0$. There is one "direct" trajectory and 3 "indirect" trajectories (which have one extra bounce near $x = 0$ or $x' = 0$ or near both). The π phase difference incurred by the hard bounces makes the Green's function vanish, corresponding in some way to the fact that $\psi_i(x = 0, z) = 0$. However, the second derivatives of G can be non-zero, as they are related to the product of the derivatives of the wave function which are non-zero $[\partial_x \psi_i(x = 0, z) \neq 0]$. The factor 4 arises from the collective contribution of the 4 members of the family, while the momenta come from the derivatives of the action (A.13).

Hence, only the first term in (5.6) is non-zero, and using (5.7), (5.8) and (5.10) we obtain

$$J = -\frac{2C}{m\sqrt{2\pi\hbar}} \mathbf{I}\mathrm{m} i^{-3/2} \int dz \int dz' \sum_{(x=0,z)\to(x'=0,z')} \sqrt{\frac{p_x p'_x}{-m_{12}}} \phi(z) \phi^*(z') e^{iS(x=0,z;x'=0,z')/\hbar} \quad . \tag{5.11}$$

We have introduced a separable form of the initial state function:

$$\Phi(x,z) = \chi(x)\phi(z) \quad , \quad C = |\chi(0)|^2 \quad , \tag{5.12}$$

which will be discussed briefly in the next subsection.

5.1.2 The initial state

Although the exact form of $\chi(x)$ is not essential –as only C appears in the current–, a clearer physical picture can be drawn from studying the initial state. One has to deal with a non-separable problem composed of two potentials (see Fig. 2.1). The voltage potential describes the effect of the bending of the conduction bands in the heterojunction, as well

as the electric field F due to the applied voltage V.[2] This creates a triangular well (for $x < -d_{\rm em}$), adjacent to a square barrier of width $d_{\rm em}$ and height $U_{\rm em}$ (for $-d_{\rm em} < x < 0$). The magnetic potential $\frac{e^2B^2}{2m}(x\sin\theta - z\cos\theta)^2$ is a consequence of $\boldsymbol{B}$ also acting in the emitter region. It mixes the x and z degrees of freedom. However, the triangular well freezes the x motion in its lowest energy level and consequently the magnetic field can only act on z, with an effective strength $B\cos\theta$. One can therefore propose a separable form (5.12) for the initial state.

Following Bogomolny and Rouben (1999), who treated the x part of $V_{\rm mag}(x,z)$ as a first order perturbation, and Narimanov and Stone (1999), we propose the initial state

$$\chi(x) \quad = \quad \begin{cases} \text{const} \times \text{Ai}\left[(2meF/\hbar^2)^{1/3}x - 2.338\right] & , \quad x < -d_{\rm em} \\ \chi(0)e^{-\gamma x/\hbar} & , \quad -d_{\rm em} < x < 0 \end{cases} \tag{5.13}$$

$$\phi(z) \quad = \quad \left(\frac{\beta}{\pi\hbar}\right)^{1/4} e^{-\frac{\beta}{2\hbar}(z-z_{\rm S})^2} \tag{5.14}$$

$$\text{with} \quad \gamma = \sqrt{2m(eU_{\rm em} - E)} \quad \text{and} \quad \beta = eB\cos\theta \quad . \tag{5.15}$$

The Airy function Ai is the solution of the triangular well with $U_{\rm em} \to \infty$, and yields an expectation value $< x >=< \chi|\hat{x}|\chi >= 1.236(\hbar^2/meF)^{1/3}$ appearing in the shift of the Gaussian

$$z_{\rm S} = (d_{\rm em} + < x >)\tan\theta \quad . \tag{5.16}$$

This shift becomes important for high tilt angles $\theta > 30°$, but we shall neglect it in the derivations presented in the next sections:

$$z_{\rm S} \equiv 0 \quad . \tag{5.17}$$

The modifications required to take the shift into account will be described explicitly in section 7.3. In (5.14) we considered that $B\cos\theta$ quantizes the z degree of freedom only in the lowest Landau level, which is the general assumption taken by the experimental groups (Fromhold *et al.* 1997c). The semiclassical formulae presented in this chapter will work with this hypothesis. However, this might become inaccurate for large θ, in which case one should consider excited Landau levels:

$$\phi_m(z) = C_m e^{-\frac{\beta}{2\hbar}(z-z_{\rm S})^2} \text{H}_{\rm m}\left[(z-z_{\rm S})\sqrt{\beta/\hbar}\right] \quad , \quad C_m = \left(\frac{\beta}{\pi}\right)^{1/4}\left(\frac{1}{2^m m!}\right)^{1/2} \quad , \quad m \geq 0 \tag{5.18}$$

[2] We consider the constant force to be due solely to the applied voltage, although the bending might have a role to play.

involving the Hermite polynomials H_m. This has been considered in Narimanov and Stone (1999), and yields much more complicated formulae. A semiclassical formula incorporating the first excited Landau level will be presented in section 7.3.

5.1.3 Gaussian integrations

The second and final step for a semiclassical theory of the current is to find an approximation, in the $\hbar \to 0$ limit, of the integral

$$\begin{aligned} \mathcal{I} &= \int dz \int dz' \sum_{z \to z'} \mathcal{P}(z,z') \phi(z) \phi^*(z') e^{iS(z,z')/\hbar} \\ &\overset{(5.14)}{=} \sqrt{\frac{\beta}{\pi\hbar}} \sum_{\ell} \iint_{\Omega_\ell} dz\, dz' \mathcal{P}(z,z') e^{\varphi(z,z')/\hbar} \qquad (5.19) \end{aligned}$$

$$\text{with} \quad \mathcal{P}(z,z') := \sqrt{\frac{p_x p'_x}{-m_{12}}} \quad , \quad \varphi(z,z') := iS(z,z') - \frac{\beta}{2}(z^2 + z'^2) \quad . \qquad (5.20)$$

Here all the trajectories start at $x = 0$ and end at $x' = 0$: the Bardeen cut selects *"emitter orbits"*, that hit the emitter wall. We have taken the sum over trajectories $z \to z'$ outside the integrals where it becomes a sum over all the different "families" $\{\ell\}$ of trajectories existing in the RTD. Each family has a specified number of bounces on the left and right walls, but several distinct families can have the same number of bounces. This comes from the fact that several trajectories $(z, p_z^j) \to (z', p_{z'}^j), j = 1, 2, ..$ can join z to z' with the same bounce structure; they are defined in a non-ambiguous way by their starting momentum p_z^j. Note that each family exists only in a certain domain $\{(z,z') \in \Omega_\ell\}$.

The tools used for this kind of integration are the *stationary phase approximation* and the *steepest-descent method* (SPA), which are explained in more detail in Appendix B.1, while a comprehensive discussion can be found in Dieudonné (1968). The method of steepest-descent applied to (5.19) prescribes finding the stationary points of $\varphi(z,z')$ (Bogomolny and Rouben 1999):

$$\frac{\partial \varphi}{\partial z}(z_0, z'_0) = i\frac{\partial S}{\partial z}(z_0, z'_0) - \beta z_0 = 0 \quad , \quad \frac{\partial \varphi}{\partial z'}(z_0, z'_0) = i\frac{\partial S}{\partial z'}(z_0, z'_0) - \beta z'_0 = 0 \quad . \qquad (5.21)$$

One should then expand quadratically $\varphi(z,z')$ [i.e., expand $S(z,z')$ as $\beta(z^2 + z'^2)/2$ is already quadratic] around (z_0, z'_0) and integrate. The trajectories which satisfy (5.21) are complex and non-periodic, and have been called "saddle orbits" (Saraga and Monteiro 1998a). However, other choices for the expansion of φ have been made.

One can follow the usual approach of the Gutzwiller trace formula and argue that $\exp(iS/\hbar)$ is highly oscillatory in the limit $\hbar \to 0$; one can therefore apply the SPA on

this function only and consider the stationary points of S. This has been considered in Bogomolny and Rouben (1999) and yields orbits which are perpendicular to the left barrier ($p_z = p'_z = 0$). On the other hand, one could argue that the Gaussian form of the initial wave functions $\exp[-\beta(z^2 + z'^2)/2\hbar]$ selects more strongly which trajectory contributes or not. This approach (Narimanov and Stone 1999) yields trajectories starting and ending at the center of the Gaussian ($z = z' = 0$). One can also follow Eckhardt *et al.* (1992) and Narimanov and Stone (1998b) and consider an expansion around periodic orbits (POs). In summary, the evaluation of (5.19) by SPA is delicate because the initial wave functions vary on exactly the *same* $\hbar$ scale as the semiclassical Green's function given by $\exp(iS/\hbar)$.

These different approaches to the SPA yield different specific *types* of orbits. However, it is worth noting that *whatever* the approach is, one will always expand the action quadratically around an "expansion orbit" $(z_0, p_z^0) \to (z'_0, p_{z'}^0)$:

$$\begin{aligned} S(z,z') &\simeq S(z_0,z'_0) + \delta z \frac{\partial S}{\partial z}(z_0,z'_0) + \delta z' \frac{\partial S}{\partial z'}(z_0,z'_0) \\ &\quad + \frac{1}{2}\left[\delta z^2 \frac{\partial^2 S}{\partial z^2}(z_0,z'_0) + 2\delta z \delta z' \frac{\partial^2 S}{\partial z \partial z'}(z_0,z'_0) + \delta z'^2 \frac{\partial^2 S}{\partial z'^2}(z_0,z'_0)\right] \quad (5.22) \\ &= S_0 - p_z^0 \delta z + p_{z'}^0 \delta z' + \frac{1}{2m_{12}}\left[\delta z^2 m_{11} - 2\delta z \delta z' + \delta z'^2 m_{22}\right] \quad (5.23) \\ &=: \mathcal{S}_2(\delta z, \delta z'; z_0, z'_0) \quad , \quad (5.24) \end{aligned}$$

where (A.13) and (A.19) have been used, and the differences $\delta z = z - z_0$ and $\delta z' = z' - z'_0$ defined. The monodromy matrix elements m_{ij} are evaluated at (z_0, z'_0).

One such type of expansion orbits $z_0 \to z'_0$ around which one expands the action satisfies a pair of conditions such as (5.21), $\{p_z = p'_z = 0\}$ or $\{z = z' = 0\}$. Such a pair of conditions is restrictive, and should be satisfied only by a *discrete* set of trajectories $\{\ell_0\}$. For each family ℓ appearing in the sum (5.19), there should exist, generically, at most *one* expansion orbit $\ell_0 : z_0 \to z'_0$.

To follow the SPA method, one has to calculate the integral (5.19) with the quadratic expansion of the action (5.24), while extending the limit of integration $\Omega \to \mathbb{R} \times \mathbb{R}$. An important fact is that the Gaussian form of the initial state makes this integration analytical for *any* choice of expansion orbit. Hence we do not limit ourselves to any particular trajectory at this stage; we shall discuss at length in section 5.2 the different choices that have been or can be made.

We follow the techniques of Bogomolny and Rouben (1999), and complete the square:

$$\mathcal{I} \overset{\text{SPA}}{\simeq} \sum_{\ell_0} \sqrt{\frac{\beta}{\pi\hbar}} \int d\gamma \mathcal{P}(\gamma) e^{\varphi_2(\gamma)/\hbar} \quad (5.25)$$

$$\varphi_2(\gamma) := iS_2(\gamma; z_0, z_0') - \frac{\beta}{2}(z^2 + z'^2) \tag{5.26}$$

$$\overset{(5.24)}{=} iS_0 - \frac{\beta}{2}(z_0^2 + z_0'^2) + \boldsymbol{\xi}^{\mathrm{T}}\gamma + \frac{1}{2}\gamma^{\mathrm{T}}\mathcal{A}\gamma \tag{5.27}$$

$$= iS_0 - \frac{\beta}{2}(z_0^2 + z_0'^2) - \frac{1}{2}\boldsymbol{\xi}^{\mathrm{T}}\mathcal{A}^{-1}\boldsymbol{\xi} + \frac{1}{2}(\gamma + \gamma_1)^{\mathrm{T}}\mathcal{A}(\gamma + \gamma_1) \tag{5.28}$$

with

$$\gamma = (\delta z, \delta z') = (z - z_0, z' - z_0') \tag{5.29}$$

$$\boldsymbol{\xi} = (-\beta z_0 - ip_z^0, -\beta z_0' + ip_{z'}^0) \quad , \quad \gamma_1 = \mathcal{A}^{-1}\boldsymbol{\xi} \tag{5.30}$$

$$\mathcal{A} = \begin{pmatrix} -\beta + i\dfrac{m_{11}}{m_{12}} & -i\dfrac{1}{m_{12}} \\ \\ -i\dfrac{1}{m_{12}} & -\beta + i\dfrac{m_{22}}{m_{12}} \end{pmatrix} . \tag{5.31}$$

Making the change of variables $\gamma' = \gamma + \gamma_1$ in (5.25), one is left with

$$\mathcal{I} = \sum_{\ell_0} \sqrt{\frac{\beta}{\pi\hbar}} \mathcal{P}_0 e^{\left[iS_0 - \frac{\beta}{2}(z_0^2 + z_0'^2) - \frac{1}{2}\boldsymbol{\xi}^{\mathrm{T}}\mathcal{A}^{-1}\boldsymbol{\xi}\right]/\hbar} \int d\gamma' e^{\left[\frac{1}{2}\gamma'^{\mathrm{T}}\mathcal{A}\gamma'\right]/\hbar} . \tag{5.32}$$

By stationary phase, one has taken the slowly varying function $\mathcal{P}(\gamma)$ outside the integral and used its value at the expansion point: $\mathcal{P}_0 = \mathcal{P}(z_0, z_0')$. The last integral is simply a 2-D Gaussian integral, which gives[3]

$$\int d\gamma' e^{\left[\frac{1}{2}\gamma'^{\mathrm{T}}\mathcal{A}\gamma'\right]/\hbar} = \frac{2\pi\hbar}{\sqrt{\det \mathcal{A}}} . \tag{5.33}$$

Using $\det M = 1$, one finds

$$\det \mathcal{A} = \frac{\mathcal{D}}{m_{12}} \quad , \quad \boxed{\mathcal{D} = -m_{21} - i\beta \mathrm{Tr} M + \beta^2 m_{12}} . \tag{5.34}$$

Finally,

$$\boxed{\mathcal{I} = \sum_{\substack{\ell_0 \\ (z_0 \to z_0')}} 2\sqrt{\frac{\beta\pi\hbar p_x p_x'}{-\mathcal{D}}} e^{\left[iS_0 + \Gamma(z_0, z_0')\right]/\hbar}} \quad , \tag{5.35}$$

with

$$\begin{aligned} \Gamma(z, z') &= -\frac{\beta}{2\mathcal{D}} \times \Big\{ z^2\left[-m_{21} - i\beta m_{11}\right] + z'^2\left[-m_{21} - i\beta m_{22}\right] + 2i\beta z z' \\ &+ \frac{1}{\beta^2} p_z^2 \left[-i\beta m_{22} + \beta^2 m_{12}\right] + \frac{1}{\beta^2} p_{z'}^2 \left[-i\beta m_{11} + \beta^2 m_{12}\right] + 2i\frac{1}{\beta} p_z p_{z'} \\ &+ 2\frac{i}{\beta} z p_z \left[i\beta m_{22} - \beta^2 m_{12}\right] + 2\frac{i}{\beta} z' p_{z'} \left[-i\beta m_{11} + \beta^2 m_{12}\right] + 2z p_{z'} - 2z' p_z \Big\} \end{aligned} \tag{5.36}$$

[3]Writing $\mathcal{A}$ in its diagonal form, one is left with a product of two 1-D complex Gaussian integrals, each giving an eigenvalue of $\mathcal{A}$ as prefactor; their product gives the determinant.

The current is then given by

$$J = -\frac{2C}{m\sqrt{2\pi\hbar}} \mathrm{Im}\, i^{-3/2}\mathcal{I} \quad . \tag{5.37}$$

Remarks

The above formula describes the *oscillatory* part of the current. We do not consider here the "smooth" part, obtained by considering zero-length trajectories (Bogomolny and Rouben 1999); this part varies slowly with the energy, and corresponds to the Weyl term in Gutzwiller's theory of the density of states (Gutzwiller 1990).

The loss of coherence due to phonon scattering is *not* considered in the formalism presented here. We could model it by adding an exponential factor $\exp(-T/\tau)$ in the sum, where T is the real part of the total time of each trajectory and τ is the damping time. We shall proceed the other way round, canceling the damping in the experiment to be in the present situation where there is no damping (see subsection 2.3.4).

Finally, the formula is valid only for *isolated* expansion orbits.

5.2 The different formulae

At this stage one should go back to (5.19) and examine which choices of expansion orbits have been or can be made.

It is a remarkable feature of the RTD that for *any starting* z, there exists generically a starting momentum $\check{p}_z$ so that the trajectory is time-reversed of itself (time-symmetric) and therefore closed (see subsection 3.1.7). We call such trajectories **time-symmetric closed orbits (TSCOs)**. They are defined by

$$\textbf{TSCO} : \quad (z, \check{p}_z) \to (z', p'_z) = (z, -\check{p}_z) \tag{5.38}$$

and satisfy the important relation (3.19)

$$m_{11} = m_{22} \quad . \tag{5.39}$$

The existence of TSCOs is a consequence of the fact that for any starting z, one can find a starting p_z so that there is either a perpendicular bounce on the right wall [$p_z(x = L) = 0$], or a turning point on the energy surface at a point (x_e, z_e) [$\boldsymbol{p}(x_e, z_e) = 0$]. *A priori*, (5.38) is as restrictive as, e.g., the periodic orbit condition and would only be satisfied by a discrete set of trajectories. In the RTD though, this is a one parameter (z) continuous

family. One actually finds that each choice of expansion orbit shown below contains a subset which is time-symmetric (TS), and that *in almost all cases only the TS subset contribute to the current.* This is the reason why we first write (5.36) for time-symmetric closed orbits (TSCOs). Using (5.38) and (5.39), one finds

$$\Gamma_{\mathrm{TSCO}}(z_0) = -\frac{\beta}{1-\delta}\left\{ z_0^2 - \left[\frac{1}{\beta^2}(p_z^0)^2 - 2\frac{i}{\beta} z_0 p_z^0\right]\delta \right\} \tag{5.40}$$

where we have defined

$$\boxed{\delta = -i\beta\frac{m_{12}}{m_{11}-1}} \quad . \tag{5.41}$$

We can also write in that case

$$\mathcal{D} = (1-\delta)\left[-m_{21} - i\beta(m_{11}-1)\right] = \left[\beta^2 m_{12} - i\beta(m_{11}+1)\right](1-\frac{1}{\delta}) \quad . \tag{5.42}$$

5.2.1 Saddle orbits (SOs)

The first expansion orbits we consider are given by the strict application of the stationary phase condition to (5.19), which gave (5.21) and defined **saddle orbits (SOs)**:

$$\mathbf{SO}: \quad \begin{cases} p_z^0 = i\beta z_0 \\ p_{z'}^0 = -i\beta z_0' \end{cases} \quad . \tag{5.43}$$

One finds then

$$\Gamma_{\mathrm{SO}}(z_0, z_0') = -\frac{\beta}{2}\left[z_0^2 + z_0'^2\right] \quad . \tag{5.44}$$

In the case where SOs are TS **(TSSOs)** one has

$$\Gamma_{\mathrm{TSSO}}(z_0) = -\beta z_0^2 \quad . \tag{5.45}$$

We shall show in chapter 6 that the SOs are the most successful types of orbits for a semiclassical description of the quantum current. One difficulty with SOs is the fact that they are *complex.* This is the reason why Bogomolny and Rouben (1999) decided to avoid them (and considered real trajectories), although they were well aware of the fact that the stationary phase approximation yields SOs.

Note also that SOs are *non-periodic*; this means that one cannot look at repetitions of a "primitive" SO, as it would not satisfy the SO condition. Instead one must search for a SO with a higher period.

5.2.2 Normal orbits (NOs)

To obtain real trajectories, one has to make a further approximation and neglect something in the SPA condition (5.43). Bogomolny and Rouben (1998) considered that the dynamics in the well are very chaotic; in that case one should expect the oscillations due to the action to dominate the Gaussian damping of the initial state. This corresponds to taking the limit $\beta \to 0$ in (5.43), and yields **normal orbits (NOs)**:

$$\textbf{NO} : \quad \left\{ \begin{array}{l} p_z^0 = 0 \\ p_{z'}^0 = 0 \end{array} \right. . \tag{5.46}$$

Essentially, this states that the contributing trajectories are determined solely by the oscillations of the Green's function: they must cancel the variations of the action, however small is their accessibility to the initial state. TS normal orbits **(TSNOs)** have moreover $z_0' = z_0$. This implies that TSNOs are actually a special subset of periodic orbits, that are time-symmetric (TSPOs) and start with p_z=0. In the non-TS case ($z_0' \neq z_0$), the *second* repetition of the NO is actually a TSPO; the first repetition of a non-TS NO is in a sense a "half PO". One finds

$$\Gamma_{\rm NO}(z_0, z_0') = -\frac{\beta}{2\mathcal{D}} \left\{ z_0^2 \left[-m_{21} - i\beta m_{11} \right] + (z_0')^2 \left[-m_{21} - i\beta m_{22} \right] + 2i\beta z_0 z_0' \right\} \quad , \tag{5.47}$$

while the TS case yields

$$\Gamma_{\rm TSNO}(z_0) = -\frac{\beta}{1-\delta} z_0^2 \quad . \tag{5.48}$$

(5.47) is Equation (109) of Bogomolny and Rouben (1999).

It is also worthwhile to suppose that β is *very* small; the first term of an expansion of Γ and $\mathcal{D}$ in powers of β yields

$$\mathcal{D}_{\rm HL} \to -m_{21} \quad , \quad \Gamma_{\rm HL} \to -\frac{\beta}{2} \left[z_0^2 + (z_0')^2 \right] \quad . \tag{5.49}$$

We refer to this kind of expansion as **"hard limit" (HL)**[4]. This was the first formula proposed in Bogomolny and Rouben (1998). It is justified in the case of extremely chaotic dynamics, where the oscillations of the Green's function [$\propto \exp(iS/\hbar)$] are supposed to be much stronger than the Gaussian decay of the initial state. In the case of a TS orbit, the precise condition for the validity of this theory is (Bogomolny and Rouben 1999)

$$\frac{\left| \frac{\partial^2 S}{\partial z^2} \right|}{B} = \left| \frac{\tilde{m}_{11} - 1}{\tilde{m}_{12}} \right| = \frac{\cos\theta}{|\delta|} \gg 1 \quad . \tag{5.50}$$

[4]The name comes from the fact that here we push the limit $\beta \ll 1$ beyond the level of the stationary phase condition, to the level of the integrations.

The HL result corresponds to the SPA method applied to the Green's function only. As β is supposed to be *very* small, the initial state function can be taken out of the integral (5.25); it is evaluated at the NO and gives the simple Gaussian factor $\Gamma_{\rm HL}$. The integral is carried out only over the Green's function, bringing in a prefactor m_{21} and the exponential of the pure action. Note that this is the usual way of proceeding with the SPA method: it is not standard to consider the variations of both functions in the SPA integrations, as we did for the intermediate formula (5.47).

5.2.3 Central closed orbits (CCOs)

Narimanov and Stone (1999) proposed a semiclassical approach[5] which effectively amounts to consideration of the other extreme case, where the Gaussian damping dominates the action oscillations; this assumption can be justified for fairly regular dynamics. This corresponds to taking the limit $\beta \to \infty$ in (5.43), and yields **central closed orbits (CCOs)**:

$$\textbf{CCO} : \quad \begin{cases} z_0 = 0 \\ z_0' = 0 \quad . \end{cases} \tag{5.51}$$

Here the contributing trajectories give maximal accessibility to the initial state, while they do not cancel the variations of the action. In this case one finds

$$\Gamma_{\rm CCO}(p_z^0, p_{z'}^0) = -\frac{1}{2\beta\mathcal{D}}\left\{(p_z^0)^2\left[-i\beta m_{22} + \beta^2 m_{12}\right] + (p_{z'}^0)^2\left[-i\beta m_{11} + \beta^2 m_{12}\right] + 2i\beta p_z^0 p_{z'}^0\right\} \quad . \tag{5.52}$$

This formula is equivalent to Equation (14) of Narimanov and Stone (1999).[6] TS central closed orbits **(TSCCOs)** have $p_{z'}^0 = -p_z^0$, and give

$$\Gamma_{\rm TSCCO}(z_0) = \frac{1}{\beta}\frac{\delta}{1-\delta}(p_z^0)^2 \quad . \tag{5.53}$$

One can also consider the hard limit, i.e. the first order expansion in $1/\beta$:

$$\mathcal{D}_{\rm HL} \to \beta^2 m_{12} \quad , \quad \Gamma_{\rm HL} \to -\frac{1}{2\beta}\left[(p_z^0)^2 + (p_{z'}^0)^2\right] \quad . \tag{5.54}$$

This is equivalent to neglecting the quadratic term of the action in the integral (5.25). The integrations of the linear term and the initial state are in effect a Fourier transform, and bring in the value of the initial state in momentum representation at the CCO,

[5] This was a complement to their periodic orbit formula presented in Narimanov *et al.* (1998b) and discussed below in subsection 5.2.4.

[6] They derived a general formula for any number of excited Laudau levels in the initial state.

$\tilde{\phi}(p_z) = (\beta\pi\hbar)^{-1/4}\exp(-p_z^2/2\beta\hbar)$.[7] A similar expression in terms of "closed orbits at the nucleus" and involving a weighting by $m_{12}^{-1/2}$ was found in the semiclassical theory of the photoabsorption spectra of a hydrogen atom in external fields.(Du and Delos 1988)[8]

5.2.4 Periodic orbits (POs)

Another possibility is to consider **periodic orbits (POs)**, defined by

$$\textbf{PO}: \quad \begin{cases} z_0' = z_0 \\ p_{z'}^0 = p_z^0 \end{cases} . \tag{5.55}$$

This is a natural choice, as it follows the expansion around POs found in the derivation of the Gutziller trace formula (Gutzwiller 1990) for the density of states. It has been proposed for general semiclassical matrix elements in Eckhardt *et al.* (1992), and for the current in the RTD by Narimanov *et al.* (1998b). A discussion of this choice is more adequately made using a phase space formalism, which is briefly introduced in Appendix B.2. Alternatively, a more direct route is to define "average-difference" coordinates:

$$\begin{cases} \bar{z} = \frac{1}{2}(z' + z) \\ \Delta z = z' - z \end{cases} , \quad \begin{cases} \bar{p_z} = \frac{1}{2}(p_z' + p_z) \\ \Delta p_z = p_z' - p_z \end{cases} \tag{5.56}$$

which one uses to write the z-part of the observable $\hat{A} = |\phi\rangle\langle\phi|$ in position space as:

$$\bar{A}(\bar{z}, \Delta z) = \phi(\bar{z} - \frac{1}{2}\Delta z)\phi^*(\bar{z} + \frac{1}{2}\Delta z) = \sqrt{\frac{\beta_{\bar{z}}^{1/2}\beta_{\Delta z}^{1/2}}{\pi\hbar}} e^{-\frac{\beta_{\bar{z}}}{\hbar}\bar{z}^2 - \frac{\beta_{\Delta z}}{4\hbar}\Delta z^2} , \tag{5.57}$$

while the Wigner transform is defined by

$$W(\bar{z}, \bar{p}_z) = \frac{1}{2\pi\hbar}\int d\Delta z\, e^{i\bar{p}_z\Delta z/\hbar}\bar{A}(\bar{z}, \Delta z) = \frac{1}{\pi\hbar} e^{-\frac{\beta_{\bar{z}}}{\hbar}\bar{z}^2 - \frac{1}{\beta_{\Delta z}\hbar}\bar{p}^2} . \tag{5.58}$$

Here we have written two different Gaussian widths $\beta_{\bar{z}}$ and $\beta_{\Delta z}$ for respectively $\bar{z}$ and Δz. Of course in reality we have $\beta_{\bar{z}} = \beta_{\Delta z} = \beta$, but retaining the distinction clarifies the

[7] Alternatively, one could express the Green's function and the initial state in momentum representation, and argue that the latter is smooth and can be taken out of the integral by stationary phase approximation.

[8] In this case, the matrix element weighting the density of states is the probability of exciting an electron from the ground state to a semiclassical energy level. Its expression involves the quantum eigenstate of the ground state, which is very localized around the nucleus. Note however that the similarity is somewhat limited, as the expression for the photoabsorption spectra is much more complicated than mere momentum wave functions (it involves matching the semiclassical Green's function to a quantum one in the vicinity of the nucleus). See also Bogomolny (1989).

following discussion. The action is $\bar{S}(\bar{z},\Delta z) = S(\bar{z}-\Delta z/2, \bar{z}+\Delta/2)$, and its quadratic expansion around a point $(\bar{z}_0, \Delta z_0)$ reads:

$$\begin{aligned}\bar{\mathcal{S}}_2(\bar{z},\Delta z) &= \bar{S}_0 + \Delta p_z^0 \delta\bar{z} + \bar{p}_z^0 \delta\Delta z \\ &+ \frac{1}{2m_{12}}\left[\delta\bar{z}^2(\mathrm{Tr}M-2) + \delta\bar{z}\delta\Delta z(m_{22}-m_{11}) + \frac{1}{4}\delta\Delta z^2(\mathrm{Tr}M+2)\right] \quad (5.59)\end{aligned}$$

with $\delta\bar{z} = \bar{z} - \bar{z}_0$ and $\delta\Delta z = \Delta z - \Delta z_0$.

The idea is to apply the SPA method to the integral (5.25) $\mathcal{I} \propto \int \Delta z \int \bar{z}\, \bar{A}(\bar{z},\Delta z)$ $\exp[i\bar{\mathcal{S}}_2(\bar{z},\Delta z)/\hbar]$, i.e., with respect to the variables (5.56). The SPA condition reads:

$$\left\{\begin{array}{l} \bar{p}_z^0 = -\frac{1}{2} i\beta_{\Delta z}\Delta z_0 \\ \Delta p_z^0 = -2i\beta_{\bar{z}}\bar{z}_0 \quad . \end{array}\right. \quad (5.60)$$

In Eckhardt *et al.*(Eckhardt *et al.* 1992), one assumes the Wigner transform to be smooth as a function of $(\bar{z},\bar{p}_z)$. This corresponds to the case $\beta_{\bar{z}} \to 0$ and $\beta_{\Delta z} \to \infty$, which gives for (5.60):

$$\textbf{POs}\ :\quad \left\{\begin{array}{l} \Delta z_0 = 0 \\ \Delta p_z^0 = 0 \quad , \end{array}\right. \quad (5.61)$$

that is, **periodic orbits (POs)**. Hence POs arise naturally when one consider a smooth Wigner transform; as $\bar{A}(\bar{z},\Delta z)$ is its Fourier transform [see eq. (B.7)], it is smooth in $\bar{z}$, but *localized* in Δz. This corresponds to a "local" operator, in the sense that $\bar{A}(\bar{z},\Delta z) \sim \bar{a}(\bar{z})\delta(\Delta z)$. This also enables one to recover the Gutzwiller trace formula, via $\hat{A} \to \mathbb{1} \Rightarrow \bar{A}(\bar{z},\Delta z) \to \delta(\Delta z)$.

Things are different for the RTD. Bardeen's observable, which is written as a projector over some initial state, is the product two functions depending separately on z and z', and *cannot* have the property of being simultaneously smooth in $\bar{z}$ and localized in Δz: either it is localized in both, or it is smooth is both. One cannot change $\beta_{\bar{z}}$ and $\beta_{\Delta z}$ independently. This fact was noted by Zobay and Alber (1993) in their work on Frank-Condon molecular transitions, which involved very similar equations.

Nevertheless, it is still fruitful to consider periodic orbits for the RTD. Putting (5.55) in (5.36), one finds

$$\begin{aligned}\Gamma_{\mathrm{PO}}(z^0,p_z^0) &= -\frac{\beta}{2\mathcal{D}}\left\{ z_0^2\left[-2m_{21} - i\beta(\mathrm{Tr}M-2)\right] + \frac{1}{\beta^2}(p_z^0)^2\left[-i\beta(\mathrm{Tr}M-2) + 2\beta^2 m_{12}\right]\right. \\ &\left. -2z_0 p_z^0\left[m_{22}-m_{11}\right]\right\} \quad . \quad (5.62)\end{aligned}$$

This formula is equivalent to Equation (19) of Narimanov and Stone (1999). An important subset of POs are TS, and have $p_z^0 = 0$ **(TSPOs)**. As mentioned above, TSPOs are

identical to TSNOs, and therefore give the same contribution:

$$\Gamma_{\mathrm{TSPO}}(z_0) = -\frac{\beta}{1-\delta} z_0^2 \quad . \tag{5.63}$$

We call this expression **the PO/NO formula.**

For the hard limit, one can show that an expansion in $\beta_{\bar{z}}$ and $1/\beta_{\Delta z}$ gives

$$\mathcal{D}_{\mathrm{HL}} \to \beta(\mathrm{Tr}M - 2)/2i \quad , \quad \Gamma_{\mathrm{HL}} \to -\beta_{\bar{z}} \bar{z}_0^2 - \frac{1}{\beta_{\Delta z}} (\bar{p}_z^0)^2 \quad . \tag{5.64}$$

This corresponds to the formula for semiclassical matrix elements proposed in Eckhardt *et al.* (1992), that was derived for an observable which is smooth in phase space. This formula is basically the GTF weighted by the Wigner transform calculated for each PO.[9] To get the hard limit directly from the integration (5.25), one neglects the variations of $e^{-\beta \bar{z}^2/\hbar}$ over the integral (i.e., use its value at the PO) and neglects the quadratic variation of S due to Δz. The integration of the linear term in S due to Δz with $e^{-\beta \Delta z^2/(4\hbar)}$ is a Fourier transform, which gives the Wigner part $e^{-(p_z^0)^2/(\beta\hbar)}$. The integration over the variations of the action due to $\bar{z}$ gives the $\mathrm{Tr}M - 2$ prefactor, as in the GTF. Alternatively, one can work in phase space and apply the SPA to (B.9), neglecting the variations of the Wigner function W in the integral. Note finally that the hard limit formula for POs expresses the heuristic approach that we used in chapter 3.

5.2.5 Average orbits (AOs)

For the sake of completeness, we mention here the last possibility for neglecting one element of (5.43). One considers the case of a Wigner transform that is very localized in $\bar{z}$ and $\bar{p_z}$. This corresponds to $\beta_{\bar{z}} \to \infty$ and $\beta_{\Delta z} \to 0$, which gives for (5.60):

$$\mathbf{AO} \; : \quad \begin{cases} \bar{z}_0 = 0 \\ \bar{p}_z^0 = 0 \quad . \end{cases} \tag{5.65}$$

We call such trajectories **average orbits (AOs)**, but shall not write nor study their contribution. It is interesting to note that for TSAOs, one has $z_0 = z_0' = 0$, which means that TSAOs are identical to TSCCOs.

[9] The result in Eckhardt *et al.* (1992) contains the *average* of the Wigner function taken along the path of the PO. In our case, the Bardeen cut at $x = x' = 0$ means that we need to evaluate the Wigner function only at the starting and final points of the PO.

5.2.6 Minimal orbits (MOs)

Narimanov and Stone (1999) proposed the CCOs in order to extend the PO formula to regions where one has no real POs (also called "ghost regions"), while avoiding the problem of complex dynamics raised by SOs. They also proposed an extension of the CCO formula in terms of time-symmetric closed orbits which had a minimal momentum transfer $\Delta p_z = -2p_z$, i.e., $\partial(\Delta p_z)/\partial z = 0$. The argument was that the Wigner transform in the PO formula has a Gaussian damping that kills the contribution of trajectories with p_z that are not small. This is the only proposed semiclassical formula for the RTD that we have not tested by comparison with quantum calculations. Instead, we will propose and test another formula which is based on a similar idea.

The steepest-descent method applied on (5.19) prescribes finding an expansion point which makes the function $\varphi_2(z, z')$ stationary. This can be achieved if one can find a point (z_0, z'_0) such that the linear term $\boldsymbol{\xi}^{\mathrm{T}}\boldsymbol{\gamma}$ in (5.27) vanishes *for all* $\boldsymbol{\gamma} = (z - z_0, z' - z'_0)$, i.e., $\boldsymbol{\xi}(z_0, z'_0) = (-\beta z_0 - ip_z^0, -\beta z'_0 + ip_{z'}^0) = (0, 0)$. As already mentioned, this requires complex trajectories. The idea here is to find the *real* trajectory which *minimizes* $\boldsymbol{\xi}^{\mathrm{T}}(z_0, z'_0)$ and therefore should gives the *minimal linear term* in (5.28). This is in some sense the best *real approximation* of the complex stationary points (the SOs). Defining

$$\mathcal{L}(z, z') = \left|\boldsymbol{\xi}^{\mathrm{T}}\boldsymbol{\xi}(z, z')\right|^2 = \beta^2\left[z^2 + z'^2\right] + p_z^2 + p_{z'}^2 \quad , \tag{5.66}$$

one will look for

$$0 = \frac{1}{2}\frac{\partial \mathcal{L}}{\partial z} = \beta^2 z - \frac{p_z m_{11} + p'_z}{m_{12}} \tag{5.67}$$

$$0 = \frac{1}{2}\frac{\partial \mathcal{L}}{\partial z'} = \beta^2 z' + \frac{p_z + p'_z m_{22}}{m_{12}} \quad . \tag{5.68}$$

The second equalities were derived using the relations found in Appendix A.2. This prescription defines **minimal orbits (MOs)**:

$$\textbf{MO} : \quad \begin{cases} z'_0 = -m_{22} z_0 + \frac{m_{21}}{\beta^2} p_z^0 \\ p_{z'}^0 = \beta^2 m_{12} z_0 - m_{11} p_z^0 \end{cases} \quad . \tag{5.69}$$

The contribution of MOs to the current will be given by using (5.36) with the $\{z_0, p_z^0; z'_0, p_{z'}^0\}$ of the MO. Again, one finds that the most important MOs are TS. **TSMOs** have

$$p_z^0 = z_0 \beta^2 \frac{m_{12}}{m_{11} - 1} = z_0 \beta |\delta| \quad . \tag{5.70}$$

Their contribution will be calculated with (5.40).

5.2.7 Summary of the formulae

All the formulae mentioned above (except the HL) are identical if the action S is exactly quadratic $S \equiv \mathcal{S}_2$, which is equivalent to having zero third and higher derivatives of S. This follows the trivial fact that a quadratic expansion of a quadratic function around any point is exact. We shall write explicitely the quadratic expansion of a SO around a PO or a CCO in section 8.4.

We show a summary of the different types of orbits and the expression of the related semiclassical formulae in Table 5.1.

One can also see Fig. 9.1 in page 204. It is a schematic representation of the different semiclassical formulae. It shows the different levels of approximations: (*i*) none (SO formula), (*ii*) at the stationary phase condition only (MO and the intermediate PO, NO, CCO and AO formulae), indicated by [COND] in the figure, and (*iii*) at both the stationary phase condition and integration (hard limit formulae) [COND + INT]. It also shows the regimes where the different orbits should be used, with respect to the relative localization scales of the Green's operator $\hat{G}$ and the observable $\hat{A}$.

5.3 Application to the RTD

5.3.1 $\theta = 0°$ and conventions

It is worth considering the case $\theta = 0°$. In this case, the main (TS)PO is the straight traversing orbit t_0, which has $(z_0 = 0, p_z^0 = 0)$. Hence this PO is identical to the CCO, the SO and the MO. Although there are other orbits off-center, they do not contribute to the current. Therefore, all the different formulae above give the same current

$$\mathcal{I}_0 = 2\sqrt{\frac{\beta\pi\hbar p_0^2}{-\mathcal{D}_0}}e^{iS_0/\hbar} \quad , \tag{5.71}$$

where the subscripts 0 refer to t_0 at 0°. Denoting its period by T_0, its scaled monodromy matrix reads

$$\tilde{M}_0 = \begin{pmatrix} \cos(T_0/m) & \sin(T_0/m) \\ -\sin(T_0/m) & \cos(T_0/m) \end{pmatrix} \Rightarrow |\mathcal{D}_0| = 2B \quad . \tag{5.72}$$

Hence the semiclassical current at $\theta = 0°$ has *constant* amplitude for a given B (it does not change with ϵ).

For $\theta > 0°$, one has usually the case where *only one* orbit (be it PO, SO, etc.) contributes to the oscillations of the current of a given voltage period. Hence, we shall always

Orbit	Def	Γ	$I^{\rm HL}/(2\pi\hbar\sqrt{p_z p_z'})$	Shape
NO	$\begin{cases} p_z = 0 \\ p_z' = 0 \end{cases}$	$-\frac{\beta}{2\mathcal{D}}\left\{ z^2\left[-m_{21} - i\beta m_{11}\right] + (z')^2\left[-m_{21} - i\beta m_{22}\right] + 2i\beta z z' \right\}$	$\frac{1}{\sqrt{m_{21}}}\phi(z)\phi^*(z')e^{iS/\hbar}$	
$TSNO \equiv TSPO$	$\begin{cases} z = z' \\ p_z = p_z' = 0 \end{cases}$	$-\frac{\beta}{1-\delta}z^2$	*	
PO	$\begin{cases} z = z' \\ p_z = p_z' \end{cases}$	$-\frac{\beta}{2\mathcal{D}}\left\{ z^2\left[-2m_{21} - i\beta(\mathrm{Tr}M - 2)\right] + \frac{1}{\beta^2}p_z^2\left[-i\beta(\mathrm{Tr}M - 2) + 2\beta^2 m_{12}\right] - 2zp_z\left[m_{22} - m_{11}\right] \right\}$	$\sqrt{\frac{2\pi i\hbar}{\mathrm{Tr}M - 2}}W(z, \bar{p}_z)e^{iS/\hbar}$	
CCO	$\begin{cases} z = 0 \\ z' = 0 \end{cases}$	$-\frac{1}{2\beta\mathcal{D}}\left\{ p_z^2\left[-i\beta m_{22} + \beta^2 m_{12}\right] + p_z'^2\left[-i\beta m_{11} + \beta^2 m_{12}\right] + 2i\beta p_z p_z' \right\}$	$\frac{1}{\sqrt{-m_{12}}}\tilde{\phi}(p_z)\tilde{\phi}^*(p_z')e^{iS/\hbar}$	
$TSCCO \equiv TSAO$	$\begin{cases} z = z' = 0 \\ p_z' = -p_z \end{cases}$	$\frac{1}{\beta}\frac{\delta}{1-\delta}p_z^2$	*	
AO	$\begin{cases} z' = -z \\ p_z' = -p_z \end{cases}$	*	*	
MO	$\begin{cases} z' = -m_{22}z + \frac{m_{21}}{\beta^2}p_z \\ p_z' = \beta^2 m_{12}z - m_{11}p_z \end{cases}$	Equation (5.36)	*	
$TSMO$	$\begin{cases} z' = z \\ p_z' = -z\beta\lvert\delta\rvert = -p_z \end{cases}$	$-\frac{\beta}{1-\delta}\left\{ z^2 - \left[\frac{1}{\beta^2}p_z^2 - 2\frac{i}{\beta}zp_z\right]\delta \right\}$	*	
SO	$\begin{cases} p_z = i\beta z \\ p_z' = -i\beta z' \end{cases}$	$-\frac{\beta}{2}\left[z^2 + z'^2\right]$	*	
$TSSO$	$\begin{cases} z' = z \\ p_z' = -i\beta z = -p_z \end{cases}$	$-\beta z^2$	*	

Table 5.1: Summary of the semiclassical formulae: type of orbit, its definition, argument Γ of the exponential in (5.35), corresponding hard limit formula and an example of the shape in the (x, z) plane.

consider the semiclassical contribution of **one** orbit. We have already named the important POs of the RTD $(t, s, 1{:}3)$. We label the orbits according to their *type* and the *related PO*. We usually drop the TS, as most of the contributing orbits are time-symmetric. For example, the SO related to t_0 is labelled t_0–SO, while the CCO related to s' is referred to as s'–CCO.

5.3.2 Normalization and $I(V)$ traces

From this point we use atomic units ($\hbar = e = 1$). As for the quantum calculations and the experimental traces, we normalize the current J to the amplitude A_0 of the current at $\theta = 0°$. Neglecting overall phases, we write

$$I_{\rm SC}[\theta] := \frac{J[\theta]}{A_0} \simeq \mathbf{Re}\sqrt{\frac{2\beta}{\mathcal{D}}}e^{iS+\Gamma} = A_{\rm SC}\cos(\Sigma+\nu) \quad , \tag{5.73}$$

with

$$A_{\rm SC} = \sqrt{\frac{2\beta}{|\mathcal{D}|}}e^{\mathrm{Re}\,\Gamma} \quad , \quad \Sigma = S + \mathbf{Im}\,\Gamma \tag{5.74}$$

and $\nu = -\arg(\mathcal{D})/2$. Here we have neglected the momenta p_x and p'_x as they are slowly varying functions of V or ϵ, and because we neglected them in the quantum results. We used $|\mathcal{D}_0| = 2B$ for 0°. Also, we did not write the sum over all expansion trajectories, as usually we consider the individual contribution of one orbit.

For complex trajectories the action is complex $[S = S_R + iS_I]$ and one has

$$A_{\rm SC} = \sqrt{\frac{2\beta}{|\mathcal{D}|}}e^{-S_I+\mathrm{Re}\,\Gamma} \quad , \quad \Sigma = S_R + \mathbf{Im}\,\Gamma \quad . \tag{5.75}$$

First we want to consider $\boldsymbol{I(V)}$ **traces**, which are obtained keeping B and $R = E/V$ constant. We show an example of $I(V)$ traces in Fig. 5.1, which corresponds to period-one (P1) oscillations. We show the trace only over the experimental range, i.e., $V \in [0.1, 1.2]$V. The amplitude at $\theta = 0°$ is constant, and equal to one because of the normalization (5.73). The amplitude at $\theta = 11°$ varies, reflecting the change in the dynamics of the SO t_0–SO responsible for the semiclassical current. The voltage periods $\Delta V(V)$ are calculated from each pair of consecutive peaks. They increase slowly over the V range[10]. Hence the Fourier transform of $I(V)$ (calculated using a Welch window) shows a wide peak. In general, we do not use FT to get periods and amplitudes from $I(V)$ traces, as they are far less clean

[10]This illustrates the intuitive argument: $V \nearrow \Rightarrow E \nearrow \Rightarrow T \searrow \Rightarrow \Delta E \nearrow \Rightarrow \Delta V \nearrow$, where T is the period or the (real part of the) total time of the orbit under consideration (t_0–SO in this case). It is based on the GTF's density of states picture, where energy levels are separated by $\Delta E = 2\pi/T$, and will be discussed in subsection 5.3.4. It is shown by the long-dashed line (G) in Fig. 5.1 (d).

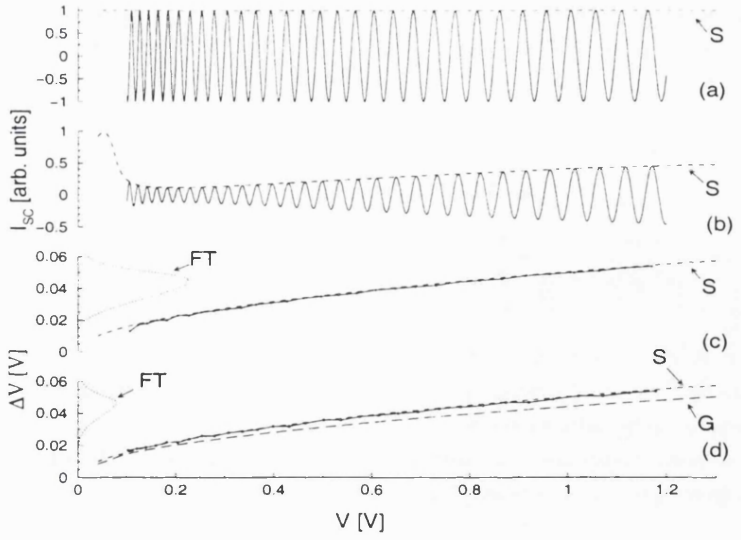

Figure 5.1: Semiclassical current-voltage traces $I_{SC}(V)$ for P1 at $B = 6$ T : (a) $\theta = 0°$ and (b) $\theta = 11°$, generated by t_0 $-SO$. We also show the amplitudes calculated from scaled dynamics [S] (see subsection 5.3.4). Corresponding voltage periods $\Delta V(V)$: (c) $\theta = 0°$ and (d) $\theta = 11°$ (solid line with circles). We also show Fourier transforms of $I(V)$ [FT] and voltage periods calculated analytically from the scaled dynamics (5.91) [S]. Curve [G] in (d) is calculated from arguments following the GTF (5.92). Here we used the saddle orbit formula given by t_0 $-SO$.

than the FT one can get using the scaled dynamics. Here one could compare directly the semiclassical trace with the experimental traces and/or quantum calculations. Note that in order to generate a semiclassical trace, one has to find the trajectory for all V in the experimental range; a different B will demand that all the trajectories are found again. This redundancy can be avoided by using scaled dynamics, which can be used to get information about the $I(V)$ traces, as explained in subsection 5.3.4. Such results are the dashed lines in Fig. 5.1.

5.3.3 Scaling and $I(\mathcal{N})$ traces

The scaling property of the classical dynamics (see subsection 3.1.2) and quantum mechanics (see subsection 4.1.3) of the RTD has also a deep influence on the semiclassical formulae. We shall use the scaled variables $\tilde{\boldsymbol{p}}, \tilde{M}$ and $\tilde{S}$, and see that actually the final formulae can also be scaled with respect to B. In general, the rule is to use scaled variables and substitute β by $\cos\theta$. However, B is not really the appropriate variable describing the semiclassical regime (the "effective $\hbar$"). The latter is derived for $\theta = 0°$ in a first order

approximation in V. First we write the classical action of the traversing orbit at $\theta = 0°$:

$$S_0 = \frac{4L}{3V}\sqrt{2m}\left[(E+V)^{3/2} - E^{3/2}\right] \overset{V \ll E}{\simeq} 2L\sqrt{2mV(R+1/2)} \quad , \tag{5.76}$$

where we used $R = E/V$. We also define[11]

$$\mathcal{N} := \frac{S_0}{2\pi} = \frac{L}{\pi}\sqrt{2mV(R+1/2)} =: C_N\sqrt{V} \quad . \tag{5.77}$$

In the WKB picture, the wave function is related to $e^{iS_0/\hbar}$ and therefore has $\mathcal{N}$ nodes across the well. Hence our effective $\hbar$ is given by

$$\hbar_{\text{eff}} = 1/\mathcal{N} \quad . \tag{5.78}$$

We shall use the same definition in the non-integrable case ($\theta, B > 0$). This is justified because most of the action in S comes from the motion across the well (along x), which is similar to the motion at $\theta = 0°$. Hence we define

$$\hat{S}(\epsilon) := \frac{S(B,V)}{S_0(V)} = \frac{S}{2\pi\mathcal{N}} = \frac{\tilde{S}(\epsilon)}{2L\sqrt{2mL\epsilon(R+1/2)}} \quad , \tag{5.79}$$

where we used $S = B\tilde{S}$. The link between B and $\mathcal{N}$ is given by

$$B[\mathcal{N},\epsilon] = \mathcal{N}\frac{2\pi}{2L\sqrt{2mL\epsilon(R+1/2)}} \quad . \tag{5.80}$$

In the experiments, the oscillations range from $V = 0.1$ V to $V = 1.1$ V with an average $\bar{V} = 0.55$ V. This corresponds roughly to $\mathcal{N} \in [12, 43], \bar{\mathcal{N}} = 27$. For each ϵ, this corresponds to a *different* B range, given by $B[\mathcal{N},\epsilon]$. $\hat{S}$ is *constant* as $\mathcal{N}, V$ or B varies, provided that ϵ is kept constant. We find that $\hat{S}$ is *approximately* constant for one orbit as ϵ varies; it is also approximately an integer, and counts the number of circuits (from emitter back to emitter) of a given trajectory, whatever ϵ is. Hence $\mathcal{N}$ counts the number of nodes of the wave function whatever ϵ or B, and can be thought of as an "effective" principal quantum number. It will play the role of the inverse of effective $\hbar$. This approximation scheme is surprisingly efficient, as shown e.g. in Table 4.1.

As the actual frequency of the current oscillations is given by Σ, we define

$$\hat{\Sigma} =: \frac{\Sigma}{2\pi\mathcal{N}} = \hat{S}_R + \mathbf{Im}\,\hat{\Gamma} \quad . \tag{5.81}$$

Then we can write the current in terms of $\mathcal{N}$:

$$I_{\text{SC}}(\mathcal{N};\epsilon) \quad = \mathbf{Re}\sqrt{\frac{2\cos\theta}{\tilde{\mathcal{D}}(\epsilon)}}e^{B[\mathcal{N},\epsilon](i\tilde{S}+\tilde{\Gamma})} = A_{\text{SC}}(\mathcal{N};\epsilon)\cos\left[2\pi\mathcal{N}\hat{\Sigma}(\epsilon)+\nu\right] \tag{5.82}$$

[11] The same definition is derived in a quantum mechanical approach in subsection 4.1.3. Note also that the condition $V \ll E$ in (5.76) is not satisfied experimentally, as $R = 0.15$.

with the semiclassical amplitude

$$A_{\rm SC}(\mathcal{N};\epsilon) = \sqrt{\frac{2\cos\theta}{|\tilde{\mathcal{D}}(\epsilon)|}} e^{B[\mathcal{N},\epsilon](-\tilde{S}_I + \mathrm{Re}\,\tilde{\Gamma})} \quad . \tag{5.83}$$

We used the scaled quantities

$$\tilde{\mathcal{D}} := \frac{\mathcal{D}}{B} \quad , \quad \tilde{\Gamma} := \frac{\Gamma}{B} \quad , \quad \tilde{S} = \frac{S}{B} \quad , \tag{5.84}$$

$$\tilde{\mathcal{D}} = -\tilde{m}_{21} - i\cos\theta \mathrm{Tr}M + \cos^2\theta \tilde{m}_{12} \quad , \tag{5.85}$$

$$\begin{aligned}\tilde{\Gamma}(z,z') = & -\frac{\cos\theta}{2\tilde{\mathcal{D}}} \times \Big\{ z^2\left[-\tilde{m}_{21} - i\cos\theta\tilde{m}_{11}\right] + z'^2\left[-\tilde{m}_{21} - i\cos\theta\tilde{m}_{22}\right] + 2i\cos\theta zz' \\ & + \frac{1}{\cos^2\theta}\tilde{p}_z^2\left[-i\cos\theta\tilde{m}_{22} + \cos^2\theta\tilde{m}_{12}\right] + \frac{1}{\cos^2\theta}\tilde{p}_{z'}^2\left[-i\cos\theta\tilde{m}_{11} + \cos^2\theta\tilde{m}_{12}\right] \\ & + 2\frac{i}{\cos\theta} z\tilde{p}_z\left[i\cos\theta\tilde{m}_{22} - \cos^2\theta\tilde{m}_{12}\right] + 2\frac{i}{\cos\theta} z'\tilde{p}_{z'}\left[-i\cos\theta\tilde{m}_{11} + \cos^2\theta\tilde{m}_{12}\right] \\ & + 2i\frac{1}{\cos\theta}\tilde{p}_z\tilde{p}_{z'} + 2z\tilde{p}_{z'} - 2z'\tilde{p}_z \Big\} \quad . \end{aligned} \tag{5.86}$$

The idea is to solve the scaled dynamics for all ϵ once in order to calculate the scaled [~] quantities. For each ϵ, one generates an **oscillatory current $I(\mathcal{N})$** ranging from $\mathcal{N}_{\rm min} = 12$ to $\mathcal{N}_{\rm max} = 43$. We show in Fig. 5.2 P1 oscillations of the current (generated by t_0–SO) for $\theta = 11°$. In the regular case (a), the amplitude of the oscillations is almost constant. In the more chaotic case (b), the damping is very strong. In both cases the frequency of the oscillations is constant.

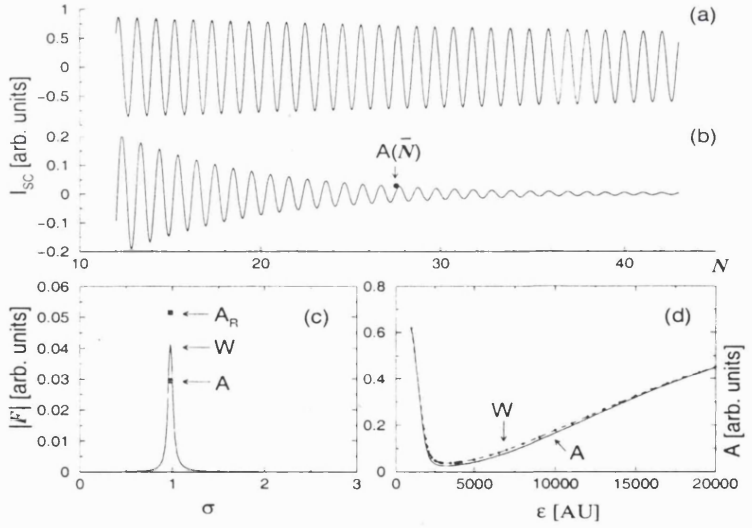

Figure 5.2: Semiclassical $I_{\rm SC}(\mathcal{N})$ traces for $\theta = 11°$: (a) $\epsilon = 40000$ and (b) $\epsilon = 4000$, generated by t_0–SO. (c) Fourier transform of (b)[W]; semiclassical amplitude A at the average $\bar{\mathcal{N}}$ [A] and peak of a rectangular FT [A_R]. (d) Comparison over a large range of ϵ of the amplitudes given by $A_{\rm SC}(\bar{\mathcal{N}})$ [A] and by the peaks of the Welch FT (dashed line with dots [W]).

Then we perform a Fourier transform over the range $\Delta\dot{\mathcal{N}} = \mathcal{N}_{\max} - \mathcal{N}_{\min}$ using a Welch window $w(\mathcal{N})$ (Press *et al.* 1989):

$$\mathcal{F}(\sigma) := \frac{1}{\Delta\mathcal{N}} \int_{\mathcal{N}_{\min}}^{\mathcal{N}_{\max}} d\mathcal{N} e^{2\pi i \sigma \mathcal{N}} I_{\mathrm{SC}}(\mathcal{N}) w(\mathcal{N}) \quad . \tag{5.87}$$

As the frequency of oscillation $\hat{\Sigma}$ is constant over that range, the Fourier transform (FT) is very clean, showing precise narrow peaks where $\sigma = \hat{\Sigma}$. Using a rectangular window $w(\mathcal{N}) \equiv 1$, one can show that the value of the FT at the peak is the amplitude taken at the mid point $\bar{\mathcal{N}}$ multiplied by a function ϱ arising from the exponential damping of the amplitude:

$$\mathcal{F}(\sigma = \hat{\Sigma}) = A_{\mathrm{SC}}(\bar{\mathcal{N}}, \epsilon)\varrho =: A_R \tag{5.88}$$

$$\varrho = \frac{\sinh(\Lambda\Delta\mathcal{N}/2)}{\Lambda\Delta\mathcal{N}} \quad , \quad \Lambda := 2\pi\left(-\hat{S}_I + \mathbf{Re}\,\hat{\Gamma}\right) \quad . \tag{5.89}$$

In Fig. 5.2 (c) we show the Welch FT of (b), together with the (analytical) amplitudes $A_{\mathrm{SC}}(\bar{\mathcal{N}})$ and the rectangular FT peak. The frequencies (σ) coincide, but we see that the amplitudes are quite different. We show in (d) the evolution of the peak of the Welch FT and the amplitude A_{SC} as ϵ changes. We see that although they differ by up to 30% relative to each other, their "global" difference relative to the maximal amplitude over the range of ϵ is negligible (2%). As generating oscillatory current and performing FTs is much more time-consuming than evaluating A_{SC} at the average $\bar{\mathcal{N}}$, we shall use the latter method from now on.[12]

5.3.4 Voltage periods

One can also use the scaled dynamics to get information about $I(V)$ traces. The amplitude of the $I(V)$ modulation is given by $A_{\mathrm{SC}}(\mathcal{N}, \epsilon)$, where one expresses $\mathcal{N}$ and ϵ in terms of V and the constant B. This is the formula used in Fig. 5.1 (a) and (b).

One can get an expression for the voltage periods either appearing in the unscaled $I(V)$ traces or related to the scaled $I(\mathcal{N})$. One has two consecutive maxima $\{V, V + \Delta V\}$ in the trace (neglecting the variation of ν) when

$$2\pi = \Delta[\Sigma] = \Sigma(V + \Delta V) - \Sigma(V) = \Delta\left[2\pi\hat{\Sigma}(\epsilon)\mathcal{N}(V)\right] = 2\pi\hat{\Sigma}\frac{C_N}{2\sqrt{V}}\Delta V \quad . \tag{5.90}$$

[12] We *did* use Fourier transforms of the semiclassical oscillatory current in problematic regions, such as the "ghost" region at $\theta = 11°$ (section 8.2) and the region involving non-isolated POs at $\theta = 27°$ (subsection 6.2.2).

This is exact in the scaled picture (where one varies $\mathcal{N}$ keeping ϵ constant). In the unscaled picture (where V varies for constant B), one neglects the small variation of $\hat{\Sigma}$ with ϵ. Then one obtains

$$\Delta V = \frac{2\mathcal{N}}{C_N^2 \hat{\Sigma}} = \frac{2\sqrt{V}}{C_N \hat{\Sigma}(\epsilon)} \quad . \tag{5.91}$$

One will use the first relation in the scaled picture, with the average $\bar{\mathcal{N}}$. The second relation shows that in the unscaled picture $\Delta V \propto \sqrt{V}$. This is the relation, calculated from scaled dynamics, that we used to get the voltage periods analytically in Fig. 5.1 (c) and (d).

A more naive model, mentioned in the footnote of page 119, is based on the GTF's density of states picture. One considers that the voltage period follows the separation of the energy levels, which is given by the real part T of the total time of the orbit:

$$\Delta V = \Delta E/R = 2\pi/(RT) \quad . \tag{5.92}$$

This is however incorrect for two reasons. (i) The current oscillations are not given by S as in the density of states, but by Σ. (ii) The density of states formula works for *constant* V, and uses $\partial S(E,B,V)/\partial E = T$, while in our case we should evaluate this derivative with constant R. A very primitive model for $B = 0$ shows that $\Delta V = \Delta E/(R + 1/2) = 2\pi/[T(R+1/2)]$. This approximation is actually fairly good, and is shown in Fig. 5.1 (d). It is based on a first order quantum perturbation theory in $1/R$ (!), using infinite square well sine functions. The classical counterpart of that model –which has already been used for the derivation of $\mathcal{N}$ in the previous subsection– is consistent, showing from (5.76) that $\partial S(R,B,V)/\partial V \simeq T(R + 1/2)$. Note that the experimental groups worked within this periodic orbit framework, and have proposed an estimate of the relationship between the voltage period, the energy period and the period of a PO. The Bell Labs group (Muller *et al.* 1995) used $\Delta V = \Delta E/0.47$, while the Nottingham group (Fromhold *et al.* 1994) used $\Delta V = \Delta E/0.40$.

5.3.5 Semiclassical regime

We defined $\mathcal{N}$ (5.77) as an approximate way of counting the number of oscillations of the wave function along the x direction. However, the integrals (5.19), which we have to evaluate semiclassically, involve the z axis only. We can define a similar "pseudo" quantum number in this direction, neglecting the voltage and considering that all the energy on the

left barrier is in the z mode and is quantized by the effective magnetic field $\beta = B\cos\theta$:

$$N_z := \frac{\mathcal{A}}{2\pi\hbar} = \frac{mE}{\hbar\beta} = \frac{S_z}{\hbar} = E\frac{2\pi}{\hbar\Omega} = \epsilon BmLR/\hbar \quad . \tag{5.93}$$

One uses the Weyl approach of counting states, and takes the ratio between the area $\mathcal{A}$ of the surface of section (SoS) on the left barrier and the phase space occupied by each quantum state ($2\pi\hbar$). The WKB picture gives an equivalent result; we take the ratio with $\hbar$ of the typical action S_z of a trajectory having a cyclotron motion *in* the SoS, with period $2\pi/\Omega = 2\pi m/\beta$.

For a fixed $\mathcal{N}$, N_z *changes* with ϵ (e.g., $N_z = 2-12$ for $\epsilon = 1000-40000$ and $\mathcal{N} = 27$). We have indicated the area occupied by $\hbar$ in Fig. 4.12, where we show a SoS and a Wigner distribution. As each state occupies an area of $2\pi\hbar$, we see that we can fill approximately $N_z \simeq 8$ states in the SoS.

Another illustration of the fact that *we are not* in a high semiclassical regime in the z degree of freedom in shown in Fig. 5.3. We see that neither the oscillations of the Green's function [$\cos(S/\hbar)$] nor the Gaussian initial state ($e^{-\beta z_0^2/\hbar}$) are semiclassical. It is very surprising that the steepest-descent method, which assumes many oscillations and a strong Gaussian damping across the range of integration, is efficient in this case.

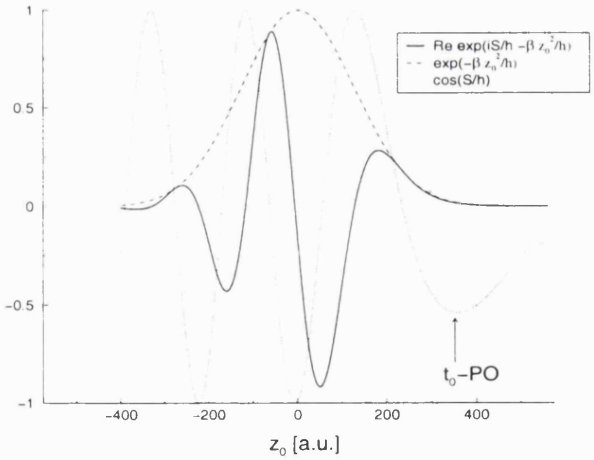

Figure 5.3: Function appearing in the semiclassical integral (5.19): Re $e^{iS(z_0)/\hbar - \beta z_0^2/\hbar}$. We also show $e^{-\beta z_0^2/\hbar}$ and $\cos[S(z_0)/\hbar]$. We used a family of real time-symmetric closed orbits around t_0 at $\theta = 11°, \epsilon = 7000$ (i.e., $z_0' = z_0$ and we have only *one* parameter), which only exist for $z \in [-400, 500]$ a.u.. Here we use atomic units: $\hbar = 1$.

Note that the x degree of freedom is not very semiclassical either, as $\mathcal{N} = 10-40$ in the experiments. This can be contrasted to spectroscopy experiments of hydrogen in external fields, which achieve an effective $\hbar$ of around $1/100$ (Honig and Wintgen 1989). Hence, the

experimental RTD is *not very semiclassical*, and the success of the semiclassical theories in chapter 6 is a rather good surprise.

Chapter 6

COMPARISONS: SC vs. QM

In this chapter we shall apply the semiclassical (SC) formulae developed in chapter 5 and compare them with quantum mechanical (QM) calculations of the current. We shall consider the *amplitudes* and *frequencies* of the oscillatory part of the current in their scaled version. We shall vary the dynamical parameter ϵ from regularity to chaos, offering a stringent quantitative test. The amplitudes will be normalized to the $\theta = 0°$ amplitude; we shall therefore use (5.83) for the semiclassics, and the peaks in the Fourier transform of the normalized QM current (4.14).

Here we shall consider period-one and two oscillations at $\theta = 0°, \theta = 11°, \theta = 20°$ and $\theta = 27°$. More results will be presented in chapter 7: comparisons with experimental amplitudes and frequencies, period-three at $\theta = 38°$, and period-two at $\theta = 20°$ specifically for the saddle orbit formula. Chapter 8 will propose a cubic integration and look into the relationship between periodic and saddle orbits.

6.1 Hard limit formulae

We start by testing the hard limit (HL) formulae obtained for normal (NOs) and periodic (POs) orbits. We shall not consider the hard limit for central closed orbits, which was never proposed in the literature. Note that the results are rather disappointing, as the HL theories are built on assumptions that are not fulfilled in the RTD experiments. We include them nevertheless in the discussion, as we gained some physical insight from this comparison. Also, the hard limit formula for POs corresponds to the standard semiclassical expression for matrix elements as proposed in Eckhardt (1992) and to our heuristic approach used in the qualitative interpretation of the experiments (chapter 2), quantum

calculations (4) and classical dynamics (3).

There is a normalization problem for both HL theories. As shown in Fig. 6.1 (a), they yield amplitudes which vary with ϵ at $\theta = 0°$. This conflicts with the quantum results, which show constant amplitudes. Therefore, we shall not normalize here with respect to the HL amplitude at 0°, but with respect to the correct constant $\theta = 0°$ amplitudes given by the non-HL formulae which have the full prefactor: $\tilde{\mathcal{D}}_0 = 2$ (5.72). The normalized and scaled oscillatory part of the current given by HL formulae reads

$$I_{\rm HL} = A_{\rm HL}\cos(2\pi\mathcal{N}\hat{S}) \quad , \quad A_{\rm HL} = \sqrt{\frac{2\beta}{\mathcal{D}_{\rm HL}}}e^{\Gamma_{\rm HL}} \quad . \tag{6.1}$$

Note that the frequency of the oscillations is given by the scaled action $\hat{S}$ like in the Gutzwiller trace formula (GTF), as $\Gamma_{\rm HL} \in \mathbb{R}$.

6.1.1 PO hard limit (HLPO)

This was the first semiclassical formula that we considered, following *intuitive* arguments based on a GTF for the density of states (DoS), weighted by the value of the Wigner distribution at the PO. We proposed this theory in the first version of our submitted article Saraga and Monteiro (1998b). However, the final published version contained the HLNO formula presented in the next subsection. The semiclassical amplitude for the PO hard limit formula is given by (6.1) and (5.64):

$$A_{\rm HLPO} = \sqrt{\frac{4}{{\rm Tr}M - 2}}e^{-\beta z_0^2 - (p_z^0)^2/\beta} \quad . \tag{6.2}$$

6.1.2 NO hard limit (HLNO)

While we were working on the HLPO, Bogomolny and Rouben (1998) proposed a semiclassical theory which was, in essence, the hard limit of the normal orbit formula. The amplitude in that case reads (5.49):

$$A_{\rm HLNO} = \sqrt{\frac{2\cos\theta}{\tilde{m}_{21}}}e^{-\beta[z_0^2 + (z_0')^2]/2} \quad . \tag{6.3}$$

Note that as *almost all relevant* POs are time-symmetric (see subsection 3.1:7), they are also NOs and both theories use the same time-symmetric (TS) POs. Then $z_0' = z_0, p_z^0 = 0$ and the only difference between the HLPO and HLNO formulae lies in their prefactor.

6.1.3 Comparisons

We show in Fig. 6.1 the semiclassical amplitudes $A_{\rm HLPO}$ and $A_{\rm HLNO}$ given by the two hard limit formulae, as the parameter ϵ varies from unstable (low ϵ) to regular (high ϵ)

dynamics. We compare them with the amplitudes obtained from quantum calculations. It is useful to refer also to the Figures in section 3.2, which show the behavior of the stability and the starting position z_0 as functions of ϵ.

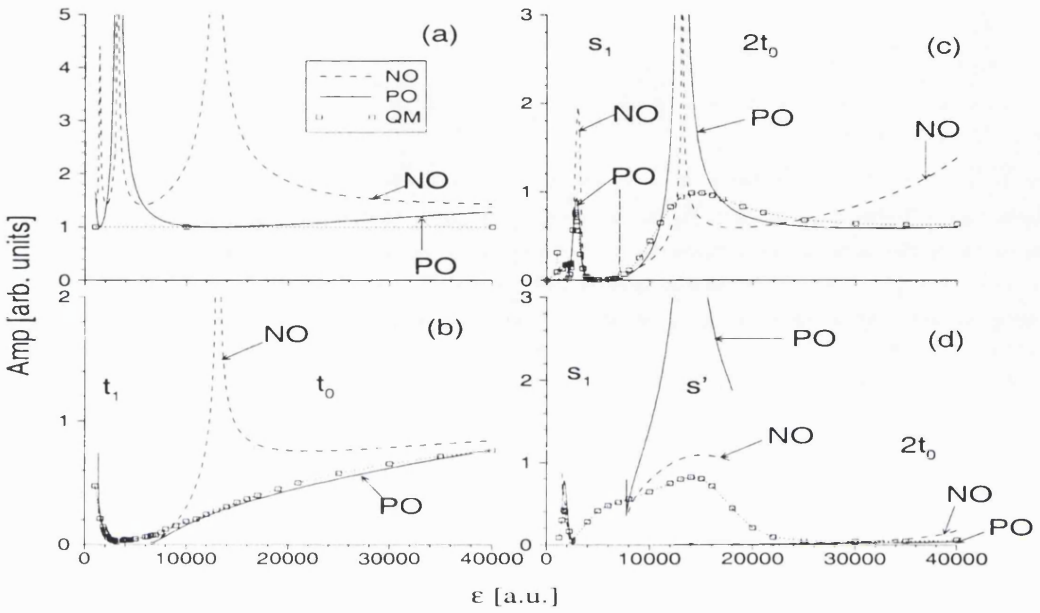

Figure 6.1: Semiclassical amplitudes of the hard limit formulae as a function of the scaled dynamics parameter ϵ. We show the hard limit normal orbit formula [NO] and the HL periodic orbit formula [PO]. For comparison, we also show the quantum amplitudes [QM]. (a) $\theta = 0°$, P1; t_0 contributions. (b) $\theta = 11°$, P1; t_0 (high ϵ) and t_1 (low ϵ) contributions. (c) $\theta = 11°$, P2; the low ϵ peak is due to s_1, the high ϵ peak to $2t_0$. (d) $\theta = 27°$, P2; the contributions come from s_1, s' and $2t_0$.

We show in (a) the period-one (P1) amplitudes at $\theta = 0°$, which come from the straight traversing PO t_0. A_{HLPO} is not constant, and diverges twice where $\mathrm{Tr}M = 2$. Similarly, A_{HLNO} diverges three times where $\tilde{m}_{21} = 0$ [see Fig. 3.1 (b) showing $\mathrm{Tr}M(\epsilon)$ and $\tilde{m}_{21}(\epsilon)$]. This is obviously wrong, as the quantum amplitudes are constant at 0°.

At $\theta = 11°$ (b), the P1 contributions come from t_0 and t_1. The HLPO amplitude is quite accurate. Its divergence at the tangent bifurcation ($\epsilon = 6540$) is very narrow and not really visible. The HLNO theory greatly overestimates the current, and shows a wide divergence at one of the pair of period-doubling bifurcations ($\epsilon = 13112$). This is surprising, as such a bifurcation yields an enhancement of the period-two (P2) signal in the DoS described by the GTF. This P1 divergence is a major failure of this model, as it conflicts seriously the idea of the current being a weighted GTF and does not correspond to the QM behavior at all. It comes from the fact that m_{21} can vanish either at a P1 tangent bifurcation or at a P2 pitchfork bifurcation where the satellite POs have $p_z = 0$

[see subsection 3.1.6]. The formula is quite accurate in the chaotic region (low ϵ). The gap in the semiclassical current between $\epsilon = 3000$ and 6500 arises from the absence of any real PO that can give P1 oscillations. This region is referred to as a "no (real) PO region", and will be discussed again later.

P2 amplitudes for $\theta = 11°$ are shown in (c). The HLNO amplitude diverges at the second period-doubling bifurcation of t_0 where $m_{21} = 0$ for both t_0 and $2t_0$. It does not diverge at the first one ($\epsilon = 12822$) where $m_{12} = 0$. It also diverges at $\epsilon = 7050$, where $m_{21}[2t_0] = 0$. This extremely narrow divergence corresponds to a P4 bifurcation ($\mathrm{Tr}M[t_0] = 0$). In the regular limit ($\epsilon \to \infty$), it does not converge towards the quantum amplitudes. The failures of this theory in this regime can be explained by the fact that the conditions for which the theory has been developed are not satisfied: the dynamics are not very chaotic. However, this theory fails as well in the more chaotic region ($\epsilon \simeq 2500$) for the s_1 contribution, where it overestimates the QM amplitude by a factor 2.

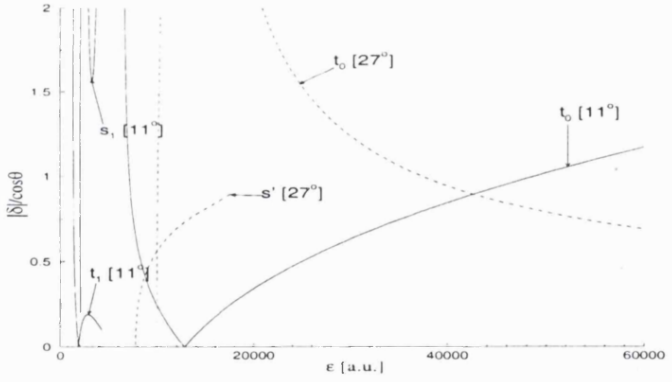

Figure 6.2: Stability coefficient $|\delta|/\cos\theta$ (5.50) for the POs at $\theta = 11°$ (solid lines) and $\theta = 27°$ (dashed lines).

We show in Fig. 6.2 the "stability coefficient" $|\delta|/\cos\theta$ for most of the P1 and P2 POs at $\theta = 11°$ and $\theta = 27°$. It has been defined in (5.50), and is a measure of the stability of the system compared to the Gaussian decay of the initial state; it should be small for the HL normal orbit formula to be valid. One sees that t_1 at 11° is the *only* PO which satisfies the condition $|\delta|/\cos\theta \ll 1$ required for the HLNO formula. Surprisingly, this relation is not satisfied by the unstable POs s_1 and s', even in the rather chaotic region at low ϵ.

The HLPO formula is altogether better. Its amplitude diverges at both P2 bifurcations —although one cannot see it with the scales used in Fig. 6.1. It approaches the quantum behavior in the regular limit, and is quite accurate for s_1 in the chaotic region.

In (d) we present the P2 amplitudes at $\theta = 27°$. Here we have two competing, non-

isolated POs ($2t_0$ and s'). Both HL theories completely underestimate the $2t_0$ contribution. This is because t_0 is off-center ($z_0 \simeq 500$ a.u.); the Gaussian damping of the HL formulae completely kills its contribution as it is proportional to $\exp(-\beta z_0^2)$. The HL formulae are simply given by the probability of the initial state being at the starting position of the PO. They cannot describe the effects of tori quantization (described in section 4.2) underlying the QM behavior, where the overlap with the initial state is significant because the outer tori extend to $z \simeq 0$. In the regular limit where tori quantization effect are very important, the HLPO theory is actually better than the HLNO one.

For s', the HLNO formula this time is better than the HLPO one, which shows a huge divergence around the synchronous pitchfork bifurcation ($\epsilon = 13600$). This is due to the metastability of s': the trace of the monodromy matrix is very close to 2, even when the PO is unstable (see subsection 3.2.4). The s_1 peak is reasonably described by both HL formulae. Again, there is a region ($5000 < \epsilon < 8000$) with no real PO accounting for the QM current. Note that we do not show P1 amplitudes at $\theta = 27°$, where both HL formulae fail badly.

6.1.4 Summary

This discussion of the HL formulae shows the following points.

1. The HLNO formula fails almost everywhere, apart for t_1 at 11° and s' at 27°.
2. Apart from s', the HLPO formula is usually better and can sometimes even give a quantitative description of the current.
3. At $\theta = 0°$ they both fail badly, because the HL prefactor is too sensitive to changes of stability.
4. Off-center stable POs are too strongly damped, because Γ_{HL} is given only by the initial state (Gaussian) evaluated at the PO.
5. They cannot describe tori quantization effect around stable POs.
6. Divergences can occur in unexpected places for HLNO.
7. Some divergences are much too wide.
8. Most of the bifurcations are too narrow to be resolved, in agreement with the quantum behavior.

9. They fail in the "no (real) PO" regions.

10. The frequency of the oscillation is given by the scaled action of the PO, and shows some discrepancy with the QM frequencies (see Fig. 6.6 in page 138).

Note that narrow divergences could in principle be removed by the use of a cubic expansion of the action in similar fashion to normal forms or uniform approximations (Schomerus and Sieber 1997). They could also extrapolate the behavior of a complex PO (ghost) beyond the tangent bifurcation where the real PO disappears. We shall present such cubic expansions for the non-HL case in section 8.3. We believe that the divergence of s' seen at $\theta = 27°$ is too "wide" to be removed by a normal form in a satisfactory manner.

6.2 Periodic/normal orbit formula

Here we discuss the improved formula expressing the current in terms of normal orbits (5.47), which was proposed in Bogomolny and Rouben (1998). As most NOs and POs are TS, this discussion is equally valid for the PO formula proposed in Narimanov *et al.* (1998b). We shall discuss their difference in subsection 6.2.4. For TSNOs, one can rewrite the (non-normalized) semiclassical current as

$$I_{\rm SC} = \sqrt{\frac{2\beta}{|\mathcal{D}|}} e^{-\beta z_0^2[1-\gamma]} \cos[S+\Delta S+\nu] \quad , \quad \gamma = \frac{|\delta|^2}{1+|\delta|^2} \quad , \quad \Delta S = \beta z_0^2 \frac{|\delta|}{1+|\delta|^2} \quad ; \qquad (6.4)$$

we refer to this expression as the *PO/NO formula.*[1] One clearly sees two key features in this formula. First the weighting due to the initial state $\sqrt{\beta/\pi}e^{-\beta z_0^2}$ is reduced via γ, enabling stable POs which are off-center (large $|z_0|$) to contribute. This can be sometimes related to tori quantization: part of an excited tori can be centered when the PO is not. Secondly the frequency of the oscillation is related to the action S of the TSNO shifted by the quantity ΔS. This can also be understood with tori quantization: each series of eigenstates has a frequency related to S, but the global frequency must also take into account the dephasing between each series (given by the winding angle). For a stable TSNO, it has been shown in Bogomolny and Rouben (1999) that the sum over the repetitions of a TSNO yields a quantization *à la* Miller (1975), which is analytically equivalent to the tori quantization model (4.27) we proposed in subsection 4.2.2.

[1] We recall that $\mathcal{D} = -m_{21} - i\beta \mathrm{Tr}M + \beta^2 m_{12}$ (5.34), $\delta = -i\beta m_{12}/(m_{11}-1)$ (5.41), and $\nu = -\arg(\mathcal{D})/2$ (page 119).

6.2.1 P1 amplitudes

First we study P1 oscillations in Fig. 6.3. In the regular regime (high ϵ), the PO/NO formula works very well at all angles. It actually reproduces the amplitudes of the tori quantization model shown in Fig. 4.6. It demonstrates that the P1 oscillations in the regular regime are related to the traversing PO t_0, and that tori quantization effects must be taken into account.

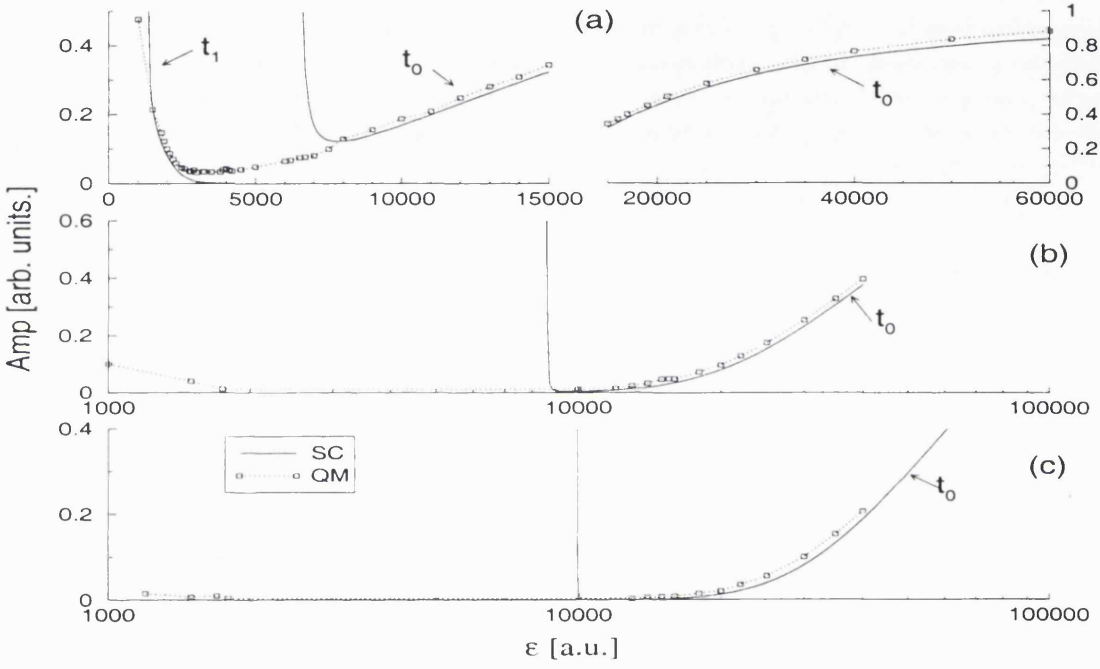

Figure 6.3: Semiclassical amplitudes of the PO/NO formula for P1 oscillations. (a) $\theta = 11°$, (b) $\theta = 20°$, (c) $\theta = 27°$. All NOs are TS, hence they are also POs. The contributions are from the TSPOs t_0 and t_1. We also show the QM amplitudes (dotted line with squares).

The PO/NO formula also works well in the chaotic regime at low ϵ (a), where the contribution of t_1 accurately describes the quantum behavior.

Note the two very sharp spikes at the two tangent bifurcations of t_0 and t_1. They are *not* divergences: the amplitudes A_{SC} are not infinite, but rather points of finite (although enhanced) value ($A_{SC} \lesssim 1$). This can be seen analytically in (5.48). At such bifurcations, one has $m_{11} \to 1, m_{21} \to 0$ and m_{12} finite. This implies $\Gamma \to 0, \mathcal{D} \to -2\beta i + \beta^2 m_{12}$ and the amplitude at the bifurcation is $A_{SC} \to |-i + \beta m_{12}/2|^{-1/2} \simeq 1$. The spikes come from the rapid variation of $\exp(-\Gamma)$. As they are linked to a bifurcation, they might be "unphysical": there the (quadratic) stationary phase approximation is not valid as the POs are not isolated, and one should use a cubic expansion of the action. This will be

discussed in section 8.3. Note that the other generic case of bifurcations where one has $m_{12} \to 0$ (see t_0 at $\epsilon = 12800$) does not bring about any noticeable enhancement.

A problem occurs at $\theta = 11°$ (a): there is no real PO between $\epsilon = 6500$ and $\epsilon = 4300$, and consequently no semiclassical current. Also, the contribution of t_1 is very small between $\epsilon = 4300$ and $\epsilon = 3000$, because of its instability and lack of accessibility (large $|z_0|$). This is obviously wrong, as the QM calculations show a significant P1 amplitude throughout this interval. Although this interval looks rather small in this graph, it covers a *third* of the experimental P1 oscillations as seen in Fig. 2.5. We shall come back to this problem in more detail in section 8.2, where we discuss ghosts (complex POs) and their contribution to the semiclassical current. We can already state the main result of that study: the amplitude of the ghost contribution is too small to describe accurately the quantum amplitude.

6.2.2 P2 amplitudes

Amplitudes of P2 oscillations are presented in Fig. 6.4. The semiclassical contributions come from $2t$ and s POs. In the three cases $2t_0$ gives an important contribution (through tori quantization), while the importance of the s' contribution increases with θ. The low maxima around $\epsilon \sim 3000$ in the chaotic regime are well described by the s_1 contributions. The height of the peaks are correct within 10%, which is a clear improvement over the HL formulae presented in section 6.1.

At $\theta = 11°$ (a) there is a secondary contribution from $2t_1$, which can be qualitatively seen on the QM calculations. The wide maximum around $\epsilon \sim 13000$ is well described by $2t_0$, in particular its height. Its position is slightly wrong ($\epsilon = 13100$ for SC, $\epsilon \simeq 15000$ for QM). The height of the SC maxima is almost unity, a consequence of the double pitchfork bifurcation where m_{12} and m_{21} are simultaneously very close to zero. This is strikingly different from the divergences present in the HL results. This maximum can be understood from the tori quantization perspective. At each of the P2 bifurcations, the winding angle of t_0 becomes π. This implies that the second tori series gets perfectly out-of-phase with the first one, bringing in a P2 signal as strong as the P1 signal at $\theta = 0°$. s' exists only in a small ϵ interval, and gives a negligible contribution.

The picture is globally similar at $\theta = 20°$. The s' contribution becomes more important. At the same time, the $2t_0$ peak becomes less accurate, in both position and height. In the regular limit the semiclassics recover their accuracy.

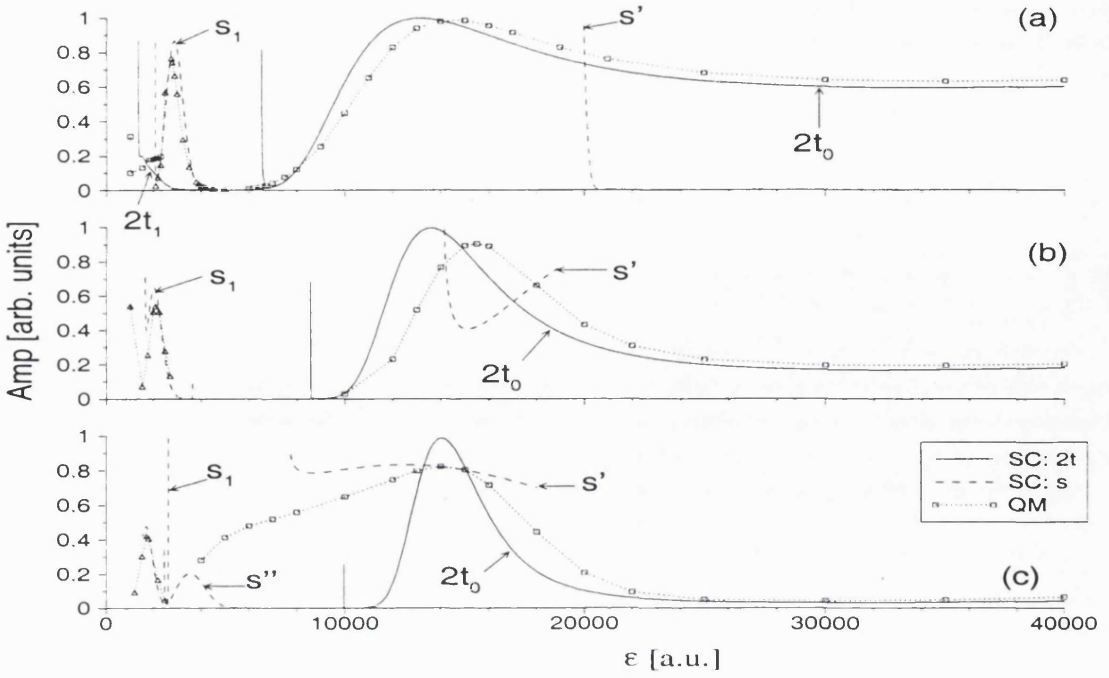

Figure 6.4: Semiclassical amplitudes of the PO/NO formula for P2 oscillations. (a) $\theta = 11°$, (b) $\theta = 20°$, (c) $\theta = 27°$. The contributions are from $2t$ POs and s POs POs. We also show the QM amplitudes (dotted line with squares and triangles). One denotes the different regions according to the underlying POs.

At $\theta = 27°$ the situation becomes even more intricate. The PO s' extends to a significant ϵ range, is quite centered with a small starting z_0, and has metastability. Those facts yield a large contribution to the PO/NO semiclassical formula. s' undergoes three different types of bifurcations (tangent at $\epsilon = 7750$, synchronous pitchfork at $\epsilon = 13600$ and cusp at $\epsilon = 18000$, see subsection 3.2.4). Only the tangent bifurcation manifests itself in the SC current, as a small spike. The pitchfork bifurcation, having $m_{12} \to 0$, does not yield anything noticeable. Similarly for the cusp bifurcation, where the current abruptly stops. Because of the nature of this bifurcation —a sort of "angle" in the potential made of a hard side (the barrier) and a soft side (the energy surface)—, one could wonder about the possibility of having diffractive effects (Bruus and Whelan 1996, Dando *et al.* 1998). To incorporate these in the semiclassics, one would have to develop a theory of the diffraction at such an edge. However, this might not be necessary as actually we have no indication from the QM results that such diffraction effects do occur. Moreover, the contribution of $2t_0$ is important in that region, and might be sufficient to explain the QM. In any case, the superposition of the competing contributions of s' and $2t_0$ is the most important problem here.

Their actions are very similar (within 5%), and one should actually consider the complete procedure of Fourier transforming the oscillatory current given by the coherent superposition of the $2t_0$ and s' contributions. As the actions are so similar, both contributions yield oscillations of almost equal frequency; the amplitude of their superposition therefore depends very strongly on their relative phase.

Here, we *must* consider the phase given by the Maslov index μ (of the energy dependent Green's function) (Creagh *et al.* 1990); the current reads $I_{\rm SC} = A_{\rm SC}\cos[S+\Delta S+\nu+\mu\pi/2]$. μ is given by the number of turning points (where the momentum vanishes) plus the number of caustics (where $m_{12}=0$) plus twice the number of hard bounces against the wall. As $\mathcal{N}$ varies (to produce the scaled oscillatory current to be Fourier transformed), each PO produces an oscillation with a constant frequency given by the scaled $\hat{S}+\Delta\hat{S}$, and a constant phase[2] given by $\mu\pi/2+\nu$. We show in Fig. 6.5 (a) the Maslov indices of $2t_0$ and s'. The only place where they can change (as ϵ varies) is at a point where $m_{12}=0$, usually a bifurcation. The Maslov index of $2t_0$ changes twice, at $\epsilon = 10082$ ($\mathrm{Tr}M[t_0]=0$) and $\epsilon = 12564$ ($\mathrm{Tr}M[t_0]=-2$); for s' the change at the pitchfork bifurcation at $\epsilon = 13652$ is important, as it brings a discontinuity in the semiclassical amplitude.

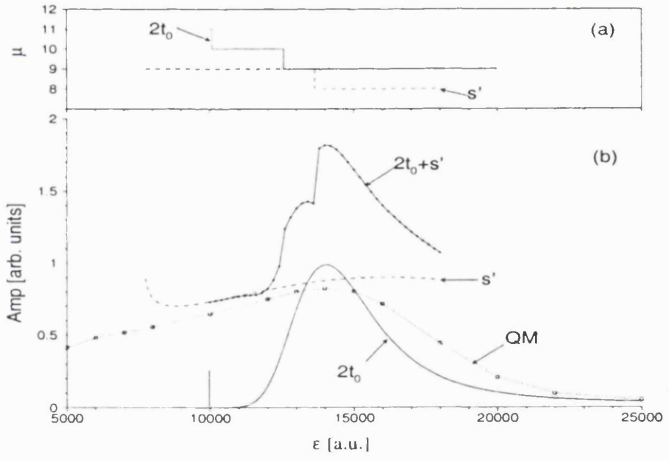

Figure 6.5: (a) Maslov index and (b) coherent superposition (solid line with dots) of the $2t_0$ and s' contributions, with QM results.

In (b) we show the complete semiclassical amplitude —i.e., the height of the peak in the FT of the current superposition—, together with the individual contribution of $2t_0$, s' and the quantum results. One sees that the coherent superposition greatly overestimates the QM results. It has a very clear discontinuity where the Maslov index of s' changes;

[2]We recall that $\nu = -\arg(\mathcal{D})/2 = -\arg(\hat{\mathcal{D}})/2$ and hence is constant as $\mathcal{N}$ varies.

this comes from the abrupt change of the dephasing between the contributions of $2t_0$ and s'.

It is clear that the superposition of $2t_0$ and s' cannot, whatever their relative phases, describe accurately the quantum results. Note that these POs are *not* involved together in a bifurcation; this is not the usual breakdown of semiclassics near a bifurcation, that one could solve with the use of normal forms. However, the reason for that failure of semiclassics might be linked to the fact that those POs are not, in some sense, really isolated —despite the fact that they are quite distant from each other in phase space. This statement follows from a comparison of the classical (via Poincaré surface of section) and quantum (via a Wigner distribution) phase space, shown in Fig. 4.12. There we see that the quantum state cannot "distinguish" between the classical structures associated with each PO; it is localized on *both* s' and an excited quantized torus of t_0. This is an "effective $\hbar$" effect, in the sense that the quantum state would be able to distinguish the two POs in a more classical regime (higher $\mathcal{N}$). Even if the POs are well separated in phase space, their contribution to the current, in some sense, is not —maybe because they can involve quantized tori which can overlap with the other POs, yielding non-isolated contributions.

We have no solution for that problem. One could try a complicated higher-order expansion of the action (similar to normal form techniques) in order to describe at the same time both POs; however, this might not be possible because these POs do not bifurcate together and actually do not have the same "topology" (i.e., number of hard bounces, caustics, turning points). Besides, we tried to take into account the fact that the (z, z') domain Ω over which one should carry out the integral (5.19) is finite; one should not carry out the Gaussian integrations over the whole plane $\mathbb{R} \times \mathbb{R}$, but on the restricted domain Ω. This yields error Erf functions. Unfortunately, the calculations we have done with this technique do not yield better results.

6.2.3 Frequencies

We show in Fig. 6.6 the scaled frequencies of P1 and P2 oscillations at $\theta = 11°$ and $\theta = 27°$. The SC frequency of the PO/NO formula is given by $\hat{\Sigma} = \hat{S} + \Delta\hat{S}$; the SC frequency of the hard limit formulae is equal to the scaled action $\hat{S}$, and the QM results is given by the position of the peak in the Fourier transform of the current. Globally, the agreement between SC and QM is very good, with differences typically less than 0.01%.

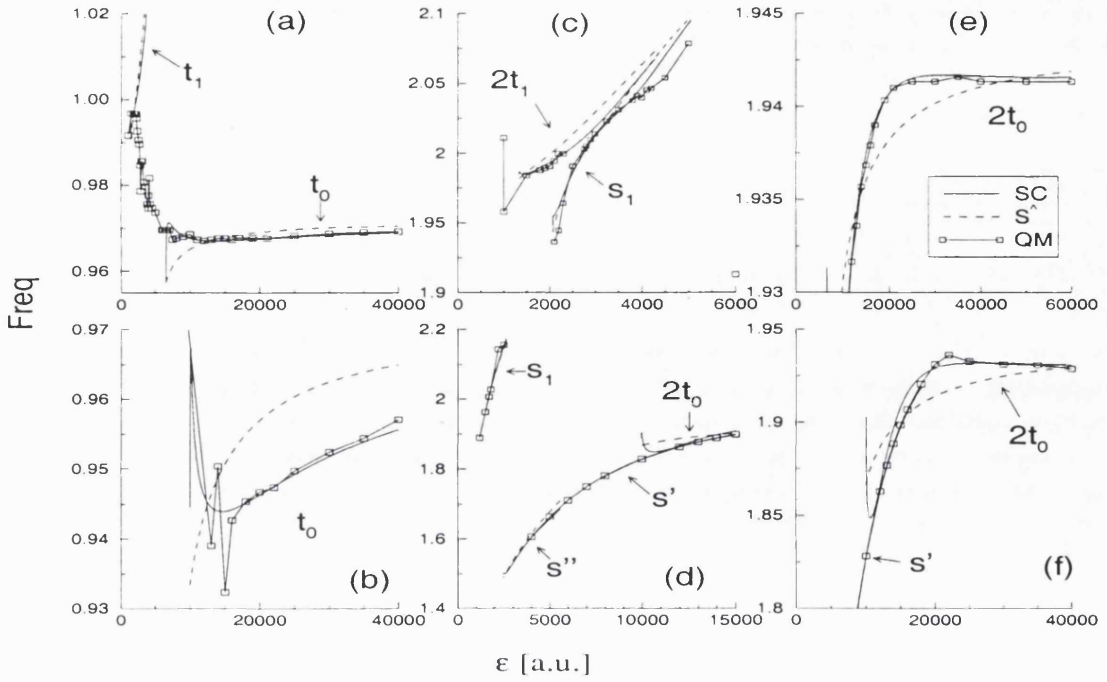

Figure 6.6: Frequencies of the oscillations. (a) P1 at $\theta = 11°$; (b) P1 at $\theta = 27°$. (c) and (e) P2 at $\theta = 11°$; (d) and (f) P2 at $\theta = 27°$. The semiclassical frequency is given analytically by $\hat{\Sigma} = \hat{S} + \Delta\hat{S}$ from the PO/NO formula. The QM frequency is given by the position of the peak in the Fourier transform of the scaled current spectrum. We show for comparison the scaled action $\hat{S}$ of the POs, which is also the frequency of the hard limit formulae discussed in section 6.1.

Although the actions $\hat{S}$ are very close to both the SC and QM, one can see the actual shift $\Delta\hat{S}$. Their relative difference lies between 0.1% (a) to 1% (b). This shows that establishing a one-to-one link between a given set of QM oscillations and one PO is a very accurate process. For example, several POs $(s_1, s', 2t_0)$ were thought to contribute to P2 oscillations; one sees in (c) and (d) that the QM current can "distinguish" them. In (f), the interval $\epsilon = 10000 - 18000$ corresponds to the region where the amplitudes of $2t_0$ and s' compete; there the QM frequency is very precisely described by the contribution of s'. Although the frequency of the PO/NO formula given by $2t_0$ is here less than 0.5% different from the quantum frequency, one can still see that the QM is closer to s'.

6.2.4 NO vs. PO

An important question at this stage is to ascertain whether the theories developed independently by Bogomolny and Rouben (1998) (the NO formula) and by Narimanov *et al.* (1998b) (the PO formula) can differ, and if so, which one is more accurate. As mentioned

already, they are strictly equivalent for time-symmetric trajectories (TSNO ≡ TSPO). Therefore, one has first to find NOs and POs which are *not time-symmetric*. We show such orbits and their contribution to the NO and PO formulae in Fig. 6.7.

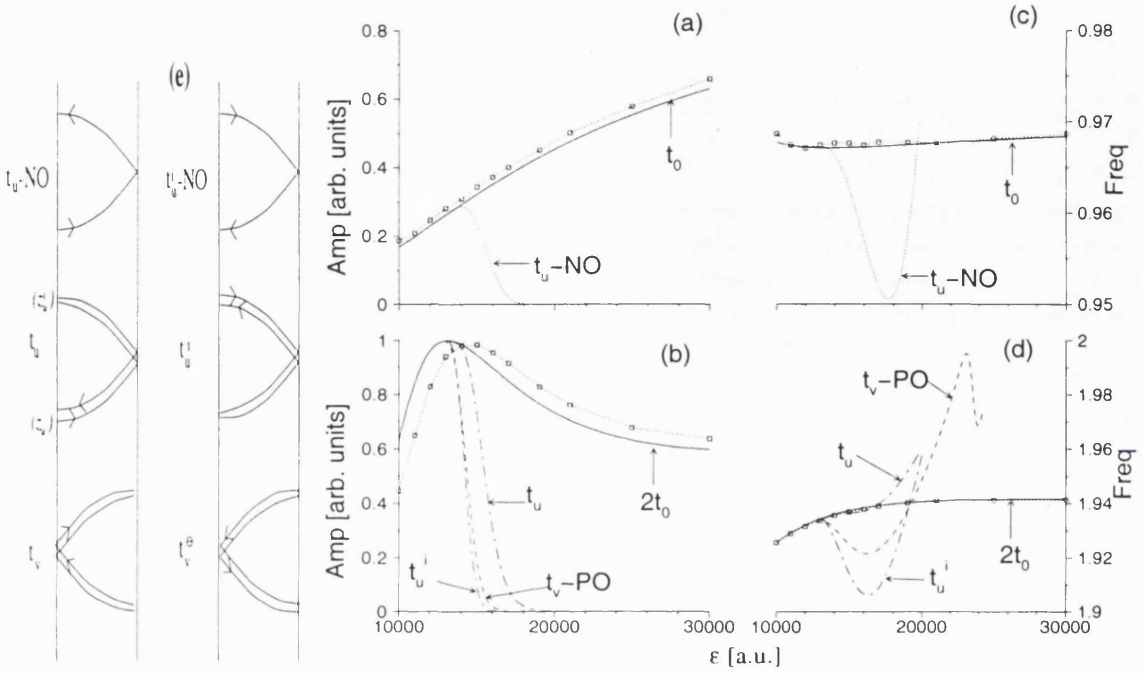

Figure 6.7: Comparison of the NO and PO formulae at $\theta = 11°$. (a) P1 and (b) P2 amplitudes. (c) P1 and (d) P2 frequencies. t_u *–NO* is a P1 non-TS NO, and appears only in the NO formula. $t_0, 2t_0, t_u$ and t_u^i are TSPOs and appear in both formulae. t_v *–PO* is a P2 non-TS PO, and appears only in the PO formula. The QM results (dotted line with squares) are shown for comparison. We write t_u *–NO* (t_v *–PO*) to emphasize the fact this PO (NO) contributes uniquely to the PO (NO) formula. (e) Shapes of the different orbits involved.

Two new P2 POs are born in the double pitchfork bifurcation of t_0 at $\theta = 11°$: t_u and t_v (see subsection 3.2.3). t_u in itself is a perpendicular (hence TS) PO, having $p_z^0 = 0$ at the starting point z_u and also at the intermediate bounce on the left wall at z_u^i [see Fig. 6.7 (e)]. One can also consider the trajectory t_u^i ($z_u^i \to z_u^i$), which is periodic and follows the same path as t_u but starts at the intermediate point of t_u. Its contribution to the P2 current is *different* to the one of t_u. t_v is a non-TS PO with $p_z^0 > 0$. Similarly, one can consider the trajectory $t_v^{\ominus}$, which starts at the same point with opposite momentum $-p_z^0$. Again it follows the same path as t_v, but starts at the midpoint of t_v. Its contribution to the current is equal to the one of t_v. The amplitudes of P2 contributions (given by $2t_0, t_u, t_u^i$ and t_v) are shown in (c), their frequencies in (d).

One has also a "half-PO" trajectory t_u–NO ($z_u \to z_u^i$), which is a non-TS NO. Its companion t_u^i–NO ($z_u^i \to z_u$) gives the same contribution to the NO current. Both give a P1 contribution to the current, in addition to the contribution coming from t_0. The amplitudes are shown in (a), the frequencies in (c).

The comparison with the QM results is clear: they are described by only considering the TSPOs t_0 and $2t_0$. The individual contribution of each of the other orbits appears to be significant by itself, but quite uncorrelated to the QM current. Both QM amplitudes and frequencies follow t_0 and $2t_0$ alone, without showing any sign of being influenced by the other orbits. Hence, one can conclude that non-TS POs and NOs, as well as satellite TSPOs (such as t_u) *do not* contribute to the current.

This is hard to explain in the semiclassical perspective where the formula (PO or NO) has been derived: all those orbits are valid expansion points of the action, and they *should* contribute. As one can see, they do not. In a more physical view, the initial state feeds the electrons onto orbits which are within the Gaussian width. Having several expansion orbits (like t_u, t_v, t_u–NO) in addition to t_0 and $2t_0$ in that area will not increase the current, as the "amount" of available electrons is fixed. Semiclassically, this might be equivalent to saying that the QM system does not, at this effective $\hbar$, "distinguish" between different orbits located in the injection area; then they would be, in a way, non-isolated (similarly to the case of $2t_0$ and s' at $\theta = 27°$ discussed above).

Note that there are still some unsolved problems concerning those orbits. Should one add the contributions of t_u and t_u^i? Count twice the one of t_v–PO and t_u–NO? Or count them only once (as for GTF), arguing that they are the same PO? As they are all bifurcating, one should maybe use cubic forms? We shall not investigate those questions further as these orbits, obviously, should not appear in the correct semiclassical current.

6.2.5 Other POs

An important question is whether other POs/NOs (such as the unstable partner in a tangent bifurcation) contribute to the current. As we can see in Fig. 8.5 (a) and (c) in page 187, this type of POs *do not* contribute to the current. It appears that one needs to consider only a very restricted ensemble of POs —t_0 for P1, s', s_1 and $2t_0$ for P2— for a complete semiclassical description of the current in the RTD. The contribution of a PO decreases very quickly as it becomes more unstable or as its starting position moves away from the center, and most POs in effect cease to contribute.

6.2.6 Extensions of the PO/NO theory

We shall present in chapter 8 two extensions of the PO/NO formula: the addition of a ghost contribution (section 8.2) and a cubic integration (section 8.3). These studies will show that the PO/NO formula is not able to describe accurately the quantum behavior in the "no (real) PO" regions.

6.3 Saddle orbits

In this section we study the saddle orbit (SO) formula, with special interest in the regions where the PO/NO formula failed. SOs were defined in (5.43).

6.3.1 P1 amplitudes

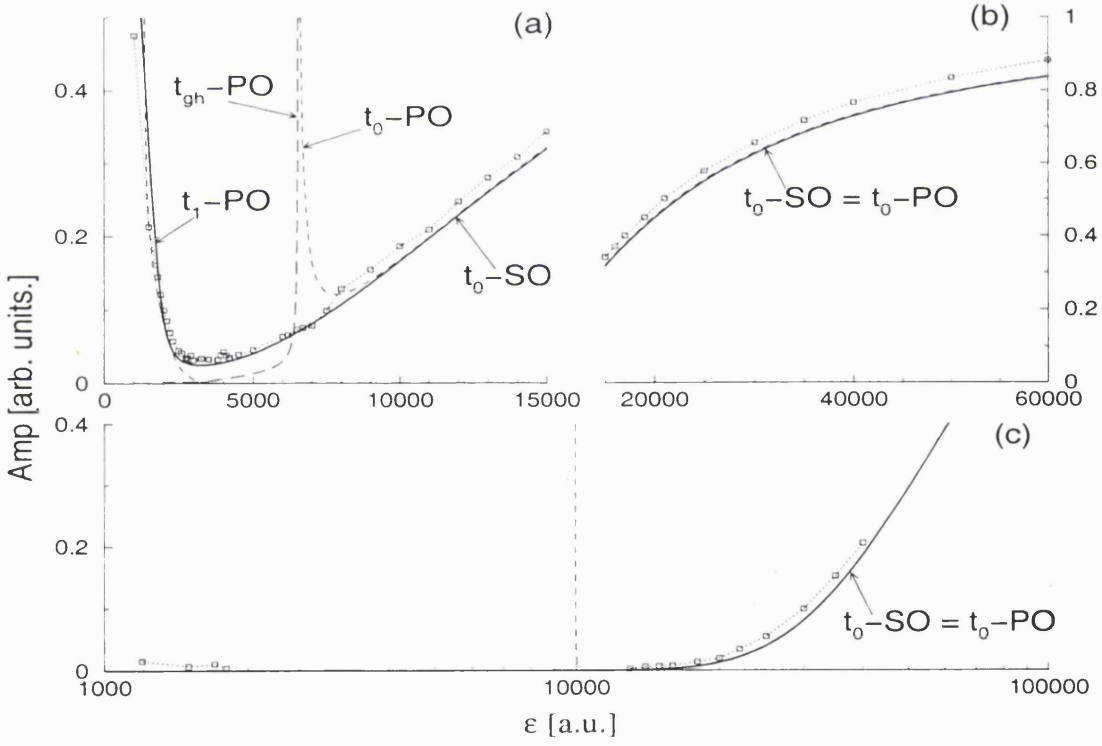

Figure 6.8: SO formula with QM results (dotted line with squares) and PO/NO formula (indicated by "$-PO$", in dashed lines), for P1 amplitudes. (a) $\theta = 11°$ for low ϵ, with the ghost contribution t_{gh} to the PO/NO formula. (b) $\theta = 11°$ for high ϵ. (c) $\theta = 27°$, where the PO/NO and SO formulae are indistinguishable.

We start by showing P1 amplitudes in Fig. 6.8. The PO/NO results, already shown in Fig. 6.3, are plotted again for a comparison with the SO results; we also included the ghost

contribution $t_{\rm gh}$–PO discussed in section 8.2. The high ϵ range at $\theta = 11°$ is shown in (b). There the SOs do not improve over the PO/NO formula, as they are indistinguishable. They both agree very well with QM calculations. We have exactly the same situation at the higher angles $\theta = 20°$ (not shown here) and $\theta = 27°$ (c).

The interesting situation here is the low ϵ range at $\theta = 11°$, shown in (a). There one has an obvious failure of the PO/NO formula in the ghost region $3000 < \epsilon < 6500$, as the tangent bifurcation occurring at $\epsilon = 6540$ removes the real t_0–PO, leaving a complex ghost PO whose contribution is too small by a factor three. The PO/NO formula recovers its accuracy around $\epsilon = 3000$, where t_1–PO (appearing at the edge of the SoS in a cusp bifurcation at $\epsilon = 4280$) starts to dominate the current. On the contrary, the SO contribution of t_0–SO describes very well the QM results all through the ghost region. It does not undergo any bifurcation, hence it does not show any "unphysical" enhancement as the PO contribution does. As ϵ decreases, t_0–SO becomes linked to three different POs: t_0–PO, its ghost $t_{\rm gh}$–PO, and t_1–PO. Its contribution describes this changeover in a perfectly smooth way.

6.3.2 P2 amplitudes

We show P2 amplitudes in Fig. 6.9.[3] For clarity we do not show all the PO/NO contributions; the reader should refer to Fig. 6.4 for a complete comparison. At $\theta = 11°$ (a), the SO formula improves the accuracy of the high ϵ enhancement due to $2t_0$, getting its position right. Also, it improves the accuracy of the low ϵ P2 amplitude coming from $2t_1$. For the s_1 peak, the SO and PO formulae are indistinguishable, apart for the fact that the SO does not show unphysical spikes like the ones found in the PO/NO formula at bifurcations.

More interesting is the situation at $\theta = 27°$ (b). s'–SO does not undergo a tangent bifurcation like s'–PO, and gives a contribution all way down to $\epsilon = 2000$, rejoining the contribution of s''–PO which appeared in a cusp bifurcation at $\epsilon = 9500$. The same SO corresponds to both s'–PO and s''–PO; it disappears in a cusp event at $\epsilon = 1900$. The agreement with QM in the ghost region $3500 < \epsilon < 7700$ is not perfect, but it is reasonable and far better than the ghost contribution [see Fig. 8.5 (c)]. It is quite close to the central closed orbit s'–CCO [see Fig. 6.16 (c)] but follows accurately the QM amplitudes after the CCO has disappeared.

[3] We shall present results for $\theta = 20°$ in chapter 7, where the SO formula shows a divergence that we shall study in more detail.

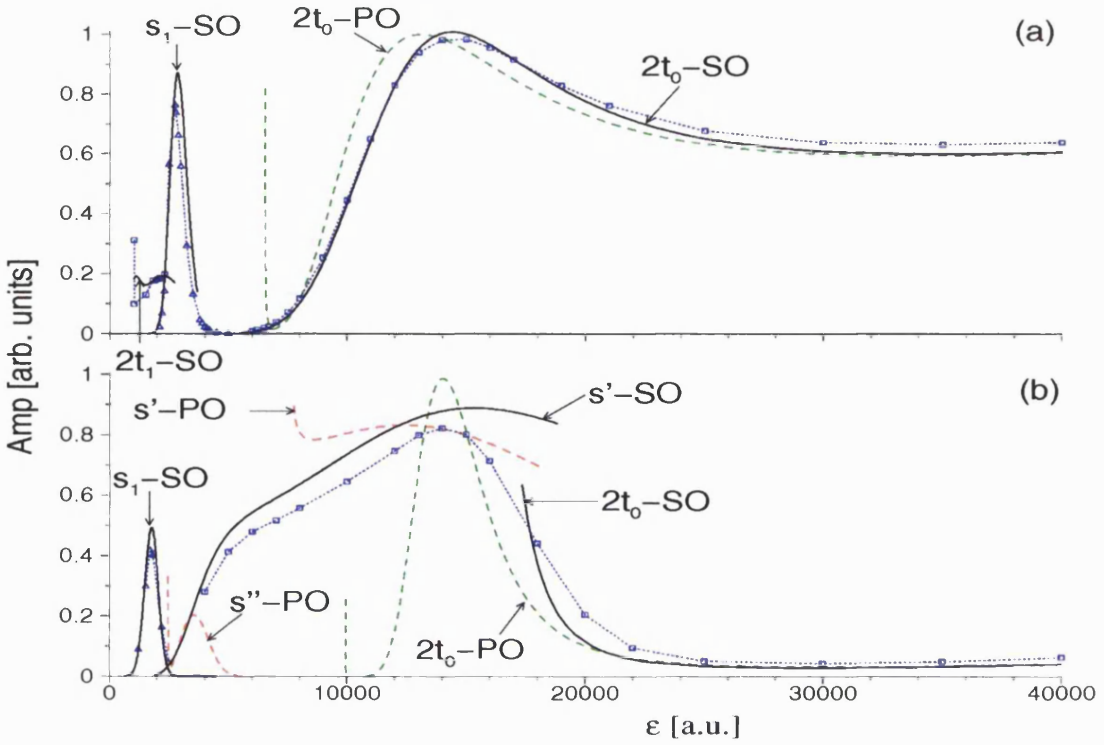

Figure 6.9: SO formula with QM results (dotted line with squares) for P2 amplitudes. We show also the PO/NO formula for some POs (dashed lines). (a) $\theta = 11°$; (b) $\theta = 27°$.

Moreover, the SO formula seems to solve the problem of the superposition of the two competing s'–PO and $2t_0$–PO. s'–SO disappears also in cusp event at $\epsilon = 18800$, roughly at the same ϵ as s'–PO. It is $2t_0$ which is dramatically changed here: $2t_0$–SO appears at $\epsilon = 17360$, in contrast to $2t_0$–PO which appears at $\epsilon = 9970$. Hence there is almost no overlap ($\epsilon = 17360 - 18800$) between s'–SO and $2t_0$–SO; one does not have the problem of choosing which orbit to consider, or of trying to consider their joint contribution as one had with POs. The SO contribution tends towards the PO result in the regular limit ($\epsilon > 30000$).

For the low ϵ peak given by s_1, there is only a small difference between the SO and PO formulae; as it is not visible on the scale used on the graph, we do not present the PO contribution. Note that the difference is smaller than the (small) disagreement with QM.

6.3.3 Frequencies

In general, the frequencies of the semiclassical oscillations of the PO/NO formula were already very precise (see Fig. 6.6, also for a comparison with the scaled action of the POs). In Fig. 6.10 we see that they also agree with the frequencies given by the SO formula.

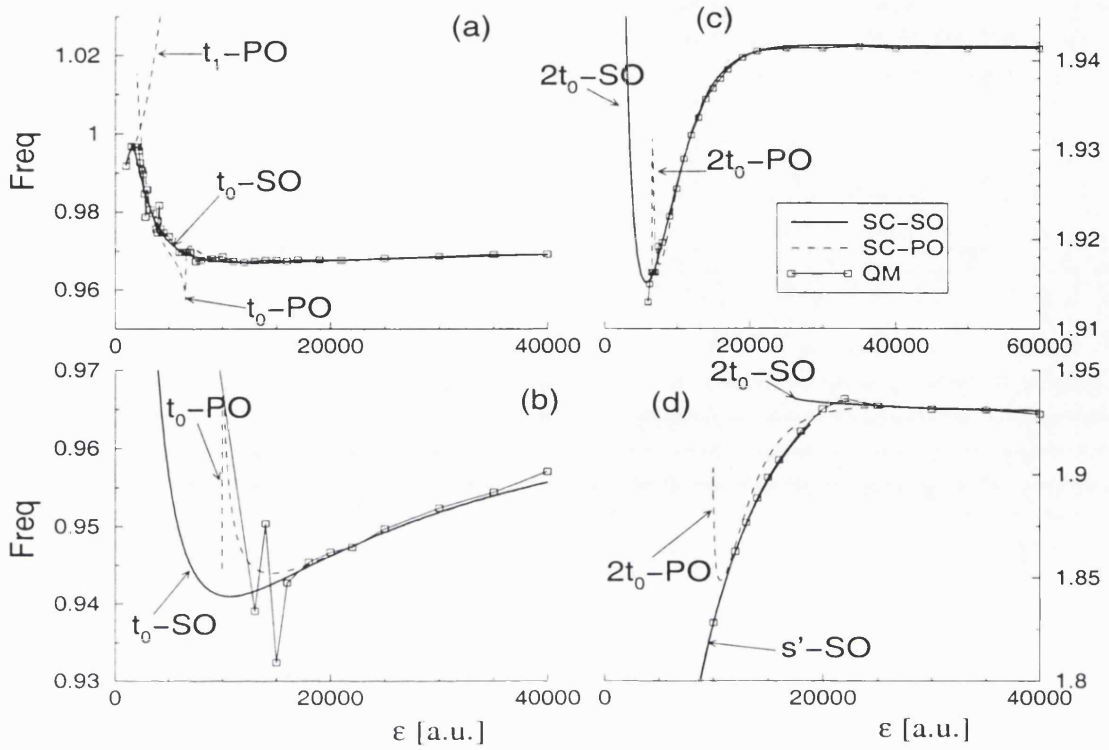

Figure 6.10: Frequencies of the SO formula with QM results and the frequencies of the PO/NO formula. (a) P1 at $\theta = 11°$; (b) P1 at $\theta = 27°$; (c) P2 at $\theta = 11°$; (d) P2 at $\theta = 27°$;

The latter brings an improvement as it does not show a "hiccup" at a bifurcation like the PO/NO frequency. Note that the disagreements in (b) is not worrying, as they occur in a region where the amplitude of the current is excessively small. The major improvement of the SO formula happens for the P1 oscillations at $\theta = 11°$ (a), in the ghost region. A more detailed figure is presented in the section on the cubic formula (Fig. 8.10).

6.3.4 Discussion

One can distinguish three general dynamical regimes in the RTD, depending on the value of ϵ, which can be illustrated on a SoS (see e.g. Fig. 3.3).

1. At low ϵ (e.g. $\epsilon < 3000$ at $\theta = 11°$), the dynamics is very chaotic, and a SoS presents a sea of unstable trajectories. There the PO/NO formula works well, as seen by looking at P1 and P2 amplitudes, and the SO formula is not strictly necessary.

2. At intermediate ϵ (e.g. $3000 - 8000$ at $\theta = 11°$, $3000 - 20000$ at $\theta = 27°$), the dynamics is more "mixed"; a SoS shows a mixture of stable islands and chaotic sea, with maybe a few competing POs and bifurcations. There the PO/NO formula seems to fail, either because of a ghost contribution which is too small, or because of

the combined effect of two non-isolated competing POs. The SO formula is necessary here if one wants a quantitative and accurate semiclassical description.

3. At high ϵ (e.g. $\epsilon > 10000$ at $\theta = 11°$, $\epsilon > 30000$ at $\theta = 38°$), the dynamics is fairly regular, and is dominated by the stable island of $t_0 - PO$. Here again the PO/NO formula works well, describing accurately the tori quantization effects — despite the fact that the hypothesis of chaotic dynamics needed for the NO formula is not satisfied. The SO formula is not strictly necessary, as both theories give a very similar contribution.

6.3.5 Classical limit

Usually one interprets complex trajectories as being a "quantum effect" which should disappear in the classical limit $\hbar \to 0$ (e.g., the tunneling effect). In the GTF of the DoS, ghost POs have a contribution which vanishes exponentially fast either in the classical limit or away from the bifurcation where they were born.

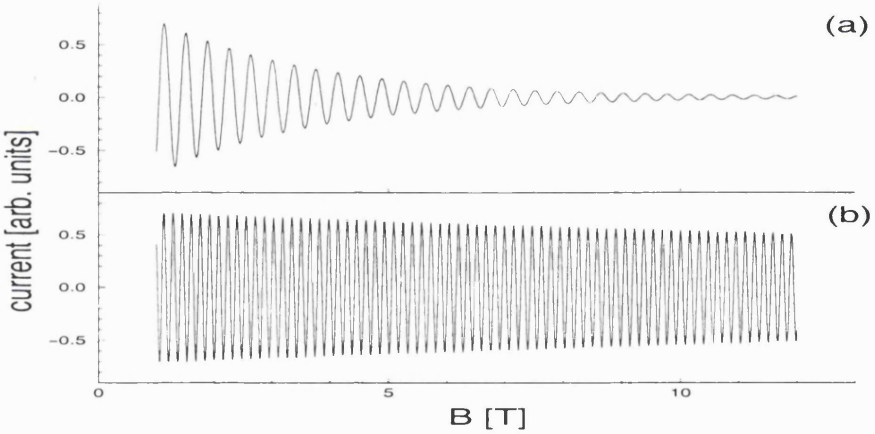

Figure 6.11: Oscillatory semiclassical current $I(B)$ in ghost regions. (a) $\theta = 11°$,$\epsilon = 4000$. (b) $\theta = 27°$,$\epsilon = 7000$.

Fig. 6.11 shows the oscillatory current given by the saddle orbit formula as a function of B. In the "no (real) PO" region at $\theta = 11°$ (a), the current is strongly damped in the classical limit $B \gg 1$. This is the standard behavior of the contribution of a ghost to the DoS. This can be seen experimentally in Fig. 2.5: the amplitude of the oscillations decreases quickly along the parabola in the direction of increasing B. Note that the amplitude does not decrease exponentially fast away from the PO's bifurcation, as one

could expect for the ghost contribution to the DoS.

On the other hand, the current at $\theta = 27°$ (b) decreases very slowly with B (linearly it seems). The amplitude of the current is proportional to $\exp\Big\{ - B[\mathbf{Im}\,\tilde{S} + \cos\theta(\mathbf{Re}\,z)^2 - \cos\theta(\mathbf{Im}\,z)^2]\Big\}$; the argument is not very negative, because the imaginary part of the starting z compensates the damping due to its real part and the imaginary part of S.[4] This persistence of the contribution of a complex orbit in the classical limit is quite surprising, and can be seen experimentally in Fig. 2.8, where the amplitude of the oscillations stay constant along the parabola.

6.3.6 SOs and POs

In this section we study the classical characteristics of the SOs. We try to see if there is a link between SOs and POs, and if one can understand the failures of the PO/NO formula from a classical study of SOs and POs. This study will be continued in section 8.4, where we shall present an "approximation" of SOs by related POs.

Shapes

In Fig. 6.12 we show a comparison of the shapes of SOs and POs in the (x, z) plane. We only show here *contributing* SOs, discarding the SOs that give a negligible contribution to the current. We start by noting a certain resemblance between one type of SO ($t_0\,$–SO or s'–SO) and its PO counterpart: by definition they have the same bounce structure, but they also look similar. The main difference is that the SOs start with a angle on the left wall (as $p_z^0 = i\beta z_0 \neq 0$), in contrast to the POs, which are perpendicular ($p_z^0 = 0$). These SOs are all TS, because of a normal bounce on the right wall (e.g., $t_0\,$–SO) or a soft bounce on the energy surface (e.g., s'–SO). We note in (b),(e) and (g) that the PO related to the SO is always the contributing PO and never the non-contributing one (e.g., the partner in the tangent bifurcation).

It is obvious from their definition (5.43) that SOs are *non-periodic* as $p_{z'}^0 = -p_z^0$ (for TS SOs). This means that one cannot look at the "repetition" of a SO: even *if* one can continue a primitive SO until one finds a repetition of the primitive bounce structure[5] , the

[4]Note that here $\mathbf{Re}\,z$ is small, which implies that the SO is "not very complex" (the PO almost satisfies the $z = 0$ condition needed to cancel the Gaussian damping).

[5]The bounce structure of the continuation of a SO can be completely different, e.g., the trajectory can be trapped on the right wall and have no more bounces on the left wall even if the primitive SO does bounce on the left wall.

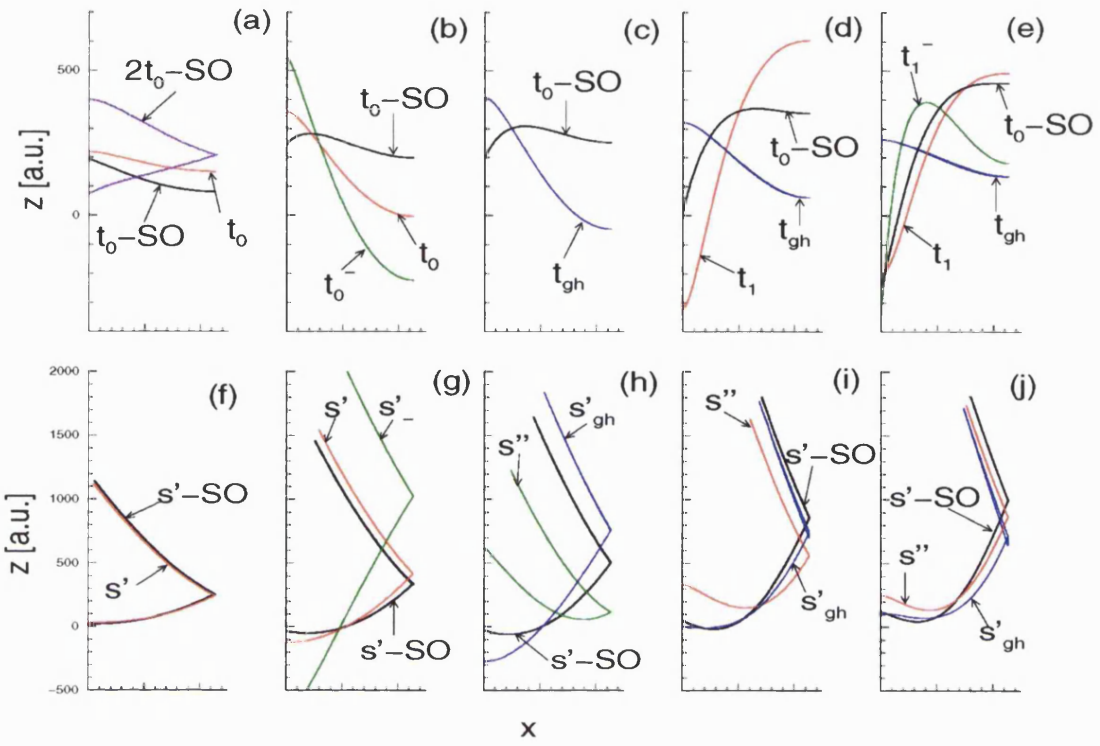

Figure 6.12: Shapes of SOs (thick line) at $\theta = 11°$, with real POs and ghost POs ($t_{\rm gh}$ and $s'_{\rm gh}$). (a) $\epsilon = 20000$, (b) $\epsilon = 7000$, (c) $\epsilon = 5000$, (d) $\epsilon = 3000$, (e) $\epsilon = 2000$; and at $\theta = 27°$ (f) $\epsilon = 16000$, (g) $\epsilon = 10000$, (h) $\epsilon = 7000$, (i) $\epsilon = 4000$, (j) $\epsilon = 3000$. We show the *real* part of complex orbits ($\mathrm{Re}\, x, \mathrm{Re}\, z$). We drop the suffix "$-PO$" when labelling POs.

trajectory one obtains that way is *not* a SO. This is very different from behavior of POs, where every repetition can in principle contribute to the current given by the PO/NO formula. As one expects to have a SO describing oscillations given by the repetition of a PO, one has to look for a SO defined by the bounce structure of the repetition of the PO, which can be quite unrelated to the SO corresponding to the primitive PO. Actually, we sometimes have the situation where one has a SO corresponding to a primitive PO, while no SO exists that would correspond to the second repetition of that PO (e.g., t_0–SO at $\theta = 27°, \epsilon < 17000$).

In (a)-(e) we study P1 SOs at $\theta = 11°$. In (a) we show the SO (t_0–SO) that is related to t_0–PO, as well as *another* SO ($2t_0$–SO) that is related to the second repetition of t_0–PO (which is indistinguishable from the primitive PO). $2t_0$–SO does not seem obviously related to $2t_0$–PO. In (b) and (c) we are on both sides of the tangent bifurcation. In this region, where the PO/NO formula cannot reproduce the SO formula, the different types of orbits do not seem closely related, although there is only one PO which could be responsible for the current. In (d) t_1–PO has appeared, but does not contribute significantly to the

current. The SO seems to be "between" that real PO and the complex ghost.[6] In (e) the shape of the SO is much closer to the t_1 $-PO$ than to the ghost; the ghost contribution to the PO/NO current has given precedence to t_1 $-PO$. Hence, one sees the shape of the SO evolving in a smooth way from being paired with t_0 $-PO$ at high ϵ to a pairing with t_1 $-PO$ at low ϵ.

The situation is somewhat similar at $\theta = 27°$ (f)-(j). In (f) the SO is extremely close in shape to the PO. This is a special situation, where the PO is very well centered ($z_0 \sim 0$); this means that the PO —which is by definition a stationary point of the action— is almost the maximum of the initial state Gaussian ($z_0 = 0$), providing that way a very good approximation of the SO. This means also that the SO is not very "complex" as $\mathrm{Im}\, p_z^0 \sim 0$, and finally both SO and PO are very similar. As ϵ decreases, a small difference grows between the SO and the PO (g),(h). This is an interesting situation as it shows strong scarring as discussed in Fig. 4.10. For example, one could wonder if the SO scars the wave function. In (i) they are closer again; the contribution of the real PO s'' $-PO$ is still small. In (j), the contribution of s'' $-PO$ has taken over and is close the quantum current; here the SOs seem to be equally close to the ghost and the real PO.

In summary we see that contributing SOs and POs show a similarity in shape that varies with the different dynamical regimes; it also seems to be related —although in an unclear way— to the similarity of their semiclassical contribution.

Classical properties

Fig. 6.13 shows the global behavior of t_0 $-SO$ at $\theta = 11°$ as ϵ changes. In particular, we look at the real and imaginary parts of the starting position, that we compare with the P1 POs t_0, t_1, etc., their partner $t_{0,1}^-$ and the ghost t_{gh}.

We see that there is *only one* SO which is related to the successive pairs of POs; the SO seems to switch from one PO to the other as ϵ decreases. First t_0 $-SO$ is related to the stable t_0 $-PO$, up to $\epsilon \simeq 8000$. Then it seems to bend towards the (still non-existent) t_1 $-PO$, while staying relatively close to the ghost t_{gh} until $\epsilon \simeq 3000$. There it veers towards the real t_1 $-PO$, stays in its vicinity until it disappears at $\epsilon \simeq 1400$ and bends towards t_2 $-PO$.[7] As each new $t_{0,1,2,..}$ $-PO$ appears on the *other* side of the SoS, the SO oscillates

[6] One could therefore think that the SO is not very close to the PO in (b) and (c) because it "feels" the presence of t_1 $-PO$ well before it appears. Here "presence" would mean some dynamical feature linked to t_1 $-PO$, such as the part of the bundle of trajectories around t_1 $-PO$ which is already present.

[7] We did not look for the ghost of t_1 $-PO$.

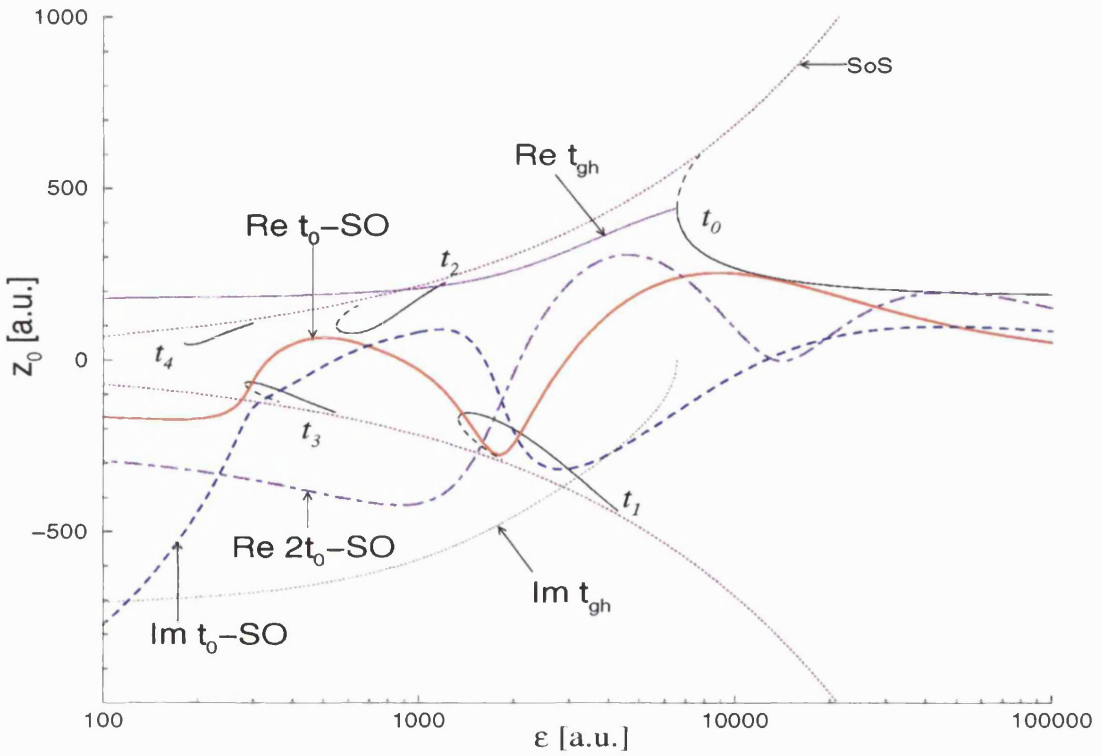

Figure 6.13: Evolution of the starting position z_0 of t_0-SO and $2t_0-SO$ with ϵ at $\theta = 11°$. We also show POs and the ghost $t_{gh}-PO$. We do not show Im $2t_0-SO$. We drop the suffix "$-PO$" for labelling POs and indicate the limit of the SoS [SoS].

between the two sides, going from one PO to the next one until it reaches t_3-PO, after which it does not change its starting position, apparently unmoved by t_4-PO. Note that the SO does *not* tend towards the PO in the regular (high ϵ) limit; this will be discussed in conjunction with Fig. 6.15.

The behavior of the SO described above might give us a clue about the reason for the failure of the semiclassical contribution of the ghost: in that region, the correct orbit (t_0-SO) already "feels" the contribution of t_1-PO; it is "between" the ghost and the real PO, as illustrated in Fig. 6.12 (d). As we shall see in section 8.4, the SO cannot be approximated by the ghost PO only, and the contribution of the latter is inaccurate.

Im z_0 also oscillates between positive and negative values; although it seems related to the (real) starting position of the POs, we shall not hypothesize a link. It is relatively close to the ghost for some interval, and ends up having a growing magnitude for $\epsilon < 300$. This behavior seems surprising, and we can note that it corresponds to a regime where the real part is outside the SoS. This is consistent: a particle can go (or even start) outside the classically allowed region (i.e., with negative kinetic energy) provided it becomes complex

enough. This is one case where a complex orbit is very different from the real ones; we did not investigate this situation further as it does not correspond to the experimental parameters.

Finally, we note that $2t_0-SO$ exists for any ϵ, and hence always coexists with t_0-SO. It also oscillates between the two sides of the SoS, but does not present a strong link with t_0-SO, as illustrated in Fig. 6.12 (a).

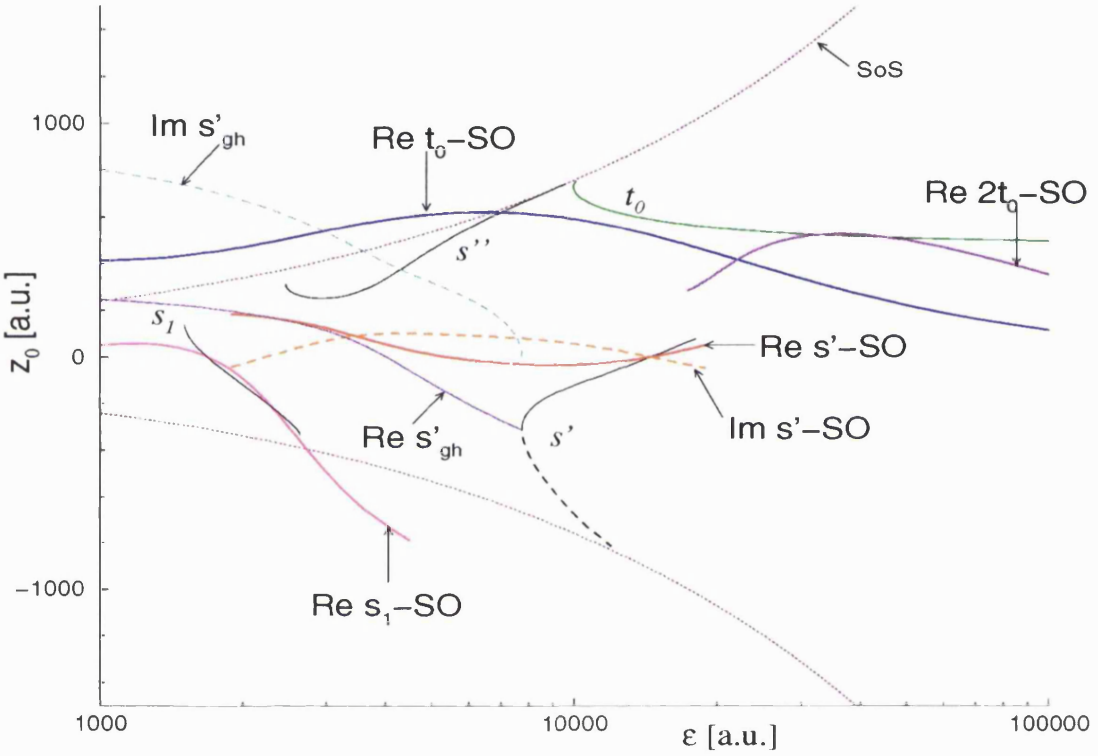

Figure 6.14: Evolution of the starting positions z_0 of t_0-SO, $2t_0-SO$, $s'-SO$ and s_1-SO with ϵ at $\theta = 27°$. We also show the related POs and the ghost $s'_{gh}-PO$. We do not present the imaginary part of all the SOs. We drop the suffix "$-PO$" and show the limit of the SoS [SoS].

In Fig. 6.14 we study starting positions at $\theta = 27°$. We see that t_0-SO oscillates less than at $\theta = 11°$. It exists for any ϵ, on the contrary to the related PO t_0-PO which disappears at $\epsilon = 9970$. It is interesting to note that $2t_0-SO$ exists only for $\epsilon > 17300$. Hence there is a large domain where one does not find the SO related to the second repetition of the primitive PO, illustrating the non-periodicity of SOs.

The real part of $s'-SO$ moves slightly from $s'-PO$ to $s''-PO$; in between it seems reasonably close to the ghost $s'_{gh}-PO$ and actually tends towards it before $s''-PO$ disappears at $\epsilon = 2470$. Their imaginary parts, on the other hand, do not agree. Maybe this is behind the failure of the ghost contribution to the semiclassical current (in contrast to the success

of the SO).[8]

Finally, we see the very close link between s_1–SO and s_1–PO. We recall that although having the same bounce structure as s' orbits (1:2), they belong to a distinct family as they have one extra cyclotron rotation. s'–PO and s''–PO on the other hand look more similar in shape, and could be said to belong to the same family. This is illustrated by the fact that there is exactly one SO for s_1, and one SO for s'–PO and s''–PO; it seems that there is one contributing SO per family.

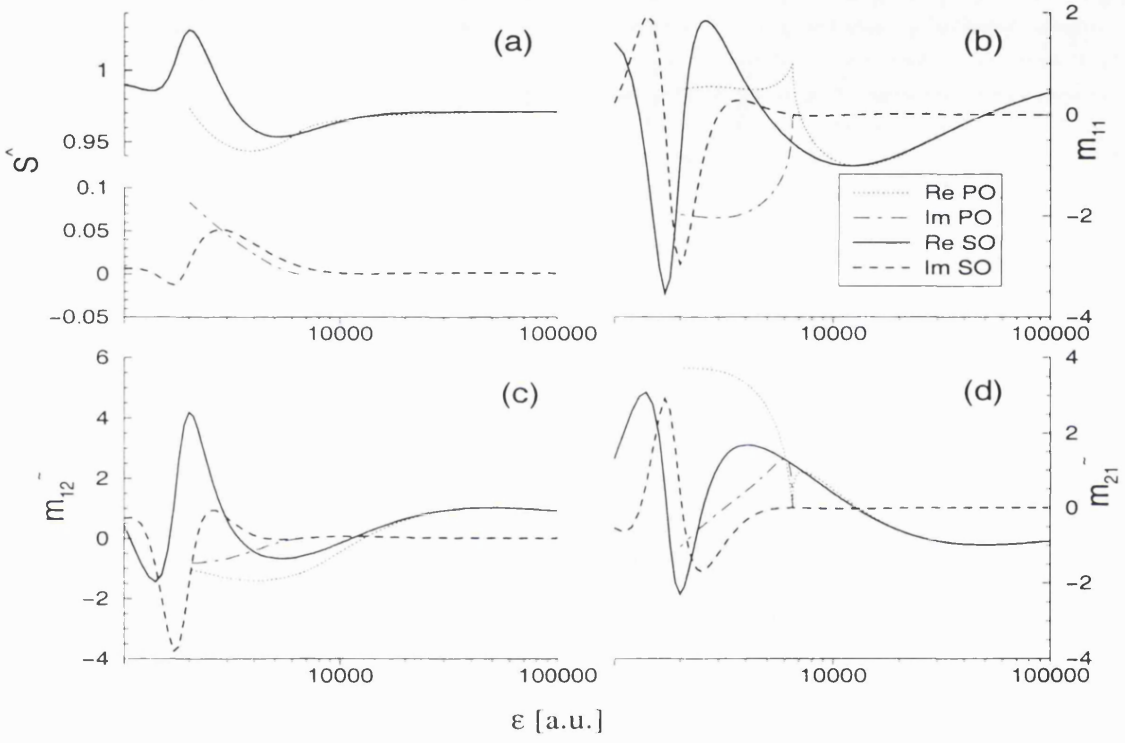

Figure 6.15: Classical characteristics of t_0–SO at $\theta = 11°$; we also show t_0–PO together with its ghost [PO]. (a) $\hat{S}$; (b) m_{11}; (c) $\tilde{m}_{12}$; (d) $\tilde{m}_{21}$.

In Fig. 6.15 we present the evolution of other characteristics of t_0–SO at $\theta = 11°$. We see that the SO becomes more real in the regular limit ($\epsilon > 10000$) as its imaginary components decrease. Its real components tend towards the related PO. Surprisingly, this is not the case for the starting position (see Fig. 6.13); while $\mathbf{Re}\, z_0$ decreases for t_0–SO, the starting position of the PO stays roughly constant. However, the size of the SoS increases

[8] As will be seen in section 8.2, the explosion of the semiclassical contribution of s'_{gh} is linked to (*i*) $|\mathrm{Im}\ z_0| > |\mathrm{Re}\ z_0|$ and (*ii*) the change of sign of $\mathbf{Im}\ \hat{S}$. It is also worth looking at Fig. 8.6 (b), where one shows the action of s'–SO at $\theta = 27°$. One sees that its real part coincides with the action of the ghost PO, while the imaginary parts are very different —in particular the SO shows monotonic behavior, in contrast to the PO.

with ϵ; this makes the ratio of z_0 over this size tend to 0 for t_0–*SO*, "effectively" tending towards the straight PO (which is also a SO) existing in the absence of magnetic field $B = 0$ (or at $\theta = 0°$).

All the classical characteristics of the SO are smooth in the regular regime, and oscillate in the chaotic regime. They do not present any abrupt behavior. For a real TSPO, $m_{11} = 1$ corresponds to a bifurcation; we see that the SO does not show any special behavior where $\mathbf{Re}\, m_{11} = 1$. So far, we have never witnessed any sign of a bifurcation of a SO, in the sense of two SOs colliding and/or a SO disappearing as ϵ is varied. It might be possible that such a "bifurcation" exists, but it would appear at a *complex* energy, which would be harder to localize, as one would need to vary two real parameters. The only mechanism which removes SOs is the *cusp event*, similar to the cusp bifurcations of periodic orbits (e.g., changing ϵ makes the SO "miss a bounce"; see also page 180 in section 8.1).

6.4 Alternative theories

6.4.1 CCO formula

Here we test the central closed orbit (CCO) formula. It was initially proposed by Narimanov and Stone (1999) in order to fix the problems of their PO formula —in particular, in regions where no real PO is present (Saraga *et al.* 1998). The CCOs were defined in (5.51).

We show in Fig. 6.16 a test for the CCO formula in the so-called "no (real) PO" regions at $\theta = 11°$ and $\theta = 27°$. In (a) the important range is $3000 < \epsilon < 6500$, where one has no contributing real PO, and where the ghost of t_0–*PO* is too small. There is a CCO resembling t_0–*PO* (i.e., it has one bounce on the left wall and one on the right wall), which we call t_0–*CCO*. Indeed it survives longer than t_0–*PO*, as it disappears at $\epsilon = 2800$ instead of the tangent bifurcation of the PO at $\epsilon = 6540$. However, the CCO formula is obviously wrong for $\epsilon > 5000$ and in particular in the regular regime; it completely underestimates the quantum current. Even the frequency (which is usually accurate) given by the CCO is quite wrong. Similarly, the t_1–*CCO* contribution is not as good as its *PO* counterpart (see Fig. 6.3).

As suggested in Narimanov and Stone (1999), one could consider the PO formula where it is significant —discarding the CCO formula—, and switch to the CCO formula where the PO disappears, that is for $\epsilon < 6500$. In the region $3000 < \epsilon < 5000$ the CCO gives a

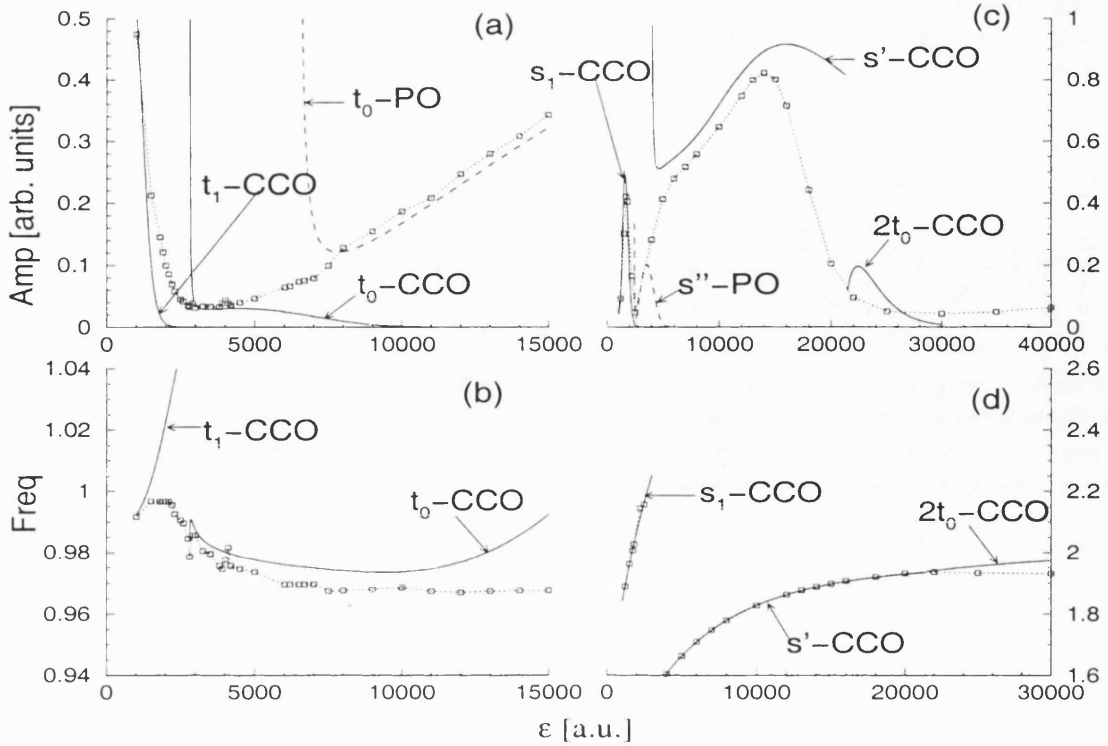

Figure 6.16: Comparison of the CCO formula (solid line) with QM results (dotted line with squares). We also show the contribution of t_0-PO and $s''-PO$ to the PO/NO formula (dashed line). (a) P1 amplitudes at $\theta = 11°$; (b) frequencies. (c) P2 amplitudes at $\theta = 27°$; (d) frequencies.

semiclassical amplitude and frequency that correspond to the quantum ones, but not for $5000 < \epsilon < 6500$ and beyond. At the lower end of the ghost region, a PO (t_1-PO) would take over correctly around $\epsilon = 2300$, leaving a small gap ($\epsilon = 2300 - 3000$) where the CCO disappears.

At $\theta = 27°$ we start by noting that the $2t_0$–CCO contribution is completely inaccurate, in both amplitude (c) and frequency (d). Once again, one can use a "multiple-orbits" strategy, and consider here only the more accurate $2t_0-PO$ contribution (see Fig. 6.4). Note that the CCO formula separates the contributions of s'–CCO and $2t_0$–CCO, avoiding the problem one has with their non-isolated PO companions. The s_1-CCO contribution is on the other hand as good as its PO counterpart. Here the PO is relatively centered on $z_0 = 0$, and therefore looks very similar to the CCO.

However, our main goal here is to succeed in the ghost region existing between the disappearance of $s'-PO$ in a tangent bifurcation at $\epsilon = 7700$ and the emergence of the similar looking $s''-PO$ joining QM results at $\epsilon = 3600$. The CCO extends considerably the range of the PO to $\epsilon = 4000$, leaving only a small gap until $s''-PO$ catches up.

The goal was to describe accurately the quantum behavior across the ghost region, using only real trajectories (in this case, CCOs). The CCOs clearly improve the PO formula at $\theta = 27°$ and more modestly at $\theta = 11°$, but is not completely satisfactory as it still leaves gaps in the ghost regions. Also, the CCO formula is very inaccurate in some other regions, showing that the underlying hypothesis (the predominance of the Gaussian over the Green's function oscillations related to the action) is not justifiable in many instances, especially in the regular limit. Finally, the strategy proposed in Narimanov and Stone (1999), although promising, is complicated to implement, as one has to switch between two different types of orbits (POs and CCOs) as the dynamics (governed by ϵ) change.

6.4.2 MO formula

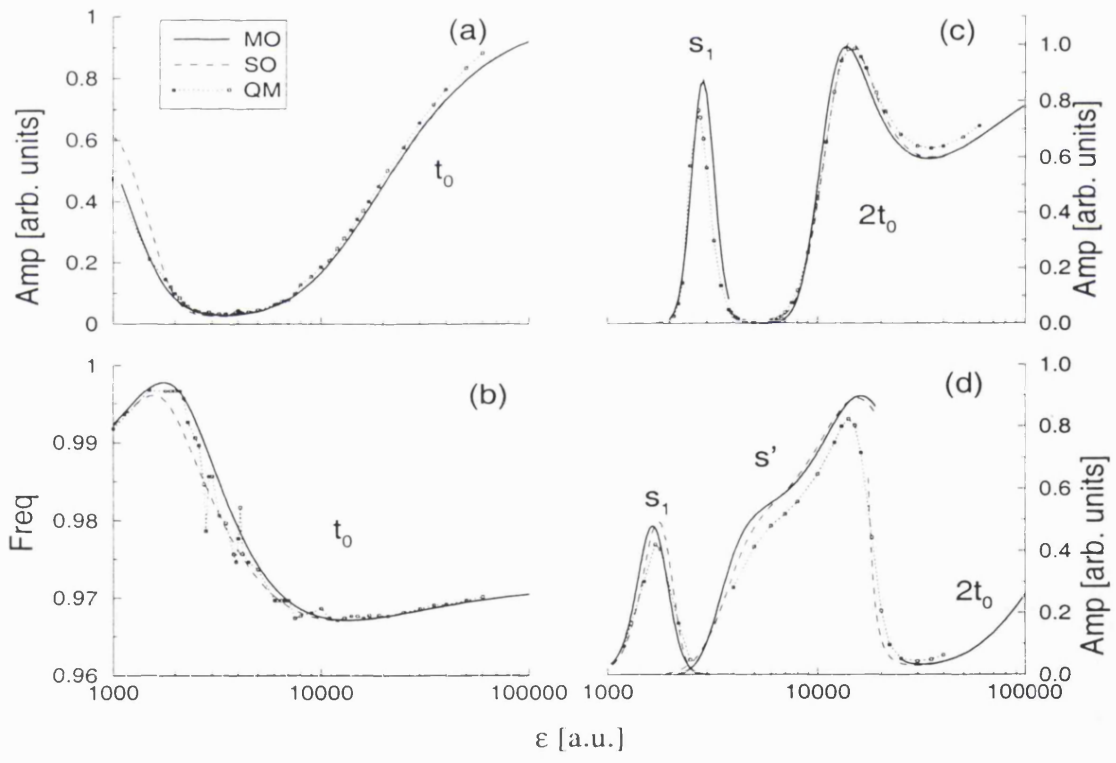

Figure 6.17: Semiclassical MO formula. (a) P1 amplitudes and (b) frequencies at $\theta = 11°$. P2 amplitudes at (c) $\theta = 11°$ and (d) $\theta = 27°$. We show the SO formula and QM results for comparison.

Here we test the minimal orbit (MO) formula; we recall that we found the MOs (5.69) when looking for the best *real* approximation of the SO. We show in Fig. 6.17 the results of the semiclassical MO formula. In (a) we see that the amplitude of t_0 –MO reproduces the SO formula extremely well, and hence, the QM results. The SO and MO formulae

are almost indistinguishable in most of the ϵ range. It is remarkable that the MO is so accurate in the ghost region where all the theories based on POs or CCOs fail. The only difference between the SO and MO amplitudes is at low ϵ; there the MO description is actually even better than the SO one. Note that as in the SO case, there is only one MO related to t_0–PO, $t_{\rm gh}$ and t_1–PO (not shown here).

The difference between the MO and the SO is stronger for the frequency of the oscillations, shown in (b). It is hard to assess which type of orbit is more efficient.

The P2 amplitudes at $\theta = 11°$ (c) are also very close the SO amplitudes, and improve the PO amplitudes (which were already quite accurate). The low ϵ peak of the s_1 orbit can be described indifferently by the MO, SO, PO or CCO corresponding to s_1.

The MOs also succeed for the P2 amplitudes at $\theta = 27°$, where the PO or CCO formulae fail. Like the SOs, $2t_0$–MO and s'–MO do not overlap, and the latter contributes correctly in the ghost region. Again, the MO and SO amplitudes are very close -within the disagreement with respect to QM results.

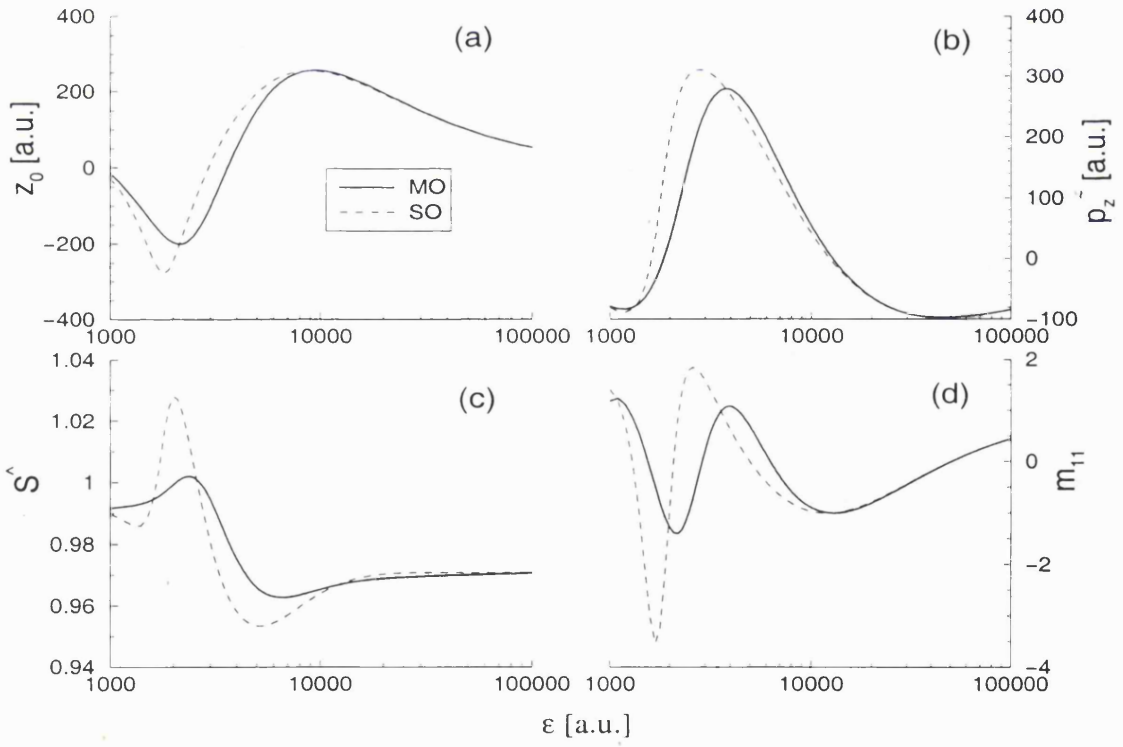

Figure 6.18: Classical characteristics of t_0–MO at $\theta = 11°$. (a) z_0; (b) $\tilde{p}_z^0$; (c) $\hat{S}$; (a) m_{11}. We show the real part of t_0–SO for comparison.

In Fig. 6.18 we investigate the evolution of the classical characteristics of t_0–MO at $\theta = 11°$. Fig. 6.19 shows s'–MO at $\theta = 27°$. The similarity between the MO and the real

part of the SO is striking. The starting momentum is a measure of how complex a SO is, as $\mathbf{Re}\, p_z^0 = -\beta \mathbf{Im}\, z_0$. Even for large values (i.e., when the SO is very complex), we see in (b) that $p_z^0[MO] \simeq \mathbf{Re}\, p_z^0[SO]$. This shows that the *real* MO, despite having no imaginary component, manages to be close to the SO.

This is well illustrated in Fig. 6.20 where we show the shape of t_0–MO at $\theta = 11°$ for different values of ϵ [they correspond to the situations in Fig. 6.12 (a)-(e)]. The shape of the MO is indistinguishable from the SO's for high ϵ; they are very slightly different for lower ϵ. We do not show shapes at $\theta = 27°$, where s'–MO and s'–SO are indistinguishable; this is not too surprising as in this situation the SO is quite real and very close to the PO already.

The starting conditions of the MOs are very close to the real part of those of the SOs. Their shapes are also very similar; this shows that the imaginary parts of the SOs do not change very much the shape and properties of the trajectories. One could therefore propose a last type of (real) orbits: the "real SOs", simply built by taking the real part of the starting conditions of the SOs, and evolving them with real time. Those trajectories would be very similar to MOs.

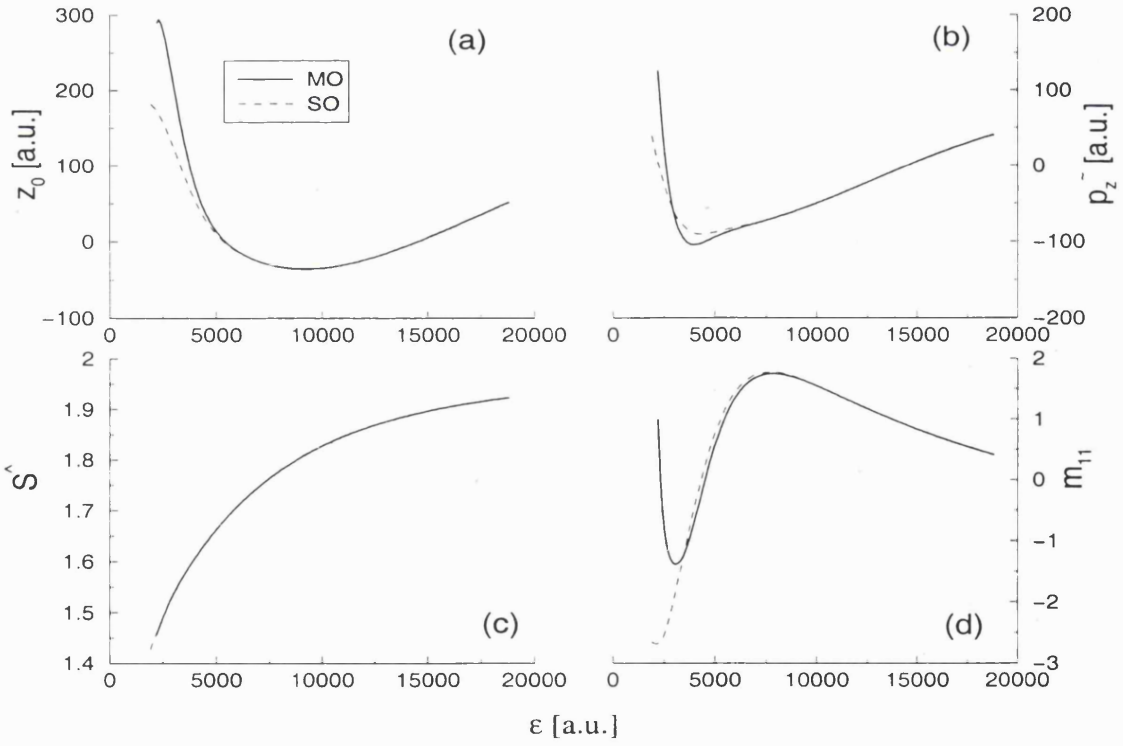

Figure 6.19: Classical characteristics of s'–MO at $\theta = 27°$. (a) z_0; (b) $\tilde{p}_z^0$; (c) $\hat{S}$; (d) m_{11}. We show the real part of s'–SO for comparison.

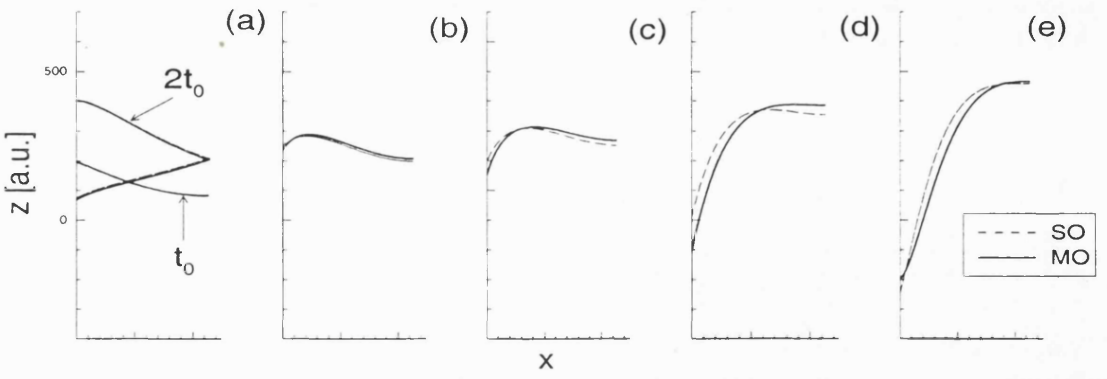

Figure 6.20: Shapes of t_0–MO at $\theta = 11°$. (a) $\epsilon = 20000$; (b) $\epsilon = 7000$; (c) $\epsilon = 5000$; (d) $\epsilon = 3000$; (e) $\epsilon = 2000$. We also show the real part of t_0–SO.

The success of the MOs shows that in our case we can relax the condition of stationary phase (which yields complex SOs) and merely demand that the orbits *minimize* the deviation from the saddle point.

6.5 Conclusion

Here we summarize the key points revealed by the comparisons presented in this chapter.

1. The hard limit formulae fail and in particular cannot reproduce the important tori quantization effects on the accessibility.

2. The periodic/normal orbit formula is successful in most regions. Only a very small subset of the orbits contribute to the current. The formula fails however in regions where one does not have an adequate real PO, and where one has two non-isolated competing POs.

3. The saddle orbit formula is very successful in all the cases presented here. It also shows a persistence in the classical limit, which is a remarkable fact for a contribution coming from a complex trajectory.

4. The central closed orbit formula improves the PO/NO theory where the latter fails, but is not as satisfactory as the SO formula.

5. The minimal orbits give a surprisingly accurate description of the current, which shows that one *can* approximate the SPA condition by real trajectories.

Chapter 7

COMPARISONS WITH EXPERIMENTS

So far, we have only assessed semiclassical theories by comparing them with results from quantum calculations; for the clarity of the graphs, we did not show experimental results. Here we present experimental amplitudes and voltage periods that we extracted from our normalized data shown in chapter 2. First we compare the amplitudes with quantum results in the situations already studied in chapter 6; the voltage periods are compared with semiclassical results. This represents a *quantitative* test of our theoretical model, across a wide range of parameters going from regular to chaotic regime.

In the following sections we present more experimental amplitudes, and discuss in detail some theoretical limitations. We discuss a divergence in the saddle orbit formula at $\theta = 20°$. This unravels interesting questions about saddle orbits, namely the presence or absence of "bifurcations".

At $\theta = 38°$ our quantum model reproduces the high ϵ region of experimental period-three oscillations, which has been at the center of a controversy (Fromhold *et al.* 1995a, Muller *et al.* 1995). Here we show that the semiclassical current is best described using the contribution of a minimal orbit 3:3 (i.e., the same bounce structure as the periodic orbit $3t_0$). We were unable to reproduce the low ϵ region of strong period-three oscillations, using both quantum and semiclassical approaches. We discuss the possible origin of the disagreement between our theoretical model and the experiments; in all likelihood, it comes from an increasing uncertainty in the position of the initial state, that has been shifted by the large tilt angle θ.

7.1 Comparisons with experiments

7.1.1 Amplitudes

We present some experimental amplitudes in Fig. 7.1; see the following sections for amplitudes at $\theta = 20°$ and $\theta = 38°$. As explained in chapter 2, we have changed the experimental amplitudes $A_{\rm EXP}(\epsilon_{\rm EXP})$ the following way:

$$\begin{cases} (i) & \epsilon_{\rm EXP} \to 1.3 \times \epsilon_{\rm EXP} \\ (ii) & A_{\rm EXP} \to e^{+(T_M - T_0)/\bar{\tau}} A_{\rm EXP} \end{cases} . \tag{7.1}$$

(i) corresponds to the shift in voltage due to the voltage dependence of the mass of the quasi-electron in the well. The factor 1.3 has been obtained empirically by studying P2 oscillations at $\theta = 11°$ (page 37). (ii) takes out the damping due to phonon emission for P2 or P3 amplitudes, as explained in subsection 2.3.4. We calculated the factor between the QM and experimental maxima (in ϵ) at $\theta = 16°, 20°, 27°$ and $38°$. We estimated the damping time τ in the four cases from the knowledge of the real part of the period T_M of the contributing minimal orbit (MO), and from the period T_0 of t_0 at $\theta = 0°$. Finally, we took their average which gave an estimated $\bar{\tau} \simeq .115$ps. We recall that we read the experimental amplitudes at $V = 0.5$ V.

At $\theta = 0°$ (a) the QM amplitudes are constant, reflecting the perfect overlap between the initial Gaussian and the contributing states in the well. The experimental amplitudes are constant at high ϵ, and are overestimated by the QM by some 15%. At lower ϵ they vary (with a maximum of 20%) around the constant value of the QM results. This disagreement is due to the fact that the envelopes of the experimental traces at $\theta = 0°$ vary with different magnetic field values (see section 2.2). This figure presents the amplitudes as a function of the scaled dynamics parameter $\epsilon = F/B^2$ taken at $V = 0.5V$, which means that different ϵ correspond to different values of B and, therefore, different envelopes. To describe these variations one would need a much better knowledge of experimental details, such as the widths and heights of the barrier, the decoherence time, and the precise voltage dependence of the mass. One could expect such disagreement at $\theta = 0°$ to add up to any disagreement seen at higher angles. However, we see in (b)-(d) that the theoretical model is quite successful at higher angles, also within some 25% accuracy. Hence, the disagreement seen at $\theta = 0°$ does not seem to be a systematic effect. (For instance, it could be due to a 1° uncertainty in θ possible in the Bell Labs experiments.)

At $\theta = 11°$ (b) the QM calculations manage to describe the increase of the experimental

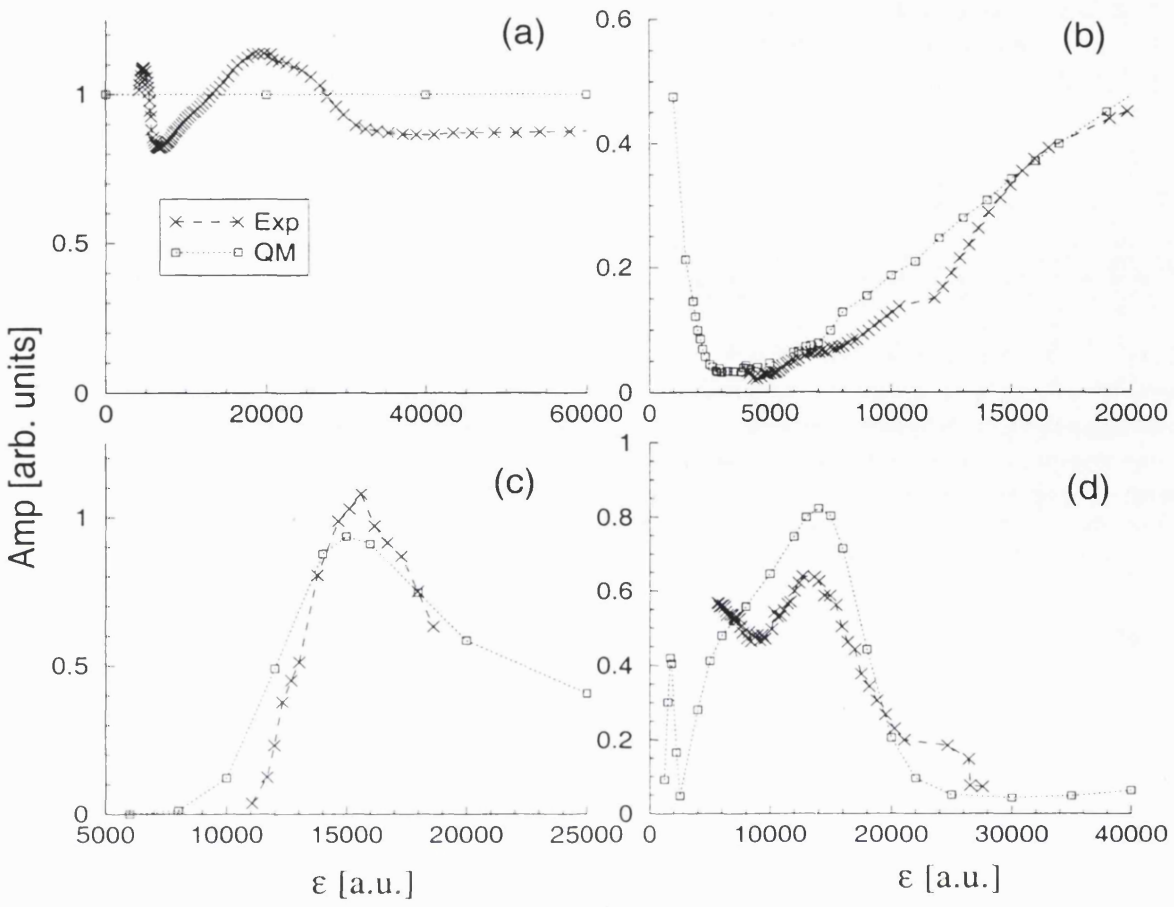

Figure 7.1: Comparison of experimental amplitudes and quantum calculations. P1 at (a) $\theta = 0°$ and (b) $\theta = 11°$. P2 at (c) $\theta = 16°$ and (d) $\theta = 27°$.

signal fairly well (within 25% accuracy). Note in particular the experimental P1 signal between $\epsilon = 4000$ and 7000, where no real periodic orbit (PO) could contribute for a corresponding semiclassical current. This the most important "no (real) PO" region that we mentioned in previous chapters; we see here that the experimental amplitudes decrease only slowly with ϵ. We were unable to get reliable P1 experimental amplitudes for $\epsilon >$ 20000 as there is also a P2 signal.

The agreement at $\theta = 16°$ (c) is quite good. The QM model describes correctly the shape of the experimental signal; the position of the maximum is right, and its height is within 15%.

At $\theta = 27°$ the QM model describes qualitatively the broad experimental region, but overestimates it by roughly 20%. This problem might be related to our taking the average of the damping times, as here the factor between the QM and experimental maxima is almost twice the factors at $\theta = 16°$ and 20°, while the periods of the classical orbits

are the same (see Table 2.3.4). The damping time might vary with the angle and the average damping time used here might be too small. Also, some experimental amplitudes presented in (c) are greater than one, i.e., greater than at $\theta = 0°$; this is not expected as the overlap is perfect in the latter case.[1]

In summary, this study shows that our theoretical model, although rather simplistic, manages to qualitatively describe the experimental behavior. It provides us with amplitudes which agree quantitatively with the experimental ones to within $\sim 25\%$.

7.1.2 Voltage periods

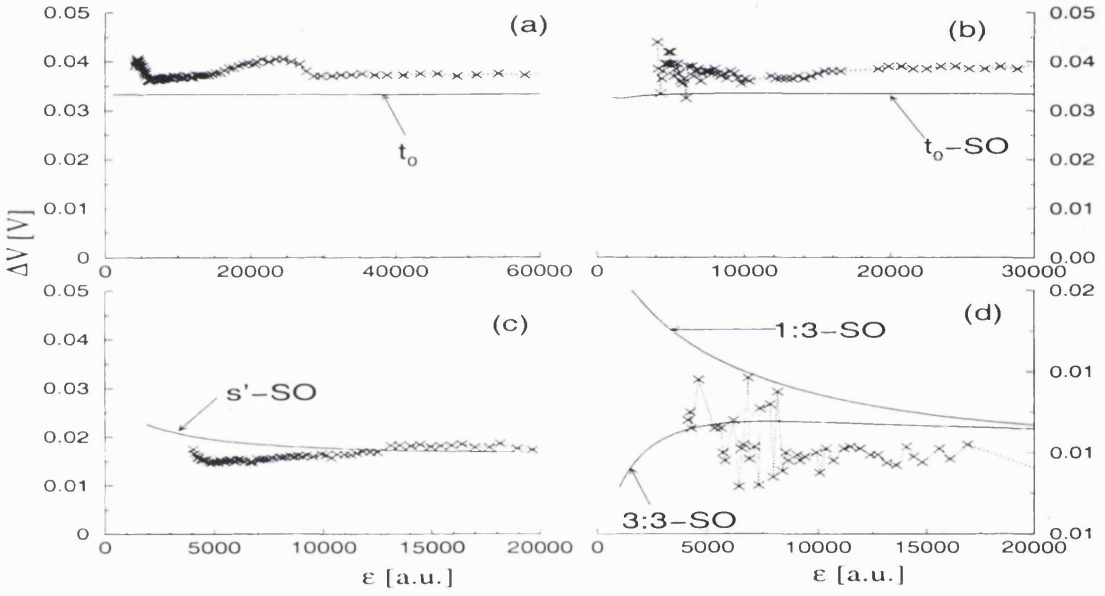

Figure 7.2: Voltage periods from experimental readings and from the SO semiclassical theory. (a) P1 at $\theta = 0°$. (b) P1 at $\theta = 11°$. (c) P2 at $\theta = 27°$. (d) P3 at $\theta = 38°$.

We show in Fig. 7.2 a comparison between semiclassical and experimental voltage periods, in order to check the relationship between classical orbits and the voltage periods of the experimental oscillations. As usual, we have displaced the experimental results ($\epsilon_{EXP} \rightarrow 1.3 \times \epsilon_{EXP}$). On the theoretical side, we use (5.91) to generate *semiclassical* voltage periods from the oscillatory factor $\hat{\Sigma}$ of saddle orbits. We use SOs because we have many more points (in ϵ) for them than for the QM; also, we know from subsection 6.3.3 that they both agree very well.

At $\theta = 0°$ (a) there is only the P1 signal coming from the straight traversing PO t_0

[1]Note that actually the experimental amplitudes at $\theta = 0°$ shown in (a) are unity within 20% only!

(which is also a SO and a MO). The semiclassical period is constant and underestimates the experimental period by 10%. The situation is similar at $\theta = 11°$ (b). These discrepancies are probably related to the voltage dependence of the mass, which displace the voltage and therefore the voltage periods.[2]

In (c) we show results for the P2 signal at $\theta = 27°$. The semiclassical period varies while the experimental periods are more constant, but the agreement is good.

At $\theta = 38°$ (d) we have two important SOs (see Fig. 7.6 in page 170): 1:3 which dominates at low ϵ, and 3:3 which describes the high ϵ period-three signal. The voltage periods for the latter are in agreement with the experiment. The low ϵ signal, however, shows a large disagreement (30%) with the 1:3 contribution. This shows that 1:3 might not be related at all to the experimental P3 oscillations (see also the discussion in subsection 7.3).

The table below summarizes the relationship between experimental oscillations and the scaled oscillatory factor $\hat{\Sigma}$ defined in (5.81). We used (5.91) to calculate an "experimental" $\hat{\Sigma}_{\rm EXP}$, that corresponds to the experimental voltage period ΔV. This can help us to identify which type of trajectory (t, s, 1:3, etc.) can explain the experimental oscillations. We see that the P3 experimental signal at low ϵ should be described by a SO having $\hat{\Sigma}_{\rm EXP} \simeq 3.23$. Unfortunately, we have not found any SO with significant amplitude giving such oscillations.

Period	ΔV[V]	$\hat{\Sigma}_{\rm EXP}$	$\hat{\Sigma}_{\rm SO}$	SO
P1	0.037	0.87	$0.94 - 0.99$	t
P2	0.017	1.90	$1.43 - 1.93$	$2t, s', s_1$
P3	0.010	3.23	$1.55 - 2.85 - 3.3$	$3t$, 1:3, 3:3

Table 7.1: Experimental oscillations, voltage periods ΔV, "experimental" oscillatory factor $\hat{\Sigma}_{\rm EXP}$ corresponding to ΔV from (5.91), semiclassical $\hat{\Sigma}$ of the different SOs.

[2] Actually, using $\epsilon \to 1.3 \times \epsilon$ would push the experimental ΔV even higher.

7.2 P2 at $\theta = 20°$ and SO divergence

7.2.1 Amplitudes

In Fig. 7.3 we present the amplitudes of the different semiclassical theories for P2 oscillations at $\theta = 20°$. We compare them with QM results and experimental readings.

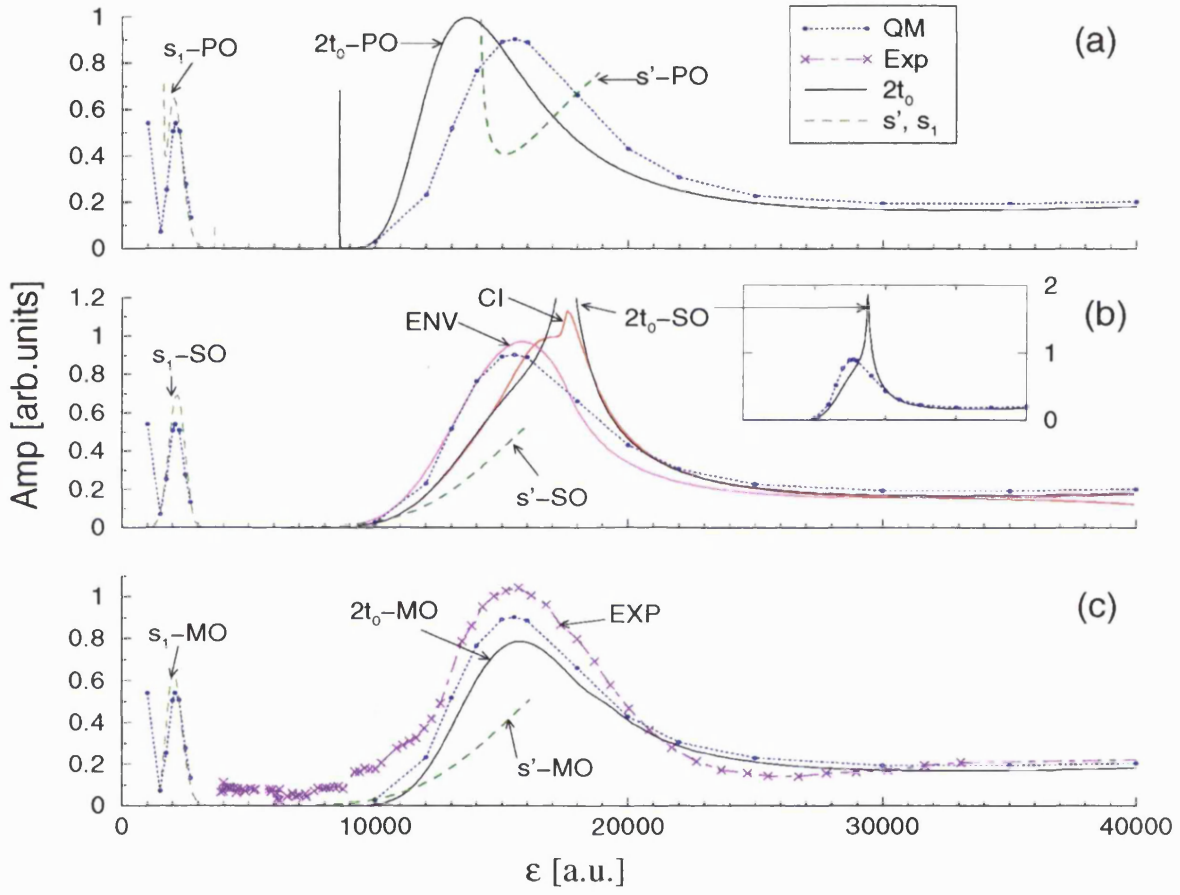

Figure 7.3: The different semiclassical theories for P2 amplitudes at $\theta = 20°$. The broad maximum is related to $2t_0$ and s' orbits, while the lower maximum is given by s_1 orbits. We show QM results (dotted line with squares) and experimental readings [EXP]. (a) PO/NO formula. (b) SO formula. We also show the exponential envelope [ENV] (i.e., we set $\tilde{\mathcal{D}} \equiv 2$ in the SO formula), as well as a cubic integration of the SO formula [CI]. The inset is in a larger scale. (c) MO formula and experimental results. The latter have been transformed through (7.1).

The PO/NO formula (a) is slightly wrong in its description of the large quantum peak around $\epsilon \simeq 15000$. Comparing with Fig. 6.4, we see that the discrepancy in the height and position of the peak grows with θ, as does the importance of the s'–PO contribution. As for $\theta = 27°$ (see subsection 6.2.2), we have the problem of the coherent superposition

of $2t_0-PO$ and $s'-PO$, which are not isolated. The latter seems to push slightly the QM maximum towards higher ϵ. The lower ϵ peak around $\epsilon = 2000$ due to s_1-PO is well described. As the related SO and MO do not have a bifurcation there, their contribution is slightly better than with the PO.

Things are more complicated for the SO formula (b). Its amplitude shows a very large peak at $\epsilon = 17540$ (see inset). As we shall explain below, this is due to the fact that the determinant $\mathcal{D}$ appearing in the semiclassical formula (5.35) almost vanishes. This yields an inaccurate contribution from the SO. We attempted to solve this problem by using a cubic integration of the SO formula; we used the same method[3] as the one we shall describe in section 8.3. Although the cubic integration result removes part of the abrupt behavior, it still does not give a satisfactory agreement with the QM results.

A simpler way to neutralize the divergence of the prefactor is to set the latter to the constant value is has at $\theta = 0°$ ($\tilde{\mathcal{D}} = 2$, see subsection 5.3.1), and to consider only the exponential envelope in the SO formula. Surprisingly, this works better. Note that $s'-SO$ (as well as $s'-MO$) behaves in a different way to $s'-PO$; it exists for lower ϵ and gives a smaller contribution. The latter is not negligible, but is not apparent in the quantum behavior. This shows that the situation at $\theta = 27°$ (where the SOs separated successfully the contributions of the POs $2t_0$ and s') was somewhat lucky; here one is confronted by the same problem of having to consider the global contribution from both SOs, or else to give a justification for neglecting $s'-SO$.

The MO results (c) are not as good as expected. $2t_0-MO$ does not show any pathological behavior and has the correct shape, but underestimates the QM by 15%.

Finally, we compared SC and QM results with experimental readings (c). We see that the theoretical quantum model underestimates the experiments by some 15%, but gets the qualitative shape correctly over a very wide range ($10000 < \epsilon < 40000$). Note that the experimental maximum is larger than one, which might indicate an inaccuracy in the damping time.

[3]In the SO case, the linear term R_1 in (8.25) is zero. We cannot define "neighbor" derivatives as we did not found any partner of the SO. The numerical derivatives that we used here are always complex, which makes the cubic integral diverge; we nevertheless considered the result in terms of an Airy function. Also, the Airy function and its argument (given by a root) are multi-valued; we chose the phase of the root that gives the good behavior, i.e., so that the result tends towards the quadratic SO formula.

7.2.2 Details of the SO divergence

In Fig. 7.4 (a) we show the scaled determinant $\tilde{\mathcal{D}} = \mathcal{D}/B$ (5.34) of $2t_0 - SO$. Both its real and imaginary parts come very close to zero at $\epsilon = 17540$. This is a remarkable coincidence, as usually one needs to vary *two* real parameters to locate the zero of a complex function —i.e., one expects $\mathcal{D}(\epsilon_z) = 0 \Rightarrow \epsilon_z \in \mathbb{C}$. As the current is proportional to $|\mathcal{D}|^{-1/2}$, this brings the abrupt enhancement of the current seen in Fig. 7.3 (b).

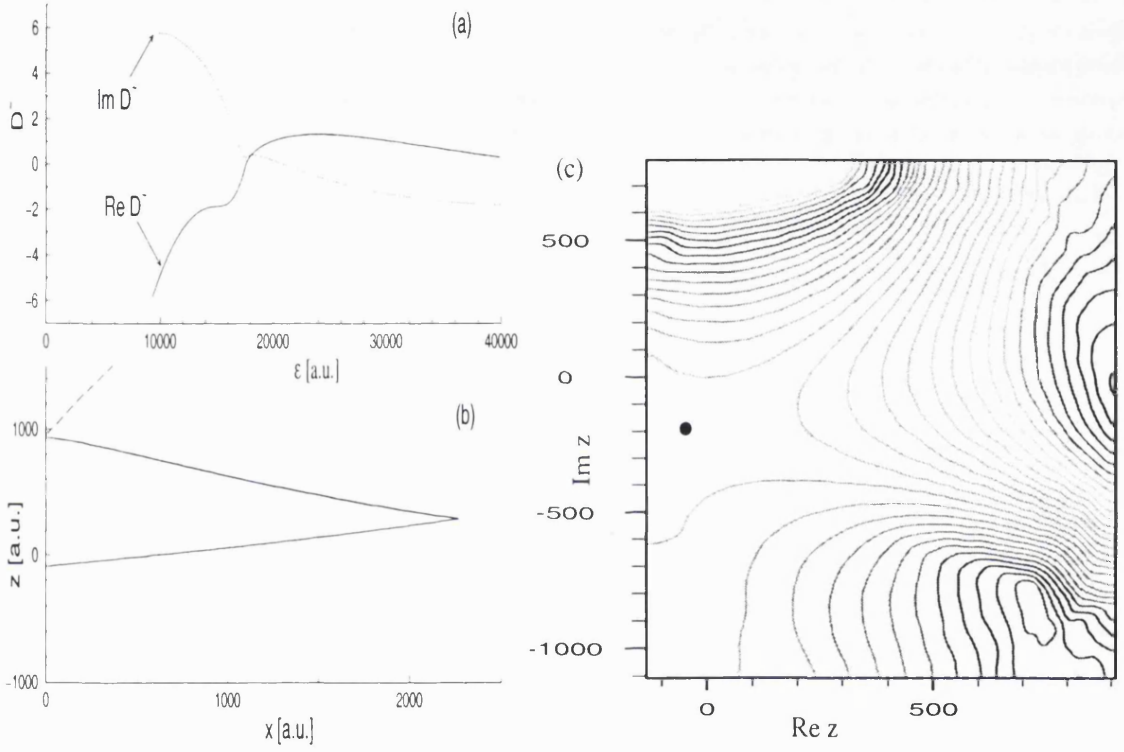

Figure 7.4: Details of $2t_0 - SO$ at $\theta = 20°$. (a) $\mathrm{Re}\,\tilde{\mathcal{D}}$ and $\mathrm{Im}\,\tilde{\mathcal{D}}$. (b) $(\mathrm{Re}\,x, \mathrm{Re}\,z)$ shape at $\epsilon = 17476$. The boundary of the energy surface is shown (dashed line). (c) Contour lines of $\mathrm{Re}\,\hat{\Gamma}$ in the $(\mathrm{Re}\,z, \mathrm{Im}\,z)$ plane at $\epsilon = 17476$, calculated for 2:2 TSCOs. The dot is $2t_0 - SO$.

As the behavior of $\mathcal{D}$ is not very smooth around that point, we show the evolution of the classical characteristics of $2t_0 - SO$ in Fig. 7.5. *Every* characteristic shows an abrupt change around $\epsilon = 17500$. $\mathbf{Re}\, z_0$ (a) reaches its minimum at $\epsilon = 17476$, where $\mathbf{Im}\, z_0$ undergoes a pronounced changeover. $\mathbf{Re}\, \hat{S}$ (b) has a peak at $\epsilon = 17588$, while its imaginary part changes abruptly over $17000 < \epsilon < 18000$. $\mathbf{Re}\, m_{11}$ (c) peaks at $\epsilon \simeq 16800$, $\mathbf{Im}\, m_{11}$ at $\epsilon = 17600$.

This kind of behavior —with dependences of the type $\epsilon^{1/n}$— is reminiscent of bifurcations, as will be shown in Fig. 8.3. One should also be able to find the complex value ϵ_z for which $\mathcal{D} = 0$, where one would have a degeneracy in the quadratic expansion (5.20,5.28)

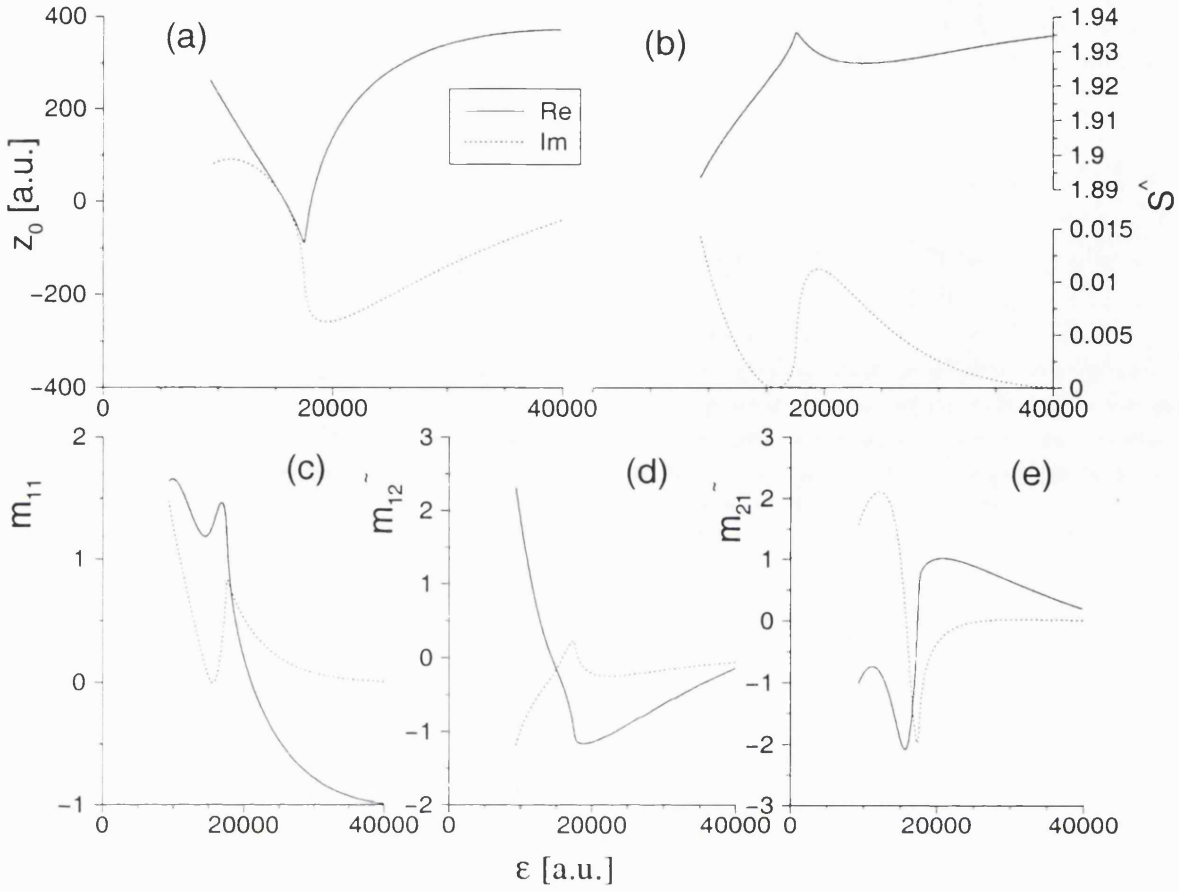

Figure 7.5: Classical properties of $2t_0$–SO at $\theta = 20°$. Real part (solid line) and imaginary part (dotted line). (a) z_0; (b) $\hat{S}$; (c) m_{11}; (d) $\tilde{m}_{12}$; (e) $\tilde{m}_{21}$.

of $\varphi(z, z') = iS(z, z') - \frac{\beta}{2}(z^2 + z'^2)$.[4] This would be in a sense the equivalent of the degeneracy of the action expansion found for bifurcating POs (where $\mathrm{Tr}M - 2 = 0$). However, we did not find another SO that should be the partner of $2t_0$–SO *if* it underwent a type of bifurcation. In Fig. 7.4 (c), we show the real part of $\hat{\Gamma}$ for 2:2 time-symetric closed orbits [TSCOs, see (5.38)]. We see the saddle point at $z = (-80, -188)$ and found no neighboring SO.[5] Note that this quasi-degeneracy makes the saddle point of $\mathbf{Re}\,\hat{\Gamma}$ very "flat".

Hence we can think that the degeneracy is not linked to a pair of SOs "bifurcating", but to some other reason. $2t_0$–SO is very close to the left limit $\mathbf{Re}\,z \simeq -100$ [see Fig.

[4]The fact that the ϵ where those changes occur are all different is somewhat surprising, but they are expected to converge in the limit $\epsilon \to \epsilon_z$.

[5]Note that a emitter PO undergoing a cusp bifurcation has a PO partner that has a different number of bounces on the emitter wall (Narimanov and Stone 1998b). We might have a similar situation for SOs, but we did not find any 1:2 or 2:2 SO in the vicinity of $2t_0$–SO.

7.4 (c)]: for $\mathbf{Re}\, z < -100$, one cannot find TSCOs making two bounces on the each wall; they miss a bounce on the left wall in a cusp event. This is seen in Fig. 7.4 (b): the outer leg of the SO is very close to the energy surface. In Fig. 7.5, $2t_0 - SO$ looks as if it were going to suffer a cusp event. Increasing ϵ, one expects $\mathbf{Re}\, z_0$ to change monotonically, i.e., to decrease, but decreasing slightly $\mathbf{Re}\, z_0$ makes the trajectory miss the bounce, changing abruptly its properties. Surprisingly, we do not have a cusp event here: one can still find the correct SO, and $\mathbf{Re}\, z_0$ increases suddenly. It appears that $2t_0$–SO manages to "escape" the cusp event.

Note that the proximity of a cusp event could have consequences on the semiclassical current. Strictly, one should not integrate (5.25) on the whole (z, z') plane, but only on the domain Ω where one does find the proper type of trajectory (2:2). Hence one should cut the integral for $z < -100$; this would yield error functions. In this case this would strongly affect the result, as the cut-off would be very close to the SO itself. We did not try this idea as we should then apply a similar cut-off in *all* regimes. We do not believe that it could improve significantly the results (we mentioned a similar study for POs in page 137).

This situation raises very interesting questions about saddle orbits.

1. *Do they undergo a type of bifurcation?* Apparently no, as a bifurcation should involve several SOs, which we have not seen.

2. *What is the origin the quasi-degeneracy?* It seems to come from a failed cusp event.

3. *Does it has an effect on the semiclassical current?* Yes, the current shows a strong enhancement.

4. *Do quantum results show any sign of it?* Apparently no, as the QM results are very smooth in that region.

5. *What techniques can be employed to solve that problem?* We tried a cubic expansion, which removed most of the enhancement but did not show good agreement with quantum calculations. One could try a cut-off in the integral. The first thing to do would be to locate the complex ϵ_z where $\mathcal{D} = 0$.

7.3 P3 at $\theta = 38°$ and theoretical limitations

The interpretation of the experimental period-three oscillations has been very controversial (see the discussion in subsection 3.2.5). It was interpreted in Müller *et al.* (1995) as a manifestation of the period-three bifurcation of t_0–PO. Fromhold *et al.* (1997a) did not agree, arguing that t_0 was not accessible; they believed that 1:3–PO was responsible. The controversy arose because no semiclassical theory for the current was available, and because the high tilt angle was expected to have important consequences on the accessibility of the different orbits.

At $\theta = 38°$ we expect the displacement of the center of the initial state Gaussian to be sufficiently large to have a deep influence on the theoretical results. Hence, we shall take it into account. Also, the large tilt angle might result in having excited states in the initial state. Both facts require modifications of the semiclassical formulae.

7.3.1 Semiclassics for a shifted initial state

We can estimate the shift of the initial state using (5.16):

$$z_S \simeq -250 \tan\theta \text{ [a.u.]} \quad . \tag{7.2}$$

The negative sign comes from the work of Fromhold *et al.* (1995a). For the PO formula, this only changes the semiclassical formula in a simple way; one has to replace z_0 by $z_0 - z_S$ in the expression of Γ_{PO} (5.62).

On the other hand, the shift of the initial state affects strongly SOs, even in their *definition*. They now have to satisfy

$$p_z^0 = i\beta(z_0 - z_S) \quad , \quad p_{z'}^0 = -i\beta(z_0' - z_S) \tag{7.3}$$

instead of (5.43). Hence, one has to find new SOs for each different z_S considered. MOs are also affected, but we did not look for displaced MOs in this situation. We found the "shifted" SOs for $\theta = 38°$, and shall use them in the study below.

7.3.2 Semiclassics for a shifted and excited initial state

The assumption that only the lowest Landau state is occupied by the electrons in the emitter can become inaccurate for higher tilt angles. The x degree of freedom can gain some energy by the z component of B, which can be transferred to the z degree of freedom.

We considered a mixture of lowest and first excited Landau levels (5.18)

$$\phi(z) = \left(\frac{\beta}{\pi\hbar}\right)^{1/4} e^{-\frac{\beta}{2\hbar}z^{\dagger 2}} \left[\mathcal{C}_0 + \mathcal{C}_1 z^{\dagger}\right] \quad , \tag{7.4}$$

with $\mathcal{C}_1 = \sqrt{(1-\mathcal{C}_0^2)\,2\beta/\hbar}$ and $z^{\dagger} = z - z_{\rm S}$.

The SOs are defined by the steepest-descent condition, which is more delicate to apply on (5.19) when the initial state has an excited component. It now involves integrals of the type

$$\int du\, e^{is(u)/\hbar - bu^2/\hbar} u = \int du\, e^{is(u)/\hbar - bu^2/\hbar + \ln u} \quad . \tag{7.5}$$

The steepest-descent condition would read $is' - 2bu + \hbar/u = 0$, which poses a problem as the $\hbar$ dependence does not scale out. In the $\hbar \to 0$ limit we would in effect neglect the linear term. In a strict semiclassical limit, this is justified as the linear u function is varies slowly compared to $e^{is(u)/\hbar - bu^2/\hbar}$, and can therefore be neglected in the steepest-descent condition and integration. However, the experimental system is not in a high semiclassical regime, and the linear term does shift the position of the maxima of the Gaussian in a noticeable manner.

As we are unable to include the excited Landau state in the saddle point condition, we neglect it, and consider *shifted* SOs (7.3) taking into account $z_{\rm S}$. On the other hand, we do not neglect the linear term (coming from the excited state) in the integrations, which finally give for time-symmetric SOs:

$$I_{\rm SC} = \mathbf{Re}\sqrt{\frac{2\beta}{\mathcal{D}}} e^{iS - \beta z_0^{\dagger 2}} \times \left[\mathcal{C}_0^2 + 2\mathcal{C}_0\mathcal{C}_1 z_0^{\dagger} + \mathcal{C}_1(z_0^{\dagger 2} + i/\mathcal{D})\right] \tag{7.6}$$

in atomic units.

7.3.3 Amplitudes

We show in Fig. 7.6 different semiclassical approaches for the P3 amplitudes, that we compare to QM calculations and experimental readings.

The first graph to look at is (f), where we show only QM and experimental results. The high ϵ experimental peak is qualitatively described by the QM calculations. Here there are only made for an unshifted initial state; the shift does not seem to be essential in this regime. We recall that this is the region at the center of the debate between the Bell Labs and the Nottingham groups. On the other hand, the low ϵ experimental region is much higher than the QM results. Even shifted calculations are not successful. This is the motivation for considering excited Landau levels in the semiclassical theories.

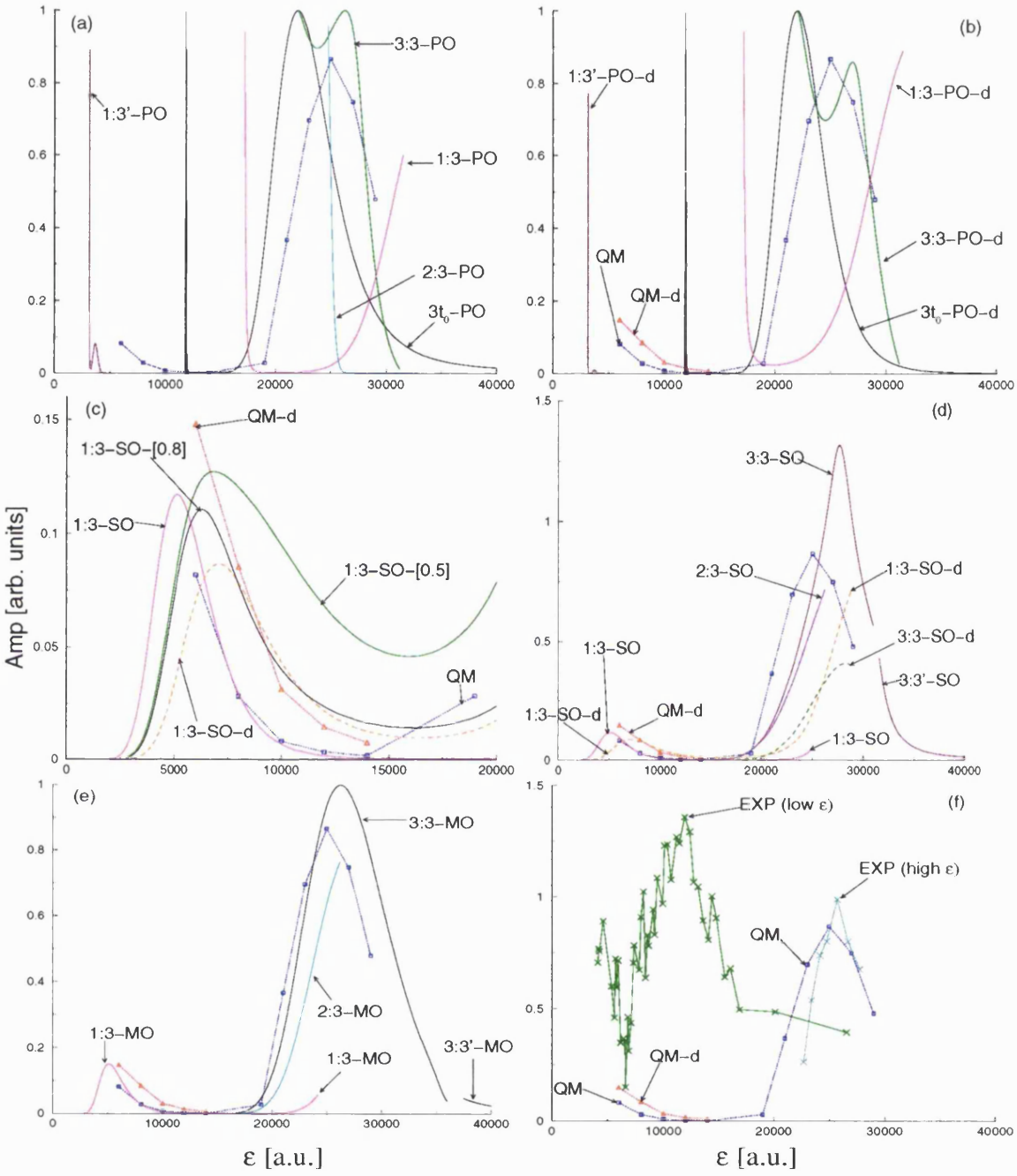

Figure 7.6: Semiclassical, quantum and experimental P3 amplitudes at $\theta = 38°$. Results with a displacement of the center of the initial state Gaussian are indicated by -d; this also applies for low ϵ QM results [see (f)]. For clarity, we do not present the contributions of all the orbits in all the cases. (a) Undisplaced and (b) displaced PO results. (c) Low ϵ detail for SOs with undisplaced and displaced Gaussian; we also show the results with an excited displaced initial state with $\mathcal{C}_0 = 0.8$ and 0.5. (d) Displaced and undisplaced SO formula. (e) Undisplaced MO formula. (f) Experimental results (showing two maxima) and QM results; for low ϵ we also show QM results with a displaced initial state.

The PO/NO formula for an unshifted initial state is shown in (a). First we see that the non time-symmetric PO 2:3 does not contribute to the current. The QM maximum around $\epsilon = 25000$ seems to be related to $3t_0$ and 3:3, which would confirm the analysis of Müller *et al.* (1995). Again, one has the problem of having too many POs contributing to the current.[6] The effect of 3:3 seems to shift the position of the maximum of $3t_0$ towards higher ϵ where the QM results peak. The PO 1:3 gives an important contribution, but is not related to the QM behavior. The small quantum P3 signal at low ϵ cannot be described by 1:3′.

The $3t_0$ and 3:3 contributions drop slightly in the shifted case (b), as the POs are even further away from the center of the Gaussian. On the other hand, 1:3 gives a more important contribution, as it is on the other side of the SoS. The QM signal at low ϵ increases slightly; this means that a classical structure localized on negative z contributes to the current (at high ϵ we only present unshifted QM results).

In (d) we present SO results, in both shifted and unshifted cases. In the unshifted case, 3:3 has a very high peak at $\epsilon = 27600$. This is similar to the situation of $2t_0$ at $\theta = 20°$: here $\mathcal{D}$ approaches 0. We did not calculate a cubic integration to attempt to solve that problem, which disappears naturally in the shifted case. 2:3 has a large contribution (in contrast to the PO case) that follows somehow 3:3; it is interesting to note that $2{:}3{-}SO$ is not time-symmetric, and therefore is not closed. The contribution of 1:3 at high ϵ is negligible in the unshifted case, but becomes more important in the shifted case. The agreement of the (unshifted) SO contributions with the quantum peak at high ϵ is not good.

Details of the low ϵ P3 signal, which is due to 1:3, are shown in (c). Here the agreement with the QM results is good, in both the unshifted and shifted cases. In the latter case, the height of the maximum of the contribution drops slightly, but its position is shifted and gives a stronger signal than in the former case. We also present the results with a shifted and *excited* initial state, given by (7.6). We do not have any *a priori* idea of the relative balance between the lowest and the first excited states; we have taken *arbitrary* values for $\mathcal{C}_0$. For $\mathcal{C}_0 = 0.8$ the signal is not changed very much apart from the increase of the height of the maximum. The balanced repartition $\mathcal{C}_0 = 0.5$ yields a stronger signal; it is however much too small to describe the large experimental amplitude seen in (f). We do

[6] A study (not shown) of the Husimi functions of a quantum state carrying the current shows that the state is linked to *both* POs; it is localized on an outer quantized torus of t_0, that is distorted and has three peaks corresponding to 3:3. This is similar to the situation at $\theta = 27°$ with t_0 and s' (Fig. 4.12).

not expect agreement with quantum calculations as those were made with the assumption of a pure lowest Landau state.

In (e) we present results for MOs, considering an unshifted lowest Landau state. 2:3 gives a significant contribution, but it is apparently not related to the QM results, which are qualitatively described by 3:3 at high ϵ and by 1:3 at low ϵ. Altogether, MOs improve slightly over SOs as there is no problem with the prefactor $\mathcal{D}^{-1/2}$.

7.3.4 Discussion

The high ϵ experimental peak can be described by quantum calculations, using an unshifted initial state. For all types of orbits (POs, SOs and MOs), we have the problem of non-isolated orbits. The SO contribution of 3:3 is too large because $\mathcal{D}$ is very small. The minimal orbit (MO) theory achieves the best result with $3{:}3-MO$, which has the same bounce structure as the PO $3t_0$. However, it is not as accurate as one could expect from the study at $\theta = 11°$ and $\theta = 27°$. The situation is similar to the one for P2 at $\theta = 20°$. One SO contribution almost diverge, and the related MO contribution is too large with respect to the quantum behavior. This might be a sign that the divergence of the SO affects the MO behavior.

PO theories are unable to give a correct description of the quantum amplitudes for both P3 regions. We have carried out a quantitative assessment of the arguments presented by the Yale and Nottingham groups. As the contribution of $3t_0$ and 3:3 are important and describe qualitatively the experiments, Fromhold *et al.* (1997a) were not right: these orbits can contribute. The reason for this is not an excited state as proposed in Boebinger *et al.* (1997), but simply the fact that the PO/NO formula enables $3t_0$ and 3:3 to contribute to the current, even if they are far off-center. Moreover, the contribution of the PO 1:3 [proposed by Fromhold *et al.* (1995a)] is not related to the quantum and experimental behavior for both regions, although it gives an important contribution at high ϵ.

We have *no* quantum or semiclassical contribution that corresponds to the very large experimental P3 signal seen at low ϵ. We tried to find all SOs up to 6:6, but the SOs giving appropriate oscillations ($\hat{\Sigma} \sim 2.5 - 3.5$, see subsection 7.1.2) have very weak amplitudes. We recall that the SO and MO semiclassical theories describe accurately the quantum signal. It is the quantum results in themselves that fail to describe the experimental amplitudes. This remains an unsolved problem.

The reasons for this failure are very probably linked to the problem of the shift of

the initial state. The value we have employed might have been too small; also, there is a possibility of a shift in the z momentum. A different shift has important consequences, as it can give an important contribution to other classical structures. For instance, it defines different saddle or minimal orbits, that might not exist for the value of the shift considered here. In particular, one should look for an orbit with the appropriate action (to give the period-three signal), but with a smaller period, so that it is not damped to strongly.

A rigorous physical picture of the shift is difficult; it should involve the complete 3-D system and should consider the propagation of a Gaussian wave packet across a tunneling barrier in *two* dimensions.[7] This could have consequences on the Bardeen tunneling matrix element, as the latter is derived for one-dimensional barriers.

Other possible explanations for this failure include:

1. We failed to find the contributing PO or SO responsible for the experimental current. However, the QM current should "know" about this classical structure; it would underestimate its contribution only if the shift of the Gaussian is completely wrong.

2. Our estimation of the phonon emission damping time is not accurate for the low ϵ P3 region. A 10% error on $\bar{\tau}$ translates into an overestimation of 50% of the experimental amplitudes. However, the experimental signal is about ten times stronger than the maximal quantum signal at low ϵ.

3. The SPA condition with a excited Landau level does not yield SOs, but a completely different type of trajectories.

4. The initial state has higher excited Landau levels.

[7] Fromhold *et al.* (1995a) estimated the shift by looking at the propagation of a classical distribution of electrons (from the emitter through the barrier), neglecting the barrier height.

Chapter 8

COMPLEX DYNAMICS AND SEMICLASSICS

It was observed in chapter 2, 3 and 6 that there are wide regions of experimental and quantum oscillations where no related real periodic orbits (POs) can be found. This is primarily a consequence of tangent bifurcations, at which pairs of real POs vanish. From preceeding work on the kicked rotor (Kus *et al.* 1993) and the hydrogen atom (Main and Wunner 1997), one can expect the current in the RTD to have contributions from *ghost* orbits (complex POs). This chapter is devoted to a detailed study of ghost POs and their connection to saddle orbits.

We start by discussing general aspects of complex dynamics in the RTD and present the classical behaviour of ghost orbits (section 8.1). Then we study their contribution to the periodic/normal orbit formula (section 8.2). Because of the presence of tangent bifurcations (where the quadratic expansion of the action becomes degenerate), we also develop a cubic integration formula (section 8.3). We shall see that none of these formulae succeed in giving an accurate estimation of the current amplitudes. We nevertheless present these detailed studies, in order to clarify the reasons for their failure. Also, we hope that it contains interesting phenomena, which may be relevant to other systems involving complex contributions.

On the other hand, we know from chapter 6 that the accurate semiclassical description is given by the complex saddle orbits (SOs). We shall try to find a relationship between SOs and POs, by the study of a third order approximation of SOs (section 8.4). Again, this will not be entirely successful, but it will help us to understand why the saddle orbit formula is necessary when there is no real adequate PO. In particular, we shall see that

the failure of the PO/NO formula is not due to the action being cubic near the tangent bifurcations, but to the fact that one has *two* POs (one real and one ghost) related to *one* SO.

8.1 Complex dynamics

This section presents a discussion of general aspects of the complex dynamics. Although this discussion is not strictly essential to the global study of quantum chaos in the RTD[1], it raises interesting questions, such as the definition of hard bounces in complex dynamics, the freedom in the evolution, and singularities.

8.1.1 General remarks

Complex classical dynamics is not very obvious conceptually, but proved surprisingly easy to be implemented on a computer. Here we complexify the position $\boldsymbol{q}$, the momentum $\boldsymbol{p}$ and the time t. We keep the energy E real, as it is a physical parameter given by the "reality" of the experiments ($E = RV$):

$$\text{complex dynamics:} \quad \begin{cases} \boldsymbol{q}, \boldsymbol{p}, t \in \mathbb{C} \\ E \in \mathbb{R} \quad . \end{cases} \tag{8.1}$$

As we know explicitly the formulae (3.13) giving the evolution $\boldsymbol{q}(t), \boldsymbol{p}(t)$ between two bounces given the starting conditions $\boldsymbol{q}_0, \boldsymbol{p}_0$ at energy E, we simply consider their analytical continuation is the complex plane. Computationally, we declare these variables as complex and evolve them following a given complex path for the time.[2]

Complex bounces

We illustrate the choice of the complex time path in Fig. 8.1. We start at the left barrier with $\mathbf{Re}\, x = 0, \mathbf{Im}\, x = 0$ and some complex initial condition $z_0, p_z^0 \in \mathbb{C}$. We evolve the time along the real axis $0 < t < t_b$ until $\mathbf{Re}\, x(t_b) = L$. For complex starting conditions, $x(t_b) = L + iq_b$ is complex. Then we search for the complex time T_c such that the imaginary

[1] Only the first paragraph of subsubsection "Cusp event" in page 180 is essential, as it explains how saddle orbits disappear.

[2] One could try to consider the real and imaginary parts of the position as independent real variables, and consider a phase space of double dimension. However, the resulting dynamics would not be Hamiltonian; $\mathbf{Re}\, p$ is not the conjugate variable of $\mathbf{Re}\, q$, because $\mathrm{Re}\,[dq/dt] \neq d[\mathrm{Re}\, q]/dt$ for a complex time path.

part of x becomes also zero [$\mathbf{Im}\, x(T_c) = 0$]. This is done with a Newton-Raphson algorithm starting at $t_0 = t_b$:

$$t_{n+1} = t_n - m\frac{x(t_n) - L}{p_x(t_n)} \quad , \quad T_c = \lim_{n\to\infty} t_n. \quad . \tag{8.2}$$

We consider that this situation *defines* a bounce on the right barrier:

$$\text{bounce}: \quad \begin{cases} \mathbf{Re}\, x(T_c) = L \\ \mathbf{Im}\, x(T_c) = 0 \end{cases} \Rightarrow \begin{cases} \mathbf{Re}\, p_x \to -\mathbf{Re}\, p_x \\ \mathbf{Im}\, p_x \to -\mathbf{Im}\, p_x \end{cases} , \tag{8.3}$$

so we flip the x momentum. A bounce on the left barrier is obtained the same way, replacing L by 0 above. Then, we evolve again keeping $\mathbf{Im}\, t = \mathbf{Im}\, T_c$, until one finds another barrier; we find the new complex time for which the bounce is "real", flip the momentum and carry on.

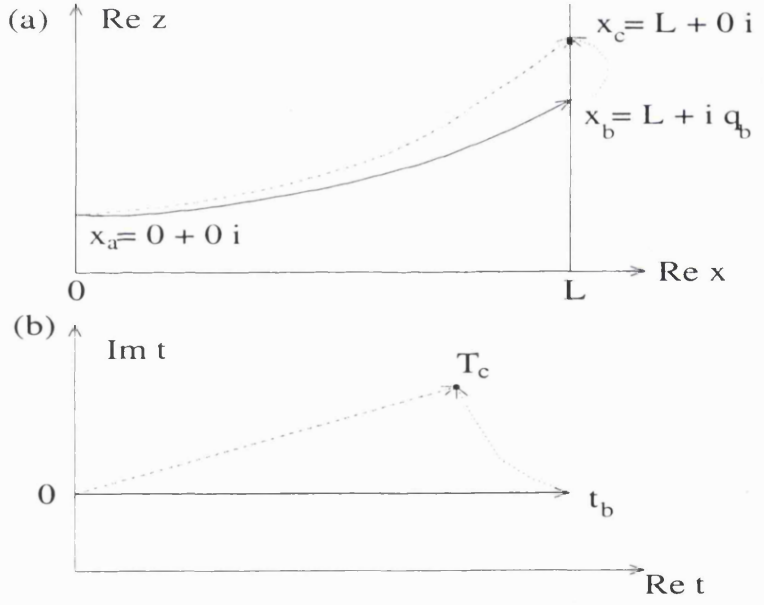

Figure 8.1: Scheme for the complex classical dynamics. (a) Real shape of a trajectory in the $(\mathbf{Re}\, x, \mathbf{Re}\, z)$ plane. (b) Time path in the complex plane $(\mathbf{Re}\, t, \mathbf{Im}\, t)$. The dashed lines correspond to the direct time path that goes to the bounce in a straight line. The dotted lines represent the Newton-Raphson algorithm (8.2).

A surprising fact in Fig. 8.1 is that $\mathbf{Re}\, x$ *decreases* just before the bounce ($t_b < t < T_c$); naively one would think that the momentum is negative, and its flipping at the bounce would make the particle go on to the right of the wall. However, the real part of the time *decreases as well* before the bounce. This means that $\mathbf{Re}\, p_x > 0$ before the bounce.[3] After

[3] Actually $\mathbf{Re}\, p_x \simeq \mathrm{Re}\, \frac{\Delta x}{\Delta t} = \frac{\Delta x_R \Delta t_R + \Delta x_I \Delta t_I}{\Delta t_R^2 + \Delta t_I^2}$, so that differences in the imaginary component x_I can also change the sign of $\mathbf{Re}\, p_x$.

the bounce, $\mathbf{Re}\, p_x < 0$ and $\mathbf{Re}\, x$ will decrease as $\mathbf{Re}\, t$ increases again.

Barrier penetration?

The trajectory shown in Fig. 8.1 (a) looks surprising, as the particle appears to penetrate the (infinitely high) barrier, whilst the real part of time goes backwards. It is important here to emphasize the fact that the trajectory beyond the barrier is only a representation of the Newton-Raphson algorithm (8.2), and *does not* represent any physical behavior. We have never defined what the potential is beyond the barrier; hence the particle does not feel any barrier until it reaches the time T_c. This is entirely different from the possibility that a particle has to tunnel through a finite height barrier, when it follows an imaginary time path or has complex momentum.

Changing time paths

In real dynamics, the functions $\boldsymbol{q}(t), \boldsymbol{p}(t)$ between the bounces are analytical, with no discontinuity, divergence, singularity or apparent restriction. Their continuation in the complex plane is therefore holomorphic and single valued: $\boldsymbol{q}(t), \boldsymbol{p}(t)$ should be uniquely defined, and not depend on the specific path one has used to reach the time t. Another important property of complex dynamics follows Cauchy's theorem, stating that the integral of a holomorphic function along a closed path in the complex plane is given by the residues of its poles inside the path. This means that one can deform a complex integral along an open path (keeping the starting and final points constant), provided one does not meet a pole of the integrated function. For example, the action $S = \int d\boldsymbol{q}\, \boldsymbol{p}$ is single valued for a given trajectory. Similarly, all the global classical properties of a trajectory (such as the monodromy matrix M) do not depend on the time path.[4] Note that even a numerical integration of the trajectory between the bounces (using a Runge-Kutta method for solving Hamilton's equations) would also yield analytical solutions, which would be independent of the chosen time path.

Hence, one can *choose* a "direct" time path which goes straight from $t = 0$ to $t = T_c$ (see Fig. 8.1). The particle will arrive on the barrier directly with $\mathbf{Im}\, x(T_c) = 0$, and will undergo the bounce without venturing "beyond the barrier". There is clearly an ambiguity

[4] We do not address here the problem of defining a Maslov index, the concept of a focal point being rather delicate for complex trajectories. Also, we can have different *real* trajectories joining two points $\boldsymbol{q}$ and $\boldsymbol{q}'$; here we discuss *one* trajectory defined non-ambiguously by its starting position and momentum, and argue that its properties do not depend on the time path used to evolve that trajectory.

related to the freedom of choosing a time path: each different time path yields a different looking trajectory [see Fig. 8.1(a)]. However, they all have the same *global* properties such as the total time T, action S, stability matrix M, final position and momentum as a consequence of the "analyticity" of the dynamics. As the current formulae or the Gutzwiller trace formula (GTF) use only the global properties of certain trajectories, one can employ any convenient time path with reasonable safety. Other topics like the study of scarring (the localization of a quantum state on a trajectory) depend strongly on the shape of the trajectory, and are therefore more problematic to address. In this work, we always plot the "direct" time paths; they give trajectories that avoid the region beyond the barrier and are more similar to the trajectories found in real dynamics. For instance, a complex orbit looks time-symmetic (TS, see subsection 3.1.7) when the corresponding real orbit is TS —while the same starting conditions with a different time path would give a complex orbit that does not look TS.

An example

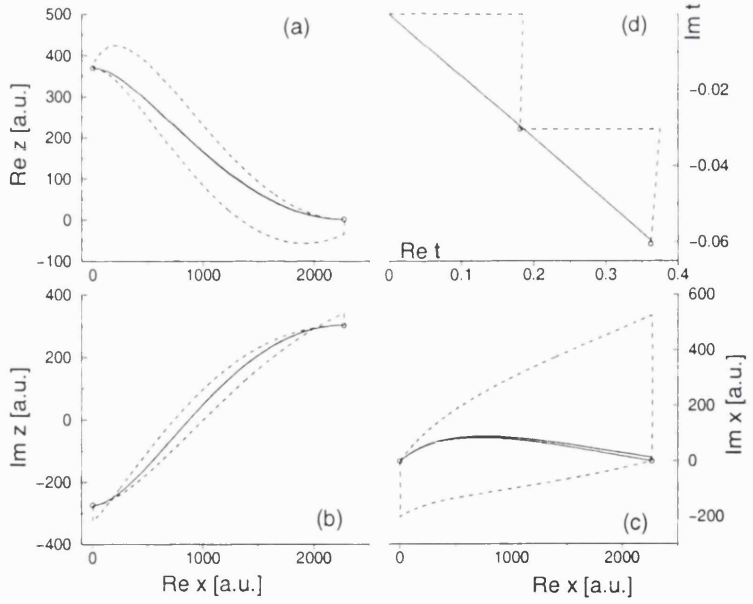

Figure 8.2: Complex PO t_0 at $\theta = 11°, \epsilon = 4000$. (a) $(\mathrm{Re}\, x, \mathrm{Re}\, z)$. (b) $(\mathrm{Re}\, x, \mathrm{Im}\, z)$. (c) $(\mathrm{Re}\, x, \mathrm{Im}\, x)$. (d) $(\mathrm{Re}\, \tilde{t}, \mathrm{Im}\, \tilde{t})$. The solid lines correspond to the direct time path that joins the times of the bounces; the dashed lines correspond to the indirect time path going first along the real axis. The bounces are indicated by circles. The time is scaled ($\tilde{t} = Bt$), and in arbitrary units.

We show in Fig. 8.2 an example of a complex trajectory in the RTD: the complex PO t_0 at $\theta = 11°, \epsilon = 4000$. In (a) we show its "real" shape in the $(\mathrm{Re}\, x, \mathrm{Re}\, z)$ plane.

The direct time path orbit looks time-symmetric, contrary to the indirect orbit. We see in (b) that **Im** z is of the same order as **Re** z. On the other hand, x is "more real than imaginary", considering the direct orbit only (c). The time is principally real (d). The global characteristics of this PO are:

$$\begin{aligned} z_0 &= z_0' = (370.3198, -274.3851) \quad , \quad p_z^0 = p_{z'}^0 = (0., 0.) \\ \hat{S} &= (0.9435, 0.02305) \quad , \quad T = (0.3640, -0.0598) \\ \tilde{M} &= \begin{pmatrix} 0.5005 & -1.4097 \\ 3.3170 & 0.5005 \end{pmatrix} + i \begin{pmatrix} -1.9372 & -0.3992 \\ 0.4361 & -1.9372 \end{pmatrix} \quad . \end{aligned} \tag{8.4}$$

Stability?

The stability classification which holds for a real PO is not possible with complex dynamics. M (as well as its trace) is complex, which means that its eigenvalues have no restriction: $\lambda_\pm = \rho^{\pm 1} \exp(\pm i\gamma) \in \mathbb{C}, |\rho| \neq 1$. Any neighboring trajectory winds around the PO (with an "angle" γ), and at the same time is repelled or attracted (by a factor ρ). One cannot separate different directions around the PO where neighboring trajectories would only wind or only be repelled/attracted. It would also be difficult to build a Poincaré SoS, as its coordinates (z, p_z) are complex and yield a 4-D real space. The "instability" component of a complex orbit is given by ρ, which is related to $|\mathrm{Tr}M| \simeq \rho$. The ghost t_0 at $\theta = 11°$ is quite "unstable": $\rho \simeq 4$ at $\epsilon = 4000$; similarly for t_0–SO: $\rho \simeq 6$ at $\epsilon = 2000$.

Singularities?

It is our definition of a bounce (8.3), and the specification of the number of left and right bounces (the "bounce structure") that determine uniquely the global structure of the time path in the complex plane. It has to go through the times $T_c^i, i = 1, 2, ..$ corresponding to each desired bounce. One could wonder if some points in the complex plane correspond to some sort of singularity (in position or time).[5] In this case one should not deform the time path beyond this singular time, as this would yield a totally different trajectory. For example, Takada *et al.* (1995) have related singularities to tunneling across a finite height potential barrier.[6] So far, we never came across such singular points. Once again, we emphasize the fact that we do not have a finite height barrier, but define the infinite

[5] By singularity we mean either a pole or a point where the derivative is not defined.

[6] In the work of Takada *et al.* (1995), there are singular points in the complex time plane that correspond to tunneling (or not) through the barrier. The time path was deformed from the time path along the real axis ($-\infty < t < +\infty$) into the complex plane; pushing the deformation beyond a singular time corresponded to a tunneling event. Hence, going around a singular time changed the structure of the trajectory. Our

barrier through the condition (8.3). This definition cannot be included in the dynamics, and must be implemented by an "omnipotent" actor; it does not permit any tunneling.

In the complex plane, multi-valued functions are behind the singular points where no derivative can be defined; they are the points where the different branches or Riemann sheets join. Semiclassical theories involve specific trajectories $(x = 0, z) \to (x' = 0, z')$, which can be "multi-valued", in the sense that several starting momenta giving several different trajectories can nevertheless connect the same z and z'. In this case, the related singular point is a focal point where $m_{12} = 0$; they appear in the $(\mathbf{Re}\, z, \mathbf{Im}\, z; \mathbf{Re}\, z', \mathbf{Im}\, z')$ plane of starting and ending positions.[7] They are entirely different from the hypothetical singularities in the time plane mentioned above.

Cusp event

An interesting case to study is a "cusp" event, as it happens at $\theta = 27°$ for the saddle orbit $2t_0$ (see also subsection 3.2.4). It is an important phenomenon, as it is the only mechanism that can make a saddle orbit (SO) disappear as ϵ is varied. At $\epsilon = 18841$ the intermediate bounce on the left wall $(x_i = 0, z_i)$ becomes tangential to the surface: $p_x^i = 0$; it is very near the soft energy surface. Decreasing ϵ will make this bounce disappear suddenly (the trajectory "misses" the left wall), changing in a discontinuous way the property of the orbit and destroying the saddle orbit condition. Energy conservation lies behind this phenomenon; complex dynamics might therefore enable the particle to "tunnel" through the soft energy surface to make a bounce on the wall.

We can try to force a bounce by evolving the time along the imaginary axis, once we have reached the point at which evolving along the real axis would make the particle return and miss the wall. Indeed, the particle can be forced to reach the wall ($\mathbf{Re}\, x = 0$), and we can locate the time T_c of the bounce when $\mathbf{Im}\, x = 0$. However, in this case $\mathbf{Re}\, p_x > 0$, which means that the flipped x momentum ($p_x \to -p_x$) will have a negative real part. The particle will therefore cross the barrier into $\mathbf{Re}\, x < 0$, and a new bounce must be enforced for consistency. Crucially, we find exactly the same time T_c, which will

approach here is different: we start at $t = 0$ and must pass through the bounce times T_c^i. In a sense, the latter times are "singular" as the momentum changes there discontinuously; however they are not a discontinuity in the potential, one cannot go "around" them and there is no apparent barrier to tunnel into.

[7] We observed such singularities in contour plots of the action of TS closed orbits in the starting $z = z'$ plane, similar to Fig. B.1. As one goes around a complex focal point, one connects the different families of closed trajectories and one has a multi-valued action.

give $\mathbf{Re}\, p_x > 0$ after this bounce, enabling the particle to re-enter the well ($\mathbf{Re}\, x > 0$). This "double bounce" amounts in effect to no bounce at all as we flip the momentum twice at the same time; the particle behaves as if its x momentum has not been flipped. By analyticity, the deformation of the time path (in order to go through T_c twice) cannot change the global properties of the trajectory. The particle will behave exactly the same as the particle which missed the left wall in the first place; e.g., they will have the same bounce on the right wall.

This example shows how the "bounce structure" of a trajectory cannot be changed by taking different time paths. Although complex dynamics can allow trajectories to have some very unexpected behavior (e.g., escaping a bounce on the right wall despite the potential drop), we shall not study such effects. Our approach to the complex dynamics is always guided, in some sense, by the trajectories found in real dynamics.

Turning points

A related situation is the question of the complex point that corresponds to a turning point appearing in a real trajectory. For example, the real PO s' has one turning point in the middle of the well where it reaches the energy surface, runs out of momentum ($\boldsymbol{p} = 0$), and starts retracing itself. The related complex saddle orbit $s'\text{–}SO$ is not very complex (i.e., its imaginary components are smaller than its real components) and the real part of its shape in the ($\mathbf{Re}\, x, \mathbf{Re}\, z$) plane is very close to the shape of $s'\text{–}PO$ [see Fig. 6.12 (f)].

The complex SO, as well, appears to run out of momentum and retrace itself. This might be somewhat surprising, as the definition of a turning point comes from energy conservation and is therefore linked to real dynamics: once it has reached the energy surface $E = H(\boldsymbol{p}, \boldsymbol{q}) = \boldsymbol{p}^2/2m + V(\boldsymbol{q})$, the particle can go no further. Indeed, $V(\boldsymbol{q})$ would then be greater than E, giving no real solution for $\boldsymbol{p}$. Therefore, it has to stop and go back.

In complex dynamics however, one could argue that a point on the energy surface has no special properties. The particle *can* go further with some imaginary momentum to counterbalance the potential; it would not stop and would not retrace itself. Looking more precisely at $s'\text{–}SO$, one can see that there is no proper turning point: the particle goes a little beyond the energy surface; the modulus of the momentum decreases strongly but does not reach zero. However, the global shape is the one of a time-symmetric trajectory. Once again, one can change the time path and modify dramatically the shape around

the pseudo-turning point to penetrate deeply in the classically forbidden region beyond the energy surface. Nevertheless, this would not modify the global properties of the trajectories, such as the position of the following bounce (in this case on the right wall).

Complex conjugation

We observe an overall symmetry with respect to complex conjugation (see e.g. Fig. B.1), which is due to the fact that the dynamics for real variables are real. This is related to the fact that $f(z \in \mathbb{R}) \in \mathbb{R} \Rightarrow f(z^*) = f(z)^*$ for a complex function f. We find that, in general, if we have a trajectory $(z, p_z) \to (z', p'_z)$ in time t with action S and stability matrix M, we shall have the complex conjugate trajectory $(z^*, p_z^*) \to (z'^*, p_z'^*)$ with t^*, S^* and M^*. This implies that the complex conjugate of a PO is also a PO. However, the complex conjugate of an SO (5.43) *is not* a SO (it satisfies the starting condition at its final point and vice versa); this is due to the presence of i in its definition.

Conclusion

It seems that the bounce structure of a trajectory cannot be changed drastically by the complex dynamics as we defined them. Again we emphasize that our definition of a bounce (8.3) restricts strongly the way one can evolve the complex dynamics; without such a definition one could follow purely imaginary time and probably witness some more "exotic" effects. However, it is unclear to us what alternative definition of a bounce one could make without introducing soft barriers in the potential.

All these comments are based on empirical observations; no systematic study has been made, and no justification through theoretical arguments has been attempted. Other effects of the complex dynamics could very well appear; it happens that we have not witnessed anything peculiar so far. Such effects probably rely on the use of the freedom of complex classical dynamics (the choice of a time path), which in our case is restricted by our wish to preserve the bounce structure of real dynamics (e.g., t_0 makes one bounce on the left and one the right, s' one on the left and two on the right with a turning point in between, etc.).

8.1.2 t_0 ghost PO at $\theta = 11°$

We study here the classical characteristics of the complex PO (called ghost) which appears at the tangent bifurcation of t_0 and t_0^- at $\theta = 11°$. We only present results for

the one complex PO ($t_{\rm gh}$) that contributes to the current, its complex conjugate giving "unphysical" contributions to semiclassical expressions.

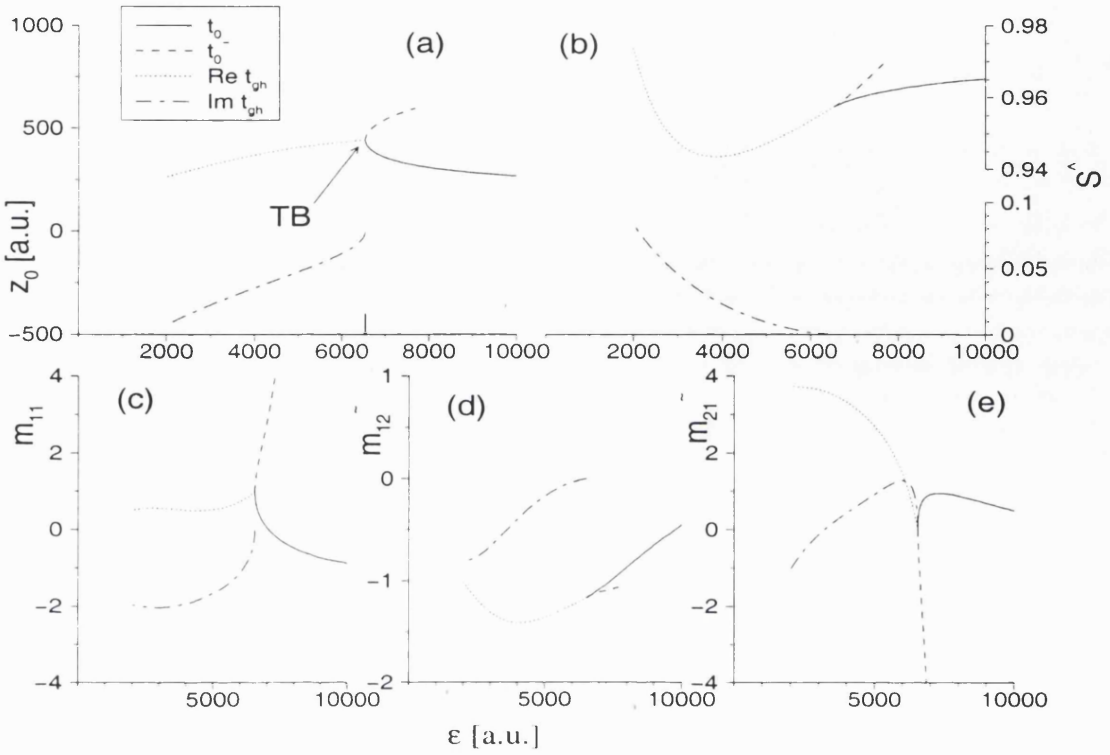

Figure 8.3: Classical properties of the ghost PO at $\theta = 11°$. We show t_0, t_0^-, $\mathrm{Re}\, t_{\rm gh}$ and $\mathrm{Im}\, t_{\rm gh}$ around the tangent bifurcation at $\epsilon_b = 6539.94$. (a) z_0; (b) $\hat{S}$; (c) m_{11}; (d) $\tilde{m}_{12}$; (e) $\tilde{m}_{21}$. The bifurcation is indicated in (a) by TB and the small vertical line on the ϵ axis.

Fig. 8.3 shows the classical characteristics of the real POs (the stable t_0 and the unstable t_0^-) and the complex PO $t_{\rm gh}$. In all graphs (a)-(e), we see the merging of the real POs at the bifurcation at $\epsilon_b = 6539.94$. The starting position z_0, as well as m_{11} and m_{21} join "smoothly" with an infinite derivative with respect to ϵ —similar to a $\sim \epsilon^{1/n}$ behavior. $\mathbf{Im}\, t_{\rm gh}$ has a similar behavior, with infinite derivatives at the bifurcation. The real values for the ghost change much slower as one moves away from the bifurcation, yielding a kind of "discontinuous" behavior as ϵ is varied. On the other hand, the values of m_{12} and $\hat{S}$ for the real POs and $\mathbf{Re}\, t_{\rm gh}$ join together with a finite derivative, similar to a $\sim \epsilon^n$ behavior. A closer study of the bifurcation is shown in Fig. 8.4.

Semiclassical theories involving normal forms (Schomerus and Sieber 1997, Atkins and Ezra 1994) often worked with an interpolation of S or $\mathrm{Tr}M$ as a function of a dynamical parameter (e.g, ϵ) on the real side of the bifurcation. The coefficient of these interpolations was used to extrapolate the behavior of the ghost PO on the complex side, in order to

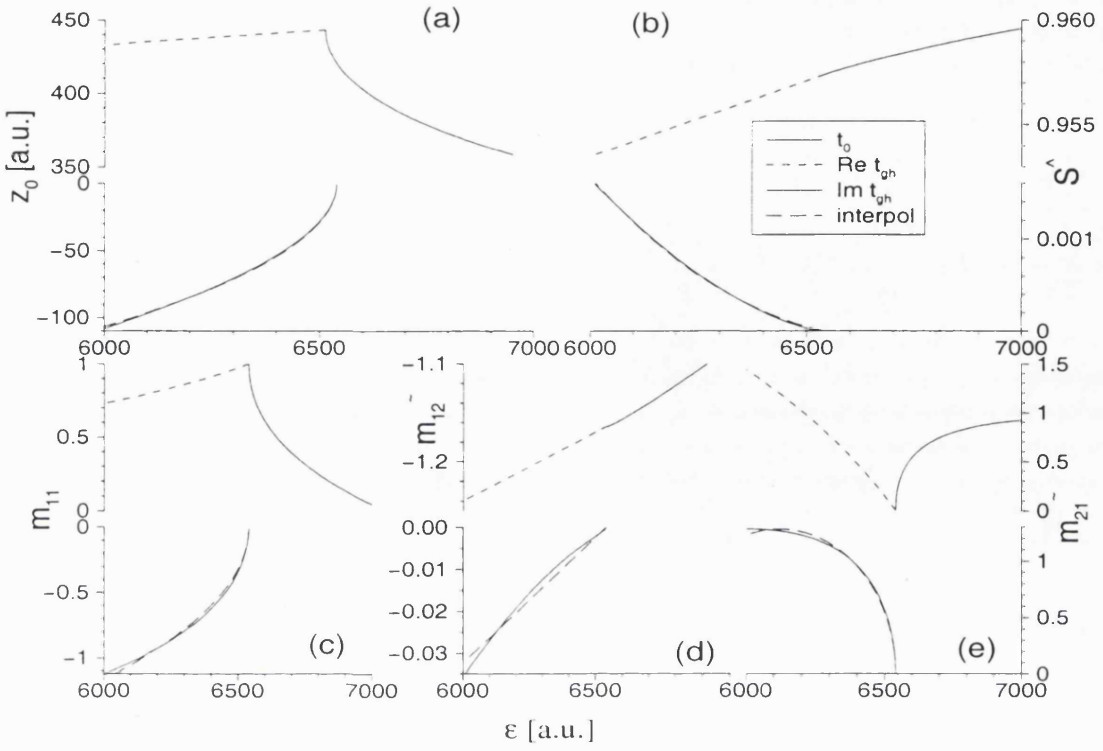

Figure 8.4: Details of the bifurcation. t_0 and $\mathrm{Re}\, t_{\mathrm{gh}}$ are in the upper graphs. For $\mathrm{Im}\, t_{\mathrm{gh}}$ in the lower graphs, we also show an example of interpolation. (a) z_0; (b) $\tilde{S}$; (c) m_{11}; (d) $\tilde{m}_{12}$; (e) $\tilde{m}_{21}$.

avoid the task of finding the complex POs numerically.

In a tangent bifurcation the quadratic expansion of the action becomes degenerate as the POs merge; normal forms technique usually expand the action up to order three or four. To understand in a qualitative manner the behavior of the POs seen in Fig. 8.3, one can propose the cubic form

$$S(\zeta) = S_0 + a\zeta + b\zeta^2 + \frac{1}{3}c\zeta^3 \Rightarrow S'(\zeta) = a + 2b\zeta + c\zeta^2 \quad , \tag{8.5}$$

where ζ is a "representation" for the position z.[8] One can assume for simplicity that $a = a_0$ and $b = b_0$ are constant, and that only c varies with ϵ: $c(\epsilon) = c_0\epsilon^k$. The zeros of S' give the positions of the POs. On the real side, one has two distinct POs:

$$\zeta_\pm = \frac{1}{c_0\epsilon^k}\left[-b_0 \pm \sqrt{b_0^2 - a_0c_0\epsilon^k}\right] \in \mathbb{R} \quad . \tag{8.6}$$

Their stability is given by the sign of $S''(\zeta_\pm) = \pm 2\sqrt{b_0^2 - ac_0\epsilon^k}$; hence the stable PO ($S'' > 0$) is ζ_+. The two real POs merge at the "bifurcation", when $S''(\zeta_\pm) = 0 \Rightarrow \epsilon_b =$

[8] The action actually depends on two variables (z, z'), making it difficult to visualize.

$[b_0^2/a_0c_0]^{1/k}$. On the complex side, the POs are complex conjugates of each other:

$$\zeta_\pm = \frac{1}{c_0\epsilon^k}\left[-b_0 \pm i\sqrt{-b_0^2 + a_0c_0\epsilon^k}\right] \in \mathbb{C} \quad . \tag{8.7}$$

This illustrates the fact that the "smooth" junctions mentioned above (related to the square root) appear on the real side of the bifurcation for both POs, and only on the imaginary part of the ghost on the complex side —the real part staying roughly constant. The power n is not *a priori* determined as it depends on the definition of the dynamical parameter ϵ. Similarly, one can write expressions for the other characteristics of the PO such as M.

For illustrative purposes, we have fitted the variations of the classical characteristics with ϵ with three functional forms:

$$f(\epsilon) = f(\epsilon_b) + \begin{cases} p_1(\epsilon - \epsilon_b) + p_2(\epsilon - \epsilon_b)^2 & \text{parabolic} \\ r_1\sqrt{|\epsilon - \epsilon_b|} & \text{square root} \\ c_1\sqrt{|(\epsilon - c_2)^2 - (\epsilon_b - c_2)^2|} & \text{circle} \quad . \end{cases} \tag{8.8}$$

For each function to interpolate ($z_0, \hat{S}$, etc.) and for each PO (t_0, $\mathbf{Re}\, t_{\rm gh}$ and $\mathbf{Im}\, t_{\rm gh}$), there is clearly *one* functional form that is adequate. The square root and circle forms can describe the smooth junctions, the parabolic form can be used for the "discontinuous" junctions of t_0 and t_0^- or the nearly constant behavior of $\mathbf{Re}\, t_{\rm gh}$. Table 8.1 lists the coefficient of the interpolations. We see clearly the similar behavior of t_0 and $\mathbf{Im}\, t_{\rm gh}$, as they are interpolated by similar functions. The interpolations for $\mathbf{Im}\, t_{\rm gh}$ are shown in Fig. 8.4.

8.2 Ghost contributions

In this section, we look at the current contributions coming from complex ghost POs. In particular, we investigate the "no (real) PO" experimental regions described in Fig. 2.5 and 2.8. We use ghosts in the PO/NO formula (5.48), as the POs here are time-symmetric (TS). We recall here the modifications of the semiclassical formulae (chapter 5) coming from complex trajectories. The amplitude of the oscillations are not only given by $\mathbf{Re}\,\Gamma$ (5.48), but also contains a damping due to the imaginary part of the action. The monodromy matrix elements are also complex, and therefore mix imaginary and real parts in $\mathcal{D}$, changing the expression of its phase.

This study will not be entirely successful; we however present it as it is a normal step in the application of periodic orbit theories in the RTD. Moreover, the failure of the ghost

	f	p_1	p_2	r_1	c_1	c_2
t_0	z_0			4.15448		
	$\hat{S}$	6.36641×10^{-6}	-3.4576×10^{-9}			
	m_{11}			-0.0613607		
	$\tilde{m}_{12}$	1.30087×10^{-4}	1.05268×10^{-7}			
	$\tilde{m}_{21}$				4.26078×10^{-4}	-5035.66
Im $t_{\rm gh}$	z_0			-4.58376		
	$\hat{S}$	-9.96551×10^{-7}	3.87192×10^{-9}			
	m_{11}			-0.0504505		
	$\tilde{m}_{12}$	-5.99191×10^{-5}	0			
	$\tilde{m}_{21}$				3.05212×10^{-3}	6120.2
Re $t_{\rm gh}$	z_0	0.015956	-6.42363×10^{-6}			
	$\hat{S}$	7.26731×10^{-6}	2.43288×10^{-10}			
	m_{11}	6.4352×10^{-4}	2.7167×10^{-7}			
	$\tilde{m}_{12}$	1.42902×10^{-4}	5.07868×10^{-9}			
	$\tilde{m}_{21}$	-3.58506×10^{-3}	-1.75514×10^{-6}			

Table 8.1: Coefficients of the interpolations (8.8) around the tangent bifurcation at $\theta = 11°$. We choose one type of the interpolating functions in each case.

contributions involves interesting phenomena. For example, we shall see at $\theta = 27°$ that the Gaussian damping of the initial state, when evaluated for a complex trajectory, can become an exponentially *growing* function (of B, or z_I). This phenomenon is linked to the steepest-descent method, and is reminiscent of Stokes' phenomenon (Heading 1962).

Period-one at $\theta = 11°$

In Fig. 8.5 we present the ghost contributions to the semiclassical current given by the PO/NO formula. At $\theta = 11°$, t_0 disappears in a tangent bifurcation at $\epsilon = 6539$, leaving a ghost below. The quantum current does not vanish; it persists over a wide range ($\epsilon = 3000 - 6500$), where there are no real adequate PO, but only $t_{\rm gh}$, the ghost of t_0. At lower ϵ, the real PO t_1 describes accurately the QM current. We see in (b) that the frequency of the ghost matches quite accurately the quantum values. The QM frequency increases

slightly as ϵ decreases, until it reaches the frequency of t_1 at low ϵ. There is a disagreement between the SC and QM frequencies at the bifurcation.

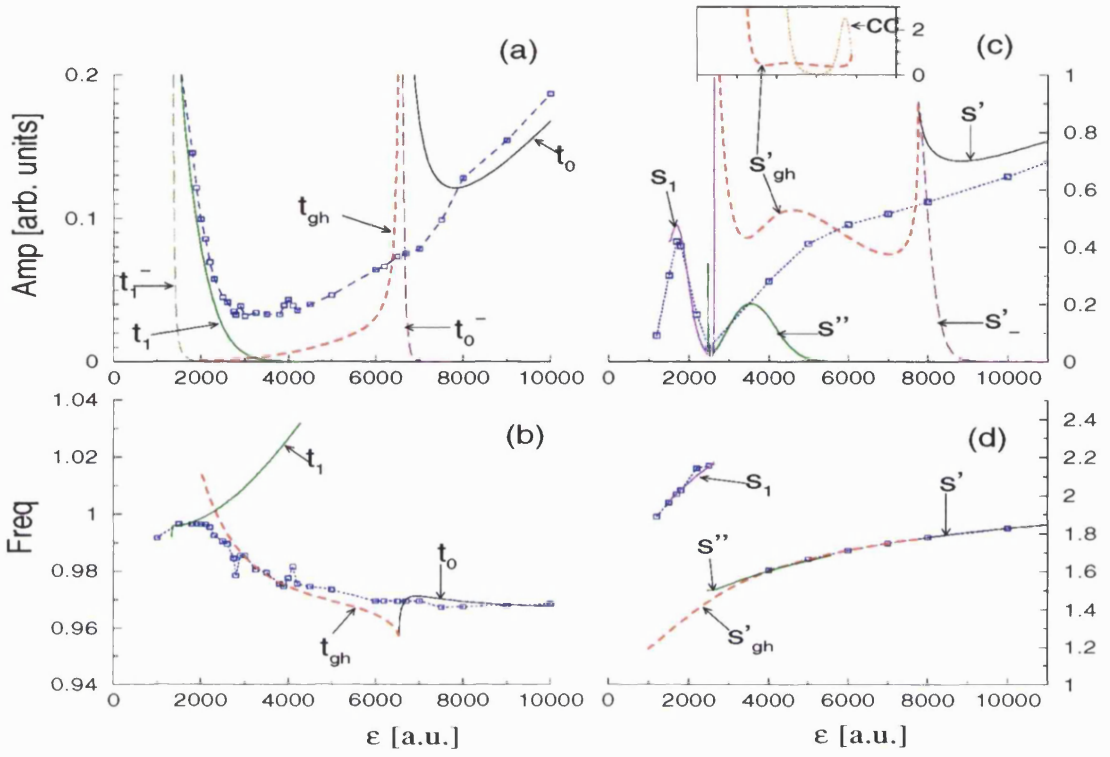

Figure 8.5: Ghost contributions to the semiclassical PO/NO formula. We show the real, contributing POs (solid line), their unstable, non-contributing partners (long dashed line), the ghost (dashed line) and QM results (dotted line with squares). (a) Amplitudes and (b) frequencies of the P1 oscillations at $\theta = 11°$. (c) Amplitudes and (d) frequencies of the P2 oscillations at $\theta = 27°$. The inset in (c) shows the amplitude of the complex conjugate PO of the ghost (CC).

The amplitude of the ghost oscillations shown in (a) has the right qualitative shape (slope), but is too small by a factor three in the range $2500 < \epsilon < 5000$. This was a rather disappointing result (Saraga *et al.* 1998), as the ghost was strongly suspected to explain the experimental and quantum oscillations. The spike at the bifurcation is not a divergence like in the GTF and has a finite value ($A \simeq 1$). However, it is "unphysical" and it will be discussed in the next section where we present a cubic expansion. Note that the amplitude of the ghost, although being too small, is still significant in a wide region. This can be contrasted with the contribution of a ghost to the density of states, which decreases exponentially away from the bifurcation (i.e., with ϵ). This fact is due to the presence of the imaginary part of the starting condition z, which can compensate partially both the Gaussian damping and the exponential decay due to the imaginary part of the action: the

amplitude of the current is proportional to $\exp\left[-\mathbf{Im}\, S - \beta(\mathbf{Re}\, z)^2 + \beta(\mathbf{Im}\, z)^2)\right]$.

Finally, we note that the other real POs t_0^- and t_1^- (the unstable partners in the bifurcations) do not contribute at all to the quantum current. The situation is the same at $\theta = 27°$ for s'_- (it is born stable in the tangent bifurcation but rapidly becomes very unstable). Their contribution decays far too quickly away from the bifurcation to influence the quantum behavior. It shows that the current in the RTD can be described using only a very small number of trajectories, unlike the density of states which demands the contribution from all emitter and collector orbits.

Period-two at $\theta = 27°$

At $\theta = 27°$ the frequencies (d) of all contributing POs are extremely close to the QM results. On the other hand, the amplitudes shown in (c) are more problematic. The contribution of the real PO s' does not agree very well with the QM results. The contribution of its ghost $s'_{\rm gh}$ qualitatively describes the quantum oscillations in the range $4000 < \epsilon < 7700$. However, its "wavy" shape is rather surprising and uncorrelated to the QM. The worst is at $\epsilon \simeq 3500$, where the ghost contribution grows exponentially, giving a completely unphysical contribution.

Studying the classical dynamics and the variation (with ϵ) of the classical properties of the ghost $s'_{\rm gh}$ can shed some light on this peculiar behavior. As mentioned earlier, complex POs come in a pair of complex conjugates; we call "ghost" the one which contributes to the current. A way to decide which one is the ghost is to refer to the GTF: the ghost should have a positive imaginary part of the action (see below) *near the bifurcation.*

We show the behavior of the classical properties of $s'_{\rm gh}$ in Fig. 8.6. They can be contrasted to $t_{\rm gh}$ at $\theta = 11°$ (see Fig. 8.3). $t_{\rm gh}$ is regular, evolving in a monotonic way as one goes away from the bifurcation, while $s'_{\rm gh}$ behaves in a more involved way. In (a) we see that $\mathbf{Re}\, z_0$ changes significantly with ϵ (while for t_0 it was roughly constant). The imaginary part of the starting position evolves as fast, and actually overtakes the magnitude of the real part: $|\mathbf{Re}\, z_0| = |\mathbf{Im}\, z_0| = 220$ at $\epsilon = 6300$. This fact can cause some peculiar effect in the semiclassical contribution to the current. To a first approximation[9], the semiclassical contribution of the ghost to the current is given by the initial Gaussian $\exp(-\beta z^2) = \exp(-\beta z_R^2 + \beta z_I^2)\exp(2i\beta z_R z_I)$. Hence for $\epsilon < 6300$ the real part of the argument of the exponential is *positive*, which means that the current grows exponentially

[9]See the hard limit formula in subsection 5.2.2 and section 6.1.

in the classical limit ($\beta \gg 1$) or away from the bifurcation (as z_I increases).

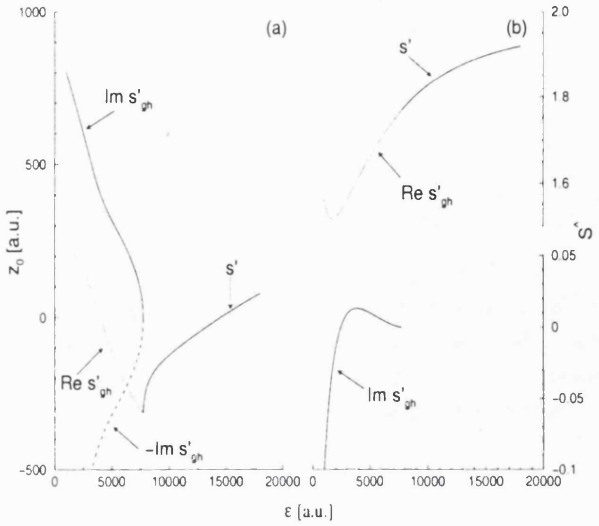

Figure 8.6: Classical properties of the ghost $s'_{\rm gh}$ at $\theta = 27°$. (a) z_0, where we also show the complex conjugate of $s'_{\rm gh}$, indicated by [-Im]. (b) $\hat{S}$.

In (b) we see that $\mathbf{Im}\,\hat{S}$ becomes negative at $\epsilon = 2450$. Again, this can be contrasted to the more regular behavior of $t_{\rm gh}$, for which the imaginary part of the action grows monotonically. The consequence is that the semiclassical density of states [given by the GTF and containing $\exp(iS/\hbar)$] suddenly shows an exponential growth in the classical limit or away from the bifurcation for $\epsilon < 2450$. This is obviously unphysical, and one could for instance consider switching to the complex conjugate PO.

A more rigorous approach is to go back to the step before the semiclassical formulae, that is, the stationary phase approximation. One should use the more general steepest-descent approach for complex saddle points, and in particular be careful about which saddle path is allowed (see Appendix B.1). We show in Fig. 8.7 contour lines of $\mathbf{Im}\,\hat{S}$ in the complex plane of the starting positions z, calculated with time-symmetric closed orbits (TSCOs) that have $z' = z, p'_z = -p_z$ (see also the discussion of Fig. B.1). Just below the tangent bifurcation at $\epsilon = 7700$ (a), the steepest-descent path (which goes through the "mountains") selects only the complex PO with $\mathbf{Im}\,z > 0$; it also has $\mathbf{Im}\,\hat{S} > 0$. The angle ϑ between that path at the PO and the real axis is very close to 0. At $\epsilon = 3000$ (b), we see that the orientation of the saddle has changed; ϑ has increased. At $\epsilon = 1000$ (c), $\vartheta > \pi/4$; this implies that it is not possible to go back to the real axis (from the saddle) avoiding the $\ominus$ valley region. The steepest-descent method should not consider the contribution of

that PO any more, but switch to the contribution of its complex conjugate. This would yield a sudden change in the behavior of the current as ϵ varies. However, we see in the inset of Fig. 8.5 (c) that the amplitude from the complex conjugate PO explodes even sooner (at $\epsilon \simeq 5000$).

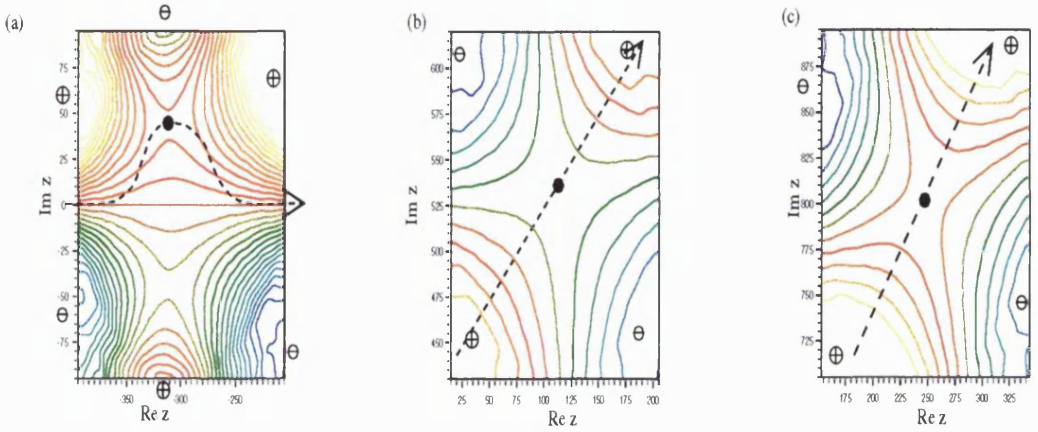

Figure 8.7: Contour lines of $\mathbf{Im}\,\hat{S}$ in the complex z plane for TSCOs at $\theta = 27°$. (a) $\epsilon = 7700$; (b) $\epsilon = 3000$; (c) $\epsilon = 1000$ (details). Yellow $\oplus$ is high, blue $\ominus$ is low.

The TSCOs that we used as an aid for visualization might be misleading us here into believing that we have only a one-dimensional (complex) integral. We recall that we need to integrate over the two independent variables (z, z'). Also, the discussion above only considered the action, while we have to take into account the Gaussian of the initial state. The Gaussian integration (5.25) only converges if both eigenvalues $\lambda_\pm$ of $\mathcal{A}$ have a negative real part. Using the fact that our POs are TS, we find

$$\lambda_\pm = -\beta + i\frac{m_{11} \pm 1}{m_{12}} \quad , \quad \lambda_G = 2i\frac{m_{11} - 1}{m_{12}} \quad . \tag{8.9}$$

For comparison, we have also defined λ_G, which would appear in a sort of a GTF obtained by a partial integration (on the left wall) over TSCOs only. λ_G is the second derivative of the action for TSCOs (multiplied by $2i$). For real POs, $\mathbf{Re}\,\lambda_\pm = -\beta < 0$ and $\mathbf{Re}\,\lambda_G = 0$.

We show these parameters in Fig. 8.8. For $t_{\rm gh}$ at $\theta = 11°$ (a), $\mathbf{Re}\,\lambda_\pm < 0$, assuring the convergence of the Gaussian integration. Similarly for $\mathbf{Re}\,\lambda_G$, which assures us that we have considered the correct complex PO (and not its complex conjugate). For $s'_{\rm gh}$ at $\theta = 27°$ (b), $\lambda_\pm$ always have a negative real part; however they get very close to zero as ϵ decreases. $\mathbf{Re}\,\lambda_G$ starts by being negative, but becomes positive for $\epsilon < 3500$. This illustrates the fact that the rotation of the saddle point and of the path going through the mountains is equivalent to the fact that $\mathbf{Im}\,S'' < 0$.

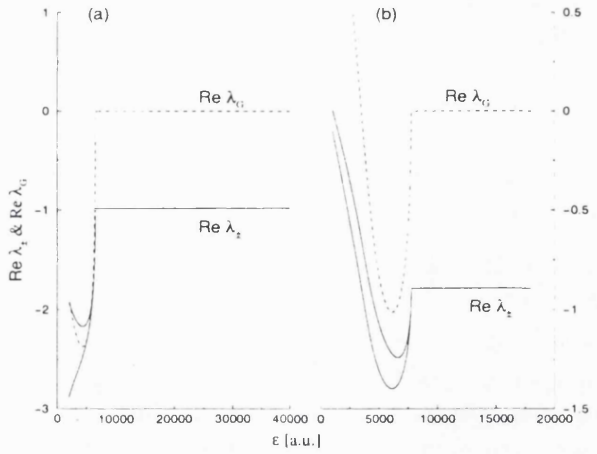

Figure 8.8: Evolution of the real part of the (scaled) $\lambda_{\pm}$ and λ_G with ϵ [see (8.9)]. (a) t_0 and $t_{\rm gh}$ at $\theta = 11°$. (b) s' and $s'_{\rm gh}$ at $\theta = 27°$.

In conclusion, we have seen here that effects arising from complexification of the dynamics are present at $\theta = 27°$. For instance, one has to consider carefully the paths of steepest-descent; this is reminiscent of Stokes' phenomenon (Heading 1962). However, even switching to the complex conjugate PO when apparently required does not remove the unphysical explosion of the amplitude. We have not attempted to solve this problem, as we doubt that the PO/NO formula can give a good description of the quantum behavior in this region, in a similar manner to the $\theta = 11°$ case. As was seen in section 6.3, the saddle orbits give the correct answer.

8.3 Cubic expansion

Bifurcations are special events where several POs coalesce and the Jacobian determinant of $S(z, z')$ vanishes. In the case of the GTF, this yields unphysical divergences in the density of states as $\mathrm{Tr}M \to 2$, which can be removed by the use of a higher order expansion of the action. These techniques are called *normal forms* or *uniform approximations* (Schomerus and Sieber 1997). The semiclassical hard limit formulae for the current in the RTD can also diverge at bifurcations. This is not the case for the intermediate formula, but there is nevertheless a very sharp rise in the current at the bifurcation. One can expect this rise to be due to the bifurcation and to be "unphysical".

An important question is whether the failure of the ghost contributions is caused by the bifurcation. We present here a formula for the current with a cubic expansion of the action, in the case of a tangent bifurcation. We initially developed this formula in the hope

that it would improve the contribution of the ghost to the (quadratic) PO/NO formula. As will be seen in this section, it will not be successful; we believe that it is nevertheless a worthwhile study, as it shows that even more elaborate PO theories fail in the "no (real) PO" region, and that the saddle orbits are necessary.

8.3.1 Derivatives

We restrict ourselves to time-symmetric normal/periodic orbits ($z_0' = z_0, p_{z'}^0 = p_z^0 = 0$). One can relate the third derivatives of the action to derivatives of the monodromy matrix (see also Appendix A.2):

$$a = \frac{\partial^3 S}{\partial z^3}(z,z') = \frac{\partial}{\partial z}\frac{m_{11}}{m_{12}}(z,p_z) - \frac{m_{11}}{m_{12}}\frac{\partial}{\partial p_z}\frac{m_{11}}{m_{12}}(z,p_z) \tag{8.10}$$

$$a' = \frac{\partial^3 S}{\partial z^3}(z,z') = \frac{1}{m_{12}}\frac{\partial}{\partial p_z}\frac{m_{22}}{m_{12}}(z,p_z) \tag{8.11}$$

$$b = \frac{\partial^3 S}{\partial z^2 \partial z'}(z,z') = \frac{1}{m_{12}}\frac{\partial}{\partial p_z}\frac{m_{11}}{m_{12}}(z,p_z) \tag{8.12}$$

$$b' = \frac{\partial^3 S}{\partial z \partial z'^2}(z,z') = \frac{1}{m_{12}}\frac{\partial}{\partial p_z}\frac{-1}{m_{12}}(z,p_z) \quad . \tag{8.13}$$

For time-symmetric (TS) trajectories, one has furthermore

$$a = a' \quad \text{and} \quad b = b' \quad . \tag{8.14}$$

We make a cubic expansion of the action around one TSPO:

$$\begin{aligned} S(z,z') &\simeq S_0 + \frac{m_{11}}{2m_{12}}[\delta z^2 + (\delta z')^2] - \frac{1}{m_{12}}\delta z \delta z' + \frac{a}{6}[\delta z^3 + (\delta z')^3] + \frac{b}{2}\delta z \delta z'[\delta z + \delta z'] \\ &=: \mathcal{S}_3(z_0; \delta z, \delta z') \quad , \end{aligned} \tag{8.15}$$

with the differences $\delta z = z - z_0, \delta z' = z' - z_0$. The subscripts 0, the monodromy matrix and the derivatives a and b refer to the TSPO. In the standard normal form procedures, one expands the action around the midpoint between the two bifurcating POs. In our case, we shall rather expand around the PO giving the dominating contribution (t_0 at $\theta = 11°$ and s' at $\theta = 27°$).

We use two methods to evaluate the derivatives a and b. The first one is "numerical": one defines the derivative of a function f by $f'(x) = [f(x+h) - f(x-h)]/(2h)$, taking smaller steps h until convergence is achieved. The second method is based on the ideas used in standard normal forms; it uses the information already given by the presence of the neighboring non-contributing TSPO. We express its characteristics (denoted by 1) using

the expansion (8.15) around the contributing TSPO:

$$S(z_1, z_1) = \mathcal{S}_3(z_0; \delta z_1, \delta z_1) \tag{8.16}$$

$$\frac{\partial S}{\partial z}(z_1, z_1) = 0 = \frac{m_{11} - 1}{m_{12}} \delta z_1 + \frac{1}{2}[a + 3b]\delta z_1^2 \tag{8.17}$$

$$\frac{\partial^2 S}{\partial z^2}(z_1, z_1) = \frac{m_{11}^1}{m_{12}^1} = \frac{m_{11}}{m_{12}} + \delta z_1[a + b] \tag{8.18}$$

$$\frac{\partial^2 S}{\partial z \partial z'}(z_1, z_1) = \frac{-1}{m_{12}^1} = \frac{-1}{m_{12}} + 2\delta z_1 b \quad , \tag{8.19}$$

with $\delta z_1 = z_1 - z_0$ the difference of the starting positions of the two POs. From these equations one gets

$$a = \frac{1}{\delta z_1}\left[\frac{m_{11}^1}{m_{12}^1} - \frac{m_{11}}{m_{12}}\right] - \frac{1}{2\delta z_1}\left[\frac{-1}{m_{12}^1} - \frac{-1}{m_{12}}\right] \quad \text{and} \quad b = \frac{1}{2\delta z_1}\left[\frac{-1}{m_{12}^1} - \frac{-1}{m_{12}}\right] \quad . \tag{8.20}$$

In the ghost side of the tangent bifurcation, one does not have a pair of stable/unstable POs, but a pair of complex conjugate POs. We expand around the contributing PO (the one selected by the steepest-descent requirement). The neighboring PO is simply given by taking the complex conjugate of the contributing one, i.e. $z_1 = (z_0)^*$, etc. and we can use these values to evaluate the derivatives in (8.20). We refer to the derivatives calculated by this method as "neighbor" derivatives, in contrast to the "numerical" derivatives mentioned above.

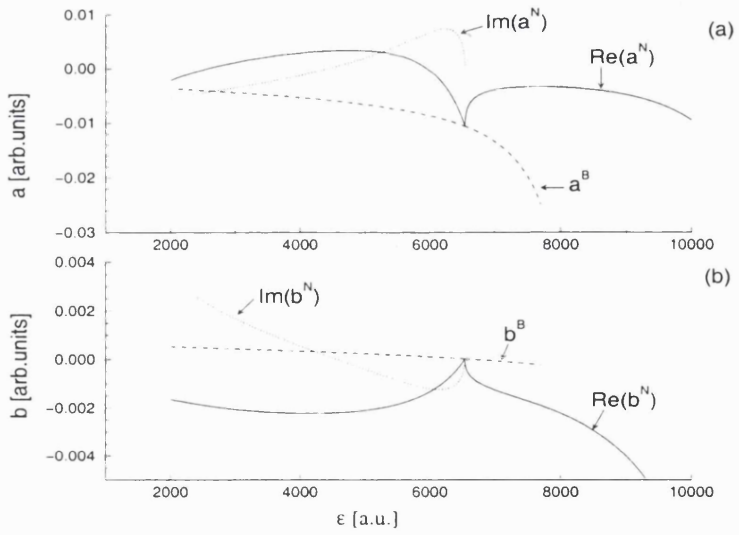

Figure 8.9: Third derivatives of the scaled action (a) $\tilde{a} = \frac{\partial^3 \tilde{S}}{\partial z^3}$ and (b) $\tilde{b} = \frac{\partial^3 \tilde{S}}{\partial z^2 \partial z'}$ for the tangent bifurcation of t_0 at $\theta = 11°, \epsilon_b = 6540$. The numerical derivatives (a^N and b^N) are complex on the ghost side of the bifurcation ($\epsilon < \epsilon_b$), while the "neighbor" derivatives (8.20) a^B and b^B are always real.

We show in Fig. 8.9 the third derivatives calculated by both methods for the tangent bifurcation of t_0 at $\theta = 11°, \epsilon_b = 6540$, in scaled coordinates: $\tilde{a} = a/B, \tilde{b} = b/B$. By

definition, the "neighbor" derivatives (8.20) a^B and b^B are real on the ghost side of the bifurcation ($\epsilon < \epsilon_b$). They join smoothly at the bifurcation. They cannot be defined beyond the point where the unstable partner t_0^- disappears ($\epsilon = 7700$). The numerical derivatives a^N and b^N are complex on the ghost side ($\epsilon < \epsilon_b$); they join in a rather abrupt manner at the bifurcation. They diverge extremely strongly at the pitchfork bifurcation ($\epsilon = 12800$, not on the graph), where $m_{12} = 0$. This bifurcation is however very far from the TB that we study here, and is in a regime where the quadratic expansion is accurate. The rather large disagreement between the two methods comes from the fact that the action is not exactly cubic. Finally, we note that $b(\epsilon_b) = 0$ with both methods.

8.3.2 Cubic integration

Now we have to carry out the integral (5.19) using the cubic expansion (8.15)

$$\begin{aligned} \mathcal{I} &= \sqrt{\frac{\beta}{\pi\hbar}} \int dz \int dz' \sqrt{\frac{p_x^0 p_{x'}^0}{-m_{12}}} e^{\varphi_3(z,z')/\hbar} \quad , \\ \varphi_3(z,z') &= iS_3(z_0, \delta z, \delta z') - \frac{\beta}{2}[z^2 + (z')^2] \quad . \end{aligned} \tag{8.21}$$

We make the change of variables $\bar{q} = (\delta z' + \delta z)/2, \Delta q = \delta z' - \delta z$, and the argument of the exponential becomes

$$\begin{aligned} \varphi_3(\bar{q}, \Delta q) &= iS_0 - \beta z_0^2 + iR_1\bar{q} + iR_2\bar{q}^2 + \frac{i}{3}R_3\bar{q}^3 + R_0(\bar{q})\Delta q^2 \quad , \\ \text{with} \quad R_1 &= 2i\beta z_0 \quad , \quad R_2 = \frac{m_{11}-1}{m_{12}} + i\beta \quad , \quad R_3 = a + 3b \quad , \\ R_0(\bar{q}) &= \frac{1}{4}\left[i\frac{m_{11}+1}{m_{12}} - \beta + i\bar{q}(a-b)\right] \quad . \end{aligned} \tag{8.22}$$

The Gaussian integration over Δz gives $\sqrt{-\pi\hbar/R_0(\bar{q})}$. In a similar fashion as in the SPA, we neglect the variations of this (slowly varying) function of $\bar{q}$, and consider its value at the TSPO ($\bar{q} = 0$), i.e. $2\sqrt{-\pi\hbar m_{12}/[im_{11} + i - \beta m_{12}]}$. The cubic exponential integral over $\bar{q}$ gives an Airy function. The final result is

$$\mathcal{I} = 2\pi\hbar^{1/3} \sqrt{\frac{\beta p_x^0 p_{x'}^0}{\beta m_{12} - i(m_{11}+1)}} R_3^{-\frac{1}{3}} e^{\rho/\hbar} \mathrm{Ai}(\xi) \tag{8.23}$$

$$\rho = iS_0 - \beta z_0^2 - i\frac{R_1 R_2}{R_3} + i\frac{2R_2^3}{3R_3^2} \quad , \quad \xi = \hbar^{-\frac{2}{3}} R_3^{-\frac{1}{3}} \left[R_1 - \frac{R_2^2}{R_3}\right] \quad . \tag{8.24}$$

We normalize to the $\theta = 0°$ amplitude. Note that the scaled prefactor contains B:

$$I_{\mathrm{SC}}(\mathcal{N}; \epsilon) = \mathbf{Re}\, B^{-\frac{1}{3}} \sqrt{\frac{2\pi\beta}{\cos\theta \tilde{m}_{12} - i(m_{11}+1)}} \tilde{R}_3^{-\frac{1}{3}} e^{B\tilde{\rho}} \mathrm{Ai}(B^{\frac{2}{3}}\tilde{\xi}) \quad , \tag{8.25}$$

where the scaled quantities are calculated as usual from the scaled dynamics ($\tilde{M}, \tilde{a}, \tilde{b}$, etc.). We plot the resulting amplitude and frequencies (obtained by Fourier transforms) in Fig. 8.10 for $\theta = 11°$ and Fig. 8.11 for $\theta = 27°$.

The "neighbor" cubic formula uses neighbor derivatives. Its amplitude therefore stops on the real side where the unstable PO t_0^- disappears on the edge of the SoS. On the ghost side, we use the complex conjugate of the t_0 ghost, so we are not limited in such a way. It goes smoothly through the bifurcation. In the ghost region it tends towards the amplitude of the quadratic PO/NO formula (5.63) as one goes away from the bifurcation.

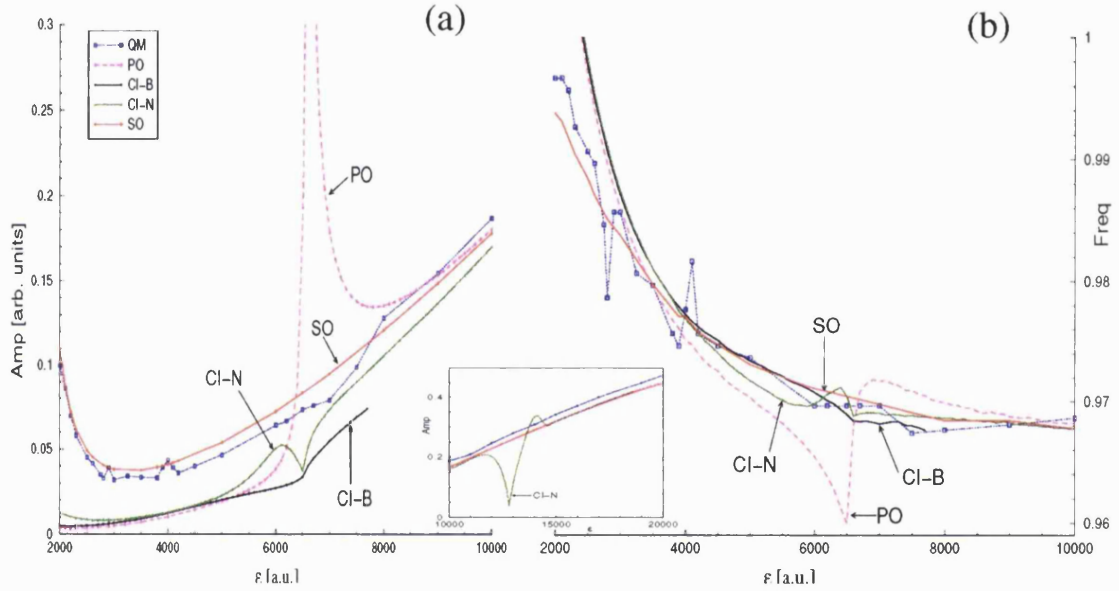

Figure 8.10: Cubic integration for P1 current at $\theta = 11°$ for the tangent bifurcation of t_0 at $\epsilon_b = 6540$. (a) Amplitudes; the inset is on a larger scale. (b) Frequencies. We show the cubic integration results for the neighbor [CI-B] and numerical [CI-N] derivatives, for the quadratic PO/NO formula [PO], the SO formula [SO] and the quantum results [QM]. The quadratic formula also contains the ghost contribution.

The "numerical" cubic amplitude, (calculated with the numerical derivatives) can be defined all along t_0. It has an abrupt behavior at the bifurcation, reflecting the behavior of the numerical derivatives. It converges towards the quadratic formula in the regular limit, before and even after the strong divergence around the pitchfork bifurcation at $\epsilon = 12800$ (see inset). On the ghost side it approaches the quadratic formula, but departs slightly from it at the low ϵ end. Note that there is a serious theoretical problem behind the numerical cubic formula on the ghost side. The numerical third derivatives are complex, therefore *the cubic term in the exponential makes the integral diverge in any case*: $\mathcal{I} \sim \int_{-\infty}^{\infty} dq \exp[-\mathbf{Im}\,(a) q^3] = \infty$. The amplitudes we show in that case are a kind of "analytic

continuation" of the Airy formula for complex arguments.

The cubic expansions with both types of derivatives achieve their goal: to avoid the unphysical rise of the quadratic amplitude at the bifurcation. We also wanted to know whether the ghost contribution could be significantly increased by a cubic expansion. This study shows that the cubic ghost contribution is still too small compared with quantum results. This was expected as a cubic expansion should tend, far from the bifurcation, towards the quadratic result (as the third derivatives of the action become small). We do not believe that a more elaborate expansion around the tangent bifurcation could increase the ghost contribution and give an agreement with the quantum calculations. We believe that the PO and NO theories are inaccurate as a result of the approximations used (neglecting a term in the SPA condition).

The cubic formula for P2 at $\theta = 27°$ is shown in Fig. 8.11. The results here are not very satisfactory. The numerical derivatives formula joins the quadratic formula on the real side for high ϵ. On the ghost side it follows approximately the SO results down to $\epsilon \simeq 4000$; below, it diverges like the quadratic contribution. It does not remove the spike at the tangent bifurcation. The neighbour derivatives formula is smoother around the bifurcation, but does not follow well the SO results. Again, we believe that the PO/NO formalism here is inadequate, and that the ghost cannot describe the QM results. We recall the fact that we also have another contribution from $2t_0$ for $\epsilon > 10000$ (not shown here, see Fig. 6.4), that is hard to reconcile with an expansion of s'–PO. We believe that one needs the SOs for an accurate semiclassical description of the P2 current at $\theta = 27°$.

8.4 Approximation of SOs by POs

In order to gain more understanding about the link existing between SOs and POs, we expand some characteristics of a SO (such as its starting position or action) around those of a PO. In particular, we want to see wether the difference between SOs and POs is due to a departure from the quadratic action hypothesis. Note that actually one should expand around normal orbits (NOs), but we consider here only time-symmetric (TS) trajectories which are both NOs and POs.

Quadratic approximation

Assuming a quadratic action (5.24)

$$S \simeq \mathcal{S}_2 \quad , \tag{8.26}$$

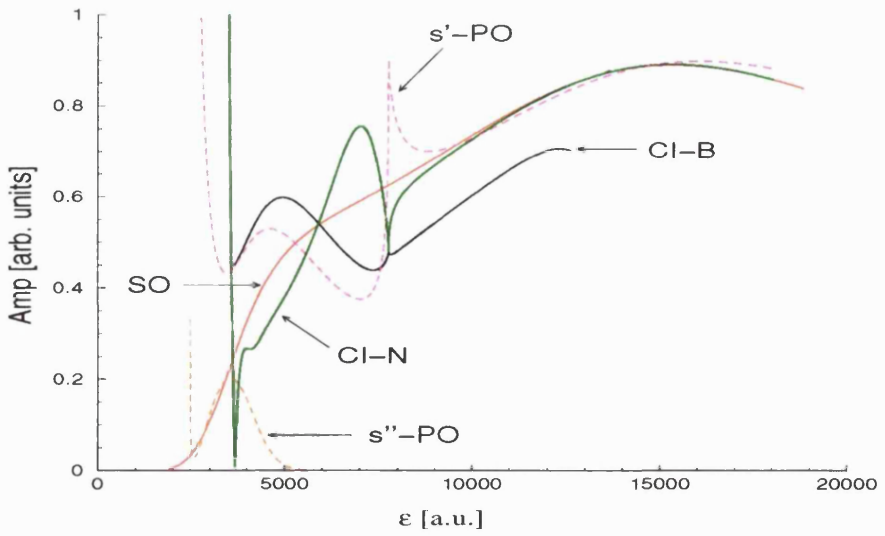

Figure 8.11: Semiclassical P2 amplitude of the cubic integration for $s'-PO$ at $\theta = 27°$ around the tangent bifurcation at $\epsilon_b = 7756$. We use both types of derivatives in the cubic formula: neighbour [CI-B] and numerical [CI-N]. We also show the PO/NO quadratic formula including the ghost contribution [PO] and the SO results, which are the most accurate (we do not show QM results).

we can write the momentum of a TS trajectory starting at z in terms of a TS trajectory starting at z_1 (see Appendix A.2):

$$\begin{aligned} p_z(z) = -\frac{\partial S}{\partial z}(z) &\simeq -\frac{\partial S}{\partial z}(z_1) - [z - z_1]\left[\frac{\partial^2 S}{\partial z^2} + \frac{\partial^2 S}{\partial z' \partial z}\right](z_1) \\ &= p_z(z_1) - [z - z_1]\frac{m_{11} - 1}{m_{12}}(z_1) \quad . \end{aligned} \tag{8.27}$$

Considering the $z = z_{SO}$ trajectory to be a SO, we have $p_z(z_{SO}) = i\beta z_{SO}$; for an expansion around a TSPO ($z_1 = z_{PO}$), we have $p_z(z_{PO}) = 0$. Hence we get

$$z_{SO}^{(2)} \simeq z_{PO}\frac{1}{1-\delta} \quad , \tag{8.28}$$

where $\delta = -i\beta m_{12}/(m_{11} - 1)$ has been defined in (5.41). We can then write the quadratic approximation of the action of the SO:

$$S_{SO}^{(2)} \simeq S_{PO} + \frac{m_{11} - 1}{m_{12}}\left(\frac{\delta}{1-\delta} z_{PO}\right)^2 \quad . \tag{8.29}$$

Inserting the approximations (8.28) and (8.29) in the SO formula (5.44), we get $\Gamma_{SO}^{(2)} \simeq -\beta z_{PO}^2/(1-\delta)$, i.e., the PO/NO formula. This merely expresses the trivial fact that a quadratic expansion of a (supposedly) quadratic function around *any* point (e.g., a SO, PO or CCO) is exact, hence, the same. However, the quadratic approximation provided us with a relation between SOs and POs, which should be valid when the action is close to quadratic.

We can also consider an expansion around a TS central closed orbit (CCO): $z_1 = 0, p_z^1 = p_z^{CCO}$. We get

$$p_z^{SO} = -p_z^{CCO}\frac{\delta}{1-\delta} \quad . \tag{8.30}$$

Similarly, one recovers the CCO formula (5.53) by inserting in the SO formula (5.45) this approximation and the related quadratic approximation of the action.

Finally, because the monodromy matrix M is given by the second derivatives of S, (8.26) implies that $M_{SO} \equiv M_{PO} \equiv M_{CCO}$. Thus $\mathcal{D}_{SO} \equiv \mathcal{D}_{PO} \equiv \mathcal{D}_{CCO}$, and one obtains the formal equivalence of the different formulae in the case of a quadratic action.

Cubic approximation

The interesting regions where SO and PO formulae disagree involve tangent bifurcations, where the quadratic action hypothesis is wrong. Hence we shall also consider a cubic approximation. Assuming a cubic action $S \simeq \mathcal{S}_3$ (8.15), we can write:

$$p_z(z) \simeq p_z(z_1) - [z-z_1]\frac{m_{11}-1}{m_{12}}(z_1) - \frac{1}{2}(a+3b)[z-z_1]^2 \quad . \tag{8.31}$$

Using the definition of SOs and TSPOs, we find a quadratic equation that we solve to get:

$$z_{SO}^{(3)} \simeq z_{PO} + \frac{i}{a+3b}\left[\beta\frac{1-\delta}{\delta} + \sqrt{\left(\beta\frac{1-\delta}{\delta}\right)^2 + 2i\beta z_{PO}(a+3b)}\right] \quad , \tag{8.32}$$

the negative root being rejected. We can then write the cubic approximation (8.15) for the action of the SO:

$$S_{SO}^{(3)} \simeq S_{PO} + \frac{m_{11}-1}{m_{12}}(z_{SO}^{(3)} - z_{PO})^2 + \frac{a+3b}{3}(z_{SO}^{(3)} - z_{PO})^3 \tag{8.33}$$

and insert those approximation in the SO formula (5.44) in order to get a cubic approximation of the SO current.[10]

We show in Fig. 8.12 and 8.13 the quadratic and cubic approximations of the starting position, action and current amplitude, for t_0–SO at $\theta = 11°$. The cubic approximation tends towards the quadratic one far from the bifurcation, where the third derivatives are small. As expected, it also smooths out the spike of the quadratic approximation at the bifurcation — the approximation using numerical derivatives shows a small spike.

[10] We do not consider here the change in the prefactor $\mathcal{D}_{SO} \simeq \mathcal{D}_{PO} + \mathcal{O}(z_{SO}^{(3)} - z_{PO})$ due to the third derivatives. We recall that here we approximate the SO formula by a third degree expansion around a PO; we do *not* write a formula resulting from a cubic expansion of the action prior to the integration, as we have done in the previous section 8.3.

However, it seems unable to describe the behavior of the SO for $\epsilon < 5000$. This shows that the failure of the PO description of the current is *not* due to the fact that the action is not quadratic (i.e., has a significant third derivative) as a result of the tangent bifurcation. It seems that it is more due to the fact that there are *two* distinct and non-bifurcating POs (the real t_1–PO and the complex $t_{\rm gh}$) involved in the current, and which are linked to the SO. The reason for the failure of the quadratic approximation (8.28) is not a large third derivative, but the fact that there are two points (POs) around which one should expand the SO.

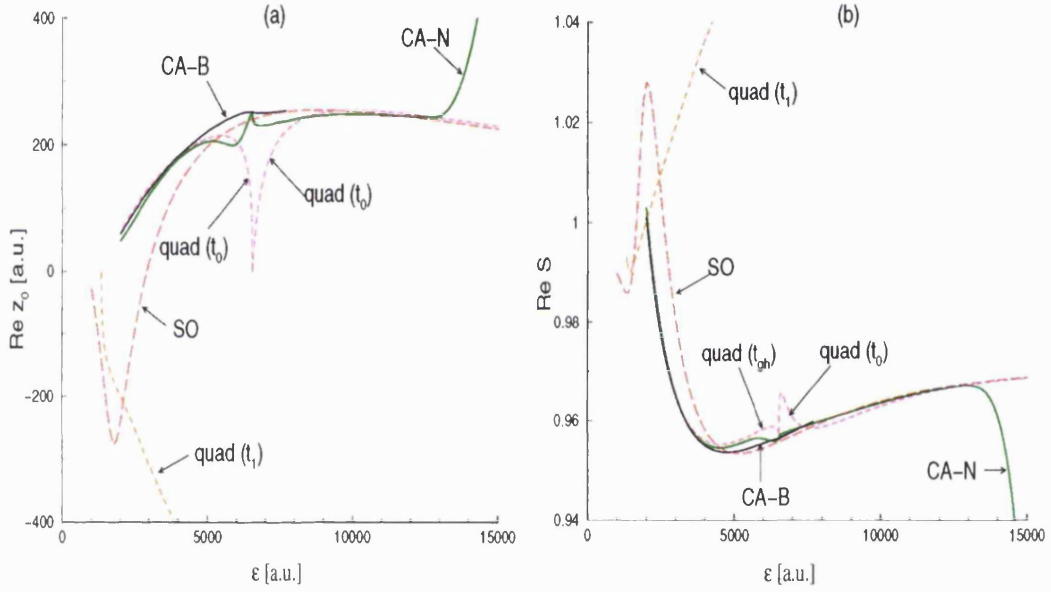

Figure 8.12: Cubic approximation of (a) the starting position z_0 and (b) the action $\hat{S}$ of t_0 at $\theta = 11°$. We use both types of third derivatives: numerical [CA-N] and neighbor [CA-B], calculated for t_0–PO and $t_{\rm gh}$. We also show t_0–SO, and the results of the quadratic approximation (around t_0–PO, $t_{\rm gh}$ and t_1–PO), indicated by [quad].

The only promising strategy one could employ to approximate the SO by POs would be to to calculate third derivatives at a "mid-point" between t_1–PO and $t_{\rm gh}$ and to build an action function interpolating the actions of both POs. We did not attempt this technique, which is not standard at all as these POs are *not* involved together in a bifurcation.[11]

We note in Fig. 8.13 (b) the similarity between the cubic approximation of the SO current and the result of the cubic integration (8.25). We would expect the latter to be equivalent to a cubic approximation of a SO current given by a cubic integration itself,

[11] This is similar to the problem of the global contribution of $2t_0$–PO and s'–PO at $\theta = 27°$ presented in subsection 6.2.2.

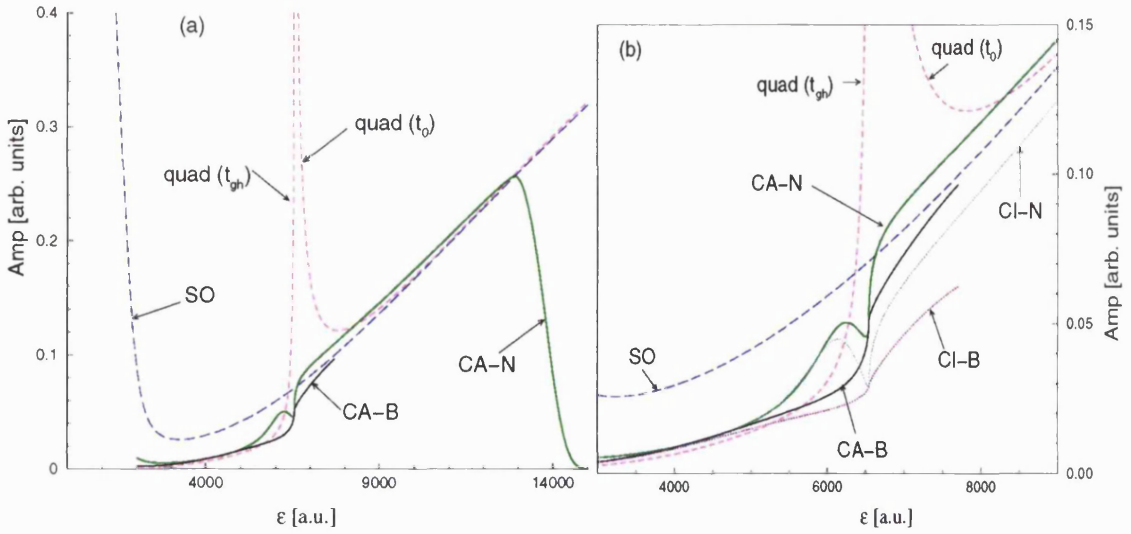

Figure 8.13: Cubic approximation of the semiclassical amplitude for t_0 at $\theta = 11°$. We use both types of third derivatives: numerical [CA-N] and neighbor [CA-B], that we compare to t_0–*SO*. We also show the results of the quadratic approximation (i.e., the PO/NO formula), indicated by [quad (t_0)] and [quad t_{gh}]. In the detailed graph (b), we also show the results from the cubic integration (8.25) [CI-N] and [CI-B].

in analogy with the equivalence of the PO/NO formula (a quadratic integration) and the quadratic approximation of the SO current.

* * *

The previous sections 8.3 and 8.4 were an attempt to understand the link between the usual POs and the SOs. The conclusion of this study is that one cannot use POs if one demands accurate agreement with QM calculations in the "ghost" regions. In these cases, one *needs* to use the saddle orbits.

Chapter 9

CONCLUSION

Our study of the resonant tunneling diode (RTD) in tilted fields from a quantum chaos perspective succeeded in finding an accurate semiclassical theory for the current: the saddle orbit formula. In the process, we showed that the heuristic, qualitative approach based on a mixture of the Gutzwiller trace formula (GTF) and considerations about the accessibility of the periodic orbits (POs) cannot explain in a satisfactory manner all the experimental features. One needs instead the more elaborate normal or periodic orbit theories to describe the shift in the frequency of the oscillations, as well as the important consequences that tori quantization has on the accessibility of stable periodic orbits. These theories nevertheless fail in the "mixed" regime where one finds non-isolated contributions (at $\theta = 27°$) or absence of real POs (at $\theta = 11°$ and $\theta = 27°$). Even more elaborate versions of PO theories (such as cubic expansions) cannot achieve accuracy.

We found that in these situations one has to use the saddle orbits (SOs) prescribed by the saddle point condition of the stationary phase approximation (SPA). They are a new type of orbits, that are complex and non-periodic. Although complex, they show a persistence in the classical limit. We also proposed the minimal orbits, which give a very good description of the quantum current. This showed that one can, in this instance, relax the strict stationary phase condition of the SPA, and consider the "best" real approximation of the complex saddle point, that minimizes the gradient.

The theoretical approaches (semiclassical and quantum) showed that it is possible to obtain a good qualitative understanding of the experimental current, and identify the dynamical reasons lying behind its behavior. A quantitative agreement for the amplitudes and frequencies of the experimental oscillations can be reached with an accuracy of around 20%, after normalization of the amplitudes and consideration of the effects of decoherence.

Some theoretical limitations appeared for the SO formula at $\theta = 20°$, where the main SO presents a degeneracy yielding an unphysical peak in the semiclassical amplitude. This raises interesting questions about the saddle orbits, in particular the existence of "bifurcations". Our model was also unable to give an accurate description of one broad region of period-three oscillations at $\theta = 38°$, where both quantum and semiclassical theories were unable to describe the strong experimental signal.

Future work should obviously include a study of these failures. The first thing to do at $\theta = 20°$ is to locate the complex scaled field ϵ_z where the quadratic expansion becomes degenerate $[\mathcal{D}(\epsilon_z) = 0]$. For $\theta = 38°$, the main problem is the nature and extent of the shift of the initial state. Quantum calculations could help to identify where the initial state should lie in order to give such strong period-three oscillations. Also, one needs an accurate estimate of the coherence time of the electrons.

A more general issue is whether the minimal orbits are always as successful as the saddle orbits. One can also look at correlations of the current: $\langle I(E)I(E+\Delta E)\rangle_E$. One could then develop a semiclassical theory involving SOs, and compare it to correlations of the density of states given semiclassically by periodic orbits. Note that including the decoherence of the current would select short SOs. One could also study the energy levels spacings distribution $P(s)$, as has been done for the atom in external fields. As the dynamics are mixed, one could try to use the Brody fit (Brody *et al.* 1981).

We started a study of a classical model for the RTD with soft exponential walls, although we did not include it in this work. This removes the non-analyticity of the hard infinite walls, and transforms the cusp bifurcations into normal tangent bifurcations with $\mathrm{Tr}M = 2$. Ghost POs and saddle orbits were difficult to locate, as the complex dynamics are harder to implement. One still has to define a surface of section at constant x, that one would prefer to be real; on the other hand ghosts can very well have a complex starting x. This study could add considerably to our knowledge of discontinuity effects in chaotic systems and the numerical search for POs in a space of higher dimensions. It also echoes the interesting problem of implementing complex dynamics: in that case, one has more freedom to choose the time path, as one does not have the $x = \{0, L\}$ conditions for the hard bounces.

This work presented in chapter 5 an unified picture of the different semiclassical formulae proposed for the RTD (see Fig. 9.1). We hope that it also clarifies the picture of the general approaches to semiclassical matrix elements. In the stationary phase approxi-

mation, one has to consider two functions: the observable $\hat{A}$ and the Green's operator $\hat{G}$. Depending on the localization length scale of A compared to the oscillations length scale of G, one will be temped to neglect one or the other. One can then use several levels of approximation.

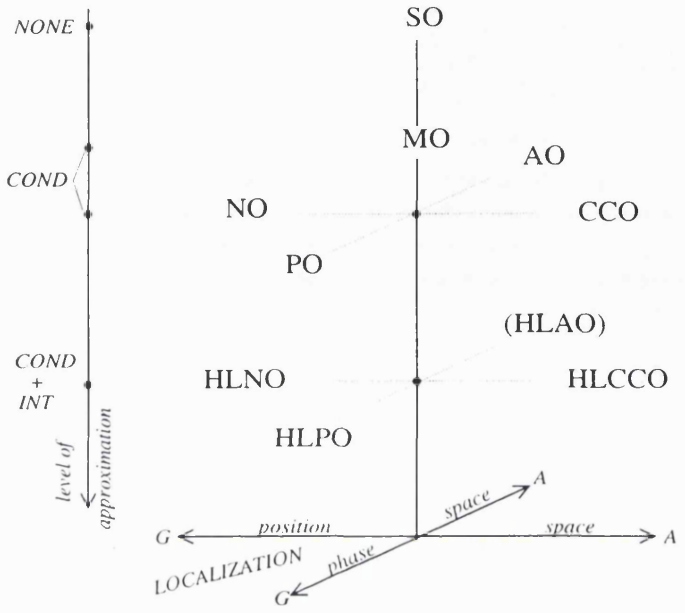

Figure 9.1: Schematic representation of the different semiclassical formulae. The vertical axis describes the three different levels of approximation; one can neglect one function (A or G) in the saddle point condition [COND], also in the integrations [COND + INT], or in none [NONE]. The horizontal plane describes the relative localization/oscillations length scales of $\hat{A}$ and $\hat{G}$ (e.g., the left end means that the oscillations of $\hat{G}$ in position space are on a much smaller scale than the localization of $\hat{A}$, etc.).

For instance, for an observable $\hat{A}$ that is smooth in phase space, one can choose to neglect it in the derivation of the stationary phase condition, as well as in the integrations. In our case, this gives the hard limit PO formula; in the generic case it is the result of Eckhardt *et al.* (1992). If one does include the variations of $\hat{A}$ in the integrations, one obtains the PO formula, which is almost equivalent to the result of Zobay and Alber (1993) derived for molecular transitions. Finally, one can make no approximation at all, and obtain the saddle orbits for the RTD, and the "angle orbits" for the semiclassical theory of the conductance in microcavities (see page 20).

The main finding of this work is the importance of the saddle orbits; they appeared from the combination of the Green's function and the Gaussian projector. The latter is found in many systems that are modeled with a harmonic potential. For instance, Franck-Condon transitions, that describe molecular photoabsorption, model the ground state

with a Gaussian (Zobay and Alber 1993). The expression of the photoabsorption involves a density of states weighted by an overlap between the ground state and the excited states. Apart from the fact that the overlap must be made in the complete space (instead of the 2-D cut at $x = 0$), this is formally equivalent to the expression of the current in the RTD. Hence, semiclassical studies of molecules with a localized ground state could also involve a type of saddle orbits; this depends on the relative length scales of the Gaussian and the oscillations of the Green's function.

Another possible application for the SOs is in a semiclassical theory of the conductance of a microcavity. The expression (1.5) is formally very close to the Bardeen expression for the current in the RTD. Usually one models the leads by hard walls, which yield standing sine waves and "angle orbits". One can also consider parabolic leads, in which case the lead functions ϕ_n are harmonic oscillator states. If one assumes further that they are in the lowest transverse energy subband, one obtains exactly the same integrals as the ones which appeared in chapter 5. If the length scale of the localization of the lead function is similar to the scale of the oscillations of the Green's function, saddle orbits might be of importance.

One can also have tunneling barriers between the leads and the cavities. The Bardeen's expression for weak tunneling has been used by Narimanov *et al.* (1998a), assuming a lowest harmonic oscillator state. They applied the theory they had developed for the RTD and found an expression involving POs. One could obviously extend their studies to find whether saddle orbits are needed.

Appendix A

Supplement on classical dynamics

A.1 Monodromy matrix

Writing $\mu = (z, p_z) = (\mu_i)$, $i = 1, 2$ the coordinates on the SoS, the components of the monodromy matrix M can be written

$$m_{ij} = \frac{\partial \mu_i}{\partial \mu_j^0}(\mu^0; T)\Big|_{x=x_{sos},\ E=\text{const}} \quad , \tag{A.1}$$

where T is the time where the central trajectory reaches the SoS, and the superscript 0 stands for the starting conditions. Although we shall work in scaled coordinates, we drop the "~" for convenience of notation. We consider a SoS taken on either the left ($x_{\text{sos}} = 0$) or right ($x_{\text{sos}} = L$) barrier. We divide the trajectory in l continuous partial trajectories between each successive bounce which occur at $x_{\text{sos}} = 0$ or $x_{\text{sos}} = L$ (here x_{sos} denotes the barriers as well). For each partial trajectory, we compute a monodromy matrix $M^{(k)}, k = 1, .., l$ given by relations similar to (A.1). The effect of each bounce is simply to redefine new initial conditions for $M^{(k)}$. Finally,

$$M = \prod_{k=1}^{l} M^{(k)} \quad . \tag{A.2}$$

Some care has to be taken when evaluating (A.1), as the conditions $x = x_{\text{sos}}$, $E = \text{const}$ yield some dependence between the arguments $(z, p_z^0, x_{\text{sos}}, p_x^0; T)$ of M. Note in particular the difference with the complete 4×4 monodromy matrix $\mathcal{M}$, which is evaluated at constant T and without energy constraints:

$$\mathcal{M}_{\alpha\beta} = \frac{\partial \eta_\alpha}{\partial \eta_\beta^0}(\eta^0; T) \quad , \tag{A.3}$$

where $\eta = (z, p_z, x, p_x) = (\eta_\alpha)$, $\alpha = 1, 2, 3, 4$. $\mathcal{M}$ can be obtained by straightforward partial derivations in (3.13).

We have:

$$E = \text{const} \quad \Rightarrow \quad p_x^0 = p_x^0[z^0, p_z^0, x^0; E] = \sqrt{2m(E + \epsilon x^0) - (p_z^0)^2 - (x^0 \sin\theta - z^0 \cos\theta)^2} \Rightarrow \tag{A.4}$$

$$\frac{\partial p_x^0}{\partial z^0} = \frac{x^0 \sin\theta - z^0 \cos\theta}{p_x^0} \cos\theta =: \mathcal{A}_1 \tag{A.5}$$

$$\frac{\partial p_x^0}{\partial p_z^0} = -\frac{p_z^0}{p_x^0} =: \mathcal{A}_2 \tag{A.6}$$

and $x(\boldsymbol{\eta}^0; T) = x_{\rm sos}$ that we solve numerically to get

$$T = T[\boldsymbol{\eta}^0; x_{\rm sos}] \quad . \tag{A.7}$$

This means that (A.1) is not evaluated with p_x^0 and T constant. To see what happens, let us take an example with $i = j = 1$. We have

$$\begin{aligned} m_{11} = & \frac{\partial z}{\partial z^0}(z^0, p_z^0, x^0, p_x^0[\ldots; E]; T[\boldsymbol{\eta}^0; x_{\rm sos}])\Big|_{p_z^0, x^0, x_{\rm sos}, E} = \frac{\partial z}{\partial z^0}(\boldsymbol{\eta}^0; T)\Big|_{p_z^0, x^0, p_x^0, T} + \\ + & \frac{\partial z}{\partial p_x^0}(\boldsymbol{\eta}^0; T)\Big|_{z^0, p_z^0, x^0, T} \frac{\partial p_x^0}{\partial z^0}[z^0, p_z^0, x^0; E]\Big|_{p_z^0, x^0, E} + \frac{\partial z}{\partial T}(\boldsymbol{\eta}^0; T)\Big|_{\boldsymbol{\eta}^0} \frac{\partial T}{\partial z^0}[\ldots]\Big|_{p_z^0, x^0, E, x_{\rm sos}} \end{aligned} \tag{A.8}$$

and

$$\frac{\partial T}{\partial z^0}[\ldots]\Big|_{p_z^0, x^0, E, x_{\rm sos}} = \frac{\partial T}{\partial z^0}[\ldots]\Big|_{p_z^0, x^0, p_x^0, x_{\rm sos}} + \frac{\partial T}{\partial p_x^0}[\ldots]\Big|_{z^0, p_z^0, x^0, x_{\rm sos}} \frac{\partial p_x^0}{\partial z^0}[\ldots]\Big|_{p_z^0, x^0, E} . \tag{A.9}$$

From $\frac{\mathrm{d}x}{\mathrm{d}z^0}(\boldsymbol{\eta}^0; T) = 0$ for $x = x_{\rm sos} = \text{const}$, we find that:

$$\frac{\partial T}{\partial z^0}[\ldots]\Big|_{p_z^0, x^0, p_x^0, x_{\rm sos}} = -\frac{\frac{\partial x}{\partial z^0}(\ldots)\big|_{p_z^0, x^0, p_x^0; T}}{\frac{\partial x}{\partial T}(\ldots)\big|_{\boldsymbol{\eta}^0}} \tag{A.10}$$

and similarly for $\frac{\partial T}{\partial p_x^0}[\ldots]\Big|_{p_z^0, x^0, p_x^0, x_{\rm sos}}$. With the velocities $\dot{\boldsymbol{\eta}}(T) = \frac{\partial \boldsymbol{\eta}}{\partial T}(\boldsymbol{\eta}^0; T)\big|_{\boldsymbol{\eta}^0}$, (A.8)-(A.10) give:

$$m_{11} = \frac{\partial z}{\partial z^0}(T) + \frac{\partial z}{\partial p_x^0}(T)\frac{\partial p_x^0}{\partial z^0} - \frac{\dot{z}}{\dot{x}}(T)\left[\frac{\partial x}{\partial z^0}(T) + \frac{\partial x}{\partial p_x^0}(T)\frac{\partial p_x^0}{\partial z^0}\right] \quad . \tag{A.11}$$

We get finally

$$m_{ij} = \mathcal{M}_{ij} + \mathcal{M}_{i4}\mathcal{A}_j - \frac{\dot{\mu}_i}{\dot{x}}(T)\left[\mathcal{M}_{3j} + \mathcal{M}_{34}\mathcal{A}_j\right] \quad . \tag{A.12}$$

A.2 Derivatives of the action

We want to relate the second derivatives of the action $S[z, z'] = S[x = 0, z; x' = 0, z']$ to the monodromy matrix M. It is obvious from the definition of the action

$$S[\boldsymbol{q}, \boldsymbol{q}'] = \int_{\boldsymbol{q}}^{\boldsymbol{q}'} d\boldsymbol{q}'' \boldsymbol{p}(\boldsymbol{q}'') \tag{A.13}$$

that

$$\frac{\partial S[z, z']}{\partial z} = -p_z[z, z'] \quad , \quad \frac{\partial S[z, z']}{\partial z'} = p_z'[z, z'] \quad . \tag{A.14}$$

For $S = S[z, z']$, one defines a trajectory by its starting and final points, while for $M = M(z, p_z)$ the trajectory is defined by its starting position and momentum. One can

write

$$\left.\frac{\mathrm{d}z'}{\mathrm{d}z}(z,p_z)\right|_{z'=\text{const}} = 0 = \frac{\partial z'}{\partial z}(z,p_z) + \frac{\partial z'}{\partial p_z}(z,p_z)\frac{\partial p_z}{\partial z}[z,z'] \Rightarrow \frac{\partial p_z}{\partial z}[z,z'] = -\frac{m_{11}}{m_{12}} \quad (A.15)$$

$$\left.\frac{\mathrm{d}p_z}{\mathrm{d}p_z}[z,z']\right|_{z=\text{const}} = 1 = \frac{\partial p_z}{\partial z'}[z,z']\frac{\partial z'}{\partial p_z}(z,p_z) \Rightarrow \frac{\partial p_z}{\partial z'}[z,z'] = \frac{1}{m_{12}} \quad (A.16)$$

$$\frac{\partial p'_z}{\partial z}[z,z'] = \frac{\partial p'_z}{\partial z}(z,p_z) + \frac{\partial p'_z}{\partial p_z}(z,p_z)\frac{\partial p_z}{\partial z}[z,z'] = m_{21} + m_{22}\frac{-m_{11}}{m_{12}}$$

$$\overset{\det M=1}{=\!=} -\frac{1}{m_{12}} \quad (A.17)$$

$$\frac{\partial p'_z}{\partial z'}[z,z'] = \frac{\partial p'_z}{\partial p_z}(z,p_z)\frac{\partial p_z}{\partial z'}[z,z'] = m_{22}\frac{1}{m_{12}} \quad . \quad (A.18)$$

The matrix of second derivatives of $S[z,z']$ reads therefore:

$$\begin{pmatrix} \dfrac{\partial^2 S}{\partial z^2} & \dfrac{\partial^2 S}{\partial z \partial z'} \\ \dfrac{\partial^2 S}{\partial z' \partial z} & \dfrac{\partial^2 S}{\partial z'^2} \end{pmatrix} = \begin{pmatrix} \dfrac{m_{11}}{m_{12}} & -\dfrac{1}{m_{12}} \\ -\dfrac{1}{m_{12}} & \dfrac{m_{22}}{m_{12}} \end{pmatrix} \quad (A.19)$$

Note that there might be several trajectories defined by $[z,z']$; this means that $S[z,z']$ is a multi-valued function while $M(z,p_z)$ is unique. The singular points associated with this are the points where $m_{12}=0$, where two families of trajectories $(z,p_z^j) \to (z',p_z'^j), j=1,2$ coalesce.

A.3 Algorithms

Here we describe algorithms used to find numerically periodic orbits or saddle orbits (5.43). It is based on a Newton-Raphson method. For a trajectory $(z,p_z) \to (z',p'_z)$, we define the function

$$\boldsymbol{f}_{\mathrm{PO}}(z,p_z) = (z'-z, p'_z - p_z) \quad (A.20)$$

that should vanish for POs. Its derivative reads:

$$\mathrm{D}\boldsymbol{f}_{\mathrm{PO}} = \begin{pmatrix} m_{11}-1 & m_{12} \\ m_{21} & m_{22}-1 \end{pmatrix} = M - \mathbb{1} \quad . \quad (A.21)$$

The PO can be found by taking the limit $n \to \infty$ of the algorithm

$$\begin{pmatrix} z^{(n+1)} \\ p_z^{(n+1)} \end{pmatrix} = \begin{pmatrix} z^{(n)} \\ p_z^{(n)} \end{pmatrix} - \left[\mathrm{D}\boldsymbol{f}_{\mathrm{PO}}\left(z^{(n)},p_z^{(n)}\right)\right]^{-1} \boldsymbol{f}_{\mathrm{PO}}\left(z^{(n)},p_z^{(n)}\right) \quad . \quad (A.22)$$

The procedure is similar for saddle orbits, with the modifications

$$f_{\mathrm{SO}}(z)\Big|_{p_z=i\beta z} = p'_z + i\beta z' \quad , \quad (A.23)$$

$$f'_{\mathrm{SO}}(z) = m_{21} - m_{12}\beta^2 + i\beta\left(m_{11}+m_{22}\right) \quad . \quad (A.24)$$

It is interesting to note that (the determinant of) the derivatives above correspond to the prefactors in the GTF of the DoS [$\det(M - \mathbb{1}) = \mathrm{Tr}M - 2$] and the current formulae [$-\mathcal{D}$, see (5.34)].

Appendix B

Supplement on semiclassical theories

B.1 Stationary phase approximation

Stationary phase approximation

The stationary phase approximation (SPA) is used to approximate, in the $h \to 0$ limit, the integral

$$I = \int_{-x_-}^{x_+} dx e^{if(x)/h} g(x) \tag{B.1}$$

where $x_\pm \gg 1$. A complete discussion can be found in Dieudonné (1968) or Heading (1962). The basic argument is as follows. Because $f(x)/h \gg 2\pi$, the contribution of most of the points x will be random-like, and therefore will cancel each other. (i) Only a small interval $[x_0 - \Delta, x_0 + \Delta]$ around the stationary point x_0 defined by

$$f'(x_0) = 0 \tag{B.2}$$

will contribute. (ii) If the function $g(x)$ is smooth, one can consider it to be constant in this interval. (iii) If $\Delta \ll 1$, one can expand $f(x)$ around x_0 up to to second order:

$$f(x) \simeq f_2(x) = f(x_0) + \frac{1}{2} f''(x_0)(x - x_0)^2 \quad . \tag{B.3}$$

Therefore

$$\begin{aligned} I &\overset{(i),(ii)}{\simeq} g(x_0) \int_{x_0-\Delta}^{x_0+\Delta} dx e^{if(x)/h} \overset{(iii)}{\simeq} g(x_0) \int_{x_0-\Delta}^{x_0+\Delta} dx e^{if_2(x)/h} \overset{(i)}{\simeq} g(x_0) \int_{-\infty}^{\infty} dx e^{if_2(x)/h} \\ \Rightarrow I &= \sum_{i=1}^{N} g(x_0^i) \sqrt{\frac{2\pi h}{|f''(x_0^i)|}} e^{if(x_0^i)/h + i\,\mathrm{sign}[f''(x_0^i)]\pi/4} \quad . \end{aligned} \tag{B.4}$$

In the second line we have generalized to the case of N stationary points x_0^i. The success of this scheme can suffer from the following limitations:

1. $|x_\pm|$ are not large. One should use therefore error functions (Erf) for $\int_{-x_-}^{x_+} dx \exp[if_2(x)/h]$ instead of extending $x_\pm$ to ∞.

2. h is not small, and the function $\exp[if(x)/h]$ does not oscillate sufficiently for the random cancellations.

3. Two stationary points x_0^1 and x_0^2 are close to each other, and might coalesce as an external parameter is varied; then $f''(x_0^{1,2}) \to 0$ and (B.4) diverges. One should use a cubic expansion.

4. There exists no real stationary points. One should use the steepest-descent approach.

Steepest-descent method

The steepest-descent method is used for the complex version of (B.1), and proceeds with the same approximations.

$$I = \int_C dz e^{if(z)/h} g(z) \quad , \quad f(z) = f_R(z) + if_I(z) \quad . \tag{B.5}$$

By analyticity, one will deform the complex integration path C so that it goes through the complex stationary points z_0^i of $f(z)$. The maximum modulus theorem for analytical complex functions implies that z_0 is a *saddle point*: $f_R(z_0)$ is max/min $\Leftrightarrow$ $f_I(z_0)$ is min/max. Cauchy-Riemann relations imply that the steepest-descent paths [paths where $f_I(z)$ changes the most] going through z_0 are identical to the stationary phase paths [paths where $f_R(z)$ is constant]. There are two sorts of such paths; the steepest-descent method prescribes that C follows the path that goes through the "mountains" regions defined by $f_I(z) > f_I(z_0)$. Finally,

$$I = \sum_{i=1}^{N} g(z_0^i) \sqrt{\frac{2\pi h}{|f''(z_0^i)|}} e^{if(z_0^i)/h + (\pi/2 - \arg[f''(z_0)])i/2} \quad . \tag{B.6}$$

Note that in this work we shall also refer to the steepest-descent method as the "stationary phase approximation" (SPA).

Application to semiclassics

In semiclassical physics, one considers a quantum object in the limit $\hbar \to 0$, which brings in oscillatory integrals like (B.1), with the substitutions $h \to \hbar$ and $f \to S$, where S is the

classical action. For example, the Feynman path integral representation of the propagator can be evaluated by SPA; the result is that only classical paths contribute to the quantum propagator in the semiclassical limit (Kleinert 1995). Similarly, the GTF for the density of states appears as the result of a SPA on the trace integral of the Green's function. The stationary points here are periodic orbits, which can bifurcate as a dynamical parameter ϵ is varied. In this case the POs are not isolated and coalesce at the bifurcation (case 3 above). In the simplest case, one should use a cubic expansion of the action, called a normal form, to avoid the divergence (Schomerus and Sieber 1997).

Ghost contributions

In a tangent bifurcation occurring at ϵ_b, two (real) POs (one stable and one unstable) approach each other on the real side, (e.g., $\epsilon > \epsilon_b$) and then coalesce at ϵ_b. Although there are no real POs on the other side ($\epsilon < \epsilon_b$), one has a pair of complex POs, which are complex conjugates of each other.

We show in Fig. B.1 contour plots of the complex scaled action $\hat{S}$ as a function of the complex starting condition $z = (z_R, z_I)$. The action depends on four real variables (the complex starting and final positions), which makes it hard to visualize. Hence one needs a restriction of the number of free variables. One could fix the starting position z at the value of one of the POs $[z_{PO}]$ and vary the starting momentum, effectively plotting $S(z = z_{PO}, z')$. One would see a saddle at the PO ($z' = z_{PO}$), but no saddle associated with *the other* PO as the fixed starting condition is not the adequate one. It is more convenient to restrict ourselves to time-symmetric closed orbits (TSCOs) defined by (5.38), especially as most POs are TS. Having restricted that way the number of free parameters, we can plot $\hat{S}(z, z' = z)$ as a function of only one complex position (i.e., two real variables).

On the real side of the tangent bifurcation ($\epsilon = 6600$), one has the stable PO t_0 ($z_0 = 410.0$) and the unstable t_0^- ($z_0 = 478.9$). They are the saddle points of the action. The path of integration can be kept to the real axis. On the complex side ($\epsilon = 6500$), one has the complex ghost PO t_{gh} ($z_0 = 410.0 - 28.3i$); its complex conjugate ($z_0 = 410.0 + 28.3i$) is also periodic. One sees clearly the fact that the contour lines of constant $\mathbf{Im}\,\hat{S}$ in (a) and (b) are perpendicular to the lines of constant $\mathbf{Re}\,\hat{S}$ in (c) and (d). This follows from Cauchy-Riemann relations for the analytic function $\hat{S}(z, z' = z)$: $\nabla \mathbf{Re}\,\hat{S} \nabla \mathbf{Im}\,\hat{S} = 0$.

The steepest-descent method requires one to take the path of maximum variation of

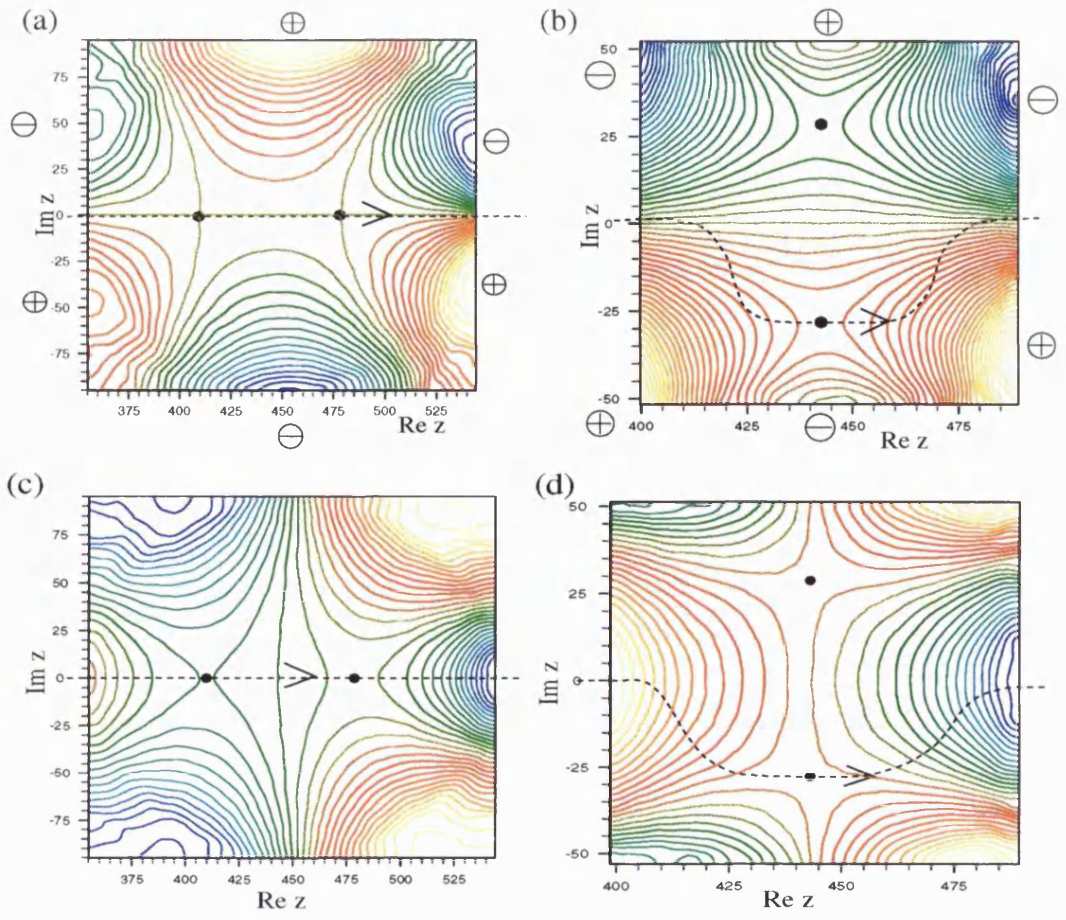

Figure B.1: Complex action $\hat{S}$ as a function of the complex starting position (z_R, z_I). We use TSCOs similar to t_0 (i.e., having one bounce on each wall), at $\theta = 11°$. Yellow contour lines are high, blue lines are low. (a) and (b): $\mathbf{Im}\,\hat{S}$. (c) and (d): $\mathbf{Re}\,\hat{S}$. The filled circles are POs, the $\oplus/\ominus$ are regions where $\mathbf{Im}\,\hat{S}$ is high/low. The dashed, arrowed line shows the path required by the steepest-descent method. (a) and (c) $\epsilon = 6600$. On the real side of the bifurcation, one has 2 real POs: the stable t_0 at $z_0 = (410.0, 0)$ and the unstable t_0^- at $z_0 = (478.9, 0)$. (b) and (d) $\epsilon = 6500$. On the complex side, one has the ghost PO t_{gh} at $z_0 = (410.0, -28.3)$ and its complex conjugate.

$\mathbf{Im}\,\hat{S}$ which goes through a saddle point via the "mountains" of $\mathbf{Im}\,\hat{S}$; they are regions (indicated by $\oplus$) where $\mathbf{Im}\,\hat{S}$ is higher than at the saddle point. In this case, this requires to consider *only* the PO with $\mathbf{Im}\,z_0 < 0$; one cannot distort the path from the real axis $(-\infty \to +\infty)$ to go through the mountains around the other PO (the complex conjugate). Actually, the latter PO (which has $\mathbf{Im}\,z_0 > 0$) has a second derivative of the action with $\mathbf{Im}\,\hat{S}'' = \mathbf{Im}\,\frac{\mathrm{Tr}M-2}{\hat{m}_{12}} < 0$; this would make the Gaussian integration following the steepest-descent method diverge.[1] Moreover, the "analytical continuation" of the result of the

[1] $\mathrm{Im}\hat{S}'' < 0 \Rightarrow \pi/4 < \vartheta < 3\pi/4$, where $(\cos\vartheta, \sin\vartheta)$ is the eigenvector in the (z_R, z_I) plane corresponding

Gaussian integral where it does not converge would explode exponentially as one moves away from the bifurcation or in the classical limit $\hbar \to 0$, as this PO has $\mathbf{Im}\, \hat{S} < 0$. This is the reason why the contribution from such POs is termed "unphysical".

In summary, one has to consider two POs on one side of the bifurcation and only one on the ghost side, discarding the "unphysical" PO. This is reminiscent of Stokes' phenomenon (see e.g. Heading 1962), as indicated in Kuś *et al.* (1993).

B.2 Phase space semiclassics

Here we describe briefly a semiclassical formalism in phase space, similar to the one used by Eckhardt *et al.* (1992) and Narimanov *et al.* (1998b). It is of course analytically equivalent to the position space formalism described in chapter 5. We write $\bar{A}(\bar{z}, \Delta z)$ (5.57) as the inverse Fourier transform

$$\bar{A}(\bar{z}, \Delta z) = \int d\bar{p}\, W(\bar{z}, \bar{p}) e^{-i\bar{p}\Delta z/\hbar} \tag{B.7}$$

of the Wigner function (5.58). We wrote $p \equiv p_z$ for convenience of notations. The integral (5.25) reads then

$$\mathcal{I} = \sum_{\ell} \int d\bar{z} \int d\bar{p} \int d\Delta z \sqrt{\frac{p_x p'_x}{-m_{12}}} W(\bar{z}, \bar{p}) e^{i\bar{\mathcal{S}}_2(\bar{z}, \Delta z)/\hbar - i\bar{p}\Delta z/\hbar} \quad , \tag{B.8}$$

where $\bar{\mathcal{S}}_2(\bar{z}, \Delta z)$ has been defined in (5.59). First one can integrate over $\delta\Delta z$ by Gaussian quadratures *without* any stationary approximation, which gives

$$\mathcal{I} = \sum_{\ell} \int d\bar{z} \int d\bar{p} \sqrt{\frac{p_x p'_x}{-m_{12} D}} W(\bar{z}, \bar{p}) e^{i[S_0 + g(\bar{y}, \bar{p})]/\hbar} \tag{B.9}$$

with

$$\begin{aligned} g(\bar{z}, \bar{p}) &= -\bar{p}\Delta z_0 + \delta\bar{z}\Delta p^0 + \delta\bar{z}^2 \frac{\mathrm{Tr}M - 2}{2m_{12}} - 2\left(\bar{p}^0 - \bar{p} + \delta\bar{z}\frac{m_{22} - m_{11}}{2m_{12}}\right)^2 \frac{m_{12}}{\mathrm{Tr}M + 2} \\ &= \left[(\mathrm{Tr}M + 2)(-\bar{p}\Delta z_0 + \Delta p^0 \delta\bar{z}) - 2m_{12}\delta\bar{p}^2 + 2\delta\bar{p}\delta\bar{z}(m_{22} - m_{11}) + 2\delta\bar{z}^2 m_{21}\right] / (\mathrm{Tr}M + 2) \\ D &= \frac{\mathrm{Tr}M + 2}{8m_{12}} \end{aligned}$$

where we have defined $\delta\bar{p} = \bar{p} - \bar{p}_0$. Integrating (B.9) with the Gaussian Wigner transform (5.58) yields the same result as the integration in position configuration (5.35). The phase space formalism might be useful for stationary phase consideration, e.g. if one supposes that W is smooth. Neglecting W in the SPA condition applied to (B.9), one find periodic orbits. Then one can either neglect W in the integration and obtain the hard limit result (5.64), or consider the variations of W and obtain the intermediate result (5.62).

to the "mountain" path, making it impossible to distort the path from the real axis.

REFERENCES

ABRAMOWITZ M AND STEGUN I A. 1964. *Handbook of mathematical functions.* Dover Publications, New York.

ATKINS K M AND EZRA G S. 1994. *Semiclassical density of states at symmetric pitchfork bifurcations in coupled quartic oscillators.* Phys. Rev. A, **50**, 93.

BARANGER H U. 1997. *Chaos in ballistic structures: theory.* In: Timp G (ed), *Nanoscience and technology.* Springer-Verlag, New-York.

BARANGER H U, JALABERT R A AND STONE A D. 1993. *Quantum-chaotic scattering effects in semiconductor microstructures.* CHAOS, **3**, 665.

BARDEEN J. 1961. *Tunnelling from a many-particle point of view.* Phys. Rev. Lett., **6**, 57.

BARTLETT M S AND MOYAL J E. 1948. *The exact transition probabilities of quantum-mechanical oscillators calculated by the phase-space method.* Proc. Camb. Phil. Soc., **45**, 545.

BERRY M V. 1989. *Some quantum-to-classical asymptotics.* In: Giannoni M J, Voros A and Zinn-Justin J (eds), *Chaos and quantum physics* (Les Houches, session LII). North-Holland, Amsterdam.

BERRY M V AND TABOR M. 1977. *Calculating the bound spectrum by path summation in action-angle variables.* J. Phys. A, **10**, 371.

BOEBINGER G S, LEVI A F J, PASSNER A, PFEIFFER L N AND WEST K W. 1993. *Direct observation of the electron spectral function in the integer and fractional quantum Hall regimes by resonant tunneling.* Phys. Rev. B, **47**, 16608.

BOEBINGER G S, NARIMANOV E E AND STONE A D. 1997. *Precursors and transition to chaos in a quantum well in a tilted magnetic field -Reply to comment.* Phys. Rev. Lett., **78**, 2866.

BOGOMOLNY E B. 1989. *Photoabsorption by atoms in external fields near the ionization threshold.* Sov. Phys. JETP, **69**, 275.

BOGOMOLNY E B AND ROUBEN D C. 1998. *Semiclassical description of resonant tunneling.* Europhys. Lett., **43**, 111.

BOGOMOLNY E B AND ROUBEN D C. 1999. *Semiclassical description of resonant tunneling.* Eur. Phys. J. B, **9**, 695.

BRACK M AND BHADURI R K. 1997. *Semiclassical physics.* Addison-Wesley, Reading, Mass.

BRODY T A, FLORES J, FRENCH J B, MELLO P A, PANDEY A AND WONG S S M. 1981. *Random-matrix physics: spectrum and strength fluctuations.* Rev. Mod. Phys., **53**, 385.

BRUUS H AND WHELAN N D. 1996. *Edge diffraction, trace formulae and the cardioid billiard.* Nonlinearity, **9**, 1023.

COHEN-TANNOUDJI C, DIU B AND LALOË F. 1973. *Mécanique quantique.* Hermann, Paris.

CREAGH S C AND WHELAN N D. 1999. *A matrix element for chaotic tunnelling rates and scarring intensities.* Ann. Phys., **272**, 196.

CREAGH S C, ROBBINS J M AND LITTLEJOHN R G. 1990. *Geometrical properties of Maslov indices in the semiclassical trace formula for the density of states.* Phys. Rev. A, **42**, 1907.

DANDO P A, MONTEIRO T S AND OWEN S M. 1998. *Periodic orbit theory for Rydberg atoms in external fields.* Phys. Rev. Lett., **80**, 2797.

DELANDE D, TAYLOR K T, HALLEY M H, VANDERVELDT T, VASSEN W AND HOGERVORST W. 1994. *Scaled energy-spectra of nonhydrogenic Rydberg atoms in a magnetic-field.* J. Phys. B, **27**, 2771.

DIEUDONNÉ J. 1968. *Calcul infinitésimal.* Hermann, Paris.

DU M L AND DELOS J B. 1988. *Effect of closed classical orbits on quantum spectra I & II.* Phys. Rev. A, **38**, 1896 and 1913.

ECKHARDT B, FISHMAN S, MULLER K AND WINTGEN D. 1992. *Semiclassical matrix elements from periodic orbits.* Phys. Rev. A, **45**, 3531.

EFETOV K. 1997. *Supersymmetry in disorder and chaos.* Cambridge University Press.

FRISCHAT S D AND DORON E. 1998. *Dynamical tunneling in mixed systems.* Phys. Rev. E, **57**, 1421.

FROMHOLD T M, EAVES L, SHEARD F W, LEADBEATER M L, FOSTER T J AND MAIN P C. 1994. *Magnetotunneling spectroscopy of a quantum well in the regime of classical chaos.* Phys. Rev. Lett., **72**, 2608.

FROMHOLD T M, FOGARTY A, EAVES L, SHEARD F W, HENINI M, FOSTER T J AND MAIN P C. 1995a. *Evidence for quantum states corresponding to families of stable and chaotic classical orbits in a wide potential well.* Phys. Rev. B, **51**, 18029.

FROMHOLD T M, WILKINSON P B, SHEARD F W, EAVES L, MIAO J AND EDWARDS G. 1995b. *Manifestations of classical chaos in the energy level spectrum of a quantum well.* Phys. Rev. Lett., **75**, 1142.

FROMHOLD T M, WILKINSON P B, SHEARD F W AND EAVES L. 1997a. *Comment on "Precursors and transition to chaos in a quantum well in a tilted magnetic field".* Phys. Rev. Lett., **78**, 2865.

FROMHOLD T M, SHEARD F W, EAVES L AND WILKINSON P B. 1997b. *Have quantum scars been observed? -Reply to comment.* Nature, **387**, 864.

FROMHOLD T M, WILKINSON P B, EAVES L, SHEARD F W, MAIN P C, HENINI M AND CARTER M J. 1997c. *Manifestations of quantum chaos in resonant tunnelling.* Chaos, Solitons & Fractals, **8**, 1381.

GRADSHTEYN I S AND RYZHNIK I M. 1994. *Table of integrals, series, and products.* Academic Press, San Diego.

GREENE J M, MACKAY R S, VIVALDI F AND FEIGENBAUM M J. 1981. *Universal behaviour in families of area-preserving maps.* Physica D, **3**, 468.

GUTZWILLER M C. 1990. *Chaos in classical and quantum mechanics.* Springer-Verlag, New York.

HEADING J. 1962. *An introduction to phase-integral methods.* Metheun, London.

HELLER E J. 1984. *Bound-state eigenfunctions of classically chaotic Hamiltonian systems: scars of period orbits.* Phys. Rev. Lett., **53**, 1515.

HILLERY M, O'CONNELL R F, SCULLY M O AND WIGNER E P. 1984. *Distribution functions in physics: fundamentals.* Phys. Rep., **106**, 121.

HONIG A AND WINTGEN D. 1989. *Spectral properties of strongly perturbed Coulomb-systems —fluctuations properties.* Phys. Rev. A, **39**, 5642.

KLEINERT H. 1995. *Path integrals in quantum mechanics, statistics, and polymer physics.* World Scientific, Singapore.

KUS M, HAAKE F AND DELANDE D. 1993. *Prebifurcation periodic ghost orbits in semi-classical quantization.* Phys. Rev. Lett., **71**, 2167.

LANDAU L D AND LIFSHITZ E M. 1977. *Quantum mechanics.* Pergamon, Oxford.

LEBOEUF P AND SARACENO M. 1990. *Eigenfunctions of non-integrable systems in generalised phase spaces.* J. Phys. A, **23**, 1745.

LICHTENBERG A J AND LIEBERMAN M J. 1983. *Regular and stochastic motion.* Springer-Verlag, New York.

MAIN J AND WUNNER G. 1997. *Hydrogen atom in a magnetic field: ghost orbits, catastrophes, and uniform semiclassical approximations.* Phys. Rev. A, **55**, 1743.

MAIN J, WIEBUSCH G, WELGE K, SHAW J AND DELOS J B. 1994. *Recurrence spectroscopy - observation and interpretation of large-scale structure in the absorption-spectra of atoms in magnetic-fields.* Phys. Rev. A, **49**, 847.

MAO J-M AND DELOS J B. 1992. *Hamiltonian bifurcation theory of closed orbits in the diamagnetic Kepler problem.* Phys. Rev. A, **45**, 1746.

MEHTA M L. 1991. *Random matrices.* Academic press, San Diego.

MILLER W. 1975. *Semiclassical quantization of nonseparable systems: a new look at periodic orbit theory.* J. Chem. Phys., **63**, 996.

MILLER W H. 1974. *Classical-limit quantum mechanics.* Adv. Chem. Phys., **25**, 69.

MONTEIRO T S AND DANDO P A. 1996. *Chaos in a quantum well in tilted fields: a scaling system.* Phys. Rev. E, **53**, 3369.

MONTEIRO T S, DELANDE D, FISHER A J AND BOEBINGER G S. 1997a. *Bifurcations and the transition to chaos in the resonant-tunneling diode.* Phys. Rev. B, **56**, 3913.

MONTEIRO T S, DELANDE D AND CONNERADE J P. 1997b. *Have quantum scars been observed? -Comment.* Nature, **387**, 863.

MULLER G, BOEBINGER G S, MATHUR H, PFEIFFER L N AND WEST K W. 1995. *Precursors and transition to chaos in a quantum well in a tilted magnetic field.* Phys. Rev. Lett., **75**, 2875.

NARIMANOV E E AND STONE A D. 1998a. *Origin of strong scarring of wave functions in quantum wells in a tilted magnetic field.* Phys. Rev. Lett., **80**, 49.

NARIMANOV E E AND STONE A D. 1998b. *Theory of the periodic orbits of a chaotic quantum well.* Phys. Rev. B, **57**, 9807.

NARIMANOV E E AND STONE A D. 1999. *Quantum chaos in quantum wells.* Physica D, **131**, 221.

NARIMANOV E E, CERRUTI N R, BARANGER H U AND TOMSOVIC S. 1998a. *Chaos in quantum dots: dynamical modulation of coulomb blockade peak heights.* eprint cond-mat/9812165.

NARIMANOV E E, STONE A D AND BOEBINGER G S. 1998b. *Semiclassical theory of magnetotransport through a chaotic quantum well.* Phys. Rev. Lett., **80**, 4024.

OTT E. 1993. *Chaos in dynamical systems.* Cambridge University Press.

OZORIO DE ALMEIDA A M. 1988. *Hamiltonian systems: chaos and quantization.* Cambridge University Press.

PRESS W H, FLANNERY B P, TEUKOLSKY S A AND VETTERLING W T. 1989. *Numerical recipes.* Cambridge University Press.

RICHTER K. 1997. *Semiclassical theory of mesoscopic quantum systems.* Habilitationsschrift, Max-Planck-Institut für Physik komplexer Systeme, Dresden. Also to be published by Springer-Verlag.

ROUBEN D C. 1997. *Description semiclassique de l'effet tunnel résonant.* Ph.D. thesis, Université de Paris XI -Orsay.

SARAGA D S AND MONTEIRO T S. 1998a. *Quantum chaos with nonperiodic, complex orbits in the resonant tunneling diode.* Phys. Rev. Lett., **81**, 5796.

SARAGA D S AND MONTEIRO T S. 1998b. *Quantum wells in tilted fields: semiclassical analysis and experimental evidence for effects "beyond" periodic orbits.* Phys. Rev. E, **57**, 5252.

SARAGA D S, MONTEIRO T S AND ROUBEN D C. 1998. *Periodic orbit theory for resonant tunneling diodes: comparison with quantum and experimental results.* Phys. Rev. E, **58**, R2701.

SCHOMERUS H AND SIEBER M. 1997. *Bifurcations of periodic orbits and uniform approximations.* J. Phys. A, **30**, 4537.

SHEPELYANSKY D L AND STONE A D. 1995. *Chaotic Landau level mixing in classical and quantum wells.* Phys. Rev. Lett., **74**, 2098.

SHUDO A AND IKEDA K S. 1998. *Chaotic tunneling: a remarkable manifestation of complex classical dynamics in non-integrable quantum phenomena.* Physica D, **115**, 234.

TAKADA S, WALKER P N AND WILKINSON M. 1995. *Transfer-matrix approach to tunneling between Kolmogorov-Arnold-Moser tori.* Phys. Rev. A, **52**, 3546.

WILKINSON M. 1987. *A semiclassical sum rule for matrix elements of classically chaotic systems.* J. Phys. A, **20**, 2415.

WILKINSON P B, FROMHOLD T M AND EAVES L. 1996. *Observation of "scarred" wavefunctions in a quantum well tieh chaotic electron dynamics.* Nature, **380**, 608.

XAVIER A L AND DE AGUIAR M A M. 1997. *Phase-space approach to the tunnel effect: a new semiclassical traversal time.* Phys. Rev. Lett., **79**, 3323.

ZOBAY O AND ALBER G. 1993. *Periodic orbits and molecular photoabsorption.* J. Phys. B, **26**, L539.